

# XXVIII Conference on Computer Methods in Materials Technology



BOOK OF ABSTRACTS



**BOOK OF ABSTRACTS**  
**OF THE**  
**XXVIII INTERNATIONAL CONFERENCE**  
**ON COMPUTER METHODS**  
**IN MATERIALS TECHNOLOGY**  
**KOMPLASTECH 2023**

March 5–8, 2023, Zakopane, Poland



Edited by:  
Danuta Szeliga, Łukasz Rauch

Book of Abstracts

XXVIII International Conference  
on Computer Methods  
in Materials Technology

# **KOMPLASTECH 2023**

March 5–8, 2023, Zakopane, Poland

Book of Abstracts  
of the XXVIII Conference on Computer Methods  
in Materials Technology KOMPLASTECH 2023  
March 5–8, 2023, Zakopane, Poland

Abstracts published based on the manuscripts submitted by authors.  
The work and all parts contained in it are protected by copyright.

Abstracts were reviewed  
by the members of the Scientific Committee KomPlasTech 2023 Conference.

Book cover design and preparation: AKNET.

Cover photos: AKNET private archives.

Desktop publishing:  [www.aknet.biz.pl](http://www.aknet.biz.pl)

## **International Scientific Committee**

Tudor BALAN	Ecole Nationale Supérieure d'Arts et Métiers, Paris, France
Markus BAMBACH	ETH D-MAVT Zurich, Switzerland
Thierry BARRIERE	FEMTO-ST Institute, Besancon, France
Wolfgang BLECK	RWTH Aachen University, Germany
Dominik BRANDS	University of Duisburg-Essen, Germany
Ryszard BUCZKOWSKI	West Pomeranian University of Technology in Szczecin, Poland
Tadeusz BURCZYŃSKI	IPPT PAN, Warszawa, Poland
Witold CECOT	Cracow University of Technology, Poland
Jose Cesar de SA	University of Porto, Portugal
Francesco CHINESTA	Ecole Centrale de Nantes, France
Zbigniew GRONOSTAJSKI	Wrocław University of Technology, Poland
Ernst KOZESCHNIK	TU Wien, Austria
Jan KUSIAK	AGH University of Science and Technology, Kraków, Poland
Wacław KUŚ	Silesian University of Technology, Gliwice, Poland
Jari LARKIOLA	University of Oulu, Finland
Maciej PASZYŃSKI	AGH University of Science and Technology, Kraków, Poland
Ulrich PRAHL	TU-Bergakademie Freiberg, Germany
Stefanie REESE	RWTH Aachen University, Germany
Jerzy ROJEK	IPPT PAN, Warszawa, Poland
Norbert SCZYGIOL	Częstochowa University of Technology, Poland
Jan SLADEK	Slovak Academy of Sciences, Bratislava, Slovakia
Christof SOMMITSCH	Graz University of Technology, Austria
Bartek WIERZBA	Łukasiewicz Research Network – Warsaw Institute of Technologies, Poland
Bradley WYNNE	University of Strathclyde, Glasgow, UK

## **Steering Committee**

Maciej PIETRZYK	AGH University of Science and Technology, Kraków, Poland
Franciszek GROSMAN	Silesian University of Technology, Katowice, Poland

## **Conference Chairs**

Danuta SZELIGA
Łukasz RAUCH
AGH University of Science and Technology, Kraków, Poland

## **Conference Secretary**

Anna SMYK
AGH University of Science and Technology, Kraków, Poland

## Local Organizer



## Partner



Department of Applied Computer Science and Modelling  
Faculty of Metals Engineering and Industrial Computer Science  
**AGH UNIVERSITY OF SCIENCE AND TECHNOLOGY**

## Supporting Organisations



European Community on Computational Methods  
in Applied Sciences  
**ECCOMAS**



Metal Forming Section, Metallurgy Committee  
**POLISH ACADEMY OF SCIENCES**



Centre of Computer Technology in Metallurgy  
and Materials Science  
**CEKOMAT**



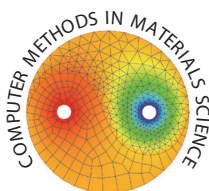
Polish Association for Computational Mechanics

## Venue



Nosalowy Dwór  
Oswalda Balzera 21d, Zakopane, Poland

## Journal



<http://www.cmms.agh.edu.pl/>



This project has received funding from the Research Fund  
for Coal and Steel under grant agreement No 899455.



---

The publication is co-financed from the state budget under the programme  
of the Minister of Education and Science called "Excellent Science" project no. DNK/SP/548041/2022  
subsidy amount 63 470 PLN, total project value: 263 470 PLN



Ministry of Education and Science  
Republic of Poland



Republic  
of Poland



## Content

The gradient theory for a dynamic analysis of interface crack between two dissimilar dielectric materials.....	15
<i>Jan Sladek, Vladimír Sladek, Maryan Hrytsyna, Slavomir Hrcek</i>	
Evolutionary multi-objective optimization of truss topology for additively manufactured components .....	19
<i>Petr David, Tomáš Mareš, Nirupam Chakraborti</i>	
Dome Shape Optimization of Composite Pressure Vessels Using Data-Driven Evolutionary Algorithms.....	22
<i>Dominik Vondráček, Zdeněk Padovec, Tomáš Mareš, Nirupam Chakraborti</i>	
Nucleation of dislocation loop in TWIP steel: Assessing the meta-atom framework .....	25
<i>Sweta Kumari, Amlan Dutta</i>	
Surrogate model assisted design optimization of composite bone plates for selective stress shielding .....	28
<i>Raja Dhason, Sandipan Roy, Shubhabrata Datta</i>	
Determination of modelling parameters for finite element analysis of electric-assisted deformation using genetic algorithm approach .....	33
<i>Jai Tiwari, Bashista Kumar Mahanta, Hariharan Krishnaswamy, Sivasrinivasu Devadula, Murugaiyan Amirthalingam</i>	
Investigating the role of hard plate hot forging process on the tensile deformation behaviour of a novel Mg-4Zn-0.5Ca-0.8Mn alloy employing visco-plastic self-consistent modelling.....	37
<i>Darothi Bairagi, Rahul Rakshit, Manas Paliwal, Sumantra Mandal</i>	
Evolutionary Algorithms in Robot Calibration .....	41
<i>Pavel Bastl, Nirupam Chakraborti, Michael Valášek</i>	
Multi-objective optimization of distillation operation using a hybrid of evolutionary algorithm and neural network .....	44
<i>Ataklti Kahsay Wolday, Manojkumar Ramteke</i>	

Multiscale modelling to study the evolution of texture and associated deformation mechanism during single point incremental forming .....	46
<i>Rahul Rakshit, Sushanta Kumar Panda, Sumantra Mandal</i>	
Automatic stabilization of difficult isogeometric analysis simulations with Deep Neural Networks .....	49
<i>Tomasz Służalec, Maciej Paszyński</i>	
Hierarchical matrices acceleration of GMRES solver in four-dimensional Finite Element Method computations .....	53
<i>Mateusz Dobija, Anna Paszyńska, Marcin Łoś, Maciej Paszyński</i>	
Physics Informed Neural Networks for wave propagation problems.....	57
<i>Paweł Maczuga, Maciej Paszyński</i>	
FEM model of Beverage Can Manufacturing Process .....	61
<i>Przemysław Wędrychowicz</i>	
Determining strains and stresses in composite based on FBG measurements .....	64
<i>Wacław Kuś, Waldemar Mucha, Iyasu Tafese Jiregna</i>	
Yarn modelling in multibody environment.....	67
<i>Maximilian Krentzien, Michael Beitelschmidt</i>	
Modelling of temperature change during deformation of TWIP steel.....	70
<i>Magdalena Barbara Jabłońska, Katarzyna Jasiak, Karolina Kowalczyk, Marek Tkocz, Zbigniew Gronostajski</i>	
Development and validation of the crystal plasticity model for AA6082 aluminum alloy during hot deformation.....	73
<i>Oleksandr Lypchanskyi, ChenChun Chiu, Faisal Qayyum, Grzegorz Korpala, Ulrich Prael</i>	
Accounting for random character of nucleation in modelling of phase transformations in steels.....	77
<i>Łukasz Poloczek, Roman Kuziak, Jakub Foryś, Danuta Szeliga, Maciej Pietrzyk</i>	
Optimization, Design and Modelling with Genetic Algorithms: Tracing Trends in Selected Applications since Year 1989.....	81
<i>Wojciech Paszkowicz</i>	
Towards Open Science with Multi-Cloud Computing using Onedata .....	83
<i>Michał Orzechowski, Michał Wrzeszcz, Bartosz Kryza, Łukasz Dutka, Renata G. Słota, Jacek Kitowski</i>	

Optimization of spring steel flat bar rolling using advanced meshless solution and genetic algorithm .....	86
<i>Miha Kovačič, Umut Hanoglu, Robert Vertnik, Aljaž Zupanc, Božidar Šarler</i>	
Powder bed operations in the model of selective laser melting process .....	90
<i>Dmytro Svyetlichnyy, Dominika Matuszyk</i>	
Application of ANN models to profile deformations analysis in RTH process.....	93
<i>Hanna Sadłowska, Andrzej Kochański</i>	
Numerical Model for Fast Predicting of Residual Stresses in Hot Rolled Profiles.....	96
<i>Andrij Milenin, Roman Kuziak, Szczepan Witek, Łukasz Rauch, Ivan Milenin, Krzysztof Bzowski, Maciej Pietrzyk</i>	
Concurrent algorithms for integrating three-dimensional B-spline functions into machines with shared memory such as GPU .....	99
<i>Maciej Woźniak, Anna Janina Szyska</i>	
Molecular dynamics simulations of the interdiffusion at $\alpha$ -Al <sub>2</sub> O <sub>3</sub> /AlSi12 interface .....	103
<i>Masoud Tahani, Eligiusz Postek, Tomasz Sadowski</i>	
Selected aspects of modelling the process of forming nickel superalloys sheets and tubes...	107
<i>Monika Hyrcza-Michalska</i>	
Hot-rolling production planning and melt shop sequencing problems.....	110
<i>Krzysztof Regulski, Łukasz Rauch, Krzysztof Bzowski, Piotr Hajder, Andrzej Opaliński, Monika Pernach, Michał Piwowarczyk</i>	
Feasibility of knowledge graphs as a tool for data storage in production planning systems .....	113
<i>Maciej Krzywda, Krzysztof Regulski, Łukasz Rauch</i>	
Prediction of Bainite Formation during Hot Deformation Processes using a Macro-scale Finite Element Analysis .....	116
<i>Missam Irani, Towhid Faraji Shovay, Grzegorz Korpala, Ulrich Prael</i>	
Electrical and thermal analysis for the copper removal process in an electric furnace.....	120
<i>Radosław Zybała, Sławomir Golak, Tomasz Sak, Piotr Madej</i>	
The modelling of the diffusion process, review .....	122
<i>Bartek Wierzba</i>	
Virtual and Augmented Reality Applications in Manufacturing of Precision Assembly Systems.....	126
<i>Tomasz Dębiński, Danuta Szeliga, Marcin Hojny</i>	

Linear welding power prediction measurement-based models .....	129
<i>Krzysztof Regulski, Łukasz Rauch, Krzysztof Bzowski, Piotr Hajder, Monika Pernach, Jan Kusiak</i>	
Spot-resistant welding process of profiled wire for precise filtration screens – experiments and modelling.....	132
<i>Marcin Kwiecień, Mateusz Kopyściański, Krzysztof Muszka, Janusz Majta</i>	
Computer modelling of the ablation casting process and prediction of strength properties of AC-42000 castings .....	135
<i>Marcin Małysha, Sabina Puzio, Katarzyna Major-Gabryś, Mirosław Głowacki, Dorota Wilk-Kołodziejczyk, Jadwiga Kamińska</i>	
Parametrization of Sieverts’ law for gaseous hydrogen solubility using electrochemical experiments – a feasibility study .....	140
<i>Andreas Drexler, Jonathan Nietzke, Josef Domitner, Klemens Mraczek, Christof Sommitsch, Thomas Böllinghaus</i>	
Evaluation of the hardware counters for neighbours’ selection algorithms in the random cellular automata grain growth model.....	144
<i>Mateusz Sitko, Kacper Pawlikowski, Łukasz Madej</i>	
Application of Finite Element Method based simulations and metamodeling techniques for prediction of liquid steel cooling rate in main ladles .....	147
<i>Łukasz Rauch, Monika Pernach, Michał Piwowarczyk, Łukasz Sztangret</i>	
Model of heat transfer in High Frequency Welding – numerical approach and laboratory investigation.....	151
<i>Ivan Milenin, Monika Pernach, Łukasz Rauch, Bogdan Pawłowski, Dorota Tyrała</i>	
Distributed system for monitoring of welding processes and prediction of final products quality .....	154
<i>Krzysztof Regulski, Łukasz Rauch, Krzysztof Bzowski, Piotr Hajder, Monika Pernach, Jan Kusiak</i>	
Fast model of phase transformations for cooling of Pyroware 53 steel .....	158
<i>Łukasz Rauch, Władysław Zalecki, Bogdan Garbarz, Krzysztof Raga, Krzysztof Bzowski, Maciej Pietrzyk</i>	
Modelling of roller levelling of plates using machine learning algorithms .....	162
<i>Łukasz Sztangret, Danuta Szeliga</i>	
Optimisation of production and quality improvement with computational fluid dynamics in the steelmaking industry .....	166
<i>Monika Zielińska, Hongliang Yang, Łukasz Madej, Łukasz Malinowski</i>	

Evolutionary Optimization Managed by Agents with Socio-Cognitive Traits.....	170
<i>Krzysztof Czech, Aleksandra Urbańczyk,</i>	
<i>Marek Kisiel-Dorohinicki, Aleksander Byrski</i>	
Long-product quality optimization through enhancement and utilisation of residual stress minimizing process strategies.....	173
<i>Volker Diegelmann, Hagen Krambeer, Andreas Wolff</i>	
Cyber-physical system for integrated management of steel and rolling mills – architecture and implementation details.....	176
<i>Krzysztof Bzowski, Monika Pernach, Piotr Hajder, Krzysztof Regulski</i>	
Pressure influence during gas quenching on mechanical properties of gears.....	179
<i>Artur Wojtyczka, Bartosz Iżowski, Kamil Dychtoń, Ryszard Filip</i>	
Computer aided design of rotary forming technology with laser beam material heating .....	182
<i>Barbara Mrzygłód, Izabela Olejarczyk-Woźeńska, Marcin Hojny,</i>	
<i>Tomasz Dębiński, Przemysław Marynowski</i>	
The true stress–strain curve evaluation in post-necking phase of tensile test using DIC and numerical simulation.....	184
<i>Sławomir Świlło, Robert Cacko</i>	
Core structure analysis of dislocations in TWIP steel under the Meta-atom framework: An assessment.....	187
<i>Sri Sadgun Reddy Pulagam, Amlan Dutta</i>	
Modelling of phase transformations in steels accounting for a stochastic character of the austenite grain size after hot forming .....	190
<i>Danuta Szeliga, Natalia Czyżewska, Jan Kusiak,</i>	
<i>Piotr Oprocha, Maciej Pietrzyk, Paweł Przybyłowicz</i>	
Experimental and numerical investigation of extrudate swell of polylactic acid (pla) via material extrusion (mex) additive manufacturing process .....	194
<i>Hong Wang, Abel Cherouat, Alexandre Gilbin, Thierry Barriere</i>	
Environment monitoring and sensor layers data integration in the production process of the electrosteel plant .....	197
<i>Andrzej Opaliński, Piotr Hajder, Monika Pernach, Łukasz Sztangret,</i>	
<i>Krzysztof Regulski, Krzysztof Bzowski, Łukasz Rauch, Michał Piwowarczyk</i>	
Index of Authors .....	201



# The gradient theory for a dynamic analysis of interface crack between two dissimilar dielectric materials

Jan Sladek<sup>1</sup>, Vladimir Sladek<sup>1</sup>, Maryan Hrytsyna<sup>1</sup>, Slavomir Hrcek<sup>2</sup>

<sup>1</sup> Institute of Construction and Architecture, Slovak Academy of Sciences,  
84503 Bratislava, Slovakia

<sup>2</sup> Faculty of Mechanical Engineering, University of Zilina, 01026 Zilina, Slovakia  
jan.sladek@savba.sk, vladimir.sladek@savba.sk,  
maryan.hrytsyna@savba.sk, slavomir.hrcek@fstroj.uniza.sk

**Keywords:** direct flexoelectricity, mixed finite element method, pure dynamic load, electric intensity vector

## 1. Introduction

The interface crack between two dissimilar dielectric materials under a mechanical load is investigated with including flexoelectricity effects. Layered structures are efficiently utilized in many advanced engineering microelectronics applications, where a thin film coating technology is applied. Due to different material properties of layers there are induced high stress gradients near the interface. Therefore, a delamination and occurrence of failure is often observed in the layered structures. To predict the failure it is needed to analyze interfacial stress and strain fields along the interface and mainly near the tip of interface cracks. The classical theory of elasticity is scale independent and applicable only to large structures, where the microstructure of the materials can be ignored [1]. The classical continuum model does not reflect the material microstructure [2]. In microelectronics it is a tendency to reduce size of devices/structures to nanoscale, where new phenomena are observed. Therefore an advanced model has to be applied to small structures, when the size of structure is comparable with the characteristic length of the material microstructure. In the present paper the gradient theory of elasticity is employed where the characteristic length of the material microstructure is involved in constitutive equations [3–4].

The flexoelectricity is the electro-mechanical coupling known as the generation of electric polarization by a strain gradient (direct flexoelectric effect) in solid dielectrics. The direct flexoelectric effect is considered in constitutive equations for electric displacement and higher-order stresses (gradient stresses) [5]. In many literature sources, one can find application of the gradient elasticity theory to small-scale structures. However, most of the existing works ignore the contribution of inertia gradient effect on structural kinetic energy [6].

The influence of flexoelectricity on an interface crack between two dissimilar dielectric materials under an impact load is investigated in this paper. The direct flexoelectricity is considered here. The Hamilton's principle is applied to derive governing equations. The variational formulation has been used to derive the mixed finite element method (FEM) equations. The C0 continuous approximation is applied independently to displacements and displacement gradients. The kinematic constraints between both approximated fields are satisfied by collocation at some internal points of elements.

---

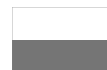
The publication is co-financed from the state budget under the programme  
of the Minister of Education and Science called "Excellent Science" project no. DNK/SP/548041/2022



**Doskonała  
Nauka**



Ministry of Education and Science  
Republic of Poland



**Republic  
of Poland**

## 2. Gradient theory for an interface crack problem

In the direct flexoelectricity, the constitutive equations in dielectric materials can be written as [7]

$$\begin{aligned}\sigma_{ij} &= c_{ijkl} \epsilon_{kl} \\ \mu_{jkl} &= -f_{ijkl} E_i + g_{jklmni} \eta_{mni} \\ D_i &= a_{ij} E_j + f_{ijkl} \eta_{jkl}\end{aligned}\quad (1)$$

where symbols  $\sigma_{ij}$ ,  $\mu_{ijk}$  and  $D_i$  denote the Cauchy stresses, higher-order stresses and electric displacement, respectively. Symbols  $\mathbf{a}$  ( $a_{ij}$ ),  $\mathbf{c}$  ( $c_{ijkl}$ ),  $\mathbf{f}$  ( $f_{ijkl}$ ) and  $\mathbf{g}$  ( $g_{jklmni}$ ) are used for the permittivity, elastic stiffness tensors, the direct flexoelectric coefficients and the higher-order elasticity coefficients, respectively.

Strains  $\epsilon_{ij}$ , electric intensity vector  $E_j$  and strain-gradient tensor  $\eta_{ijk}$  can be expressed by the displacements  $u_i$  and electric potential  $\phi$

$$\begin{aligned}\epsilon_{ij} &= \frac{(u_{i,j} + u_{j,i})}{2} \\ E_j &= -\phi_{,j}\end{aligned}\quad (2)$$

$$\eta_{ijk} = \epsilon_{ij,k} = \frac{(u_{i,j} + u_{j,i})}{2}\quad (3)$$

The higher-order elastic parameters  $g_{jklmni}$  are assumed to be proportional to the conventional elastic stiffness coefficients  $c_{klmn}$

$$g_{jklmni} = l^2 c_{jklmni} \delta_{ii}\quad (4)$$

where the internal length material parameter  $l$  is considered as the only one additional material coefficient.

A similar approach is utilized for the direct flexoelectric coefficients  $f_{ijkl}$  which are represented by only two independent parameters  $f_1$  and  $f_2$ :

$$f_{ijkl} = f_1 \delta_{ij} \delta_{kl} + f_2 (\delta_{ij} \delta_{kl} + \delta_{ik} \delta_{jl})\quad (5)$$

The governing differential equations for this problem are derived from the Hamilton's principle

$$\delta \int_0^t (U - W - K) d\tau = 0\quad (6)$$

where  $\delta U$  is the variation of potential energy,  $\delta W$  is the work done by external forces,  $\delta K$  is the variation of kinetic energy, and  $\tau$  is the time variable.

Consistently with the above constitutive equations in gradient theory, the variation of electric enthalpy density  $U$  is given by

$$\delta U = \sigma_{ij} \delta \epsilon_{ij} + \mu_{ijk} \delta \eta_{ijk} + D_k \delta \phi_{,k}$$

Assuming the micro-inertia according to Askes and Aifantis [6], the variation of kinetic energy is described by

$$\begin{aligned}
\delta \int_0^t K d\tau &= \int_0^t \int_V \rho (\dot{u}_i \delta \dot{u}_i + l_1^2 \dot{u}_{i,j} \delta \dot{u}_{i,j}) dV d\tau = \\
&= - \int_0^t \int_V \rho (\ddot{u}_i \delta u_i + l_1^2 \ddot{u}_{i,j} \delta u_{i,j}) dV d\tau = \\
&= - \int_0^t \int_V \rho (\ddot{u}_i + l_1^2 \ddot{u}_{i,j} \delta u_{i,j}) \delta u_i dV d\tau - \int_0^t \int_V \rho l_1^2 n_j \ddot{u}_{i,j} \delta u_i dV d\tau
\end{aligned} \tag{7}$$

where  $\rho$  is the mass density and  $l_1$  is the micro-inertia length scale parameter.

Then, the following governing equations can be derived

$$\begin{aligned}
s_i &:= \frac{\partial u_i}{\partial \mathbf{n}} = \frac{\partial u_i}{\partial x_j} n_j \\
D_{k,k}(\mathbf{x}, \boldsymbol{\tau}) &= 0
\end{aligned} \tag{8}$$

The mixed FEM will be developed in the full length paper, where the displacements and strains are approximated by  $C^0$  continuous interpolation with using correspondingly nodal values of approximated fields.

The weak-form of a boundary value problem in gradient elasticity can be written as

$$\begin{aligned}
&\int_V [(\sigma_{ij} + \rho l_1^2 \ddot{u}_{i,j}) \delta u_{i,j} + \mu_{ijk} \delta u_{i,jk} + D_k \delta \phi_{,k} + \rho \ddot{u}_i \delta u_i] dV = \\
&= \int_{\Gamma_i} \bar{l}_i \delta u_i d\Gamma + \int_{\Gamma_x} \bar{R}_i \delta s_i d\Gamma + \int_{\Gamma_q} \bar{Q}_i \delta \phi_i d\Gamma
\end{aligned} \tag{9}$$

where

$$s_i := \frac{\partial u_i}{\partial \mathbf{n}} = \frac{\partial u_i}{\partial x_j} n_j \quad R_i := n_k n_j n_{ijk} \quad Q_i := n_k D_k$$

Substituting the spatial approximations of elastic displacements and electric potential on each element into the weak form (9), we get the discretized FEM equations as a system of ordinary differential equations (ODE). The system of ODE can be solved by a time integration procedure.

## References

1. Askes H., Gitman I.: *Non-singular stresses in gradient elasticity at bi-material interface with transverse crack*. International Journal of Fracture, 156, 2009, 217–222.
2. Buhlmann S., Dwir B., Baborowski J., Murali P.: *Size effects in mesoscopic epitaxial ferroelectric structures: increase of piezoelectric response with decreasing feature-size*. Applied Physics Letters, 80, 2002, 3195–3197.
3. Aravas N., Giannakopoulos A.E.: *Plane asymptotic crack-tip solutions in gradient elasticity*. International Journal of Solids and Structures, 46, 2009, 4478–4503.
4. Sladek J., Sladek V., Stanak P., Zhang C., Tan C.L.: *Fracture mechanics analysis of size-dependent piezoelectric solids*. International Journal of Solids and Structures, 113, 2017, 1–9.

5. Sladek J., Sladek V., Jus M.: *The MLPG for crack analyses in composites with flexoelectric effects*. Composite Structures, 204, 2018, 105–113.
6. Askes H., Aifantis E.C.: *Gradient elasticity in statics and dynamics: An overview of formulations, length scale identification procedures*. International Journal of Solids and Structures, 48, 2011, 1962–1990.
7. Hu S.L., Shen S.P.: *Electric field gradient theory with surface effect for nano-dielectrics*. CMC-Computers, Materials & Continua, 13, 2009, 63–87.

**Acknowledgements.** The authors acknowledge the support by the Slovak Science and Technology Assistance Agency registered under number APVV-18-0004 and VEGA-2/0061/20.

# Evolutionary multi-objective optimization of truss topology for additively manufactured components

Petr David<sup>1</sup>, Tomáš Mareš<sup>1</sup>, Nirupam Chakraborti<sup>1</sup>

<sup>1</sup> Department of Mechanics, Biomechanics and Mechatronics, Faculty of Mechanical Engineering, Czech Technical University in Prague, Technická 4, 160 00, Prague, Czech Republic  
Petr.David@fs.cvut.cz, Tomas.Mares@fs.cvut.cz,  
Nirupam.Chakraborti@fs.cvut.cz

**Keywords:** Truss, topology, evolutionary, algorithms, optimization

## 1. Introduction

This work focuses on the use of truss topology optimization to produce optimized designs with respect to multi-objective heat transfer and mechanical compliance formulation for additively manufactured components. Firstly, the motivation behind the problem is laid out, then, optimization formulation and solver environments are presented, and finally, the results and discussion conclude the manuscript.

A lot of scientific effort was put into researching topology optimization and its many different subfields in the past 20 years, however, there are still uncharted, or little explored areas. Inspired by a problem from an industrial partner, we focus on the multi-objective formulation, including heat transfer and structural compliance. An example problem schematic is depicted in Figure 1 below.

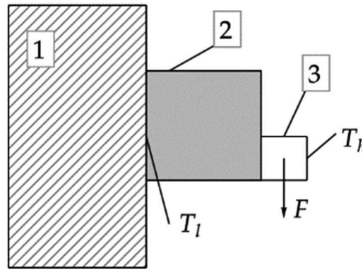


**Figure 1.** The problem schematic. 1 denotes a testing machine, 2 labels the design area for a clamp, and 3 is a tested component.

There, we can see a testing machine, denoted by 1, measured component, which is denoted by 3 and a design area, denoted by 2. Our goal is to design such a structure, that would be as stiff as possible, meaning if the testing machine 1 were to move, the tested component 3 would move as similarly as possible. At the same time, however, the tested component is heated to an elevated temperature  $T_h$ . In order to maintain the proper functioning of the testing machine, its temperature ( $T_l$ ) should be as close to ambient temperature as possible. In other words, we wish to isolate component 3 from component 1 in terms of heat transfer.

---

The publication is co-financed from the state budget under the programme of the Minister of Education and Science called "Excellent Science" project no. DNK/SP/548041/2022

## 2. Problem statement

As has been mentioned previously, we shall tackle the problem of finding such optimized component by the means of truss topology optimization. In particular, we use the so-called ground structure approach, where one discretizes the design area by a ground structure and looks for the optimized substructure with respect to the boundary conditions and optimization formulation [1]. For the present problem, we used a  $9 \times 9$  node grid, where the neighbouring nodes are connected by bars. The individual bars' areas are our design variables, of which there are 272 for this particular discretization.

### 2.1. The stiffness model

The stiffness model uses static analysis of the truss. Our cost function represents compliance minimization by minimizing the work of external forces on the structure, with a constraint on the maximum volume to reconstruct the truss. Taken as equations, we can write:  
minimize:

$$\mathbf{f}^T \mathbf{u}(a)$$

subject to:

$$\sum_{i=1}^n a_i l_i \leq V \quad (1)$$

where  $a_i$  denotes area of bar  $i$  of which there are  $n$  in the whole truss, similarly,  $l_i$  denotes the length of bar  $i$ ,  $\mathbf{f}$  denotes the global force vector, which induces corresponding global displacement vector  $\mathbf{u}$ , and finally  $V$  is the volume of available material to construct the optimized truss [1].

### 2.2. The heat transfer model

The heat transfer model is based on a steady state heat conduction analysis. In equation form, we can write:  
minimize:

$$\sum_{j=1}^m Q_j(a_j)$$

subject to:

$$\sum_{i=1}^n a_i l_i \leq V \quad (2)$$

where the subscript  $j$  marks the bars, which are connected to the testing machine 1,  $Q_j$  denotes heat flux through bar  $j$ .

## 3. Optimization and results

The presented optimization problem was solved by two evolutionary algorithms. The first one being EvoDN2, complemented by cRVEA, which were written in Matlab [2]. The second one was NSGA II, which was running in Python [3]. The number of individuals for the optimization was

set to 1000 and the number of generations to 300. The optimization by NSGA II took on average between 25 to 30 minutes, whereas the optimization by cRVEA took around 5 minutes for the same parameters. However, the optimization by cRVEA was preceded by the training of the metamodells by a deep neural network, which for this problem took up to 5 days. When a good enough fitness was found for the metamodells, one could then only work with the cRVEA, which was fast. The Pareto plot of the two optimization runs can be seen in Figure 2. There, we can see the filtered results of the NSGA-II algorithm and the ones from EvoDN2, by removing the dominated results. It can be seen that the results obtained through EvoDN2 have shown a lesser spread as compared to the NSGA-II results, however, most of the non-dominated ones have reached a better optimum than NSGA-II. Three results from the optimization are shown, two of them from the extremes, found by NSGA-II and one intermediate results, which was found by EvoDN2 and cRVEA.

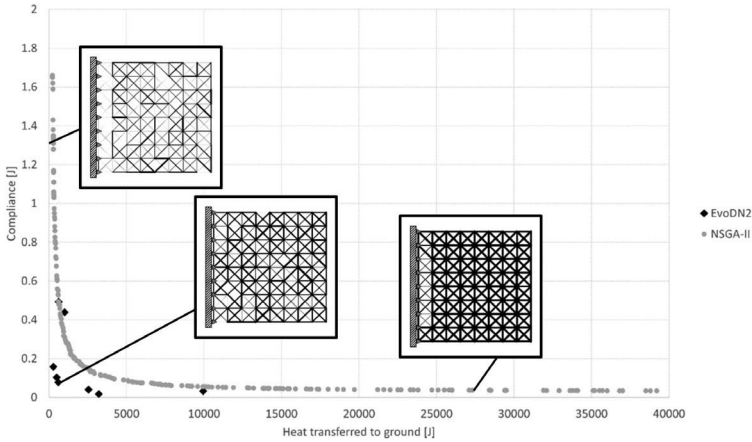


Figure 2. Pareto plot of both optimization runs.

## 4. Conclusion

In this work, a multi-objective heat transfer and compliance topology optimization was introduced. The models, as well as problem statement were presented, and later used to solve an example problem, inspired by an industrial problem. The optimization was solved by two algorithms, EvoDN2 coupled with cRVEA, and NSGA-II. Finally, the results were shown and discussed.

## References

1. Bendsøe M., Sigmund O.: *Topology optimization: theory, methods and applications. Second edition, corrected printing.* Springer, Berlin, 2004.
2. Chakraborti N.: *Data-Driven Evolutionary Modeling in Materials Technology.* CRC Press, Boca Raton, 2023.
3. Deb K., Pratap A., Agarwal S., Meyarivan T.: *A fast and elitist multiobjective genetic algorithm: NSGA-II.* IEEE Transactions on Evolutionary Computation, 6, 2002, 182–197.

**Acknowledgements.** This study received support from the Grant Agency of the Czech Technical University in Prague, under grant No. SGS21/151/OHK2/3T/12.

# Dome Shape Optimization of Composite Pressure Vessels Using Data-Driven Evolutionary Algorithms

Dominik Vondráček<sup>1</sup>, Zdeněk Padovec<sup>1</sup>, Tomáš Mareš<sup>1</sup>, Nirupam Chakraborti<sup>1</sup>

<sup>1</sup> Department of Mechanics, Biomechanics and Mechatronics, Faculty of Mechanical Engineering, Czech Technical University in Prague, Prague, Czech Republic  
Dominik.Vondracek@fs.cvut.cz, Zdenek.Padovec@fs.cvut.cz,  
Tomas.Mares@fs.cvut.cz, Nirupam.Chakraborti@fs.cvut.cz

**Keywords:** pressure vessels, end dome, composite materials, data-driven modelling, multi-objective optimization

## 1. Introduction

Pressure vessels are essential for modern industry because many technical applications require the storage capacity for gas or liquid at a pressure significantly higher than the ambient. However, conventional (metal) pressure vessels are not able to meet all requirements of modern industrial applications (primarily aimed at achieving weight savings), especially in the aerospace industry, automotive industry, etc... Possible solution of this problem is the use of composite pressure vessels manufactured by means of filament winding technology. This method is widely used because it allows manufacturing the entire pressure vessels (cylindrical part and the end dome) in one manufacturing operation [1]. In the following sections, the solved problem will be briefly described.

## 2. Solved problem

In this study a new end dome shape for filament wound pressure vessels was designed according to the Hoffman strength criterion using a data-driven evolutionary approach along with a classical mechanics-based analysis. The analysis of four end dome shells (a spherical shell, a geodesic-isotenoid shell [2], a shell based on minimizing of the Tsai-Hill's criterion [3] and a newly designed shell) of the revolution of double curvature manufactured by means of helical winding were performed. The meridian curves and stresses were evaluated analytically and compared with each other. The analytical solution is based on the classic lamination theory (CLT). However, in this case it is possible to use a simplification in the form of the netting theory [4] for obtaining the thickness of the dome. The netting theory assumes only fiber loading (there is no participation of matrix to the load).

Multi-criterial optimization was used to find the optimal shape of the end dome. Surrogate models were created through two different evolutionary optimization algorithms: Evolutionary Neural Net (EvoNN) and Bi-objective Genetic Programming (BioGP) and bi-objective evolutionary optimization studies were carried out using them. The main task of this study was to design the end dome shape, that would be able to carry the greatest possible internal pressure and have

---

The publication is co-financed from the state budget under the programme of the Minister of Education and Science called "Excellent Science" project no. DNK/SP/548041/2022



Doskonała  
Nauka



Ministry of Education and Science  
Republic of Poland



Republic  
of Poland

the shallowest end dome at the same time. Meridian curves of the newly designed end dome were approximated by ellipses. This method is based on the approach proposed by Fukunaga in his work [3]. The optimization task can be written as

$$f(x) = \begin{cases} \max F_1 \\ \min F_2 \end{cases} \quad (1)$$

where  $x$  is the variable that represent the semi-minor axis of the ellipse (nine hundred end dome shapes were created for  $x$  from 100 mm to 900 mm for both material systems), function  $F_1$  represents the damage pressure  $p_d$  and function  $F_2$  represents the depth of the dome at the polar hole. Hoffman strength criterion is used for computing the damage pressure and can be written as

$$u = \frac{\sigma_L^2}{F_{Ll}F_{Lc}} + \frac{\sigma_T^2}{F_{Tl}F_{Tc}} - \frac{\sigma_L\sigma_T}{F_{Ll}F_{Lc}} + \frac{F_{Lc} - F_{Ll}}{F_{Ll}F_{Lc}}\sigma_L + \frac{F_{Tc} - F_{Tl}}{F_{Tl}F_{Tc}}\sigma_T + \frac{\sigma_{LT}^2}{F_{LT}^2} = 1 \quad (2)$$

where  $F_{Ll}$  is longitudinal tensile strength,  $F_{Lc}$  is longitudinal compressive strength,  $F_{Tl}$  is transversal tensile strength,  $F_{Tc}$  is transversal compressive strength and  $F_{LT}$  is shear failure strength along fibers. The two objectives  $F_1$  and  $F_2$  that are presented in Eq. (1) were firstly calculated analytically for different values of the decision variable  $x$  and the data were fed to two different evolutionary optimization algorithms: Evolutionary Neural Net (EvoNN) and Bi-objective Genetic Programming (BioGP) [5,6]. These algorithms are able to create lighter surrogate models which were passed on to the optimization module of these paradigms to carry out their simultaneous optimization in order to generate the Pareto front [7] between the two objective functions.

### 3. Results and discussion

Two different material systems, a glass/epoxy and a carbon/epoxy systems (volumetric fiber content of 60 %) were considered in this study. Analytical solutions were obtained for them with the elastic properties shown in Table 1 and the strength properties shown in Table 2. The other analysis input characteristics comprised a radius of the polar hole of  $r_0 = 200$  mm, an equator radius of  $R = 500$  mm ( $r_0/R = 0.4$ ), and a thickness on the equator of  $h_0 = 1.3$  mm (obtained by netting analysis of cylindrical part of the pressure vessel). The computations were prepared in the MATLAB code, which allows both for the rapid determination of the results and the simple changing of the input parameters (the material parameters, the polar opening and the equator radius and the thickness).

**Table 1.** Elastic properties of the lamina in the appropriate directions.

Material	$E_L$ [MPa]	$E_T$ [MPa]	$G_{LT}$ [MPa]	$\nu_{LT}$ [MPa]
Glass/epoxy	46 200	16 513	5 998	0.31
Carbon/epoxy	139 800	9 830	6 395	0.34

**Table 2.** Strength properties of the lamina in the appropriate directions.

Material	$F_{Ll}$ [MPa]	$F_{Lc}$ [MPa]	$F_{Tl}$ [MPa]	$F_{Tc}$ [MPa]	$F_{LT}$ [MPa]
Glass/epoxy	1 200	600	45	145	65
Carbon/epoxy	2 940	900	50	230	100

Pareto plots were obtained for each material system. An area close to the intersection point of EvoNN and BioGP Pareto lines was chosen for detailed analysis in both material systems. The intersection points of the Pareto lines obtained from EvoNN and BioGP were chosen as the preferred

optimal solution for both material systems. Variable  $x = 282$  mm was chosen as the optimal solution for the glass/epoxy system and variable  $x = 284$  mm was chosen as the optimal solution for the carbon/epoxy system. The optimal solutions are very similar for both material systems however the damage pressure is almost two times higher when the carbon/epoxy system is used.

The meridian curves of the analyzed domes are shown in Figure 1 (glass/epoxy system is shown in Figure 1 (a) and carbon epoxy system is shown in Figure 1 (b)). In the case of the geodesic isotensoid shell and shell based on minimizing the Tsai-Hill's criterion only the analyzed wide concave part of the curve is displayed. Interesting results were achieved, and the newly designed end dome shapes are shallower than the known end dome shapes.

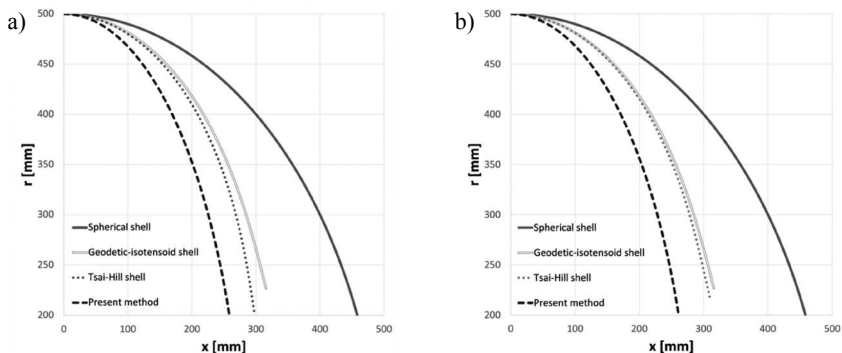


Figure 1. Meridian curves of the analyzed domes.

## References

1. Madhavi M.: *Design and Analysis of Filament Wound Composite Pressure Vessel with Integrated-End Domes*. Defense Science Journal, 59, 2009, 73–81.
2. Zickel J.: *Isotensoid Pressure Vessels*. ARS Journal, 32, 1962, 950–951.
3. Fukunaga H., Uemura M.: *Optimum Design of Helically Wound Composite Pressure Vessels*. Composite Structures, 1, 1983, 31–49.
4. Young R.E.: *History and Potential of Filament Winding*. 13<sup>th</sup> Annual Technical Conference SPI – RP, 1958.
5. Chakraborti N.: *Data-Driven Evolutionary Modeling in Materials Technology*. CRC Press, Boca Raton, 2023.
6. Pettersson F., Chakraborti, N., Saxén, H.: *A Genetic Algorithms Based Multi-Objective Neural Net Applied to Noisy Blast Furnace Data*. Applied Soft Computing, 7, 2007, 387–397.
7. Chakraborti N.: *Critical Assessment 3: The Unique Contributions of Multi-Objective Evolutionary and Genetic Algorithms in Materials Research: The Unique Contributions of Multi-Objective Evolutionary and Genetic Algorithms in Materials Research*. Materials Science and Technology, 30, 2014, 1259–1262.

**Acknowledgements.** This study received support from the Grant Agency of the Czech Technical University in Prague, under grant No. SGS21/151/OHK2/3T/12.

# Nucleation of dislocation loop in TWIP steel: Assessing the meta-atom framework

Sweta Kumari<sup>1</sup>, Amlan Dutta<sup>1</sup>

<sup>1</sup> Department of Metallurgical and Materials Engineering,  
Indian Institute of Technology Kharagpur, West Bengal 721302, India  
sweta1993@iitkgp.ac.in,  
amlan.dutta@metal.iitkgp.ac.in

**Keywords:** Meta-atom potential, Dislocation, Nucleation, Twinning, TWIP steel

## 1. Introduction

The scope of application and reliability of classical molecular dynamics (MD) simulations depend upon the development of suitable interatomic potentials, which is a significantly challenging job for simulating complex materials like multi-component alloys. In this regard, Wang et al. have proposed and demonstrated the idea of meta-atom molecular modeling, where the atoms of different elements are replaced by the meta-atoms of a single type [1]. It is based on the concept that if meta-atoms effectively emulate a material's basic intrinsic properties, simulations using those meta-atoms should also perfectly model the secondary properties, which in turn depend on the primary intrinsic characteristic of metals. The existing studies with meta-atom potentials have explored the primary properties on one hand [1,2], and the final deformation simulations on the other [3,4] while the intermediate properties connecting them remain uncharted. Using the nudged-elastic-band approach and the meta-atom interatomic potential, we perform atomistic computations to investigate the homogenous nucleation of dislocation loops in TWIP steel. These results also present a chance to interpret the dislocation's nucleation mechanism in terms of the intrinsic length scale of the meta-atom potential.

## 2. Result and discussion

The EAM potential used in this study for TWIP steel was developed by matching it to the results of DFT calculations [2]. The composition used for the DFT computations was Fe-22 wt.% Mn-0.6 wt.% C is one of the most widely studied compositions of TWIP steel [5,6]. The proposed intrinsic length scale for the meta-atom potential for its applications in the deformation behavior of the alloy is 4–6 nm, at which both unstable and stable SFEs exhibit statistical variations below 10% standard deviation. The findings of our calculations are compared and analyzed only in accordance with this length scale. Energy barriers of the dislocation nucleation process have been measured for a range of applied shear stresses, and an atomistically informed nucleation model is fitted to the results for both Shockley and twinning dislocation loops. Figure 2(a) shows an example of NEB calculations by showing the structural energy variations along the transition paths of nucleation of Shockley and twinning loops, corresponding to the disregistry energies shown in Figure 1(a) and (b), respectively. We find that the NEB results exhibit energy maxima representing the barriers to

---

The publication is co-financed from the state budget under the programme  
of the Minister of Education and Science called "Excellent Science" project no. DNK/SP/548041/2022



loop nucleation for both types of dislocation loops. Figure 2(b) shows the variation of energy barrier measured at various applied shear loads.

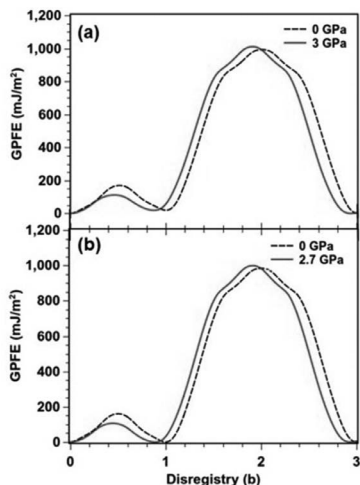


**Figure 1.** (a) GSFE and (b) GPFE profiles for the stress-free and stressed crystals. The indicated non-zero shear stress values are the maximum stresses at which the nucleation barriers have been estimated in this study.

The nucleation model shows excellent concordance with the direct atomistic data and predicts the dislocation loop’s critical size. A comparison of the critical loop diameters with the intrinsic spatial scale of the meta-atom potential reveals that the loop nucleation is driven by local compositional change. As a result, it is shown that critical analysis is crucial to fully comprehend the simulation outcomes produced with a meta-atom potential.

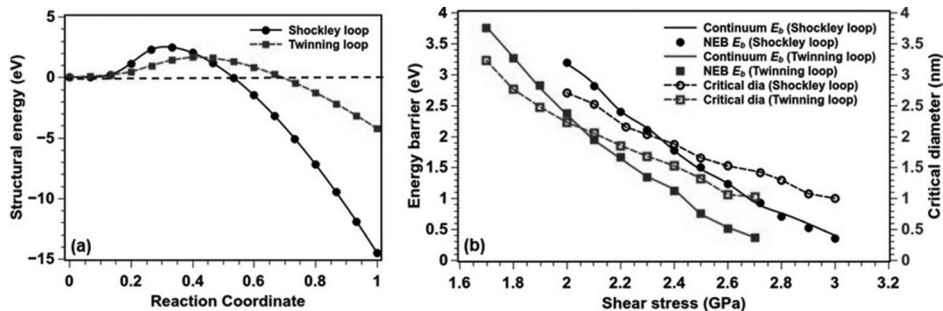


**Figure 2.** (a) Structural energies plotted against the reaction coordinates for the Shockley and twinning loop nucleation in TWIP steel. (b) Energy barriers and the corresponding critical diameters are displayed as the functions of applied shear stress.

### 3. Conclusion

In conclusion, the present study investigates the nucleation process of partial dislocation loops in TWIP steel within the meta-atom framework. Atomistic calculations show that the computed energy barriers for Shockley and twinning loops using the meta-atom interatomic potential are in

very good agreement with the mathematical model. We further observe that the critical size of such a loop is small enough for the chemical heterogeneity to play a role in its nucleation. A sequel of this study may explore the process of heterogeneous loop nucleation, where the critical loop size can exceed the intrinsic length scale due to smaller nucleation stress.

## References

1. Wang P., Wang H.: *Meta-atom molecular dynamics for studying material property dependent deformation mechanisms of alloys*. Journal of Applied Mechanics Transactions ASME, 84, 2017.
2. Wang P., Xu S., Liu J., Li X., Wei Y., Wang H., Gao H., Yang W.: *Atomistic simulation for deforming complex alloys with application toward TWIP steel and associated physical insights*. Journal of Mechanics and Physics of Solids, 98, 2017, 290–308.
3. Mohammadzadeh R.: *Reversible deformation in nanocrystalline TWIP steel during cyclic loading by partial slip reversal and detwinning*. Materials Science and Engineering A, 782, 2020, 13921.
4. Mohammadzadeh R., Mohammadzadeh M.: *Inverse grain size effect on twinning in nanocrystalline TWIP steel*. Materials Science and Engineering A, 747, 2019, 265–275.
5. Tian Y.Z., Bai Y., Zhao L.J., Gao S., Yang H.K., Shibata A., Zhang Z.F., Tsuji N.: *A novel ultrafine-grained Fe–22Mn–0.6C TWIP steel with superior strength and ductility*. Materials Characterization, 126, 2017, 74–80.
6. Gutierrez-Urrutia I., Raabe D.: *Dislocation and twin substructure evolution during strain hardening of a Fe-22 wt.% Mn-0.6 wt.% C TWIP steel observed by electron channeling contrast imaging*. Acta Materialia, 59, 2011, 6449–6462.

**Acknowledgements.** We sincerely appreciate the Science and Engineering Research Board, Govt. of India, for supporting this research through the ECRA scheme. We also acknowledge the financial support provided by the Indian Institute of Technology Kharagpur through the ISIRD grant.

# Surrogate model assisted design optimization of composite bone plates for selective stress shielding

Raja Dhason<sup>1</sup>, Sandipan Roy<sup>2</sup>, Shubhabrata Datta<sup>3</sup>

<sup>1</sup> Assistant Professor, SRM Institute of Science and Technology,  
Kattankulathur, Tamilnadu India

<sup>2</sup> Research Assistant Professor, SRM Institute of Science and Technology,  
Kattankulathur, Tamilnadu India

<sup>3</sup> Research Professor, SRM Institute of Science and Technology,  
Kattankulathur, Tamilnadu India

rajad@srmist.edu.in, sandipag@srmist.edu.in,  
shubhabp@srmist.edu.in

**Keywords:** Composite bone plate, Movements, Finite element analysis, Artificial neural network, Genetic algorithm

## 1. Abstract

Optimal composite bone plate is designed for Periprosthetic Femoral Fracture (PFF) fixation using multi-objective Genetic algorithm (GA) by varying fibre materials and orientations in the laminate. The bone plate desires to be premeditated, that should allow higher displacement in axial direction and minimum movement in shear direction without compromising the rigidity in the other direction. The considerable movement in the fracture site is required for a better callus formation. Composite material was considered for the bone plate, the most important constraint in this design problem is that the axial movement and shear movement are limited to 2 mm and 0.5 mm, respectively. The above attributes are achieved by varying the material and fibre orientation in the bone plate to develop for PFF Fixation. The simulated data from the Finite Element Analysis (FEA) is used to develop Artificial Neural Network (ANN) surrogate models for the bone displacements in both the directions. The surrogate models are used as the objective functions for multi-objective optimization. FEA is used to validate the solutions derived through the design optimization process. The results showed only 10% deviation in the simulation output when compared to optimum solutions achieved from GA.

## 2. Introduction

Fractured bone was fixed with a metal bone plate, and fragments decrease fractures, restrict mobility, and protect fracture sites from stress for better healing [1]. However, stress shielding soon after fracture fixation delays callus formation, bone regeneration, and causes periprosthetic fractures (B1 type) around the implant, mostly in the femur following Total Hip Replacement (THR). Most periprosthetic femur fractures happen after surgery because of stress shielding, which is caused by improper load sharing. This reduces bone stress and slows healing [2,3]. Several researchers studied PFF fixation using metal plates in different structures. They did experiments and used finite element analysis to find that metal plates carried more stress than bone, which could lead to stress

---

The publication is co-financed from the state budget under the programme of the Minister of Education and Science called "Excellent Science" project no. DNK/SP/548041/2022



Doskonała  
Nauka



Ministry of Education and Science  
Republic of Poland



Republic  
of Poland

shielding. Further, low-modulus composite bone plates were used to reduce stress shielding and enhance the fracture site's relative movement and compression force [4–7]. Relative movement in the axial direction is important for better healing, anisotropic bone plate allows longitudinal mobility and less shear movement on the fracture gap. To do this, the mechanical performance of composite bone plates made of different materials needs to be studied so that a plate with selective stress shielding can be made. Composite bone plate fabrication and trials cost more. The finite element method (FEM) solves a complex three-dimensional geometry problem to analyse the inner structural behaviour, which cannot be studied in-vivo. The author proposed guidelines for designing composite bone plates with the desired characteristics. The laminate stacking sequence and material contributions in each layer were changed to construct bone plates using laminate theory and FEM [8]. To find the optimum design, a Genetic Algorithm (GA) is employed. A surrogate model (ANN) was developed using simulation results. GA-based optimization uses these models to create materials and hybrid composites [9–11]. In the proposed work, using the simulated database from carbon/epoxy, glass/poxy, flax epoxy and hybrid, ANN models were developed and used as objective functions for GA-based optimization to find the optimal composite bone plate material and fibre orientation.

### 3. Finite element analysis

The surface model extracted from dry femur bone using surface scanner machine and further it was smoothen using Geomagic Design X software. The cemented hip implant was fitted in proximal region after removing the cancellous bone. 4 mm fracture gap was created just below the cement potting cube in transverse direction. FE model of Composite bone plate with 12 holes was modelled with various material, orientation (14 configurations) and different combination of material is shown in Figure 1. Material properties of composite bone plate, fibre orientation and laminate stacking sequence are assigned based on published literature [8]. Only Immediately Post-Operative (IPO) stage was simulated to extract the database from different combination. The femur was loaded in the proximal section of the stem with maximum load of 2300 N and the end of the femur was fixed in all the directions to study the behaviour of the PFF fixations with different combination of composite materials and to observe the axial movement and shear movement at the fracture site. Total of 126 numbers of FE analysis were carried out of IPO condition [8,12]. The database generated from FE analysis results were used for generating a ANN models for further process.

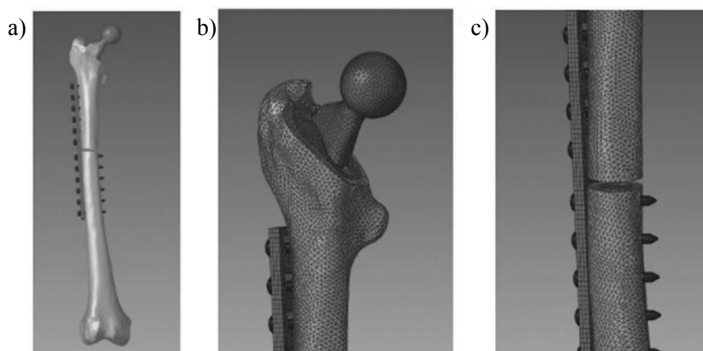


**Figure 1.** (a) Periprosthetic femoral fracture fixation with 12-hole plate  
 (b) shows the stem and bone cement in the fixation and  
 (c) Shows the fracture gap of 4 mm.

## 4. ANN modelling

The first ANN surrogate model, developed using the FE simulation data, consists of twenty-eight inputs of material properties (14) and fibre orientation (14) for fourteen layers and the one output, i.e. axial movement. It has 15 hidden neurons in a single hidden layer. A trial-and-error method is used to determine the number of neurons that provide the best predictability (Figure 2(a)). The second ANN model for shear movement had the same inputs. The scatter plot showing the predictability of the model is shown in Figure 2(b). A sensitivity analysis can be used to find out the influence of the input. It is possible to analyse the sensitivity of the input variables in many ways, but here we used the connection weight approach to analyse the sensitivity of the neural network trained model [13]. Based on the results of sensitivity analysis (Figure 3), we can see there is a clear indication that the relationships with the axial movement are different from that of shear movement for most of the inputs.

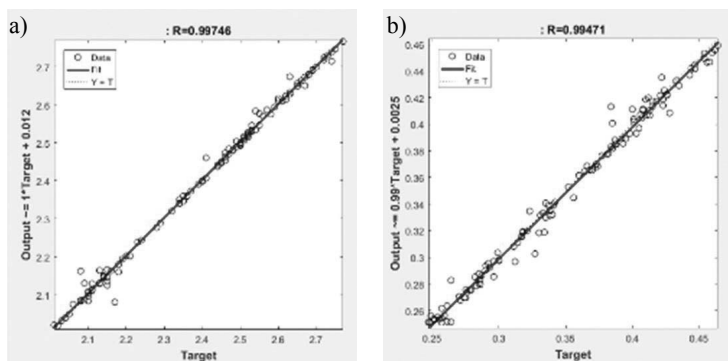


Figure 2. Scatter plot showing targets (T) vs. achieved output (Y) values for (a) axial movement and (b) shear movement.

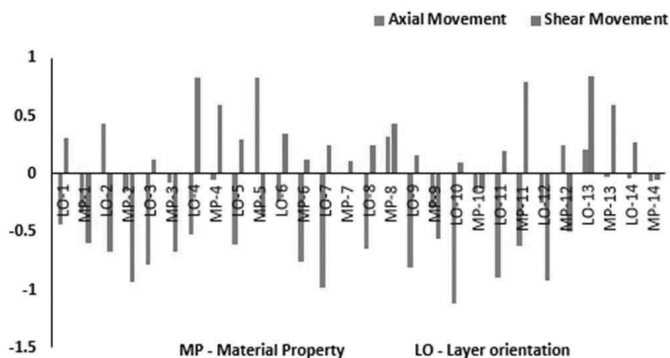
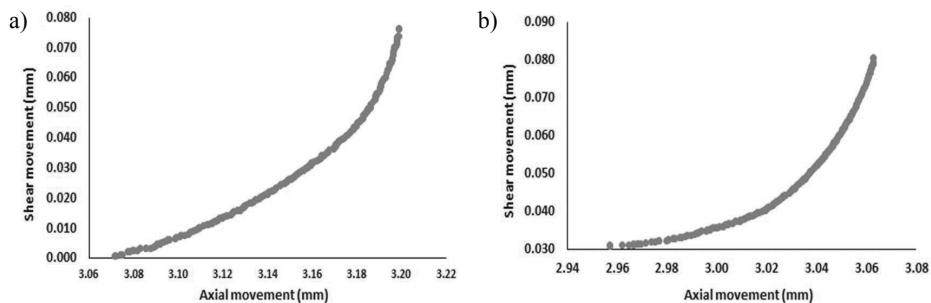


Figure 3. Sensitivity analysis plot for Axial movement and Shear movement.

## 5. Multi-objective optimization

Using GA, multi-objective optimization is carried out using ANN surrogate models as objective functions, which are developed for axial movement and shear movement for matching input variables related to achieve optimal solutions that combine the material property and layer orientation

effects of both. Optimization is performed with and without considering restraints of the total material property. Pareto plots for both axial movement and shear movement on changing the material property with and without constraints, which was shown in Figure 4. The material properties are non-constrained and constrained based on the availability of the material for further studies in this work, so that the problem of assigning the material properties which is not closer to the available could be avoided during manufacturing.



**Figure 4.** Pareto front for (a) Axial movement and Shear movement without 7 and material property control (b) Axial movement and Shear movement without restraint with material property control.

## 6. Conclusion

- The data generated through finite element simulation is successfully used to develop surrogate models using ANN tool. The ANN provided the role of the fibre materials and directions in determining the axial and shear movements in the composite bone plate.
- GA-based multi-objective design optimization of the composite structure, for achieving high axial displacement and low shear displacement, provides several solutions, which can be used for future experimental trials.

## References

1. Taljanovic M.S., Jones M.D., Ruth J.T., Benjamin J.B., Sheppard J.E., Hunter T.B.: *Fracture Fixation*. Radiographics, 23, 2003, 1569–1590.
2. Ganesh V.K., Ramakrishna K., Ghista D.N.: *Biomechanics of bone-fracture fixation by stiffness-graded plates in comparison with stainless-steel plates*. BioMedical Engineering Online, 4, 2005, 46.
3. Ridzwan M.I.Z., Shuib S., Hassan A.Y., Shokri A.A., Mohammad Ibrahim M.N.: *Problem of stress shielding and improvement to the hip implant designs: A review*. Journal of Medical Sciences, 7, 2007, 460–467.
4. Lever J.P., Zdero R., Nousiainen M.T., Waddell J.P., Schemitsch E.H.: *The biomechanical analysis of three plating fixation systems for periprosthetic femoral fracture near the tip of a total hip arthroplasty*. Journal of Orthopaedic Surgery and Research, 5, 2010, 45.
5. Ebrahimi H., Rabinovich M., Vuleta V., Zalzman D., Shah S., Dubov A., Roy K., Siddiqui F.S., Schemitsch E.H., Bougherara H., Zdero R.: *Biomechanical properties of an intact, injured, repaired, and healed femur: An experimental and computational study*. Journal of the Mechanical Behavior of Biomedical Materials, 16, 2012, 121–135.
6. Kim J.H., Kim S.H., Chang S.H.: *Estimation of the movement of the inter-fragmentary gap of a fractured human femur in the presence of a composite bone plate*. Journal of Composite Materials, 45, 2011, 1491–1498.
7. Fouda N., Mostafa R., Saker A.: *Numerical study of stress shielding reduction at fractured bone using metallic and composite bone-plate models*. Ain Shams Engineering Journal, 10, 2019, 481–488.

8. Samiezadeh S., Tavakkoli Avval P., Fawaz Z., Bougherara H.: *On optimization of a composite bone plate using the selective stress shielding approach*. Journal of the Mechanical Behavior of Biomedical Materials, 42, 2015, 138–153.
9. Sinha A., Sikdar Dey S., Chattopadhyay P.P., Datta S.: *Optimization of mechanical property and shape recovery behavior of Ti-(~49at.%) Ni alloy using artificial neural network and genetic algorithm*. Materials and Design, 46, 2013, 227–234.
10. Sultana N., Sikdar (Dey) S., Chattopadhyay P.P., Datta S.: *Informatics based design of prosthetic Ti alloys*. Materials Technology, 29, 2013, B69–B75.
11. Vinoth A., Dey S., Datta S.: *Designing UHMWPE hybrid composites using machine learning and metaheuristic algorithms*. Composite Structures, 267, 2021, 113898.
12. Dhasan R., Roy S., Datta, S.: *A biomechanical study on the laminate stacking sequence in composite bone plates for vancouver femur B1 fracture fixation*. Computer Methods and Programs in Biomedicine, 196, 2020, 05680.
13. Olden J.D., Joy M.K., Death R.G.: *An accurate comparison of methods for quantifying variable importance in artificial neural networks using simulated data*. Ecological Modelling, 178, 2004, 389–397.

# Determination of modelling parameters for finite element analysis of electric-assisted deformation using genetic algorithm approach

Jai Tiwari<sup>1</sup>, Bashista Kumar Mahanta<sup>2</sup>, Hariharan Krishnaswamy<sup>1</sup>,  
Sivasrinivasu Devadula<sup>1</sup>, Murugaiyan Amirthalingam<sup>3</sup>

<sup>1</sup> Manufacturing Engineering Section, Department of Mechanical Engineering, Indian Institute of Technology Madras, Chennai-600036, India

<sup>2</sup> Tribology and Combustion Division, Indian Institute of Petroleum, Council of Scientific and Industrial Research, Dehradun-248005, India

<sup>3</sup> Department of Metallurgical and Materials Engineering, Indian Institute of Technology Madras, Chennai-600036, India  
me18d006@smail.iitm.ac.in, bashista\_mahanta@yahoo.co.in,  
hariharan@iitm.ac.in, devadula@iitm.ac.in, murugaiyan@iitm.ac.in

**Keywords:** Electric-assisted forming, Joule heating fraction, Multi objective optimization, EvoNN, cRVEA

## 1. Introduction

Application of electric current pulses during plastic deformation of a material, commonly known as electric-assisted forming (EAF) is known to improve the formability and, reduce the forming force and springback. The process modelling and optimization of electrical assisted forming have gained significant attention in recent times to understand the underlying physical phenomena [1].

The flow stress drop observed during EAF is due to the combined action of thermal effect (Joule's heating) and the independent effect of electric current interaction with moving dislocations. Both the thermal and electrical effects exhibit similar trend (flow stress softening) during loading. The electrical effect on mechanical behaviour should be decoupled from the thermal response for effective modelling of the EAF. The primary concern in such attempt is the successful prediction of temperature profile observed during EA deformation. In finite element simulation of EAF process, the temperature profile due to Joule heating is predicted by providing various thermo-physical material properties. Out of all the input properties for such an analysis, effective heat transfer coefficient ( $h_{eff}$ ) and Joule heat fraction ( $\eta$ ) are sensitive to the microstructure, geometry of the specimen and the ambient conditions. As there is no established methodology to identify these two coefficients available in open literature, these are identified through various iterations of FE simulation. In the present work, a genetic algorithm based procedure is developed to predict these coefficients with greater accuracy, by replacing the traditional iterative methods [2]. Subsequently, FE simulation is carried out with the optimized coefficients to predict the time-temperature profile, which is in reasonable agreement with the experimentally obtained result from the pulsed current assisted uniaxial tension tests.

## 2. Methodology

A typical temperature vs. time profile during electropulsing is shown below in Figure 1. The pulsating time-temperature behaviour of electric-assisted deformation can be defined using three

---

The publication is co-financed from the state budget under the programme of the Minister of Education and Science called "Excellent Science" project no. DNK/SP/548041/2022



Doskonała  
Nauka



Ministry of Education and Science  
Republic of Poland



Republic  
of Poland

parameters, (i) peak temperature ( $T_p$ ), (ii) background temperature ( $T_b$ ) and (iii) rate of cooling ( $\Theta_T$ ) to the ambient temperature, as shown schematically in the Figure 1.

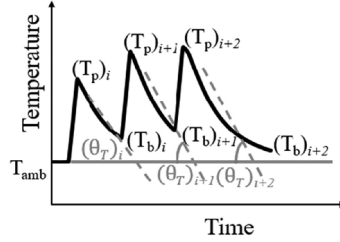


**Figure 1.** A representation of time-temperature profile showing the three variables (i) peak temperature ( $T_p$ ), (ii) background temperature ( $T_b$ ) and (iii) rate of cooling ( $\Theta_T$ ) in each of the applied pulses.

An efficient model should predict all the three parameters accurately in each pulse cycle. Alternatively, the error between the modelled and experimental results of these parameters should be minimized for the prediction of time temperature profile. Using this approach, three objective functions are identified for the optimization procedure, as shown in Eqs. (1)–(3).

$$\Phi_1 = \sum_{i=1}^n \sqrt{\left( \frac{(T_p)_{pred} - (T_p)_{exp}}{(T_p)_{exp}} \right)^2} \quad (1)$$

$$\Phi_2 = \sum_{i=1}^n \sqrt{\left( \frac{(T_b)_{pred} - (T_b)_{exp}}{(T_b)_{exp}} \right)^2} \quad (2)$$

$$\Phi_3 = \sum_{i=1}^n \sqrt{\left( \frac{(\Theta_T)_{pred} - (\Theta_T)_{exp}}{(\Theta_T)_{exp}} \right)^2} \quad (3)$$

Experimental data of EA tension test is used to verify the accuracy of the predicted coefficients from the data driven modelling. Evolutionary algorithms such as BioGP (bi-objective genetic programming) and EvoNN (Evolutionary Neural Network) are used to train the models with the objective functions for the subsequent optimization. After successful validation and testing of the trained models, multi-objective optimization is carried out using BioGP, EvoNN and cRVEA techniques to obtain the optimum solutions of the thermal coefficients [3,4].

### 3. Result and discussion

Hariharan et al., have suggested that the peak temperature was sensitive to  $\eta$  and the cooling rate was influenced primarily by  $h_{eff}$  [5]. Therefore, it is necessary to evaluate whether bi-objective optimization using only two of the three identified objectives could give optimum solution. Initially, only two-objective functions i.e., peak temperature error ( $\Phi_1$ ) and error in cooling rate ( $\Phi_3$ ), are used for the optimization of the trained dataset. However, the simulated temperature profile using the optimized coefficients does not match the experimentally measured one satisfactorily. Therefore, a constraint-based reference vector evolutionary algorithm (cRVEA) is used for minimization of all the three objectives ( $\Phi_{1-3}$ ). The Pareto solutions generated from the tri-objective optimization procedure are tabulated in the Table 1.

**Table 1.** Comparison of modelling parameters obtained by genetic algorithm and reference [4].

Parameters	$\eta$	$h_{eff}$
Genetic Algorithm	0.57	0.085
Reference (Iterative procedure)	0.6	0.1

The simulations carried out using the optimized thermal coefficients obtained by tri-objective optimization process match reasonably well with the experimental results (Figure 2). Thus, it can be concluded that the tri-objective optimization technique provides the best estimation of thermal modelling parameters of EA deformation processes.

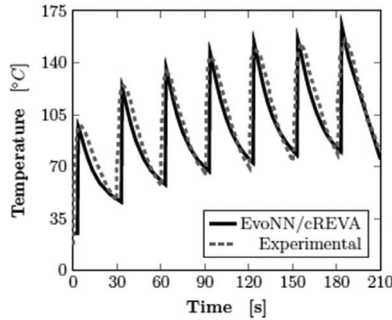


**Figure 2.** FE simulation results of electric assisted tension test carried out with the optimized modelling parameters obtained using EvoNN as training and cREVA as optimization technique.

## 4. Conclusion

It is shown that the evolutionary data-driven modelling and optimization approaches can be utilized to identify the thermal modelling parameters of the EA deformation process. Usage of genetic algorithm-based approaches is justified considering the complexities involved in analysis of such a process. The proposed methodology provides best estimation of modelling parameters required for FE analysis of an electric-assisted deformation process, highlighting the benefits of using this novel approach.

## References

1. Tiwari J., Balaji V., Krishnaswamy H., Amirthalingam M.: *Dislocation density based modelling of electrically assisted deformation process by finite element approach*. International Journal of Mechanical Sciences, 277, 2022, 107433.
2. Chakraborti N.: *Data-driven evolutionary modeling in materials technology*. CRC Press, 2022.
3. Pettersson F., Chakraborti N., Saxén H.: *A genetic algorithms based multi-objective neural net applied to noisy blast furnace data*. Applied Soft Computing, 7, 2007, 387–397.
4. Giri B.K., Hakanen J., Miettinen K., Chakraborti N.: *Genetic programming through bi-objective genetic algorithms with a study of a simulated moving bed process involving multiple objectives*. Applied Soft Computing, 13, 2013, 2613–2623.
5. Hariharan K., Lee M.-G., Kim M.-J., Han H. N., Kim D., Choi S.: *Decoupling thermal and electrical effect in an electrically assisted uniaxial tensile test using finite element analysis*. Metallurgical and Materials Transactions, 46, 2015, 3043–3051.

**Acknowledgements.** Authors would like to acknowledge the financial support from Science and Engineering Research Board (Project reference: CRG/2019/0D3539), Department of Science and Technology (DST) India.

# Investigating the role of hard plate hot forging process on the tensile deformation behaviour of a novel Mg-4Zn-0.5Ca-0.8Mn alloy employing visco-plastic self-consistent modelling

Darothi Bairagi<sup>1</sup>, Rahul Rakshit<sup>1</sup>, Manas Paliwal<sup>1</sup>, Sumantra Mandal<sup>1</sup>

<sup>1</sup> Department of Metallurgical and Materials Engineering, Indian Institute of Technology Kharagpur, West Bengal-721302, India

darothi94@gmail.com, rahul.rakshit00647@gmail.com,

manas.paliwal@metal.iitkgp.ac.in,

sumantra.mandal@metal.iitkgp.ac.in

**Keywords:** Mg alloy; Thermomechanical processing; Texture; Tensile curves; VPSC modelling

## 1. Introduction

In the last few decades, biodegradable Mg-based alloys have garnered huge attention in the field of temporary implants owing to their close resemblance to natural bone in terms of density and elastic modulus [1,2]. However, the hexagonal close packed (HCP) crystal structure of Mg-based alloys limits the slip activity in the material, leading to a difficulty in forming the intricate shapes required for temporary fixtures [1,2]. Although the requirement of mechanical properties varies depending upon the application site and design of the implant, a material should have at least 200 MPa yield strength (YS) and 10% elongation to be applicable for fabrication of temporary fixtures [1,3]. Towards this, a novel Mg-4Zn-0.5Ca-0.8Mn alloy system has been developed which has shown promising results in terms of *in-vitro* bio-corrosion resistance in homogenized condition (heat treated at 360°C for 24 h, referred as HT24 afterwards). However, the YS (132 MPa) and elongation (~5%) were insufficient in this condition for temporary implant applications. After carrying out hard plate hot forging (HPHF) at 300°C on the homogenized alloy (referred as F300 afterwards), a significant improvement in the YS (270 MPa) has been obtained along with a considerable increase in the ultimate tensile strength (UTS, 334 MPa) and elongation (~10%) value. Moreover, the F300 specimen shows basal texture, which is reported to significantly improve the corrosion resistance of the alloy [1] and this makes the specimen highly potential for implant applications. Although some researchers have experimentally observed that HPHF process can improve the mechanical properties, the role of slip systems and their relative activity in improving the YS and ductility of this particular alloy through thermomechanical processing is not yet investigated. Therefore, in this study, the critical resolved shear stress (CRSS) and related deformation mechanism of the Mg-4Zn-0.5Ca-0.8Mn alloy has been simulated using a visco-plastic self-consistent (VPSC) framework.

## 2. Results and discussion

In the VPSC model, HCP crystal structure with basal, prismatic, pyramidal slip systems and tensile twinning has been considered. The micro-texture of HT24 and F300 specimens have been analysed employing electron back scatter diffraction (EBSD) scans. These set of orientations

---

The publication is co-financed from the state budget under the programme of the Minister of Education and Science called "Excellent Science" project no. DNK/SP/548041/2022



have been discretized into 9000 orientations which has been used as input texture to the VPSC model. The hardening behavior of the specimens have been characterized using modified Voce hardening model. In order to match the experimental and VPSC simulated flow curves, a monotonic velocity gradient of uniaxial deformation has been applied into the VPSC code. The experimental and VPSC simulated stress-strain curves of the HT24 and F300 specimens are presented in Figure 1. The optimized hardening parameters used in the VPSC simulation are provided in Table 1. From the stress-strain curves, it can be observed that the HPHF process has significantly improved the YS, along with a moderate increase in UTS and ductility of the alloy.

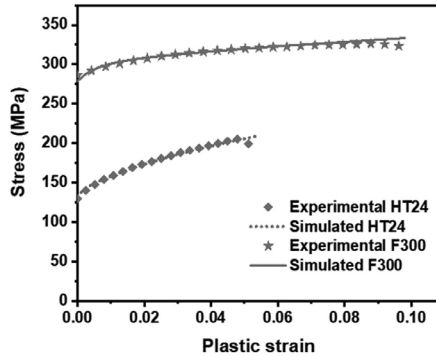


**Figure 1.** Experimental and VPSC simulated tensile stress-strain curve obtained at 0.0001/s strain rate.

**Table 1.** Hardening parameters for the specimens used in VPSC simulation.

Slip mode	Specimens							
	HT24				F300			
	$\tau_0$	$\tau_1$	$\theta_0$	$\theta_1$	$\tau_0$	$\tau_1$	$\theta_0$	$\theta_1$
Basal	80	10	5 000	1 200	150	70	4 500	280
Prismatic	135	8	72	60	280	10	100	40
Pyramidal <c+a>	155	8	270	119	290	1	600	40
Tensile twinning {10 $\bar{1}2$ }	75	40	2 000	110	150	30	2 000	40

Figure 2 shows the relative activity of different slip systems and tensile twinning during tensile deformation of the specimens, as obtained through simulation. The basal slip is considered the predominant slip mode in HCP material and hence should be given the highest importance. In the homogenized specimen, the basal slip activity is observed to be higher than that of the forged specimen at the initiation of tensile deformation (Figure 2a). It can be attributed to the random orientation of the grains present in the specimens. The weak texture of the specimen easily activates the basal slip mode in each grain at the initiation of deformation [4]. However, the activity of the basal mode is observed to decrease very steeply with increase in plastic strain during deformation (Figure 2a). It can be attributed to the easier rotation of the grains present in the specimen which alters the slip mode at later stage of deformation and limits basal slip [5,6]. Whereas, in case of the F300 specimen, the relative basal slip activity is lower than that of the HT24 specimen at the start of deformation (Fig. 2b). It results in the high YS observed in the specimen (Figure 1). However, in this case, the activity of the basal slip is maintained at a constant value throughout the complete span of deformation (Figure 2b). Since the F300 specimen shows basal texture before deformation and the texture is maintained due to restricted grain rotation

during the deformation process, the basal slip mode is observed to be quite active throughout the deformation process and thus contributes significantly towards enhanced ductility [5,6]. The ratio of  $CRSS_{\text{basal}}$  to  $CRSS_{\text{prismatic}}$  is obtained as 1.68 and 1.80 for the HT24 and F300 specimens, respectively. A low value of the ratio indicates that prismatic slip is activated very easily in material. It indicates that the alloy system under consideration is highly potential for intricate forming required for implant fabrication. Apart from that, the pyramidal  $\langle c+a \rangle$  activity is much higher in this specimen during the initiation of tensile deformation process. However, in both the specimens, the activity of this slip mode is considerably high throughout the deformation process. Therefore, it also acts as an additional mode for non-basal slip, which increases the ductility of the specimens. Nevertheless, further studies are being carried out to understand the implication of this mode in deformation process.

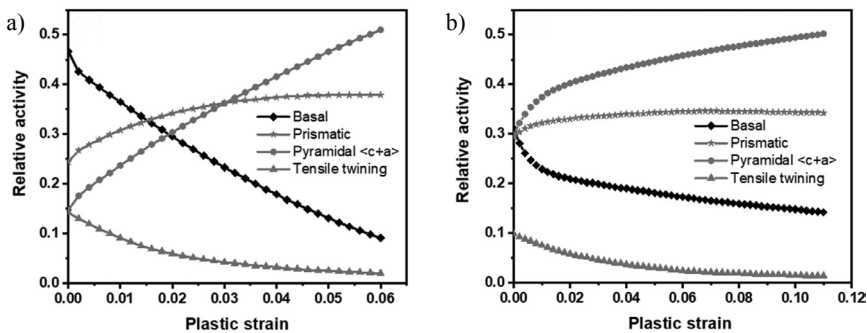


**Figure 2.** VPSC simulated relative activity plots of four main slip modes as a function of applied strain in (a) HT24, (b) F300 specimens.

### 3. Conclusions

- The alloy depicts a very low  $CRSS_{\text{basal}}/CRSS_{\text{prismatic}}$  value, indicating easier activation of prismatic slip in material.
- The HPHF process improves the YS due to presence of strong basal texture at the initiation of deformation.
- The HPHF process enhances the ductility from 5% to around 10%. This is mainly attributed to the basal slip activity in the specimen which is maintained throughout the tensile deformation process.

### References

1. Bairagi D., Mandal S.: *A comprehensive review on biocompatible Mg-based alloys as temporary orthopaedic implants: Current status, challenges, and future prospects*. Journal of Magnesium and Alloy, 10, 2022, 627–669.
2. Chen Y., Xu Z., Smith C., Sankar J.: *Recent advances on the development of magnesium alloys for biodegradable implants*. Acta Biomaterialia, 10, 201, 4561–4573.
3. Ding W.: *Opportunities and challenges for the biodegradable magnesium alloys as next-generation biomaterials*. Regenerative Biomaterials, 3, 2016, 79–86.
4. Maldar A., Wang L., Zhu G., Zeng X.: *Investigation of the alloying effects on deformation behaviour in Mg by Visco-Plastic Self-consistent modeling*. Journal of Magnesium and Alloys, 8, 2020, 210–218.

5. Zhao C., Li Z., Shi J., Chen X., Tu T., Luo Z., Cheng R., Aterns A., Pan F.: *Strain hardening behaviour of Mg-Y alloys after extrusion process*. Journal of Magnesium and alloys, 7, 2019, 672–680.
6. Chen S.F., Song H.W., Zhang S.H., Cheng M., Lee M.G.: *Effect of shear deformation on plasticity, recrystallization mechanism and texture evolution of Mg-3Al-1Zn alloy sheet: Experiment and coupled finite element-VPSC simulation*. Journal of Alloys and Compounds, 805, 2019, 138–152.

**Acknowledgements.** The authors wish to acknowledge Dr C.N. Tomé for sharing VPSC code. The authors also acknowledge the instrumental facilities provided by IIT Kharagpur.

# Evolutionary Algorithms in Robot Calibration

Pavel Bastl<sup>1</sup>, Nirupam Chakraborti<sup>1</sup>, Michael Valášek<sup>1</sup>

<sup>1</sup> Department of Mechanics, Biomechanics, Faculty of Mechanical Engineering,  
Czech Technical University in Prague, Technická 4, Prague  
pavel.bastl@fs.cvut.cz, nirupam.chakraborti@fs.cvut.cz,  
michael.valasek@fs.cvut.cz

**Keywords:** robots, calibration, evolutionary algorithms, EvoDN2, BioGP

## 1. Introduction

A robot can be considered as a universal kinematic structure which is driven by its drives and can be programmed based on its application. The structure of robot can take many forms including parallel or hybrid structures but the most commonly used structure is based on a serial arrangement as shown in Figure 1. What is common for the technical requirements of robot is accuracy which can be achieved by the structure. The accuracy of the robot is influenced by many factors. To mention the most important ones are namely the accuracy of the mechanical parts, accuracy and resolution of sensors used for acquiring the real position of the robot and also the accuracy of the assembly in the robot. Imperfections are often not known or are difficult to be described or even sources of these imperfections are unknown. Also each robotic structure is manufactured individually and therefore each particular robot has individual accuracy properties. Accuracy properties of robot also change by the time and operation circumstances based on individual application. Therefore it is important to identify real parameters of any robot, which is deployed in industry and manufacturing processes. The process of identification of real parameters of robot is called robot calibration.



**Figure 1.** Industrial robot with 6 joints.

---

The publication is co-financed from the state budget under the programme  
of the Minister of Education and Science called "Excellent Science" project no. DNK/SP/548041/2022

## 2. Robot calibration

The kinematic model describes relationship between parameters to be identified and required position and spatial orientation of robot's end point effector. The kinematic model of a serial robot is based on extended transformation matrices as described for example in [3,4]. Schematics of the robot is shown in Figure 2 and it's kinematic description is given by matrix Equation 1.

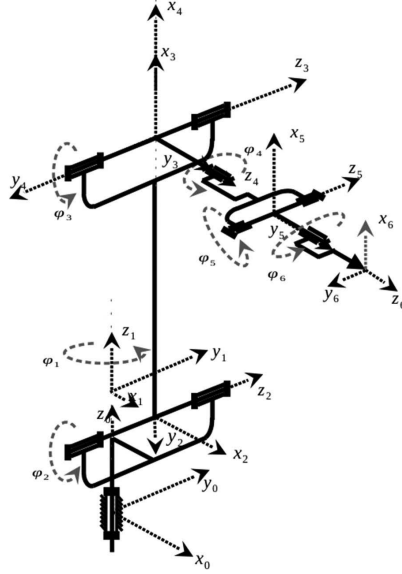


Figure 1. Schematics of the robot with 6 joints.

$$T_{Z123}(x_E, y_E, z_E) \cdot T_{Z456}(\phi_{xEN}, \phi_{yEN}, \phi_{zEN}) - T_{1N}(p_1, \dots, p_m, q_1, \dots, q_n) = 0 \quad (1)$$

where parameters  $x_{EN}, y_{EN}, z_{EN}$  describes required position of reference point of the end effector and  $\phi_{xEN}, \phi_{yEN}, \phi_{zEN}$  describe its orientation in the 3D space. The second part of the equation contains design parameters  $p_i$ , set of independent joint's coordinates  $q_j$ . The equation 1 gives vector of implicit functions which can be written in generic form 2 where 6 required parameters of position  $x_{EN}, y_{EN}, z_{EN}$  and orientation  $\phi_{xEN}, \phi_{yEN}, \phi_{zEN}$  of end effector are denoted by  $s_k$ .

$$[f_1(p_i, q_j, s_k), \dots, f_m(p_i, q_j, s_k), \dots, f_{m+n}(p_i, q_j, s_k)] = [0] \quad (2)$$

### 2.1. Traditional calibration methods

Traditional methods for robot calibration uses set of over constrained Equation (2) to estimate robot parameters in such a way that the required end effector position and orientation accuracy minimized. Iterative methods based on Jacobi matrix are usually used for this purpose. The iterative process is then based on iterations described by Equation (3).

$$F(\bar{p}, q, s) + J_p \delta p + \dots = 0 \quad (3)$$

where  $J_p$  is Jacobi matrix of function  $F$  and  $\delta J_p$  is correction factor for real robot parameters. The Jacobi matrix is usually not square due to the different amount of design parameters to be identified and amount of points used for calibration. process. Therefore matrix pseudo inversion is used to compute  $\delta J_p$  from Equation (4).

$$\delta p = -(J_p^T J_p)^{-1} F(\bar{p}, q, s) \quad (4)$$

## 2.2. Evolutionary calibration

Pseudo inversion for solution of matrix Equation 4 is usually used in traditional methods of robot calibration. The reason of pseudo inversion is that the Jacobi matrix is usually not a square matrix as the amount of identified parameters are smaller then the amount of coordinates describing required positions in calibration points. Pseudo inversion gives results which does not correspond to exact solution of the Equation 2. This leads into a question of optimal solution of the problem using evolutionary algorithms. Multi-objective optimization methods are natural choice for this purpose. For this purpose the EvoDN2 evolutionary algorithm was used together with cRVEA optimization in order to find optimal estimates of the robot parameters. It is also well know that evolutionary algorithms are capable of dealing with noisy data. In general any measured data are affected by noise and inaccuracies therefore it is important capability of these methods for real applications. Both algorithms EvoDN2 and cRVEA are originally described in [1].

EvoDN2 and cRVEA algorithms are implemented freely and are available in Matlab and Python languages. Simulation of the kinematic model of the kinematic model of the robot is performed in Matlab environment. Simulations were performed for two tasks:

- Simulate behavior of ideal model of robot kinematic for the purpose of traditional calibration process,
- Simulate behavior of the robot with imperfections and generate data sets for evolutionary algorithms.

Data generated for evolutionary algorithms involves imperfections in two cases. In the first case imperfections in dimensions of mechanical parts are simulated. The real dimensions of mechanical parts of he robot are unknown but it is known vlaue is the accuracy the parts were manufactured. This gives the range where the imperfections was simulated by adding realistic constant value to nominal dimensions. The second significant source of imperfections are data from sensors used to measure independent coordinates  $q_j$  and end point position values  $s_k$ . These data are simulated with added noise in ranges of accuracy of sensors used. Based on simulations results from both, traditional approach and approach based on evolutionary algorithms are compared and discussed.

## References

1. Chakraborti N.: *Data-Driven Evolutionary Modeling in Materials Technology*. CRC Press, 2022.
2. Simon D.: *Evolutionary Optimization Algorithms*. Wiley, 2013.
3. Stejskal V., Valášek M.: *Kinematics and Dynamics of Machinery*. Marcel Dekker Inc., 1996.
4. Brát V.: *The Matrix Methods in Analysis and Synthesis of Spatial Constrained Mechanical Systems*. Academia Prague, 1981.

# Multi-objective optimization of distillation operation using a hybrid of evolutionary algorithm and neural network

Ataklti Kahsay Wolday<sup>1</sup>, Manojkumar Ramteke<sup>1</sup>

<sup>1</sup> Department of Chemical Engineering, Indian Institute of Technology Delhi, 110016, India  
mcramteke@chemical.iitd.ac.in, ramtekemanoj@gmail.com

**Keywords:** Methanol-Water, Distillation; Multi-Objective Optimization; Neural-Networks

## 1. Abstract

The manufacturing industry prioritizes achieving high purity of material products. Distillation is a commonly used purification process [1,2]. It is a well-known unit operation that works on the concept of the relative volatility of different components of the liquid mixture and involves vaporization and condensation [3]. It is an energy-intensive process that uses nearly 40% of the given energy. Therefore, optimizing its operation is the main concern for all industrial sectors [4]. Distillation is utilized in synthesis and other fine and bulk chemical processes. One such process is methanol synthesis. Syngas, primarily a mixture of H<sub>2</sub>, CO, and CO<sub>2</sub>, is used to make methanol. Machine learning can help to model and then optimize the distillation column operations to improve its economic performance. Such use of ANNs as a surrogate model for multi-objective optimization (MOO) problems is also performed in literature [5]. Mitra [6] used a genetic algorithm (GA) hybridized with ANN to enhance industrial sintering. Sarkar and Modak [7] used hybridized simulated annealing with ANN for online control of a continuously stirred tank reactor.

In this work, the methanol-water separation in an industrial distillation column is modeled in Aspen Plus 12.0 with 60% methanol and 40% water, fed to the distillation column. The decision variables used are the molar reflux ratio, the number of stages, and the feed stage and their operating ranges are selected using sensitivity analysis. This Aspen Plus simulation is then used for generating the data of 100 samples. The ANN-based surrogate model is first trained on 80 samples and then validated on the remaining 20 samples. The regression coefficient of the ANN model with the Aspen Plus model is found to be more than 99% which illustrates the suitability of the developed ANN model for representing the complex non-linear process such as distillation. This trained and validated ANN model is then used for the MOO of the process to minimize the economic objectives of annual capital expenditure cost (CAPEX) and annual operating expenditure cost (AOC). The MOO is conducted using Artificial Neural Networks (ANNs) based genetic algorithm. The Pareto optimal front is obtained for 200 generations 100 population size on Intel® Core™ i7-10700K CPU® 3.80 GHz Windows PC with 32.0 GB RAM as shown in Figure 1 with corner solutions of  $(0.2 \cdot 10^7, 2.72 \cdot 10^5)$  and  $(1.45 \cdot 10^7, 2.39 \cdot 10^5)$  \$/year, for CAPEX and AOC, respectively.

The optimal Pareto front obtained using ANN-based GA is found to be close to ASPEN-based GA results as shown in Figure 1 which further illustrates the suitability of ANN-based surrogate modeling for the distillation process. Also, ANN-based GA was found to be reducing the optimization computing time by almost 50 % from 11 hours. To reduce the computational time further, a lighter version with a lower number of generations and population size is used for optimization.

---

The publication is co-financed from the state budget under the programme of the Minister of Education and Science called "Excellent Science" project no. DNK/SP/548041/2022



Doskonała  
Nauka



Ministry of Education and Science  
Republic of Poland



Republic  
of Poland

This lighter ANN-based GA reduces the computational time by 96 % with reasonably good quality solutions as shown in Figure 1.

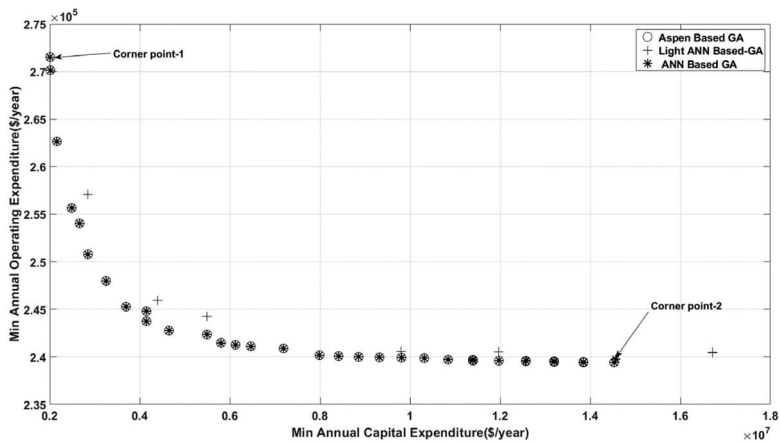


Figure 1. Pareto optimal fronts for simultaneous minimizations of ACAPEX and AOC costs.

## References

1. Amir Ghoreishi S., Nekoui M.A., Partovi S., Omid Basiri S.: *Application of Genetic Algorithm for Solving Multi-Objective Optimization Problems in Robust Control of Distillation Column*. International Journal of Advanced Computer Technology, 3, 2011, 32–43.
2. Kockmann N.: *History of Distillation*. Elsevier, 2014.
3. Moreira L.C., Borges P.O., Cavalcante R.M., Young A.F.: *Simulation and Economic Evaluation of Process Alternatives for Biogas Production and Purification from Sugarcane Vinasse*. Renewable and Sustainable Energy Reviews, 163, 2022, 112532.
4. Osuolale F.N., Zhang J.: *Energy Efficiency Optimisation for Distillation Column Using Artificial Neural Network Models*. Energy, 106, 2016, 562–578.
5. Park H., Kwon H., Cho H., Kim J.: *A Framework for Energy Optimization of Distillation Process Using Machine Learning-Based Predictive Model*. Energy Science and Engineering, 10, 2022, 1913–1924.
6. Mitra K.: *Evolutionary Surrogate Optimization of an Industrial Sintering Process*. Materials and Manufacturing Processes, 28, 2013, 768–775.
7. Sarkar D., Modak J.M.: *ANNSA: A Hybrid Artificial Neural Network/Simulated Annealing Algorithm for Optimal Control Problems*. Chemical Engineering Science, 58, 2003, 3131–3142.

# Multiscale modelling to study the evolution of texture and associated deformation mechanism during single point incremental forming

Rahul Rakshit<sup>1</sup>, Sushanta Kumar Panda<sup>2</sup>, Sumantra Mandal<sup>1</sup>

<sup>1</sup> Department of Metallurgical and Materials Engineering, Indian Institute of Technology  
Kharagpur 721302, India

<sup>2</sup> Department of Mechanical Engineering, Indian Institute of Technology  
Kharagpur 721302, India

rahul.rakshit00647@gmail.com, sushanta.panda@mech.iitkgp.ac.in,  
sumantra.mandal@metal.iitkgp.ac.in

**Keywords:** Crystal plasticity, Finite element analysis, Texture, Incremental forming, VPSC

## 1. Introduction

Single point incremental forming (SPIF) has gained wide acceptance in manufacturing sector for batch production of intricate shaped components due to its low tooling cost and flexible part design. In addition, higher formability of the material can also be achieved in SPIF process as compared to conventional forming processes. Many research studies have revealed that higher formability is related to the evolution of shear strain which delays the onset of localised necking [1,2]. As the evolution of shear strain is not monotonic, so finite element (FE) simulations are generally preferred to analyse the complex non-homogeneous SPIF deformation. Further, it has been reported that significant micro-textural evolution occurs during SPIF deformation which also affects the formability [3]. However, SPIF deformation mechanism from the perspective of micro-texture evolution is lacking in literature. In regard, FE coupled visco-plastic self-consistent (VPSC) model has been utilised to accurately predict the texture evolution and understand the underlying SPIF deformation mechanism.

## 2. Results and Discussion

In the present study, a truncated pyramidal geometry of 60° degree wall angle and 30 mm height has been fabricated employing SPIF test setup. The FE simulation of this geometry has been conducted using LS DYNA explicit software. The deformable sheet has been modelled by Hill48 anisotropic yield model. The experimental thickness distribution has been compared with FE predicted thickness distribution to validate the simulation, as shown in Figure 1(a). Two elements has been selected from the wall (element E1) and corner region (element E2) of FE simulated geometry (at a height of approximately 15 mm) to analyse the evolution of effective ( $\epsilon_{eff}$ ), normal ( $\epsilon_{11}$ ,  $\epsilon_{22}$  and  $\epsilon_{33}$ ) and shear strain ( $\epsilon_{12}$ ,  $\epsilon_{23}$  and  $\epsilon_{31}$ ) components, illustrated in Figure 2(a). The evolution of six strain components with forming depth for the selected elements from wall and corner regions are illustrated in Figure 1(b) and Figure 1(c), respectively. It is observed that wall region undergoes plain strain deformation with through thickness shear whereas corner region experience biaxial deformation with marginal amount of in-plane shear. The FE deformation history (strain rate vs time) has been used to design the variable velocity gradient (VVG)

---

The publication is co-financed from the state budget under the programme  
of the Minister of Education and Science called "Excellent Science" project no. DNK/SP/548041/2022



Doskonała  
Nauka



Ministry of Education and Science  
Republic of Poland



Republic  
of Poland

to carry out VPSC simulation. The hardening parameters in modified Voce hardening model has been optimized by matching the experimental tensile flow with VPSC simulated flow curve, presented in Figure 2. In addition, VPSC simulation has also been conducted employing monotonic velocity gradient (MVG) in which the effect of shear strain components has been neglected. Using both velocity gradients, texture evolution has been predicted in absence (using MVG) and presence (using VVG) of shear components. In order to compare the experimental and simulated texture, texture index (TI) has been estimated. TI values reveal simulated texture employing VVG matches well with experimental micro-texture.

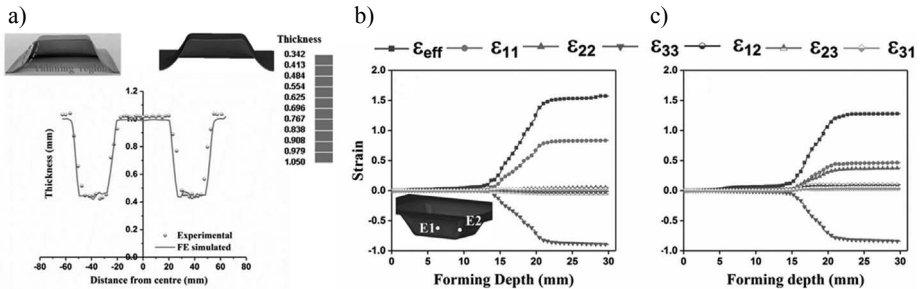


**Figure 1.** (a) Experimental and FE simulated thickness distribution, (b) evolution of effective and six strain components in wall region and (c) corner regions. The inset in figure b shows the location of selected elements.

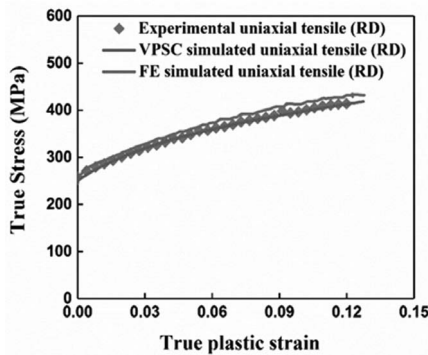


**Figure 2.** Experimental, VPSC and FE simulated tensile stress-strain flow curve.

To gain detailed insights into the effect of shear strain on deformation mechanism, the rotation behaviour of three representative orientations (selected from simulated ND inverse pole figure of as-received specimen) has been studied in absence and presence of shear strains. The rotation path of three orientations employing both velocity gradients from corner regions is shown in Figure 3. It is observed that all the orientations tends to rotate towards  $\langle 011 \rangle$  orientation when shear component is absent. This could be linked to the evolution of high intensity  $\langle 011 \rangle // \text{ND}$  fiber in the corner regions. Contrarily, the rotation path of all the orientations tends to deviate from ideal orientations in presence of shear strains, resulting in weakening of  $\langle 011 \rangle // \text{ND}$  fiber. So, it can be inferred that the shear strains lowers the sharpness of developed micro-texture, which could be associated with delay in onset of necking, resulting in improvement in formability.

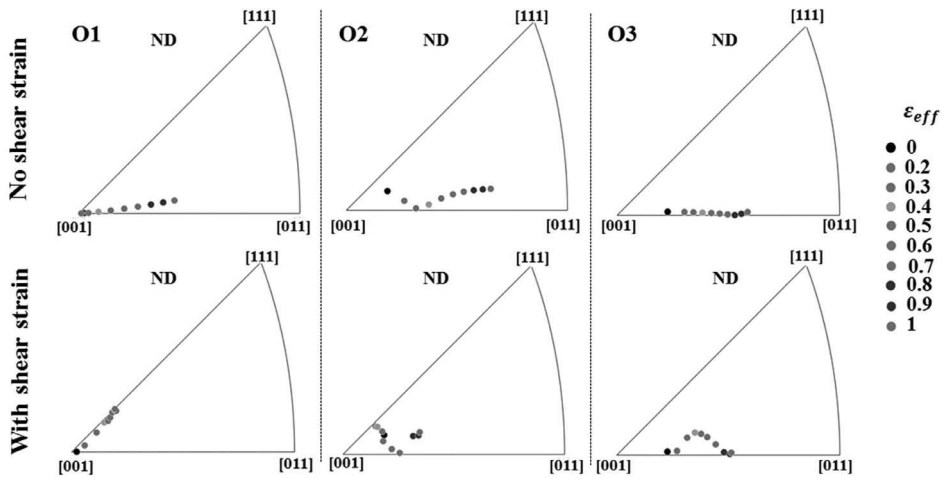


**Figure 3.** The rotation path of three representative orientations in presence (using VVG) and absence (using MVG) of shear components in corner regions.

### 3. Conclusions

- The texture predicted employing variable velocity gradient are in well accordance with the experimental micro-texture for both wall and corner regions.
- The presence of shear strains alters the rotation path of different orientations, thereby reducing the intensity of ideal texture components
- The weakening of texture could be associated to delay in onset of necking, thus enhancing the formability during SPIF as compared to conventional forming.

### References

1. Ai S., Long H.: *A review on material fracture mechanism in incremental sheet forming*. The International Journal of Advanced Manufacturing Technology, 104, 2019, 33–61.
2. Eyckens P., Moreau J.D.L., Dufloy J.R., van Bael A., van Houtte P.: *MK modelling of sheet formability in the incremental sheet forming process, taking into account through-thickness shear*. International Journal of Material Forming, 2, 2009, 379–382.
3. Kumar A., Shrivastava A., Narasimhan K., Mishra S.: *Microstructure and texture evolution during incremental sheet forming of AA1050 alloy*. Journal of Materials Science, 57, 2022, 6385–6398.

**Acknowledgements.** The authors wish to acknowledge Dr C.N. Tomé for sharing VPSC code. The authors also acknowledge the instrumental facilities provided by IIT Kharapur.

# Automatic stabilization of difficult isogeometric analysis simulations with Deep Neural Networks

Tomasz Służalec<sup>1</sup>, Maciej Paszyński<sup>2</sup>

<sup>1</sup> Jagiellonian University, Gołębia 24, 31-007 Kraków, Poland

<sup>2</sup> AGH University of Science and Technology, Al. Mickiewicza 30, 30-059, Kraków, Poland  
tomasz.sluzalec@gmail.com, maciej.paszynski@agh.edu.pl

**Keywords:** residual minimization, deep neural networks, stabilization of isogeometric analysis simulations

## 1. Introduction

Numerical solutions of Partial Differential Equations with Finite Element Method have multiple applications in science and engineering. Several challenging problems require special stabilization methods to deliver accurate results of the numerical simulations. The advection-dominated diffusion problem is an example of such problems. Unstable numerical methods generate unphysical oscillations, and they make no physical sense. Obtaining accurate and stable numerical simulations is difficult, and the method of stabilization depends on the parameters of the partial differential equations. They require a deep knowledge of an expert in the field of numerical analysis. We propose a method to construct and train an artificial expert in stabilizing numerical simulations based on partial differential equations. We create a neural network-driven artificial intelligence that makes decisions about the method of stabilizing computer simulations. It will automatically stabilize difficult numerical simulations in a linear computational cost by generating the optimal test functions. These test functions can be utilized for building an unconditionally stable system of linear equations. The optimal test functions proposed by artificial intelligence will not depend on the right-hand side, and thus they may be utilized in a large class of PDE-based simulations with different forcing and boundary conditions. We test our method on the model one-dimensional advection-dominated diffusion problem. But the methodology presented here can also be applied in two and three dimensions. It can be extended to challenging computational problems, including Navier-Stokes simulations with high Reynolds number or high contrast Maxwell equations. The artificial neural network's optimal test functions can be used to generate a sparse system of linear equations. This system of equations will have a structure allowing for a fast, accurate, and stable solution of the considered PDE.

## 2. Automatic stabilization with neural networks

Recently, there is a significant interest in research of possible application of Deep Neural Networks into finite element method simulations [13,14]. Paper [14] is an introduction to Deep Neural Network for computational scientists working already with the simulations. In [15] the authors consider the problem of representing some classes of real-valued univariate functions used in approximation with deep neural networks (deep NN, DNN) based on rectified linear unit (ReLU) activation functions. They show how the so-called ReLU NN calculus rules can be applied to obtain

---

The publication is co-financed from the state budget under the programme of the Minister of Education and Science called "Excellent Science" project no. DNK/SP/548041/2022



the representation of piecewise linear continuous functions. In particular, DNN approximation rates match those achieved by free-knot (h-adaptive) and order-adaptive (hp-adaptive) approximations. In [13] the authors show that it is possible to guide goal-oriented adaptivity for stationary problems using DNN. The finite element method utilizes high-order basis functions, e.g., Lagrange polynomials in the classical finite element method (FEM) [4] or B-spline basis functions in isogeometric analysis (IGA) [1]. There are several challenging problems solved by FEM and IGA, such as analysis of the construction of civil engineering structures, cars or airplanes [6], geophysical applications like identification of oil and gas bearing formations [12], bioengineering simulations like modeling of cancer growth [7], blood flow simulations [11], wind turbine aerodynamics [3] or modeling of propagation of acoustic and electromagnetic waves over the human head [2]. They require special stabilization methods to deliver high accuracy numerical solution.

We plan to train the neural network to find the optimal test functions stabilizing the time-dependent IGA FEM simulations. We also propose a method to solve a Petrov-Galerkin formulation with the optimal test functions in a linear computational cost on tensor product grids. The simulations of difficult, unstable time-dependent problems, like advection-dominated diffusion [8], high-Reynolds number Navier-Stokes equations [9], or high-contrast material Maxwell equations, have several important applications in science and engineering.

There are several stabilization methods, such as Streamline-Petrov Upwind Galerkin method (SUPG) [5], discontinuous Galerkin method (DG) [10], as well as residual minimization (RM) method [8,9]. We will use the Petrov-Galerkin formulation with the optimal test functions. It can be derived directly from the RM method. The RM for a given trial space it uses the larger test space, while for the Petrov-Galerkin formulation, we can compute the optimal test functions living in the subspace of the test space. The number of the optimal test functions is equal to the dimension of the trial space. The Petrov-Galerkin formulation, used for stabilization, enables interfacing with DNN. The DNN can be trained by running several simulations and using the computations of the optimal test functions. The test functions will be parameterized using the B-spline basis. The input to the DNN will be the problem parameters and the trial space. The output from the DNN will be the optimal test functions coefficients. Later, by running the simulations in every time step, using the actual configuration of parameters from the current time step, we can ask the DNN to provide the optimal test functions that will stabilize the computations for a given trial space. Such an efficient, ultra-fast, and automatic way of stabilization of time-dependent simulations is not available nowadays, and it may have a big impact on the computational science community.

### 3. Applications

We develop a method for ultra-fast solvers using Petrov-Galerkin formulations with optimal test functions for time-dependent problems. These solvers for a given approximation space require determining the optimal test functions that will stabilize the simulations. The solver itself, if properly designed using the alternating-directions algorithms, can deliver a linear computational cost, but the problem of finding the optimal test spaces is computationally hard. We also claim that for transient simulations, where the model parameters change from one time step to another, the test spaces that stabilize the simulations may change from one time step to another.

Thus, we construct and train DNN to find optimal test functions to stabilize Petrov-Galerkin formulations with classical and isogeometric finite element method simulations of time-dependent problems, perform on regular patches of elements. The DNN will approximate the coefficients of linear combinations of B-spline basis functions used to test the Petrov-Galerkin formulation employed within the classical and isogeometric finite element method. Trained on the simulations' parameters, different deep neural networks for different classes of problems, they will deliver in a linear computational cost, the parameters of the optimal test functions that can be used for stabilization of the simulations.

The simulations of difficult, unstable time-dependent problems, like advection-dominated diffusion-reaction, high-Reynolds number Navier-Stokes equations, or high-contrast material Maxwell equations, have several important applications in science and engineering.

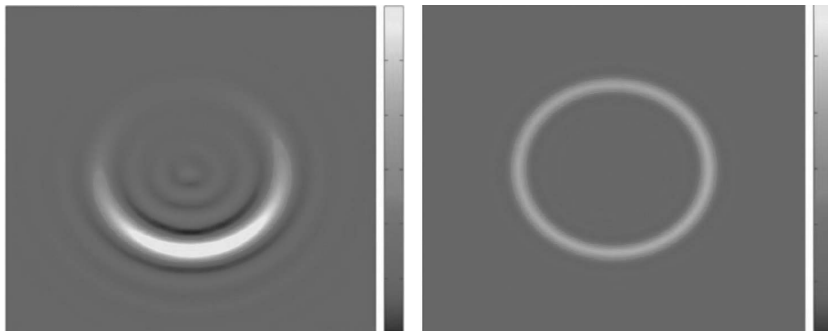


**Figure 1.** Stabilization of advection-diffusion simulations.

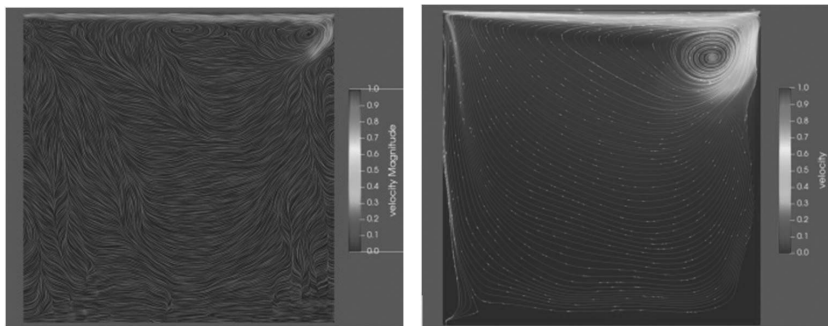


**Figure 2.** Stabilization of Navier-Stokes simulations.

## References

1. Cottrell J.A., Hughes T.J.R., Bazilevs Y.: *Isogeometric analysis: toward integration of CAD and FEA*. John Wiley & Sons, 2009.
2. Demkowicz L., Gatto P., Kurtz J., Paszyński M., Rachowicz W., Bleszynski E., Bleszynski E.: *Hamilton M., Champlin C., Pardo D., Modeling of bone conduction of sound in the human head using hp finite elements i. code design and verification*. Computer Methods in Applied Mechanics and Engineering, 21-22, 2011, 1757–1773.
3. Hsu M.-C., Akkerman I., Bazilevs, Y.: *High-performance computing of wind turbine aerodynamics using isogeometric analysis*. Computers & Fluids, 49, 2011, 93–100.
4. Hughes T.J.R., Belytschko T.: *The finite element method: Linear static and dynamic finite element analysis*. Computer-Aided Civil and Infrastructure Engineering, 4, 1989, 245–246.
5. Hughes T.J.R., Franca L., Mallet M.: *A new finite element formulation for computational fluid dynamics: Vi. convergence analysis of the generalized supg formulation for linear time-dependent multidimensional advective-diffusive systems*. Computer Methods in Applied Mechanics and Engineering, 63, 1987, 97–112.
6. Hughes T.J.R., Cottrell J.A., Bazilevs Z.: *Isogeometric analysis: CAD, finite elements, NURBS, exact geometry and mesh refinement*. Computer methods in applied mechanics and engineering, 194, 2005, 4135–4195.

7. Łoś M., Klusek A., Hassaan M.A., Pingali K., Dzwiniel W., Paszyński M.: *Parallel fast isogeometric l2 projection solver with galois system for 3d tumor growth simulations*. Computer Methods in Applied Mechanics and Engineering, 343, 2019, 1–22.
8. Łoś M., Munoz-Matute J., Muga I., Paszyński M.: *Isogeometric residual minimization method (igrm) with direction splitting for non-stationary advection–diffusion problems*. Computers & Mathematics with Applications, 79, 2019, 213–229.
9. Łoś M., Munoz-Matute J., Muga I., Paszyński M.: *Isogeometric residual minimization for time-dependent stokes and navier-stokes problems*. Computers & Mathematics with Applications, 95, 2021, 200–214.
10. Pietro D., Ern A.: *Mathematical Aspects of Discontinuous Galerkin Methods*. Springer, 2011.
11. Taylor C.A., Hughes T.J.R., Zarins C.K.: *Finite element modeling of blood flow in arteries*. Computer Methods in Applied Mechanics and Engineering, 158, 1998, 151–196.
12. Pardo D., Torres-Verdin C., Nam M.J., Paszyński M., Calo V.M.: *Fourier series expansion in a non-orthogonal system of coordinates for the simulation of 3d alternating current borehole resistivity measurements*. Computer Methods in Applied Mechanics and Engineering, 45–48, 2008, 3836–3849.
13. Brevis I., Muga I., van der Zee K.: *Data-driven finite elements methods: Machine learning acceleration of goal-oriented computations*. arXiv:2003.04485, 2020, 1-24.
14. Higham C.F.: *Deep learning: An introduction for applied mathematicians*. SIAM Review, 61, 2019, 860–891.
15. Opschoor J.A.A., Petersen P.C., Schwab C.: *Deep relu networks and high-order finite element methods*. Analysis and Applications, 18, 2020, 715–770.

**Acknowledgements.** This work is partially supported by The European Union’s Horizon 2020 Research and Innovation Program of the Marie Skłodowska-Curie grant agreement No. 777778, MATHROCKs. Scientific paper published within the framework of an international project co-financed with funds from the program of the Ministry of Science and Higher Education entitled „PMW” in years 2022-2023; contract no. 5243/H2020/2022/2.

# Hierarchical matrices acceleration of GMRES solver in four-dimensional Finite Element Method computations

Mateusz Dobija<sup>1</sup>, Anna Paszyńska<sup>1</sup>, Marcin Łoś<sup>2</sup>, Maciej Paszyński<sup>2</sup>

<sup>1</sup> Jagiellonian University, Gołębia 24, 31-007 Kraków, Poland

<sup>2</sup> AGH University of Science and Technology, Al. Mickiewicza 30, 30-059 Kraków, Poland  
 mateusz.dobija@doctoral.uj.edu.pl, anna.paszynska@uj.edu.pl,  
 los@agh.edu.pl, maciej.paszynski@agh.edu.pl

**Keywords:** finite element method, hierarchical matrices, GMRES, iterative solvers, space-time formulations

## 1. Introduction

The hierarchical matrices have been introduced by Hackbusch [1]. Usually, in scientific computing, the rank of the entire matrix is equal to the size of the matrix. This is because the low-rank matrices are not invertible [2]. However, if we partition the matrix recursively into blocks, we discover that the off-diagonal blocks are low-rank. The idea of the hierarchical matrices is to decompose the matrix recursively into off-diagonal low-rank blocks. The matrices resulting from finite element method computations decompose by recursive partitioning into the diagonal, with the low-rank off-diagonal blocks. The rows and columns in the matrices are related to basis functions spread over the computational mesh nodes. The non-zero entries in the matrices result from the overlapping of basis functions from different nodes of the mesh. The further the nodes, the less the overlap, and the lower is the rank of the off-diagonal block of the matrix.

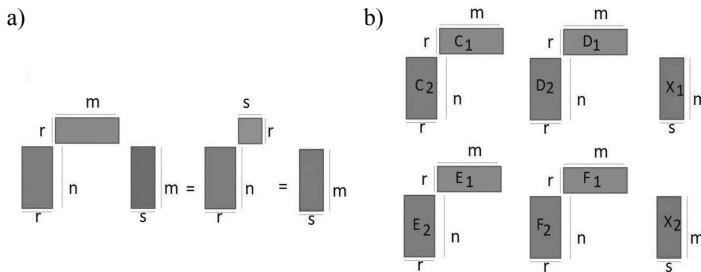


**Figure 1.** Panel (a) Multiplication of an  $(n,m)$ -size block of a matrix compressed with rank  $r$  by  $s$  vectors of size  $m$ . Panel (b) Multiplication of a matrix partitioned into four  $(n,m)$ -size blocks compressed with rank  $r$  by  $s$  vectors of size  $2m$ .

The benefit of having a matrix compressed into recursive low-rank blocks is that the multiplication of this matrix by a vector can be performed in a linear  $O(N)$  computational cost. This is illustrated in Figure 1. Panel (a) presents a single block of a matrix of size  $n$ -rows and  $m$ -columns. In the compressed format, this block is represented by a matrix of  $n$  rows and  $r$  columns, multiplied by another matrix of  $r$  rows and  $m$  columns. The low-rank blocks are kept in this compressed

The publication is co-financed from the state budget under the programme of the Minister of Education and Science called "Excellent Science" project no. DNK/SP/548041/2022

format without multiplication back into the full block. A block can be decomposed into two blocks if it has a low-rank  $r$ . Such the block, when multiplied by  $s$  vectors of  $m$ -rows, requires  $O(N)$  floating-point operations. The first multiplication of a green block of size  $r$ -rows and  $m$ -columns by a pink vector of  $m$ -rows and  $s$ -columns is performed using  $O(rms)$  operations. The resulting orange block of  $r$ -rows and  $s$ -columns is multiplied by a blue block of  $n$ -rows and  $r$ -columns, using  $O(srn)$  operations. The total number of operations is  $O(mrs + nrs) = O(\max(m, n)rs) = O(N)$  where  $N = \max(m, n)$  and  $r, s \ll N$ .

This low computational cost multiplication of blocks by multiple right-hand sides generalizes into several blocks, as presented in panel (b). This is because the right-hand side vector can be partitioned into sub-blocks of the sizes corresponding to particular sub-blocks of the matrix. The multiplication can be performed then in the following way:  $C_2(C_1X_1) + D_2(D_1X_2)$  for the first block, and  $E_2(E_1X_2) + F_2(F_1X_2)$  for the second block. Each of the intermediate results, namely  $C_2(C_1X_1)$ , and  $D_2(D_1X_1X_2)$ , and  $E_2(E_1X_2)$ , and  $F_2(F_1X_2)$  is computed in a linear computational cost, using the scheme from panel (a), and they are aggregated into the resulting vectors.

## 2. Four-dimensional finite element method

The four-dimensional finite element method employs discretizations over the four-dimensional computational grids. It is employed for space-time formulations. Usually, the discretization over the first three dimensions concerns the spatial dimensions,  $x$ ,  $y$ , and  $z$ , and the fourth dimension concerns the time variable. The space-time formulations are widely used nowadays in the finite element method community [4–7]. The idea of the space-time formulation is that it can be applied to time-dependent problems, where the dynamic of the system is more intense in one part of the computational domain than in the others. Thus, to follow the complexity of the dynamical changes of the modeled system, we can perform smaller time steps in one part of the domain and, at the same time, larger time steps in the other parts. This can be expressed by multi-dimensional grids, where we adapt the four-dimensional hexhedrals in spatial and temporal dimensions.

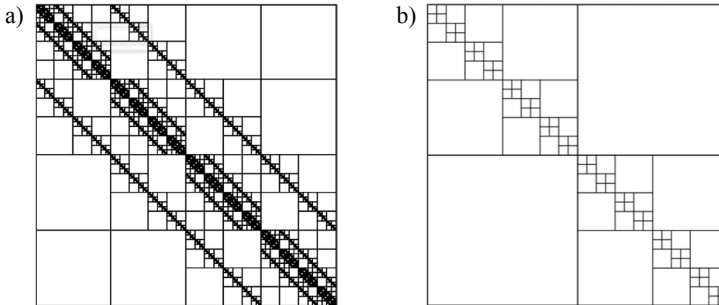


**Figure 2.** Panel (a) Matrix of four-dimensional finite element method compressed with rank  $r = 1$  into a hierarchical matrix. Panel (b) Ideal recursive decomposition of a matrix, where we refine towards the diagonal blocks, and all off-diagonal blocks have rank 1.

As the example, on panel (a) in Figure 2, we present the structure of the hierarchical matrix (after the rank 1 compression) of the four-dimensional mesh expressing the heat transfer problem on a uniform four-dimensional mesh. In this work, we focus on developing efficient solvers for space-time formulations. We employ the hierarchical format of the matrix discretized over the four-dimensional space-time grid. We show that this matrix can be employed to speed up the iterative GMRES solver algorithm.

### 3. Accelerating the GMRES algorithm

The Generalised Minimum RESidual (GMRES) iterative algorithm [3] is the generalization of the Minimal RESidual (MINRES) solver. Unlike MINRES, which only works for symmetric matrices, it can be applied for unsymmetric systems. The algorithm can be summarized as follows:

- 1) Compute  $r_0 = b - Ax_0$ ,
- 2) Compute  $v_1 = r_0 / \|r_0\|$ ,
- 3) Loop  $j = 1, 2, \dots, k$ ,
  - a) Compute  $h_{ij} = (Av_j, v_i)$  for  $i = 1, 2, \dots, j$ ,
  - b) Compute  $w_{j+1} = Av_j - \sum_{i=1, \dots, j} h_{ij} v_i$ ,
  - c) Compute  $h_{j+1,j} = \|w_{j+1}\|_2$ ,
  - d) Compute  $v_{j+1} = w_j + 1 / h_{j+1,j}$
- 4) Form solution  $x_k = x_0 + V_k y_k$  where  $V_k = [v_1, \dots, v_k]$  and  $y_k$  minimizes  $J(y) = \|\beta e_1 - H_k y\|$  where  $H$  is the matrix of  $h_{i,k}$ .

In this algorithm, the matrix  $A$  is employed in line 1, where it is multiplied by the  $x_0$  vector, as well as in lines 3a and 3b, where it is multiplied by the vector  $v_j$ . Now, with matrix  $A$  being sparse and having NNZ non-zero entries, the multiplication of a matrix by a vector can be performed with NNZ computational cost. We must multiply each non-zero entry of  $A$  by a non-zero entry of the vector. For space-time formulations, though, the NNZ can be large.

What is the cost of multiplication of the hierarchical matrix of size  $N$  by a vector? For the ideal case, presented in panel a in Figure 2, our matrix is partitioned recursively into the diagonal blocks, and the off-diagonal blocks have rank 1. The computational cost of the matrix-vector multiplication is the following. When we recursively partition the matrix into four blocks, the total cost is  $C(N) = 2C(N/2) + 2O(r2N/2) + O(N)$ , where  $C(N)$  is the cost of multiplication for the entire matrix of size  $N$ , recursively partition into blocks into the diagonal, the  $C(N/2)$  is the cost of multiplication of the recursively partitioned into the diagonal of two halves of the original matrix, and  $O(r2N/2)$  is the cost of multiplication of the off-diagonal blocks of size  $N/2$  with rank  $r$ , by the vector. Additionally, we count  $N$  additions related to the aggregations of the resulting vector. The solution to this recursive equation is  $C(N) = O(M \log N)$ . Thus, in our method, we can perform the matrix-vector multiplications with quasi-linear computational cost.

### 4. Numerical experiments

To summarize the paper, we have generated the space-time matrix for the heat transfer problem over the computational mesh of size of 8 elements in each direction. In order to obtain a stable numerical solution, we employed the residual minimization method [8]. We have employed the isogeometric analysis for discretization, which can be understood as the finite element method with higher-order B-spline basis functions [9]. We have used quadratic B-splines in each direction for trial and quadratic B-splines with C0 separators for testing (equivalent to the Lagrange basis). For such the setup of the residual minimization method, the size of the matrix is  $([\text{trial space size}] + [\text{test space size}])^4 = ([8 + 2] + [8 + 7 + 2])^4 = 274 = 531\ 441$ . Thus, we have a matrix of 531 441 rows and columns. We have employed the GMRES solver for the original uncompressed matrix, and we compared it with the matrix generated in a rank one compressed format. We set up the solver accuracy to 0.000001.

- 1) For the original full matrix, the GMRES solver required ten iterations with 25 112 040 total number of floating-point operations (25 112 204 flops per iteration)
- 2) For the compressed hierarchical matrix, the GMRES solver requires seven iterations with 2 307 760 total flops (329 680 flops per iteration).

Thus, we have shown that our method reduces the computational cost of the GMRES solver by one order of magnitude on the space-time formulations solved with isogeometric analysis methods.

## References

1. Hackbusch W.: *Hierarchical Matrices: Algorithms and Analysis*. Springer, 2009.
2. Horn R.A., Horn R.A., Johnson C.R.: *Matrix analysis*. Cambridge university press, 1990.
3. Saad Y.: *Iterative Methods for Sparse Linear Systems*. Society for Industrial and Applied Mathematics, 2<sup>nd</sup> edition, 2003.
4. Schafelner A., Vassilevski P.S.: *Numerical Results for Adaptive (Negative Norm) Constrained First Order System Least Squares Formulations*. Computers and Mathematics with Applications, 95, 2020, 256–270.
5. Voronin K., Lee C.S., Neumüller N., Sepúlveda-Salaz P., Vassilevski P.S.: *Space-time discretizations using constrained first-order system least squares (CFOSLS)*. Journal of Computational Physics, 373, 2018, 863–876.
6. Steinbach O., Yang H.: *Comparison of algebraic multigrid methods for an adaptive space–time finite-element discretization of the heat equation in 3D and 4D*. Numerical Linear Algebra with Applications, 2018.
7. Demkowicz L., Gopalakrishnan J., Nagaraj S., Sepúlveda P.: *A Spacetime DPG Method for the Schrödinger Equation*. SIAM Journal of Numerical Analysis, 2016.
8. Chan J., Evans J.A.: *A Minimum-Residual Finite Element Method for the Convection-Diffusion Equations*. ICES-Report 13–12, 2013.
9. Cottrell J.A., Hughes T.J.R., Bazilevs Y.: *Isogeometric analysis: toward integration of CAD and FEA*. John Wiley & Sons, 2009.

**Acknowledgements.** This work is partially supported by The European Union’s Horizon 2020 Research and Innovation Program of the Marie Skłodowska-Curie grant agreement No. 777778, MATHROCKs. Scientific paper published within the framework of an international project co-financed with funds from the program of the Ministry of Science and Higher Education entitled „PMW” in years 2022-2023; contract no. 5243/H2020/2022/2.

# Physics Informed Neural Networks for wave propagation problems

Paweł Maczuga<sup>1</sup>, Maciej Paszyński<sup>1</sup>

<sup>1</sup> AGH University of Science and Technology, Al. Mickiewicza 30, 30-059 Kraków, Poland  
pmaczuga97@gmail.com, maciej.paszynski@agh.edu.pl

**Keywords:** wave propagation problems, Physics Informed Neural Networks

## 1. Introduction

The modeling and simulation of wave propagation problems has multiple applications in the geophysics, material science, propagation of seismic waves, identification of formation layers using acoustic tools. [1,2].

The family of Physics Informed Neural Network (PINN) solvers have been introduced by prof. George Karniadakis in 2019 [3,4]. The method gained exponential growth in the number of papers and citations, with several new papers and modification of the method introduced every year [5–7]. The method, however, has some difficulties of the training process, some of them discussed in [8,9]. In this paper we focus on investigation of the applicability of the modern PINN methodology for modeling of the wave propagation problems.

## 2. Physics Informed neural network for wave equations

We focus on a model one-dimensional wave equation

$$\frac{\partial^2 u(x,t)}{\partial t^2} - \frac{\partial^2 u(x,t)}{\partial x^2} = 0 \quad (1)$$

with initial conditions

$$\begin{aligned} u(x,0) &= \sin(n\pi x) \\ u'(x,0) &= 0 \end{aligned} \quad (2)$$

and boundary conditions

$$u'(0,t) = u'(1,t) = 0 \quad (3)$$

In the PINN method, the neural network represents the solution

$$u(x,t) \approx NN(x,t) \quad (4)$$

---

The publication is co-financed from the state budget under the programme of the Minister of Education and Science called "Excellent Science" project no. DNK/SP/548041/2022

where  $NN$  is a fully connected neural network with 5 layers, 100 neurons per layer and non-linear activation function, e.g. sigmoid. The PINN method introduces the loss function being the residual of the method

$$lossPDE(x,t) = \left( \frac{\partial^2 NN(x,t)}{\partial^2 t} - \frac{\partial^2 NN(x,t)}{\partial^2 x} \right)^2 \quad (5)$$

loss functions enforcing the boundary conditions

$$\begin{aligned} lossBC0(0,t) &= (NN'(0,t) - 0)^2 \\ lossBC1(1,t) &= (NN'(1,t) - 0)^2 \end{aligned} \quad (6)$$

as well as the loss functions for the initial conditions

$$\begin{aligned} lossInit(x,0) &= (NN(x,0) - \sin(n\pi x))^2 \\ lossInitD(x,0) &= (NN'(x,0) - 0)^2 \end{aligned} \quad (7)$$

Loss for the whole network is sum of all the partial losses

$$loss(x,t) = lossPDE + lossBC0 + lossBC1 + lossInit + LossInitD \quad (8)$$

The training procedure is the following

**Repeat  $n$  times**

- Select randomly points  $x$  and  $t$  from  $(0,1)$  interval,
- Compute derivatives  $\frac{dNN(x,t)}{dx}$  and  $\frac{dNN(x)}{dt}$ ,
- Compute second derivatives  $\frac{\partial^2 NN(x,t)}{\partial x^2}$  and  $\frac{\partial^2 NN(x,t)}{\partial t^2}$ ,
- Compute the loss function  $loss(x,t)$ ,
- Compute the derivatives of loss with respect to weights and biases,
- Modify weights and biases according to that derivative.

This procedure is repeated several times. In practice, it is augmented with the method to “jump out” from the local minima, like the ADAM method [10] commonly used nowadays. It is like “stretching the neural network carpet in multi-dimensional space to fit the solution of the problem.

Also, instead of selecting single point in each iteration, vector of points is selected and the loss is calculated as mean over these points.

### 3. Numerical experiments

We have generated some preliminary results with Pytorch and Collab on applications of the PINN model for solution of the wave equation. Figure 1 presents the initial state and the progress of the wave equation simulation. Figure 2 presents the convergence of the training procedure, and the error of the solution in space and time. We can conclude that the training process with ADAM optimizer and PINN method has successfully discovered and learnt the solution the hyperbolic wave equation.

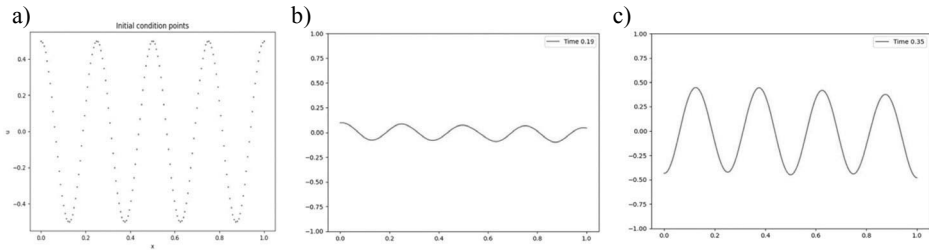


**Figure 1.** (a) The initial condition, (b) configuration at time moment  $t = 0.2$ , (c) configuration at time moment  $t = 0.35$ .

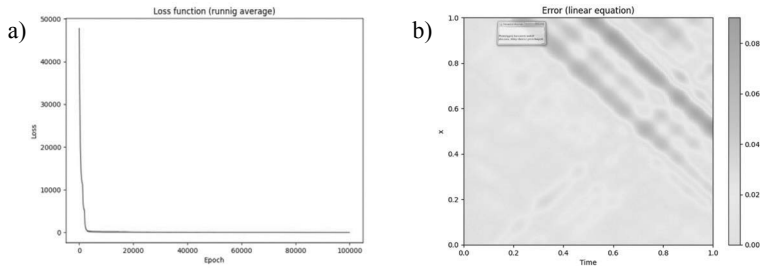


**Figure 2.** The convergence of the training (the convergence of the loss function), (b) The accuracy of the solution in space and time.

## References

1. Matuszyk P.J., Demkowicz L., Torres-Verdin C.: *Solution of coupled acoustic–elastic wave propagation problems with anelastic attenuation using automatic hp-adaptivity*. Computer Methods in Applied Mechanics and Engineering, 213–216, 2012, 299–313.
2. Łoś M., Behnoudfar P., Dobija M., Paszyński M.: *ADI-based, conditionally stable schemes for seismic P-wave and elastic wave propagation problems*. Bulletin of the Polish Academy of Sciences. Technical Sciences, 70, 2022, 1–11.
3. Raissi M., Perdikaris P., Karniadakis G.E.: *Physics-informed neural networks: A deep learning framework for solving forward and inverse problems involving nonlinear PDEs*. Journal of Computational Physics, 378, 2019, 686–707.
4. Kharazmi E., Zhang Z., Karniadakis G.E.: *Variational Physics-Informed Neural Networks For Solving PDEs*. arxiv.org/abs/1912.00873, 2019.
5. Lei Yuan, Yi-Qing Ni, Xiang-Yun Deng, Shuo Hao: *A-PINN, Auxiliary physics informed neural networks for forward and inverse problems of nonlinear integro-differential equations*. Journal of Computational Physics, 462, 2022, 111260.
6. Kharazmi E., Zhang Z., Karniadakis G.E.: *hp-VPINNs: Variational physics-informed neural networks with domain decomposition*. Computer Methods in Applied Mechanics and Engineering, 374, 2021, 113547.
7. Shin Y., Darbon J., Karniadakis G.E.: *On the convergence of physics informed neural networks for linear second-order elliptic and parabolic type PDEs*. arXiv:2004.01806, 2020.
8. Wang S., Yu X., Perdikaris P.: *When and why PINNs fail to train: A neural tangent kernel perspective*. Journal of Computational Physics, 449, 2020, 110768.
9. Qin S.-M., Li M., Xu T., Dong S.-Q.: *RAR-PINN algorithm for the data-driven vector-soliton solutions and parameter discovery of coupled nonlinear equations*. arXiv:2205.10230, 2022.
10. Kingma D.P., Lei Ba J.: *ADAM: A method for stochastic optimization*. arXiv:1412.6980, 2014.

**Acknowledgements.** This work is partially supported by The European Union's Horizon 2020 Research and Innovation Program of the Marie Skłodowska-Curie grant agreement No. 777778, MATHROCKs. Scientific paper published within the framework of an international project co-financed with funds from the program of the Ministry of Science and Higher Education entitled „PMW” in years 2022-2023; contract no. 5243/H2020/2022/2.

# FEM model of Beverage Can Manufacturing Process

Przemysław Wędrychowicz<sup>1,2</sup>

<sup>1</sup> CANPACK S.A., Business Support Service, 32-800 Brzesko, Poland

<sup>2</sup> Faculty of Metals Engineering and Industrial Computer Science,  
AGH University of Science and Technology, Al. Mickiewicza 30, 30-059 Kraków, Poland  
przemysla.wedrychowicz@canpack.com

**Keywords:** beverage can, large strains, AA3104-H19 alloy, manufacturing, forming simulation

## 1. Introduction

Aluminium beverage can forming process is the process which was improved by many years in terms of forming speed and raw material usage efficiency. All this improvements through the years was developed thanks to many physical prototypes and tests. Since some time it is most common to use numerical models to simulate this process and to increase its efficiency. Building numerical model of can manufacturing process is essential to understand the can structural behaviour and its manufacturing process. Because of tight tolerances in this process its required to use precise data regarding: material model and boundary conditions. Significant part of developing numerical model of can forming process was focused on aluminium alloy AA3104-H19 sheets of thickness about 240  $\mu\text{m}$  which are commonly used in beverage can manufacturing process. During forming process initial thickness of raw material is reduced to about 90  $\mu\text{m}$ , this results with local plastic strains reaching value of 2. That is why developing flow stress model of AA3104-H19 for strain range from 0–2 was crucial. Based on the FEM modelling of the technological process, data on the history of deformation and the trajectory of movement of the selected points of the material at all stages of the production were obtained. Microspecimens for the tensile tests were taken from the points of the beverage can wall that were determined in this way. The initial strain of each sample was taken from the FEM simulation. In this way, the tensile curves were obtained for the material points at different stages of the production. The processing of these curves allowed the creation of a flow stress model for large strains, corresponding to beverage can production conditions [1].

## 2. Methodology

### 2.1. Numerical Simulations

FEM simulation of the beverage can forming process was performed using a 2D axisymmetric model. Model was prepared in LS-Prepost preprocessor. During early stage of building numerical model of can forming process observed that increasing number of finite elements on wall thickness results in lower wall thickness of final can. Through series of simulation with different element number on can wall thickness established that 10 number of elements give enough accuracy. The forming tools were modeled as rigid bodies with discrete shell elements representation. The static and dynamic friction coefficients between the sheet and the tools were assumed to be  $\mu_s = 0.1$  and  $\mu_d = 0.05$ , correspondently. For contact between the sheet and the punch, static and dynamic friction coefficients were accordingly  $\mu_s = 0.15$  and  $\mu_d = 0.1$  [2]. The blank holder force for the cup

---

The publication is co-financed from the state budget under the programme  
of the Minister of Education and Science called "Excellent Science" project no. DNK/SP/548041/2022



Doskonała  
Nauka



Ministry of Education and Science  
Republic of Poland



Republic  
of Poland

drawing step was set to 9.3 kN and in the next redrawing step increased to 24 kN. Based on those parameters, the preliminary FE simulations of the first five stages of the beverage can forming process were performed.

Next step of simulation procedure was to build numerical model of can necking stage which is performed in 14 forming steps. Once again one of the most important step to simulate this necking process was research about process temperature, on can material parameters impact.

### 2.2. Experimental Study

The Hansel–Spittel [3] equation was used to develop a new flow stress model of the AA3104-H19 alloy. The choice of the Hansel-Spittel equation to create a new flow stress model was due to two circumstances. Firstly, this equation is widely used in the practice of modeling metal forming processes. For this reason, the developed model can be used in various FEM programs, for example, in QForm or Forge3. Secondly, the Hansel-Spittel equation contains a sufficiently large number of coefficients to potentially approximate more complex flow stress–strain dependences.

For the isothermal conditions (cooling during the process with a heat carrier to a temperature of about 40–45°C) and a lack of sensitivity to strain rate, this equation was simplified to the following form:

$$\sigma = A\epsilon^{m_1} \exp\left(\frac{m_2}{\epsilon}\right)(1 + \epsilon)^{m_3} \exp(m_4\epsilon) \tag{1}$$

where  $A, m_1-m_4$  – empirical parameters (Table 1).

**Table 1.** Parameters of the (Equation (1)) model for the first iteration of the fitting algorithm.

$A$	$m_1$	$m_2$	$m_3$	$m_4$
377.524	0.024674	-0.00088	-0.73833	0.4027

The flow stress-strain curves for each stage of the beverage can forming process were shifted according to the deformations obtained from the numerical simulation (Figure 1).

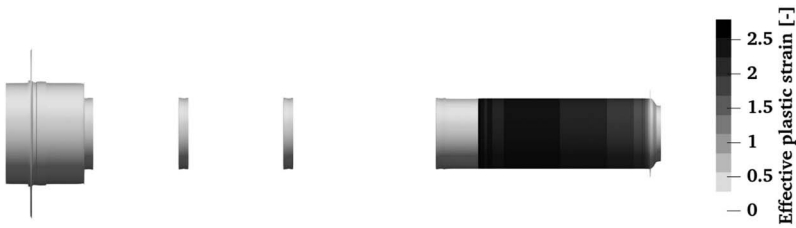


**Figure 1.** Distribution of the effective strain after the first five steps of the beverage can forming process.

After investigating of flow stress model, next step was to study impact of process temperature on aluminum alloy softening. To test temperature influence on AA3104-H19, tensile specimen was cut from can body wall after its treatment in stage of: washing, drying in internal coating oven and drying of external lithography. This research deliver information about aluminum alloy softening and how this can impact final can performance Figure 2. Data characterizing material of can body after exposure to temperatures reaching 200°C was also important as input data for numerical model of last can forming stage which is neck and flange of the can creating.

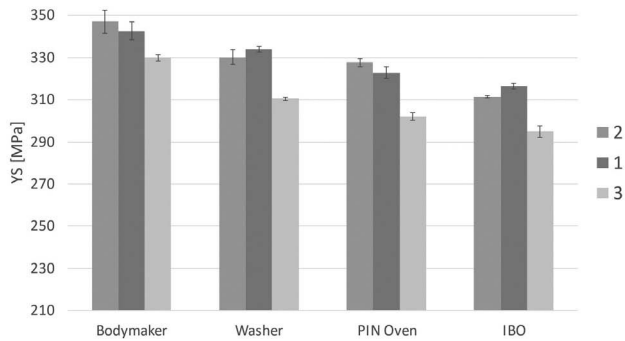


**Figure 2.** AA3104-H19 Yield Strength change after stages of: Bodymaker forming, washing, PIN oven drying and IBO drying.

### 3. Summary

Development of flow stress model of AA3104-H19 for large plastic deformation, such as observed in the production process of beverage can was one of the first step for further beverage can body shape optimization and technological process improvement by FEM. As mentioned earlier tight tolerances of this process required input data such as those from flow stress model, to be provided as accurately as possible. The literature lacks the flow stress curves of the AA3104 alloy for large plastic deformations, such as those observed in the production process of a beverage can. There are papers in the literature using numerical models for this purpose for the maximum effective strain of 0.02 [4,5], or 0.3 [6]. Validation of the developed model based on the can wall thicknesses at different stages of the forming process showed that the model was correctly developed. Therefore, this model can be used in the optimization of can forming process or in the can wall thinning process.

Because of characteristic of can manufacturing process and construction of drying oven it was impossible to investigate process temperature impact on AA3104-H19 material in laboratory conditions. Research on temperature influence on aluminum alloy mechanical properties give better understanding about process of can manufacturing and allow to create more precise numerical model of beverage can necking and flange forming steps.

### References

1. Wędrychowicz P., Kustra P., Paćko M., Milenin A.A.: *Flow Stress Model of the AA3104-H19 Alloy for the FEM Simulation of the Beverage Can Manufacturing Process under Large Plastic Deformations*. Materials, 14, 2021, 6408.
2. Mackey A.: *Numerical analysis of the effect of orthogonal friction and work piece misalignment during an AA5042 cud drawing process*. 14<sup>th</sup> Int. LS-DYNA User Conf., Alcoa Technical Center, PA, 2016, 1–13.
3. Hansel A., Spittel T.: *Kraft- und Arbeitsbedarf bildsamer Formgebungsverfahren*. VEB Deutscher Verlag für Grundstoffindustrie, Lipsk, Germany, 1978.
4. van Haafden W.M., Magnin B., Kool W.H., Katgerman L.: *Constitutive behaviour of as-cast AA1050, AA3104, and AA5182*. Metallurgical and Materials Transactions A, 33, 2002, 1971–1980.
5. Sun F., Liu P., Liu W.: *Multi-level deep drawing simulations of AA3104 aluminium alloy using crystal plasticity finite element modelling and phenomenological yield function*. Advances in Mechanical Engineering, 13, 2021, 16878140211001204.
6. Mirfalah-Nasiri S.M., Basti A., Hashemi R.: *Forming limit curves analysis of aluminum alloy considering the through-thickness normal stress, anisotropic yield functions and strain rate*. International Journal of Mechanical Sciences, 117, 2016, 93–101.

# Determining strains and stresses in composite based on FBG measurements

Wacław Kuś<sup>1</sup>, Waldemar Mucha<sup>1</sup>, Iyasu Tafese Jiregna<sup>1</sup>

<sup>1</sup> Silesian University of Technology, Department of Computational Mechanics and Engineering,  
ul. Akademicka 2A, 44-100 Gliwice, Poland  
wacław.kus@polsl.pl, waldemar.mucha@polsl.pl,  
iyasu.tafese.jiregna@polsl.pl

**Keywords:** multiscale, localization, FEM, FBG, SHM

## 1. Introduction

When diagnosing or monitoring condition of a structure and its elements, it is particularly important to be able to determine the field of strains and stresses on the micro scale of the composite in selected areas that are most exposed to destruction or loss of stability. Method presented in this paper may be used in structural health monitoring (SHM) for determination of structure state [6]. Typically, it is not possible to measure at the micro level, but macro measurement methods are available. The aim of the article is to present a method for determining the strain and stress values in composites on a micro scale based on measurements using fiber Bragg grating sensors (FBG) [3] in macro scale. Measurements using FBG allow to determine temperatures and deformations in vast areas, where the distances between the sensor and the interrogator can be very long (even km), as well as due to the use of optical sensors and optical fibers, in the vicinity of large electromagnetic interference. FBG sensors can also be embedded into the structure during its manufacture. Depending on the analyzed problem, a different number of sensors with different arrangement is used. The location of the sensor is not necessarily planned in places of greatest risk to the structure, so the measured values cannot always be taken into account as, for example, maximum values of deformations in the structure. It is often necessary to use inverse methods to obtain information on the distribution of deformations in the structure on a macro scale, and then to determine the stress field at the most vulnerable points on a micro scale. To solve the inverse problem, which enables obtaining information on deformations on a macro scale based on sensor values, it is possible to use methods based on bioinspired algorithms and numerical modelling methods such as FEM or BEM [1]. Knowledge of deformations on a macro scale allows to determine deformations on a micro scale using multi-scale modelling methods [2,5]. The paper uses the multiscale method to determine the field of deformations and stresses in the micro scale.

## 2. Multiscale approach

The problem is analyzed at least in two scales: macro and micro. It is assumed that length scale of macro and micro problems differs and scales can be separated:

$$\frac{l}{L} \ll 1 \quad (1)$$

---

The publication is co-financed from the state budget under the programme of the Minister of Education and Science called "Excellent Science" project no. DNK/SP/548041/2022



where  $L$  and  $l$  are macro and micro length scales. The Representative Volume Element (RVE) is used to model material behaviour at micro scale. The Hill-Mandel condition is assumed:

$$\sigma_{ij}^{macro} \epsilon_{ij}^{macro} = \frac{1}{V_{RVE}} \int_{V_{RVE}} \sigma_{ij}^{RVE} \epsilon_{ij}^{RVE} dV_{RVE} \quad (2)$$

where:  $\sigma_{ij}^{macro}$  – averaged stress at macro scale,  $\epsilon_{ij}^{macro}$  – averaged strain at macro scale,  $\sigma_{ij}^{RVE}$  – stress at micro scale (in RVE),  $\epsilon_{ij}^{RVE}$  – strain at micro scale (in RVE).

The macro average strains can be applied as boundary condition for microscale FEM model of composite for chosen macro points. The results of analysis allows us to determine the stresses in micro scale, and define the areas with huge probability of failure for given macro loads and measurements.

The example of micromodel of composite built from two materials, epoxy matrix and spherical glass inclusions is shown in Figure 1. The Figure 1a shows isolated inclusions, Figure 1b matrix and Figure 1c example of Huber-von Mises stress distribution on the surface of inclusions.

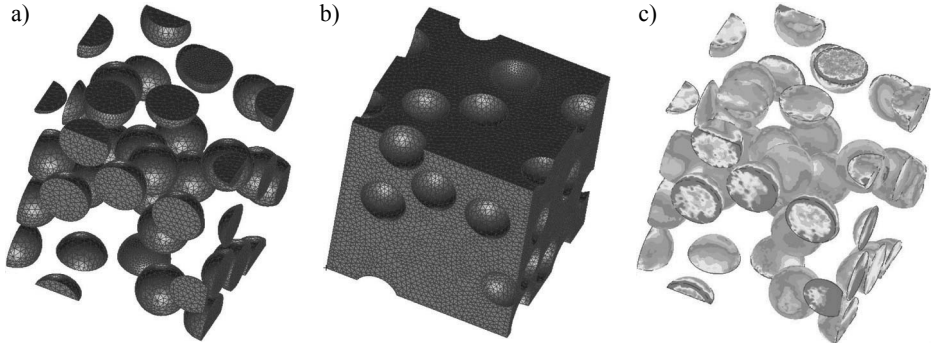


**Figure 1.** Micro model of the composite: a) separated inclusions, b) matrix, c) example of stress distribution in inclusions.

The macro strains can be obtained on the base of FBG measurements however, it should be noted that the FBG strain/displacement sensors work properly only during tension, so in the case of presence of negative axial strains the FBG should be prestressed. The prestressed FBG with initial strain can work for positive and negative axial strains. The FBG is also sensitive on the strains perpendicular to the sensor, so similar like for strain gauges the pair or more sensors are needed to determine proper strain values in many cases. However the FBG sensor are immune to electromagnetic field and radiation the strains depend on temperature so the compensation sensors are also needed in presence of temperature gradients.

The inverse methods should be used when the FBG sensors are not placed in areas of maximal strains in the macro structure, it is important to take into account proper material properties for the macro scale analyses. The composite micro RVE model can be used to obtain macro material properties using proper boundary conditions for the physical linear and also nonlinear material properties of the composite components.

### 3. Conclusions

The FBG sensors measurements in macro scale can be used to determine the areas of highest strains and the strain tensor can be used in micro scale model to determine strains and stresses in the

RVE for composite components. The stress field can be later used to determine the state of the structure for given moment of time and decide if the dangerous situation occurred. Such approach can be used in SHM problems to diagnose potential failure at early stage or track fatigue of the material.

## References

1. Burczyński T., Kuś W., Beluch W., Długosz A., Poteralski A., Szczepanik M.: *Intelligent Computing in Optimal Design*. Springer Nature Switzerland AG, 2020.
2. Burczyński T., Pietrzyk M., Kuś W., Madej Ł., Mrozek A., Rauch Ł.: *Multiscale Modelling and Optimization of Materials and Structures*. John Wiley & Sons, 2022.
3. Hisham K.H.: *Fiber Bragg Grating Sensors: Development and Applications*. CRC Press, Boca, 2020.
4. Jiregna I.T.: *The influence of mounting place of FBG sensor in composite on the base of FEM simulation*. Archives of Mechanics, submitted for publication in 2022.
5. Madej Ł., Mrozek A., Kuś W., Burczyński T., Pietrzyk M.: *Concurrent and upscaling methods in multi scale modelling – case studies*. Computer Methods in Materials Science, 8, 2008, 1-15.
6. Mucha W.: *Comparison of Machine Learning Algorithms for Structure State Prediction in Operational Load Monitoring*. Sensors, 20, 2020, 7087.

**Acknowledgements.** The research is partially financed from subsidiary funds of Faculty of Mechanical Engineering, Silesian University of Technology in 2023.

# Yarn modelling in multibody environment

Maximilian Krentzien<sup>1</sup>, Michael Beitelschmidt<sup>1</sup>

<sup>1</sup> Technical University Dresden (Technische Universität Dresden, Institut für Festkörpermechanik, Professur für Dynamik und Mechanismentechnik, 01062 Dresden, Germany)

Maximilian.krentzien@tu-dresden.de,  
Michael.beitelschmidt@tu-dresden.de

**Keywords:** yarn modelling, multibody dynamics, nonlinear beam, Simpack, warp knitting

## 1. Introduction

Yarn modelling is one of the basic aspects understanding the system behaviour of textile machines, such as warp knitting machines during stitch formation. In order to model the yarn with its properties like viscoplasticity and contact ability several approaches exist. While in [1] a FEM approach is used, in [2] a stream filament description is utilised [1,2]. A general overview of continuous models is described in [3]. The focus of this research is to show the feasibility of a yarn modelling approach based on a new nonlinear beam formulation implemented in the multibody system environment Simpack.

## 2. Methodology

As defined in [4] multibody systems (MBS) are special mechanical systems of bodies that are coupled to each other by joints, moving in space under the influence of forces. They are used as mechanical substitute models to describe the movements and stresses in complex mechanical systems [4].

In this research the new body modelling approach *nonlinear SIMBEAM* is utilised to map the yarn as a transported and discrete beam based on the finite difference method aiming to map the process of stitch formation in a warp knitting machine [5]. Here modelling requirements exist, namely:

Full coupling of yarn dynamics and rigid-body-based machine dynamics; coupled longitudinal and transversal dynamics of the yarn; yarn-machine-contact: belt friction at deflections; yarn-yarn-contact: at knitting space and in knitted fabrics; yarn: efficient transversal dynamics providing numerically stable results at quasi-loose states; yarn: arbitrary material's law: viscoelasticity and plasticity, additionally frequency-dependent effects.

A set of basic models – operating as test candidates for certain modelling aspects – is derived from these requirements and a feasibility study was started. The design of this study consists of two steps for each model: first a topology is developed and then implemented as multibody system in Simpack. Afterwards based on the simulation results it is decided whether the results are valid and so the aspect of modelling is feasible.

## 3. Analysis and results

The following Table 1 lists the basic models and the current feasibility status related. Time integration (TI) and static equilibrium (SE) are the two relevant analysis types.

---

The publication is co-financed from the state budget under the programme of the Minister of Education and Science called "Excellent Science" project no. DNK/SP/548041/2022



**Table 1.** Basic test models.

Model ID	Modelling purpose	Analysis type	Feasibility status
1	Deflection	TI	feasible
2.1	Friction yarn-machine: dynamic	TI	feasible
2.2	Friction yarn-machine: static	TI, SE	investigating
3.1	Friction yarn-yarn: dynamic	TI	investigating
3.2	Friction yarn-yarn: static	TI, SE	pending
4.1	Free span: transversal dynamics	TI	feasible
4.2	Free span: longitudinal dynamics	TI	investigating
5.1	Bearing yarn-deflection: rigid-flexible	TI	investigating
5.2	Bearing yarn-deflection: flexible-rigid	TI	investigating
6	Quasi-loose state	TI, SE	investigating
7	Detachment and contact finding for yarn-needle	TI	pending
8	Arbitrary material's law: Viscoelasticity and plasticity	TI	investigating
9	Minimal curvature radius	TI	pending
10	Performance dependencies	TI	investigating

Model 4.1 “Free span transversal dynamics” is used as an example to explain the way the feasibility study is conducted: This model is used to simulate a free transversal oscillation of a longitudinally pretensioned yarn. The frequency occurring after disabling the initial transversal force, see figure 1, during free oscillation is the eigen frequency that is dependent on the pretension force magnitude.

The topology of model 4.1 is shown in Figure 1. The simulation results of the free oscillation frequency, respectively eigen frequency are shown in Table 2 and are compared against the theory in order to decide about the feasibility.

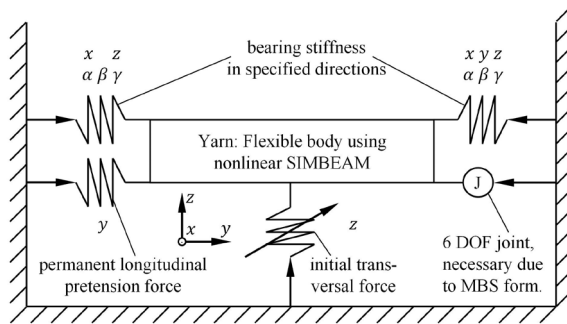


**Figure 1.** MBS topology of model free span transversal dynamics.

**Table 2.** Simulation results of model free span transversal dynamics.

Model	4.1.1	4.1.2
Longitudinal pretension force, N	10	5
Eigen frequency simulation, Hz	384.62	272.11
Eigen frequency theory, Hz	378.35	275.41
Deviation of simulative frequency to theory, %	1.7	-1.2

The theoretical analytical solution contained in [6] is derived from Equation 1 [6].

$$f = \frac{\pi}{2l^2} \sqrt{\frac{EI}{\rho A}} \sqrt{1 + \frac{Fl^2}{\pi^2 EI}} \quad (1)$$

where  $f$  – transversal eigen frequency,  $l$  – length of the yarn,  $E$  – E-modulus of the yarn,  $I$  – area moment of inertia of the ideal yarn,  $\rho$  – density of the yarn,  $A$  – cross section area of the ideal yarn,  $F$  – longitudinal pretension force of the yarn.

In both cases of Table 2 the frequencies deviate not more than 2% from the theoretical value. In conclusion modelling transversal dynamics with *nonlinear SIMBEAM* is feasible.

#### 4. Conclusion and outlook

As shown in Table 1 the feasibility of three models is proven but several models are pending or undergo further investigations so that the feasibility study is still in progress.

#### References

1. Metzkes K., Schmidt R., Martin J., Hoffmann G., Cherif C.: *Simulation of the yarn transportation dynamics in a warp knitting machine*. Textile Research Journal, 83, 2013, 1251–1262.
2. Beiteltschmidt M.: *Simulation of warp and cloth forces in weaving machines*. Melliand Textilberichte, 81, 2000, 45–48.
3. Berger R.: *Instationäre Bewegung und Stabilitätsverhalten eindimensionaler Kontinua*. VDI Verlag, Düsseldorf, 1996.
4. Woernle C.: *Mehrkörpersysteme: eine Einführung in die Kinematik und Dynamik von Systemen starrer Körper*. Springer Vieweg, Berlin, Heidelberg, 2016.
5. Simpack 2023.2: *Documentation, Simpack, Modeling Element Library, Bodies, Bodies: User Interface*. Nonlinear SIMBEAM Bodies, 2022.
6. Dresig H., Holzweißig F., Rockhausen L.: *Maschinendynamik*. Springer Verlag, Berlin, Heidelberg, 2012.

**Acknowledgements.** The DFG research project BE 4791/3-1 is supported by the Deutsche Forschungsgemeinschaft (DFG, German Research Foundation). The financial support is gratefully acknowledged.

# Modelling of temperature change during deformation of TWIP steel

Magdalena Barbara Jabłońska<sup>1</sup>, Katarzyna Jasiak<sup>2</sup>,  
Karolina Kowalczyk<sup>2</sup>, Marek Tkocz<sup>1</sup>,  
Zbigniew Gronostajski<sup>2</sup>

<sup>1</sup> The Silesian University of Technology, Faculty of Materials Science and Metallurgy,  
Krasinskiego Street 8, 40-019 Katowice, Poland

<sup>2</sup> Wrocław University of Science and Technology, Faculty of Mechanical Engineering,  
Łukasiewicza Street 5, 50-371 Wrocław  
magdalena.jablonska@polsl.pl, katarzyna.jasiak@pwr.edu.pl,  
karolinakowalczyk992@gmail.com, Marek.Tkocz@polsl.pl,  
zbigniew.gronostajski@pwr.edu.pl

**Keywords:** tensile test, TWIP steel, heat generation

## 1. Introduction

The temperature due to the change of the work of deformation into heat has influence on the microstructure and mechanical properties of TWIP steel. It could be determined by FEM or measured by thermal camera. In the research the both methods were applied to determine the real temperature of deformed material.

## 2. Research

The effort to reduce the weight of vehicles results in the use of various groups of materials such as composites, polymers or light alloy materials [1], however, the most important and the most responsible elements of safety are made of steel [2]. The approach to the design of modern steels with a wide range of strength and plastic properties changes has recently become more and more important [3].

The temperature of sample during deformation TWIP steel increases due to the change of the work of deformation into heat. Unfortunately the literature in this area is very limited. Some such tests were carried out for TRIP and DP steels. For example Gao et al. (2015) claimed [4], that the temperature rise during adiabatic heating of TRIP and DP steel had increased with increasing strain rate. For the experiments performed under strain rates from 0.1 up to 2000 s<sup>-1</sup> the temperature rise of TRIP steels was in the range of 100–300°C, while that of DP steel was in the range of 100–220°C. More detailed research was carried out by the authors, who showed that at strain rate 1000 s<sup>-1</sup> temperature increases almost by 100°C and at moment of necking, it could increase locally to over 300°C [5].

The tensile tests were performed with strain rates 0.001 and 0.1 s<sup>-1</sup>. For the analysis of the effect of the strain rate on the temperature increase in the area of sample rupture, during the test, the temperature was measured by means of a thermovision camera FLIR T840 with the frame rate 30 fps. Figure 1 shows an exemplary thermogram at the moment of sample rupture, with a measurement rectangle 8×8 mm marked in red (denoted as B1).

---

The publication is co-financed from the state budget under the programme  
of the Minister of Education and Science called "Excellent Science" project no. DNK/SP/548041/2022



**Doskonała  
Nauka**



Ministry of Education and Science  
Republic of Poland



**Republic  
of Poland**

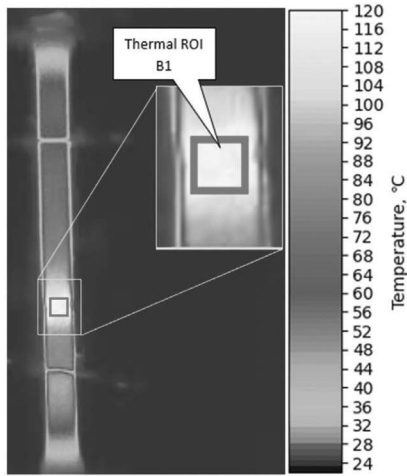


**Figure 1.** Thermogram at the moment of sample rupture with a marked measurement rectangle B1.

A 2D finite element thermo-mechanical model of uniaxial tensile tests was developed using MARC software. Constitutive material model data were obtained from experimental stress-strain curves. Isotropic hardening is assumed in this study. Young's modulus of 210 GPa and Poisson ratio of 0.3 were assumed. The two parameters – ratio of plastic work converted into heat and coefficient of heat exchange with environment – in the model were changed in order to get best fit of temperatures obtained in experiment and in FEM for TWIP steel for strain rate 0.001 and 0.1  $s^{-1}$ .

Next, these coefficients were applied in modelling by FEM of the temperature field in the deformed sample of TWIP steel at strain rate 1000  $s^{-1}$  steel. In the fig. 2 the change of the temperatures during deformation is presented.

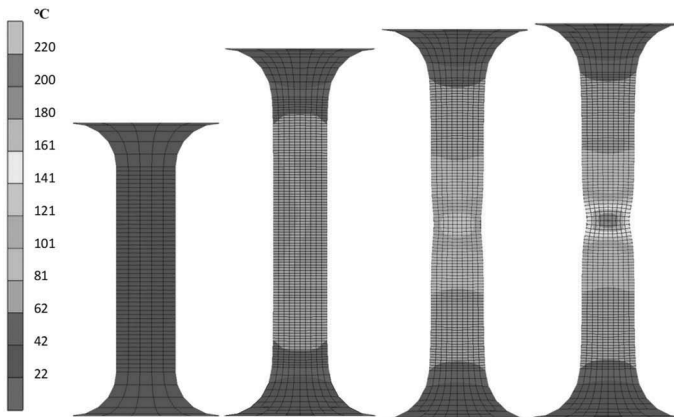


**Figure 2.** Temperature distribution obtained from FEM for strain rate 1000  $s^{-1}$ .

The temperature rises almost linearly together with the deformation and at the moment of deformation localization, a significant localized temperature increase occurs with the progressing development of the necking. In the necking area for steel for the highest strain rate at the moment of rupture, the temperature reaches over 200°C.

## References

1. Frómota D., Lara A., Grifé L., Dieudonné T., Dietsch P., Rehr J., Suppan C., Casellas D., Calvo J.: *Fracture Resistance of Advanced High-Strength Steel Sheets for Automotive Applications*. Metallurgical and Materials Transactions A: Physical Metallurgy and Materials Science, 52, 2021, 840–856.
2. Kuziak R., Kawalla R., Waengler S.: *Advanced high strength steels for automotive industry*. Archives of Civil and Mechanical Engineering, 8, 2008, 103–117.
3. Gronostajski Z., Niechajowicz A., Polak S.: *Prospects for the use of new-generation steels of the AHSS type for collision energy absorbing components*. Archives of Metallurgy and Materials, 55, 2010, 221–230.
4. Gao Y., Xu C., He Z., Li L.: *Response characteristics and adiabatic heating during high strain rate for TRIP steel and DP steel*. Journal of Iron and Steel Research International, 22, 2015, 48–54.
5. Gronostajski Z., Niechajowicz A., Kuziak R., Krawczyk J., Polak S.: *The effect of the strain rate on the stress- strain curve and microstructure of AHSS*, Journal of Materials Processing Technology, 242, 2017, 246–259.

**Acknowledgements.** Work carried out within the framework of the project UMO-2019/35/B/ST8/02184 „Effect of the heat generated during deformation at high strain rates on the structure and properties of high manganese steels with twinning as the dominant deformation mechanism” financed by The NCN.

# Development and validation of the crystal plasticity model for AA6082 aluminum alloy during hot deformation

Oleksandr Lypchanskyi<sup>1,2</sup>, ChenChun Chiu<sup>1,3</sup>, Faisal Qayyum<sup>1</sup>,  
Grzegorz Korpala<sup>1</sup>, Ulrich Prahl<sup>1</sup>

<sup>1</sup> Institut für Metallformung, TU Bergakademie Freiberg, 4 Bernhard-von-Cotta-Straße,  
09599 Freiberg, Germany

<sup>2</sup> AGH University of Science and Technology, Faculty of Metals Engineering and Industrial  
Computer Science, Av. Mickiewicza 30, 30-059 Krakow, Poland

<sup>3</sup> Department of Mechanical Engineering, National Taiwan University of Science and Technology,  
Taipei 106335, Taiwan

Oleksandr.Lypchanskyi@imf.tu-freiberg.de,  
chenchun0101@gmail.com, Faisal.Qayyum@imf.tu-freiberg.de,  
Grzegorz.Korpala@imf.tu-freiberg.de,  
Ulrich.Prahl@imf.tu-freiberg.de

**Keywords:** crystal plasticity, aluminum alloy, constitutive model, simulation

## 1. Introduction

The wide use of aluminum alloy is due to the high resistance to fatigue of structural elements made of these alloys as well as good specific strength [1]. The 6XXX series contains age-hardenable aluminum alloys that provide a good combination of ductility and strength, and the main alloying elements include Si and Mg. [2]. The low resistance to plastic forming of such alloys allows forming them both at elevated temperatures and at room temperature. Obtaining finished products is possible through the use of forging or stamping under isothermal and non-isothermal conditions [1], as well as extrusion techniques can be carried out at high temperatures [3] to ensure stable material flow.

Homogenization processes are successfully used in order to increase the quality and mechanical properties after aging and to homogenize the cast microstructure before deformation [4]. Another important aspect is the controlled homogenizing cooling, which will affect the precipitation due to the content of Mg and Si [5].

In addition, increasing the formability of these alloys can be achieved by heating the dies to elevated temperatures. Through the appropriate selection of plastic deformation parameters (temperature, strain, and strain rate), it is possible not only to close defects or porosities resulting from the casting process but also to obtain a fine-grained structure as a result of recrystallization. In this way, strength properties, fatigue strength, and impact strength are improved as well as a uniform structure is obtained [6].

Understanding the behavior of individual precipitates depending on temperature allows the optimization of thermo-mechanical parameters. The typical Al-Mg-Si alloy precipitation sequence includes [7]: supersaturated solid solution SSSS → clustering (Mg/Si clusters and co-clusters) → Guinier–Preston (GP)-I zones →  $\beta''$  →  $\beta'$  →  $\beta$  ( $Mg_2Si$ ). AA6082 aluminum alloy also contains the so-called intermetallic  $\alpha$ -Al(FeMn)Si precipitates formed during casting and homogenization [8]. Mn in this alloy increases corrosion resistance and deformation uniformity [9] while Fe is an

---

The publication is co-financed from the state budget under the programme  
of the Minister of Education and Science called "Excellent Science" project no. DNK/SP/548041/2022



Doskonała  
Nauka



Ministry of Education and Science  
Republic of Poland



Republic  
of Poland

impurity element [10]. Generally, Mg and Si are the main elements that create hardening precipitates and thus increase the strength of Al Mg-Si alloys [11].

## 2. Material, methods and results

Table 1 presents the chemical composition of AA6082 aluminum alloy. An important aspect is the distribution of individual precipitates in the microstructure, especially within grains, which will affect both the mechanical properties of the alloy and its formability. Figure 1 presents precipitates distribution in the grain area after isothermal holding at 400°C for 4 min AA6082 aluminum alloy investigated by electron backscatter diffraction (EBSD) method with energy dispersive X-ray spectrometry (EDS) as well as scanning electron microscope (SEM). EDS (Mn) and EDS (Si) elements peaks correspond to the distribution of  $\alpha$  Al(FeMn)Si precipitates. This type of intermetallic fine precipitate does not affect the hardening of the alloy [12]. Cooling from the supersaturated state and subsequent aging causes, above all, high susceptibility of grain boundaries (GB) to the formation of large  $\beta$ -Mg<sub>2</sub>Si precipitate [13] (EDS(Si) with EDS(Mg) peaks).

**Table 1.** Chemical composition of the investigated AA6082 alloy.

Si	Fe	Mn	Mg	Al
1.05	0.37	0.662	0.80	Bal.

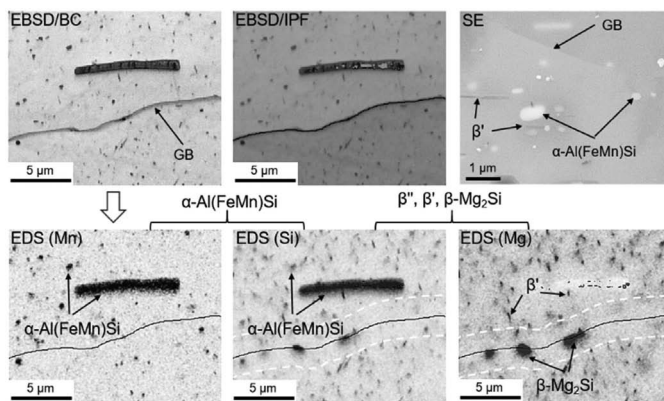


**Figure 1.** EBSD maps with corresponding EDX maps of the distribution of Mn-, Si- Mg- elements (indicating  $\alpha$  Al(FeMn)Si,  $\beta'$ ,  $\beta$ -Mg<sub>2</sub>Si precipitates respectively) and SE image of AA6082 aluminum alloy after solution annealing and isothermal holding at 400°C for 4 min. The maps as well as the image present grain boundaries (GB).

Optimization of the deformation parameters in this situation and control of strain during plastic deformation is possible basing on the understanding of crystal plasticity behavior with particular consideration of factors such as crystallographic orientation, type, and distribution of individual precipitates as well as the density of dislocations.

### 2.1. Dislocation-based model

Basing on the constitutive laws of dislocation-based model the deformation gradient for kinematics can be calculated as follows:

$$F = F_e F_p \quad (1)$$

where:  $F_e$  – the rigid body rotations and elastic deformation of the lattice,  $F_p$  – the plastic deformation gradient and for the evolution of plastic deformation where the plastic velocity gradient depends on dislocation slip.

More information about the model and methodology of such simulations can be found in work [14]. Figure 2 presents crystal plasticity simulation results. It can be observed that stress concentration is along the edges of the particles and high-strain interlocked regions.

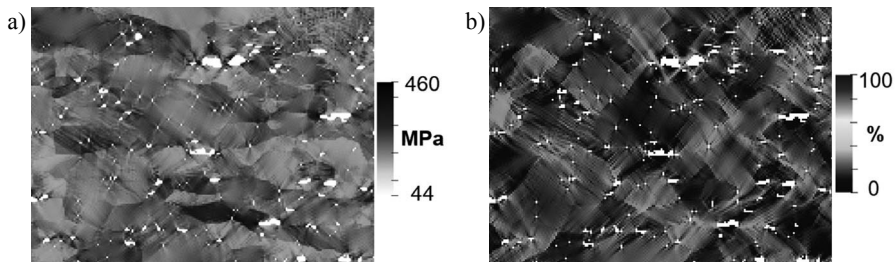


**Figure 2.** Simulation results after 20% global true tensile strain along the horizontal axis at 200°C. Local (a) True Mises stress (b) True Mises strain, distributions. White areas indicate precipitates.

## References

- Deng L., Wang X.Y., Jin J.S., Xia J.C.: *Precision forging technology for aluminum alloy*. *Frontiers of Mechanical Engineering*, 13, 2018, 25–36.
- Hirsch J.: *Automotive Trends in Aluminium – The European Perspective*. *Materials Forum*, 28, 2004, 15–23.
- Singh K., Nayak R.K., Das D., Sahoo S.K.: *Improvement of hardness of short fork (6082 alloy)-A case study*. *Materials Today: Proceedings*, 18, 2019, 2515–2519.
- Rinderer B.: *The metallurgy of homogenization*. *Materials Science Forum*, 693, 2011, 264–275.
- Birrol Y.: *The effect of homogenization practice on the microstructure of AA6063 billets*. *Journal of Materials Processing Technology*, 148, 2004, 250–258.
- Czechowski D., Schott A.: *Gefügeuntersuchungen beim Aluminiumschmieden*. *Schmiede-Journal*, 2004, 26–27.
- Lai Y.X., Jiang B.C., Liu C.H., Chen Z.K., Wu C.L., Chen J.H.: *Low-alloy-correlated reversal of the precipitation sequence in Al-Mg-Si alloys*. *Journal of Alloys and Compounds*, 701, 2017, 94–98.
- Kuijpers N.C.W., Kool W.H., Koenis P.T.G., Nilsen K.E., Todd I., van der Zwaag S.: *Assessment of different techniques for quantification of  $\alpha$ -Al(FeMn)Si and  $\beta$ -AlFeSi intermetallics in AA 6xxx alloys*. *Materials Characterization*, 49, 2002, 409–420.
- Nam S.W., Lee D.H.: *The Effect of Mn on the Mechanical Behavior of Al Alloys*, *Metals and Materials*, 6, 2000, 13–16.
- Ji S., Yang W., Gao F., Watson D., Fan Z.: *Effect of iron on the microstructure and mechanical property of Al-Mg-Si-Mn and Al-Mg-Si diecast alloys*, *Materials Science and Engineering A*, 564, 2013, 130–139.
- Birrol Y.: *Pre-aging to improve bake hardening in a twin-roll cast Al-Mg-Si alloy*. *Materials Science and Engineering A*, 391, 2005, 175–180.
- Nowotnik G.M., Sieniawski J.: *Intermetallic phase particles in 6082 aluminum alloy*, *Journal of Materials Processing Technology*, 162 163, 2005, 367–372.

13. Hidalgo-Manrique P., Cao S., Shercliff H.R., Hunt R.D., Robson J.D.: *Microstructure and properties of aluminium alloy 6082 formed by the Hot Form Quench process*. Materials Science and Engineering A, 804, 2021, 140751.
14. Han F., Roters F., Raabe D.: *Microstructure-based multiscale modeling of large strain plastic deformation by coupling a full-field crystal plasticity-spectral solver with an implicit finite element solver*. International Journal of Plasticity, 125, 2020, 97–117.

**Acknowledgements.** The research was financed by the German Research Foundation DFG (Project number 456415464).

# Accounting for random character of nucleation in modelling of phase transformations in steels

Lukasz Poloczek<sup>1</sup>, Roman Kuziak<sup>1</sup>, Jakub Forys<sup>2</sup>,  
Danuta Szeliga<sup>2</sup>, Maciej Pietrzyk<sup>2</sup>

<sup>1</sup> Łukasiewicz Research Network – Upper Silesian Institute of Technology,  
ul. K. Miarki 12, 44-100 Gliwice, Poland

<sup>2</sup> AGH University of Science and Technology, Al. Mickiewicza 30, 30-059 Kraków, Poland  
lukasz.poloczek@imz.lukasiewicz.gov.pl,  
roman.kuziak@imz.lukasiewicz.gov.pl,  
jakubforys@student.agh.edu.pl,  
szeliga@agh.edu.pl, maciej.pietrzyk@agh.edu.pl

**Keywords:** stochastic model, dislocation density, grain size, phase transformations, laminar cooling

## 1. Introduction

There is a continuous search for construction materials that combine high strength with good formability, as well as a high strength-to-density ratio. Steels have met these requirements for many decades. Modern multiphase steels, which were developed in the last decades of the 20<sup>th</sup> century, benefit from the best features of phases they are composed of. Advanced numerical models, which can predict heterogeneity of the microstructure are needed to gain knowledge on distributions of microstructural features and to design thermal-mechanical cycles allowing to obtain optimal microstructure and resulting properties. Hypothesis was put forward in [1] that application of the stochastic internal variables to the modelling of multiphase steels will allow to build the model with the capability to predict various features of heterogeneous microstructures.

Following this motivation, we developed the stochastic model, which describes evolution of the dislocation density and the grain size during multistage hot deformation. Analysis and optimization of the numerical parameters of the model are described in [2] while its description, identification, validation and application are presented in [3]. This model calculates histograms of the dislocation density and the grain size after multi-step hot deformation. On the other hand, the properties of the products are obtained by control of the phase transformation during cooling after hot forming. Therefore, the objective of our work is to extend the model by including phase transformations, accounting for the random character of nucleation of a new phase.

Literature review shows that the stochastic models were widely used to describe random nucleation during phase transformations. However, majority of the approaches consider nucleation in the microstructure represented explicitly (full-field models). Probabilistic approach was used in the Cellular Automata models [4], as well as in the Monte Carlo method, see review in [5]. Our objective is to avoid costly computations in the microstructure represented explicitly and to develop a mean-field model based on a statistical description of the phenomena occurring in the microstructure. In the case of steels, this model must be based on the non-classical nucleation theory, which occurs in a diffusional growth where diffusion field gives rise to reduced nucleation probability around growing nuclei [6]. This aspect is considered in the present work.

---

The publication is co-financed from the state budget under the programme  
of the Minister of Education and Science called "Excellent Science" project no. DNK/SP/548041/2022



## 2. Model and results

In the model under development, equilibrium state of the metallurgical system is described by the thermodynamics. The phase transformation model predicts changes of the state of the system between the two equilibrium states during the transient process. The equilibrium is represented by the Fe-C phase equilibrium diagram. Development of the stochastic phase transformation model for diffusion-controlled transformations is our objective. The models, which account for the probability of both nucleation and growth, can be encountered in the scientific literature, but they are based on the explicit representation of the microstructure [7] and are computationally expensive. Moreover, several published models deal with the solidification process [8] or solid-state phase transformations in other materials than steels [9]. Thus, in the first approach we focus on modelling of random character of the nucleation only and the deterministic model is used to describe growth of the new phase.

### 2.1. Nucleation

An initial step of transformations in solids is that of nucleation. To model nucleation, one must specify nuclei location in space as well as how nuclei appear as a function of time. In the JMAK theory, there are two nucleation modes [5]: 1) Classical theory, which assumes that the thermodynamic properties of a nucleus are uniform and the same as the equilibrium bulk counterparts within the nucleus.; 2) Non-classical nucleation theory of Cahn and Hilliard, which is based on the diffuse-interface description of the interfaces. In this theory a coalescence of subcritical clusters and stepwise nucleation is introduced [10].

For years a stochastic character of nucleation was accounted for in the modelling of phase transformations and the JMAK approach based on Poisson statistics was used. Although most of the published papers deals with the crystallization process, solid-state transformations are addressed in some publications, as well. Early papers were focused on collecting a large set of nucleation data [11]. In the homogeneous Poisson Point Process no correlation among nuclei is present and in the case of steels the probability of nucleus to appear depends on undercooling below  $A_{e3}$ , state of the austenite, etc. Thus, assuming Poisson homogenous nucleation, the probability that the nucleus of the new phase occurs in the time  $\Delta t = t_{i+1} - t_i$  is:

$$\begin{aligned} \mathbf{P}[\xi(t_i) = 0] &= \begin{cases} p(t_i) & \text{if } p(t_i) < 1 \\ 1 & \text{otherwise} \end{cases} \\ \mathbf{P}[\xi(t_i) = 1] &= 1 - \mathbf{P}[\xi(t_i) = 0] \end{aligned} \quad (1)$$

In Equation (1)  $p(t_i)$  is a function, that bounds together the probability that the material point becomes a critical nucleus in a current. Assuming Poisson homogenous nucleation the following equation was used:

$$p(t_i) = b_1 D_\gamma^{-b_2} \rho^{b_3} (A_{e3} - T)^{b_4} \quad (2)$$

where:  $D_\gamma$  – grain size,  $\rho$  – dislocation density,  $b_1, b_2, b_3, b_4$  – coefficients.

Our objective was to introduce non-Poisson statistics, which account for the interaction between existing grains of a new phase and a new nucleus. The solution is based on the method of the critical region [12]. Additionally, in the case of the austenite decomposition, carbon is pushed out from the ferrite grains and carbon content in the austenite  $c_\gamma$  increases. Thus, probability of nucleation in the neighbourhood of the new ferrite grains is decreased. The idea of this stochastic approach to modelling

austenite-ferrite transformation is shown in Figure 1a. The effect of microchemical bands, which occur during the solidification process [13], is the next factor, which we considered. The independent variables in the model were the width of the high manganese enriched band  $w$  and the distance between the bands  $d$ . The improved model accounts for a difference in the nucleation rate and the grain size between high and low manganese bands. Thus, equation (2) is revised to the following form:

$$p(t_i) = [b_{1\max}(1 - \xi) + b_{1\min}\xi] D^{-b_2} \rho^{b_3} (A_{e3} - T)^{b_1} [1 - X_f(t_i)] \left[ \frac{C_0}{C_f(t_i)} \right]^{b_5} \quad (3)$$

where:  $\xi = w/d$  – relative thickness of the high manganese band,  $b_{1\min}$ ,  $b_{1\max}$  – coefficients.

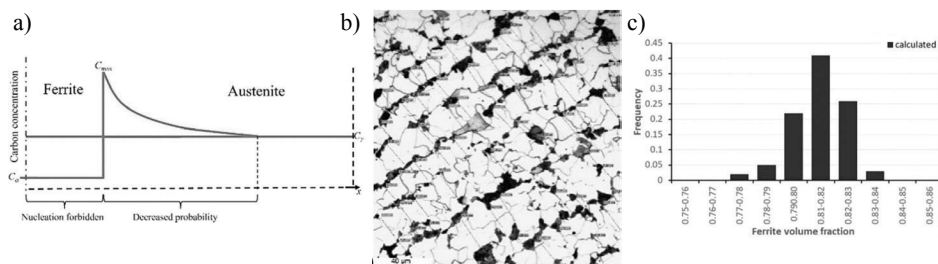


**Figure 1.** Carbon distribution as a function of the distance from the centre of the ferrite grain and the idea of the stochastic approach to the nucleation model based on the method of the critical region (a) and image of the microstructure with high and low manganese bands (b).

## 2.2. Results and conclusions

The stochastic model predicts distributions (histograms) of such parameters as volume fractions of phases and size of ferrite grains. Simulation of cooling of the flat rod was performed and the calculated histogram of the ferrite volume fraction is shown in Figure 1c. Measured average ferrite volume fraction was 0.82. It was concluded that: The model does not require explicit representation of the microstructure, which allows to decrease the computing times radically; ii) The model predicts distribution of the microstructure features in a statistical way. It allows to calculate distributions (histograms) of the microstructural features accounting for the state of the microstructure prior to transformations, including the effect of the microchemical bands.

## References

1. Szeliga D., Chang Y., Bleck W., Pietrzyk M.: *Evaluation of using distribution functions for mean field modelling of multiphase steels*. Procedia Manufacturing, 27, 2019, 72–77.
2. Klimczak K., Oprocha P., Kusiak J., Szeliga D., Morkisz P., Przybyłowicz P., Czyżewska N., Pietrzyk M.: *Inverse problem in stochastic approach to modelling of microstructural parameters in metallic materials during processing*. Mathematical Problems in Engineering, 2022, article ID 9690742.
3. Szeliga D., Czyżewska N., Klimczak K., Kusiak J., Kuziak R., Morkisz P., Oprocha P., Pietrzyk M., Poloczek Ł., Przybyłowicz P.: *Stochastic model describing evolution of microstructural parameters during hot rolling of steel plates and strips*. Archives of Mechanical and Civil Engineering, 22, 2022, 239.
4. Czarnecki M., Sitko M., Madej Ł.: *The role of neighborhood density in the random cellular automata model of grain growth*. Computer Methods in Materials Science, 21, 2021, 129–137.

5. Liu X., Li H., Zhan M.: *A review on the modeling and simulations of solid-state diffusional phase transformations in metals and alloys*. Manufacturing Review, 5, 2018.
6. Bruna P., Crespo D., González-Cinca R.: *On the validity of Avrami formalism in primary crystallization*. Journal of Applied Physics, 100, 2006, 054907.
7. Lyrio M.S., Alves A.L.M., Silveira de Sá G.M., da Silva Ventura H., da Silva Assis W.L., Rios P.R.: *Comparison of transformations with inhomogeneous nucleation and transformations with inhomogeneous growth velocity*. Journal of Materials Research and Technology, 8, 2019, 4682–4686.
8. Maggioni G.M.: *Modelling and data analysis of stochastic nucleation in crystallization*. PhD thesis, ETH Zurich, 2018.
9. Helbert C., Touboul E, Perrin S., Carraro L., Pijolat M.: *Stochastic and deterministic models for nucleation and growth in non-isothermal and/or non-isobaric powder transformations*. Chemical Engineering Science, 59, 2004, 1393–1401.
10. Ou X., Sietsma J., Santofimia M.J.: *Fundamental study of nonclassical nucleation mechanisms in iron*. Acta Materialia, 226, 2022, 117655.
11. Izmailov A.F., Myerson A.S., Arnold S.: *A statistical understanding of nucleation*. Journal of Crystal Growth, 196, 1999, 234–242.
12. Alekseechkin N.V.: *On calculating volume fractions of competing phases*. Journal of Physics: Condensed Matter, 12, 2000, 9109–9122.
13. Rivera-Díaz-Del-Castillo P.E.J., Sietsma J., Van Der Zwaag S.: *A model for ferrite/pearlite band formation and prevention in steels*. Metallurgical and Materials Transactions A, 35A, 2004, 425–433.

**Acknowledgements.** Financial assistance of the NCN, project no. 2021/43/B/ST8/01710, is acknowledged.

# Optimization, Design and Modelling with Genetic Algorithms: Tracing Trends in Selected Applications since Year 1989

Wojciech Paszkowicz<sup>1</sup>

<sup>1</sup> Institute of Physics, Polish Academy of Sciences, Aleja Lotników 32/46,  
PL-02-668 Warsaw, Poland  
paszk@ifpan.edu.pl

**Keywords:** genetic algorithm, global optimization, design, modelling

## 1. Introduction

Genetic algorithms form a family of well-known and rapidly developing numerical methods devoted to global optimization, design and modeling, particularly suitable for tasks of high computational complexity. Their applications include various fields of science, technology, economics, medicine, data mining, etc. The algorithms, constructed using the principles of Darwinian evolution began to develop widely right after the publication of the Goldberg's book describing multiple examples of applications [1]. Since then, multiple reviews of this type have been published, including one of the most recent, devoted to metallurgical computational tasks [2]. This presentation describes the analysis of progress of the application of such algorithms.

## 2. Results

The studies described are based on topics recorded in the SCI-Ex database. Topics related to genetic/evolutionary algorithms have been appearing in the database since year 1986; Figure 1 shows the temporal evolution of number of articles with identified topic „genetic algorithms or evolutionary algorithms”). The figure illustrates thus the growing interest in these methods.

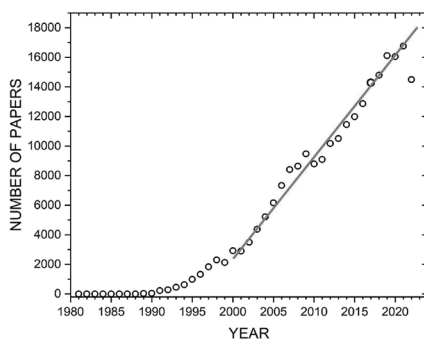


**Figure 1.** Nearly linear increase of scientific publications on evolutionary computation with time; the data, collected on 8<sup>th</sup> Dec, 2022, refer to papers with genetic algorithms or evolutionary algorithms as one of topics.

---

The publication is co-financed from the state budget under the programme of the Minister of Education and Science called "Excellent Science" project no. DNK/SP/548041/2022

A significant interest was initiated in 1990 just after the appearance of the above-mentioned Ref. [1]. A nearly linear upward trend is observed since 2000. Since 1990, both, the methods and computer codes, have been constantly developing, enabling the work to a broad user community.

In this work, various fields of application, belonging to science, technology, economics, ecology etc. were a subject of investigation. It was found that the interest in the use of genetic methods strongly depends on the field. It has been found that in many broad as well as narrow fields, about one per two hundred scientific publications describes some practical application of a genetic or evolutionary approach. In some areas, this share is even five or ten times higher. These observations document that algorithms are now of great importance as a numerical method useful in computational tasks of high complexity. Their optimization, modelling and design related uses developed quite fast. Thirty years ago the algorithms were only a little-known curiosity. After a period of only a single generation their status changed completely.

Interestingly, the analysis of literature data shows that in some fields the share of the genetic methods increases approximately linearly over time. Some other fields have already reached a certain level of saturation, which means that the methods' status is well established. For the example of Internet-related applications, the behavior is more complex. It is characterized by a renaissance of rapid application development during the last few years, as concluded after analyzing the simple „internet” topic.

### **3. Summary**

The presented various examples of temporal evolution of the genetic/evolutionary algorithms allow to formulate a forecast of the future development of genetic methods and the expected directions of their use. Both, the growing availability of universal and specialized software, as well as the expected wide availability of quantum computers, are to lead to the increasingly widespread presence of genetic methods in science, technology and everyday life.

### **References**

1. Goldberg D.E.: *Genetic Algorithms in Search, Optimization and Machine Learning*. Addison-Wesley, Reading, MA, 1989.
2. Chakraborti N.: *Data-Driven Evolutionary Modeling in Materials Technology*. CRC Press, Boca Raton, FL, 2022.

# Towards Open Science with Multi-Cloud Computing using Onedata

Michał Orzechowski<sup>1</sup>, Michał Wrzeszcz<sup>1</sup>, Bartosz Kryza<sup>1</sup>,  
Lukasz Dutka<sup>1</sup>, Renata G. Słota<sup>1,2</sup>, Jacek Kitowski<sup>1,2</sup>

<sup>1</sup> Academic Computer Centre CYFRONET AGH, Nawojki 11, 30-950 Kraków, Poland

<sup>2</sup> AGH University of Science and Technology, Faculty of Computer Science,  
Electronics and Telecommunications, Institute of Computer Science,  
Al. Mickiewicza 30, 30-059 Kraków, Poland

morzech@agh.edu.pl, wrzeszcz@agh.edu.pl,  
bkryza@agh.edu.pl, lukasz.dutka@cyfronet.pl,  
rena@agh.edu.pl, kito@agh.edu.pl

**Keywords:** multi-cloud, cloud computing, data access, distributed systems, open science

## 1. Introduction

Running and deploying applications on different and varied infrastructures is still a major difficulty, particularly for scientific applications which often take the form of intricate workflows made up of multiple steps and require specialized software or libraries, and the use of a Workflow Management System (WMS). Solutions such as virtualization, application containers, and infrastructure automation can help to alleviate this complexity.

Cloud providers offer advanced tools for setting up infrastructure and deploying applications. However, the variety of cloud solutions, such as OpenStack, AWS, or GCP, can make it hard to avoid vendor lock-in. Kubernetes [1] offers a mature set of well-standardized principles and practices for running software in a distributed virtualized environment, which can help to solve this problem. Recently, Kubernetes has been referred to as a “Cloud Native Operating System” in a number of articles, and major cloud providers and platforms now offer “one-click” Kubernetes deployments.

In this study, we present an ongoing project that aims to automate the deployment and execution of scientific workflows. This kind of applications is getting more and more popularity in the field of computational science, including simulations and big data problems in different domains, like for example metallurgy, high energy physics, biotechnology, medicine and others. Our approach utilizes Kubernetes and Onedata data management systems to eliminate differences between various infrastructure providers. The main contributions of this work include the following:

- 1) we provide an initial implementation of Kubernetes native support for running scientific workflows on multiple cloud infrastructures,
- 2) we offer a unified solution that allows for data to be delivered to the scientific workflow transparently,
- 3) we present an architecture of a solution that automates the entire workflow lifecycle, including provisioning, deployment, execution, and monitoring.

## 2. Onedata Data Management System

Onedata [2,3] is a globally distributed, high-performance data management system that offers transparent and unified access to storage resources worldwide. It can be used for various purposes,

---

The publication is co-financed from the state budget under the programme  
of the Minister of Education and Science called “Excellent Science” project no. DNK/SP/548041/2022

such as personal data management and data-intensive scientific computations. The fully distributed architecture of Onedata enables creation of hybrid-cloud infrastructure deployments that include private and commercial cloud resources. With Onedata, users can share, collaborate, publish data and perform high-performance computations on distributed data. Furthermore, it supports POSIX-compliant data access for applications.

Onedata is composed of three primary services: Onezone, Oneprovider, and Oneclient. Onezone manages authorisation and metadata distribution, giving users access to the Onedata ecosystem. Oneprovider serves data to users and connects storage systems to Onedata, while Oneclient allows for seamless POSIX-compatible data access on user nodes. Oneprovider can be deployed as a single node or an HPC cluster and can handle large amounts of data with high speeds, even on parallel storage solutions with petabytes of data and GB/s throughput.

Recently it has been featured with a robust workflow engine, powered by OpenFaaS [4], which enables creation of advanced data processing pipelines that can access distributed data seamlessly. The workflow feature can be used to establish a comprehensive data archiving and preservation system in compliance with OAIS standards, including ingestion, validation, curation, storage, and publication. The workflow function library provides pre-built functionalities (implemented as Docker images) for typical archival tasks such as metadata extraction, format conversion, checksum validation, virus checks, and more. Custom functions can be added and shared among user groups easily. For further flexibility, to enable transparent data access from the Onedata ecosystem, the functions that execute legacy code can be accompanied by Oneclient, which exposes data using the abstraction of the POSIX filesystem. In case of new implementations, functions can leverage Oneprovider API to fetch data directly via REST.

### 3. Multi-Cloud Deployment and FaaS Integration

Onedata makes it simple to establish a multi-cloud architecture with seamless access, as shown in Figure 1. It provides also means to expose data located on not cloud-native, legacy storage systems. The data is indexed by Oneprovider and made it globally accessible through Onezone. From the data perspective, Oneprovider connected to a legacy storage system functions as a source Oneprovider, as it holds the original replica of the data. To effectively process data from a legacy storage system on an external cloud, we deploy another instance of Oneprovider on Cloud A, which is connected to a cloud-native storage system that functions as a cache for replicated data. When accessing the data, missing data blocks are automatically replicated between Oneproviders. Additional Oneproviders can be deployed on clouds where we want to process data, creating a network of caching Oneproviders. The data is replicated between them depending on which Oneprovider stores the necessary replica.

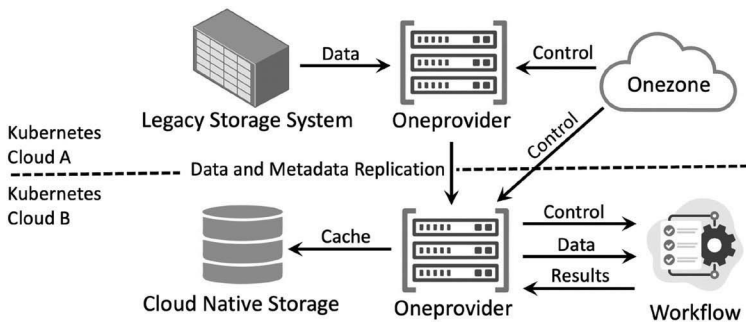


Figure 1. Data Transfer and Workflow Execution on Multi-Cloud.

On a cloud where computation takes place, on a Kubernetes cluster an instance of OpenFaaS is deployed next to Oneprovider. The scientific workflow, that uses data stored on Cloud A can be executed on Cloud B. Oneprovider manages the transfer of needed data blocks from Cloud A, caches them on Cloud B and then transfers them to individual OpenFaaS function, used to realize the workflow execution. This architecture highly leverages the mature ecosystem of Kubernetes that enables easy multi-cloud execution of scientific workflows, independently of physical location of data.

#### 4. Conclusion and future work

The proposed multi-cloud architecture and mechanism for executing scientific applications using scientific workflows can greatly simplify the automation of complex workflow scenarios such as:

- 1) Reproducibility: upon completion, the full execution state (including the runtime environment) of the workflow is recorded and can be used to repeat the execution in the future.
- 2) Live migration: if the workflow needs to be moved to a different computing infrastructure, its execution state can be used to restore the environment and resume the workflow after migration is complete.
- 3) Fault tolerance: in case of failure due to infrastructure or software error, the workflow execution can be resumed as soon as the cause of the failure is resolved.
- 4) Smart-rerun: as the state of each execution step of the workflow is recorded (including intermediate data), parts of the workflow can be replaced and re-run, allowing the workflow engine to reuse already computed data or repeat the execution as needed.

The results show feasibility of the proposed solution and confirm that under certain conditions the proposed new approach for making use of legacy data systems can lead to improvements in workflow execution time. Future work includes automating deployment of Kubernetes clusters on different cloud providers and improvement of existing procedures of deploying Onedata and OpenFaaS components, based on supplied requirements and environments characteristics.

#### References

1. Container Orchestration Kubernetes: <https://kubernetes.io>.
2. Wrzeszcz M., Kitowski J., Słota R.G.: *Towards Transparent Data Access with Context Awareness*. Computer Science, 19, 2018, 201–221.
3. Wrzeszcz M., Dutka Ł., Słota R.G., Kitowski J.: *New approach to global data access in computational infrastructures*. Future Generation Computer Systems, 125, 2021, 575–589.
4. Cloud Operating system.
5. <https://blogs.oracle.com/cloud-infrastructure/kubernetes-a-cloud-and-data-center-operating-system>.
6. OpenFaaS – Serverless Functions Made Simple: <https://openfaas.com>.

**Acknowledgements.** MO and JK are grateful for support from Proteus-RS project (EU RFCS grant, contract 899455). RGS is grateful for support from the subvention of Polish Ministry of Education and Science assigned to AGH University. This scientific work was supported in part by an international project co-financed by the program of the Minister of Science and Higher Education entitled “PMW” in the years 2020-2021; contract No. 5145/H2020/2020/2.

# Optimization of spring steel flat bar rolling using advanced meshless solution and genetic algorithm

Miha Kovačič<sup>1,2,3</sup>, Umut Hanoglu<sup>2,4</sup>, Robert Vertnik<sup>1,2</sup>,  
Aljaž Zupanc<sup>1</sup>, Božidar Šarler<sup>2,4</sup>

<sup>1</sup> ŠTORE STEEL, d.o.o., Research and Development, 3220 Štore, Slovenia

<sup>2</sup> Laboratory for Fluid Dynamics and Thermodynamics, University of Ljubljana,  
Faculty of Mechanical Engineering, 1000 Ljubljana, Slovenia

<sup>3</sup> College of Industrial Engineering, 3000 Celje, Slovenia

<sup>4</sup> Institute of materials and technology, 1000 Ljubljana, Slovenia

miha.kovacic@store-steel.si, umut.hanoglu@fs.uni-lj.si,  
robert.vertnik@store-steel.si, aljaz.zupanc@store-steel.si,  
bozidar.sarler@fs.uni-lj.si

**Keywords:** hot rolling, optimization, meshless methods, simulation, genetic algorithm

## 1. Abstract

Štore Steel ltd. is one of the biggest flat spring steel producers in Europe. For hot rolling also continuous rolling line (10 stands) is used. The rolling schedules contains more than 400 different shapes (flat, square and round bars) and dimensions which are rolled monthly. When changing from one dimension to another, the adjustment of individual stands occurs in the way that with the new settings we can achieve the desired dimension. In this work in-house developed rolling simulation system for the hot rolling of steel was used and also universal GA system was made using AutoLISP, which is integrated into AutoCAD (i.e. commercial computer-aided design software), capable of manipulating text files containing rolling simulation system input and output data. In this paper genetic algorithm (GA) was used for optimization of the rolling gap (i.e. distance between roll surfaces) optimization during rolling of spring steel 51CrV4, dimension 80×53 mm. Six gap values (for six continuous rolling line stands) have been used as the genes from which the organisms were composed. For changing organisms, the following genetic operations were being used: crossover, mutation and permutation. The overflowing at vertical rolling stand number 3 of continuous rolling line was avoided successfully in practice.

## 2. Introduction

Štore Steel ltd. is a small flexible steel plant, where more than 200 steel grades with varying chemical compositions are produced. The scrap is melted in an electric arc furnace and, after tapping, ladle-treated and finally cast using a two-strand continuous caster. Cooled down cast billets (180 mm x 180 mm) are reheated up to 1250°C and rolled. After exiting the reheating furnace, the material goes through the descaling device and duo reversible rolling stand with 800 mm diameter rolls. The rolled material makes 7 passes. The final rolling diameters achieved using the same rolling stand range from 95 to 110 mm [1,2].

Before it enters the continuous rolling line with 460 mm diameter rolls (700 mm length), the material is rolled using a duo reversible rolling stand with 650 mm diameter rolls. After exiting the

---

The publication is co-financed from the state budget under the programme  
of the Minister of Education and Science called "Excellent Science" project no. DNK/SP/548041/2022



Doskonała  
Nauka



Ministry of Education and Science  
Republic of Poland



Republic  
of Poland

duo reversible stand, where material makes 5 passes (the last is a by-pass), the material cools down while rolling temperature is achieved. The temperature is measured using infrared pyrometer.

The continuous rolling line itself consists of a descaling device, 6 horizontal and 4 vertical stands, three hot shears – of which two are used for cutting the first and the last end of the rolled bar, while the third is used for cutting the final dimensions before the material enters the cooling bed.

In this work, in-house developed rolling simulation system for the hot rolling of steel is used [3,4]. The system is capable of simulating rolling of slabs and blooms, as well as round or square billets, in different symmetric or asymmetric forms in continuous, reversing, or combined rolling. Groove geometries are user-defined and an arbitrary number of rolling stands and distances between them may be used. A slice model and meshless local radial basis function collocation method are used [5]. Groove (groove shape) and parameters and geometry of rolling line (e.g. distances between stands, type of rolling stands) as well as rolling parameters (e.g. gaps, rolling temperature and speed) or material properties can be accessed or manipulated using simple text files. Similar is with simulation results (e.g. geometry, stresses, strains). For informational purposes, in this paper, genetic algorithm (GA) was used for optimization of the rolling gap (i.e. distance between roll surfaces) rolling of spring steel 51CrV4, dimension 80×53 mm. The overfilling at vertical rolling stand number 3 of continuous rolling line was avoided successfully in practice. The actual overfilling and calculated overfilling using rolling simulation system are presented in Figure 1 and 2, respectively.

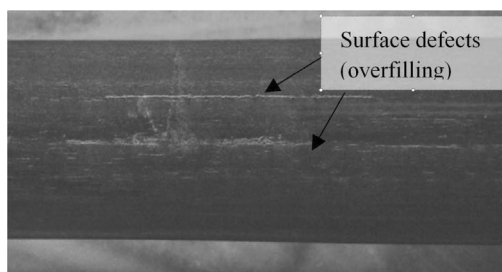


**Figure 1.** Magnetic particle inspection – surface defects on 51CrV4 rolled bar, dimension 80×53 mm, in the location of overfilling occurrence at vertical rolling stand number 3 of continuous rolling line.

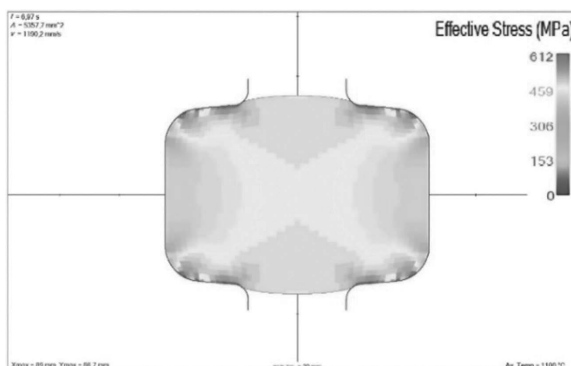


**Figure 2.** Simulation result for 51CrV4, dimension 80×53 mm at vertical rolling stand number 3 of continuous rolling line obtained by rolling simulation system.

### 3. Rolling gaps optimization using GA

Universal GA system was made using AutoLISP, which is integrated into AutoCAD (i.e. commercial computer-aided design software), which can manipulate text files containing rolling simulation system input and output data.

Six gap values (for six continuous rolling line stands) have been used as the genes from which the organisms were composed (i.e. (66, 55, 33, 53, 23, 52)). For changing organisms, the following genetic operations were being used: crossover, mutation and permutation). In addition, the reproduction operation, which does not change the organisms, is implemented. In the paper, the population size of 100 organisms was used. The maximum number of generations was 100 for all 100 runs. For selection of organisms, the tournament method with the tournament size of 4 was used. The maximum number of generations was selected as the stopping criteria.

For fitness function the average absolute distance between surface points within the central 60% of rolled bar width (e.g.  $d_1, d_2, d_i$ ) and also from ideal final rolling bar dimension (Figure 3). The actual gaps and gaps obtained using genetic algorithm are presented in the Table 1. The overfilling at vertical rolling stand number 3 of continuous rolling line was avoided successfully also in practice.

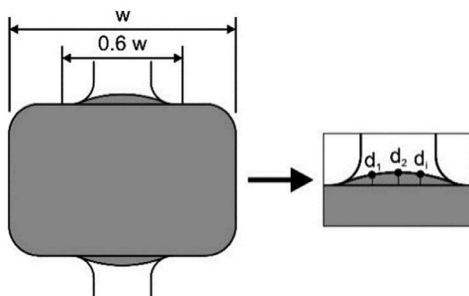


**Figure 3.** Distance between randomly selected surface points within the central 60% of rolled bar width (e.g.  $d_1, d_2, d_i$ ).

**Table 1.** The actual gaps and gaps obtained using genetic algorithm for rolling of dimension 80×53 mm.

Rolling stand	Actual gaps, [mm]	Gaps obtained using GA, [mm]
Horizontal 1	66.2	67.5
Horizontal 2	55.3	54.0
Vertical 3	33.1	33.2
Horizontal 4	53.8	54.8
Vertical 5	23.5	24.0
Horizontal 6	52.6	53.6

### References

1. Kovačić M., Župerl U.: *Genetic programming in the steelmaking industry*. Genetic Programming and Evolvable Machines, 21, 2020, 99–128.
2. Gračnar A., Kovačić M., Brezočnik M.: *Decreasing of guides changing with pass design optimization on continuous rolling mill using a genetic algorithm*. Materials and Manufacturing Processes, 35, 2020, 663–667.

3. Hanoglu U., Šarler B.: *Hot Rolling Simulation System for Steel Based on Advanced Meshless Solution*. Metals, 9, 2019, 788.
4. Hanoglu U., Šarler B.: *Developments towards a Multiscale Meshless Rolling Simulation System*. Materials, 14, 2021, 4277.
5. Šarler B., Vertnik R.: *Meshfree explicit local radial basis function collocation method for diffusion problems*. Computers and Mathematics with Applications, 51, 2006, 1269–1282.

# Powder bed operations in the model of selective laser melting process

Dmytro Svyetlichnyy<sup>1</sup>, Dominika Matuszyk<sup>1</sup>

<sup>1</sup> AGH University of Science and Technology, Faculty of Metals Engineering and Industrial Computer Science, Al. Mickiewicza 30, 30-059 Kraków, Poland  
svetlich@metal.agh.edu.pl, dmatuszyk@student.agh.edu.pl

**Keywords:** additive manufacturing, 3D printing, powder bed fusion, selective laser melting, modeling

## 1. Introduction

Additive manufacturing or 3D printing processes are highly fast-developing industrial fields and require strong scientific accompaniment and support. Additive manufacturing processes can be grouped into several categories (seven categories according to ISO/ASTM52900-15), and one of them collects Powder Bed Fusion (PBF) techniques. Among the different branded processes, Selective Laser Melting (SLM) was chosen to be supported by our research teams for analysis, development, and optimization. During the SLM process, the powder is completely melted by the high-energy laser with consequent solidification manufacturing the final product in a layer-by-layer method. The mechanical properties of the final product are close to those of the products manufactured by the conventional method. The holistic model of the entire SLM process has been developed but its components are still being improved.

The holistic model was developed after analysis of the SLM in three levels: technological, associated physical processes and phenomena, and associated mathematical models. The last with appropriate connections or interfaces are the content (components) of the holistic model. On the first, technological level, SLM can be schematically represented as a cyclic process with powder deposition, pause, laser beam treatment, pause, and powder removal sequence. This sequence can be repeated many times until the product is finished. The following six basic processes are considered on the second level of analysis, and then can be consequently modeled: powder deposition, laser beam heat treatment, melting, liquid flow (free flow of melted material), solidification, and powder removal. The defined processes and phenomena associated with SLM are modeled using the following five submodels: the powder deposition model, the heat transfer model with the laser treatment, the phase transition model, the model of fluid flow with the free surface, and the powder removal model. The work under the model development made some adjustments to the structure of the holistic model and its components. Now, the structure and functioning of the model can be presented by a block diagram (Figure 1) [1]. The diagram has two circuits. The first external circuit contains the powder bed generation (PBG) model, cycle initialization, and its realization (represented by the internal circuit – LBM calculation module) and the powder removal (PR) model.

The PBG and PR models currently communicate between themselves and with the other parts of the main algorithm with the use of files. Consideration of these two models is the main objective of this paper.

---

The publication is co-financed from the state budget under the programme of the Minister of Education and Science called "Excellent Science" project no. DNK/SP/548041/2022



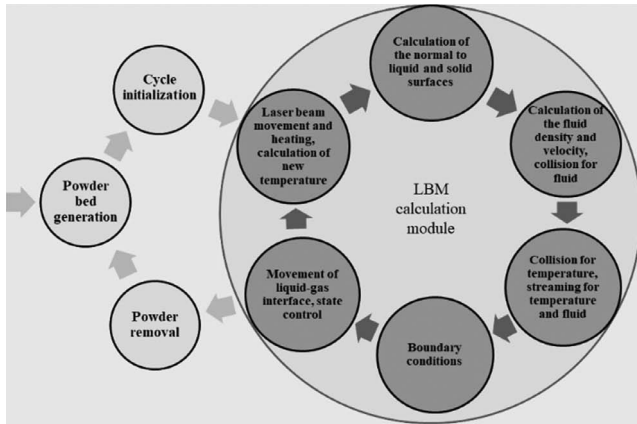


Figure 1. Schematic representation of the main algorithm of the holistic model [1].

## 2. The powder deposition models

Four variants of the powder deposition model have been developed during the work under the project. The first three variants use a quasi-kinematic approach with a simplified static stability test and are based on a similar algorithm. Shortly, each particle falls to the basement (flat, curved, or arbitrary shape after treatment) or the previously deposited particles. First of all, the first contact of the falling particle is searched, it restricts the first degree of freedom. Then, the particle begins to roll, slide, or rotate over the surface or other particles until it seeks the second contact. After the tests, the algorithm can go further or return to the previous stages. Next, the particle continues to move with a restriction of two degrees of freedom. When the third contact point is found and the last degree of freedom is restricted, the stability of the particle is tested. If the stability conditions are satisfied, the location of the particle is treated as final and the algorithm passes to the next particle. Algorithms of the variants differ in detail depending on the particle's shape and accepted assumptions.

The first variant considers a powder with atomized particles (spherical shape). The algorithm only considers rolling movement. A detailed description of this variant, simulation results, and model verification and validation can be found in the previous publication [2]. Validation confirms high accuracy in terms of packing density. The second variant has been developed for the articles of arbitrary shape), as well as the previous variant uses 2.5 cellular automata, with the particle represented by the rigid cloud of points on the surface of the particles. The particle can be translated (fall or slide) or rotated around an axis fixed by one or two points. Simulation results presented in the papers [3-5] were obtained with this variant of the model. Then, to improve simulation quality, the particles' surfaces were presented in a vector manner by vertices, edges, and faces (triangles). After deposition, the results can be represented in two forms: vector (continuous) and discrete. Simulation results with this variant can be found elsewhere [1]. The next version uses only the vector representation of the particles without the discrete transformation of deposited particles into the basement. During movement (translation and rotation), two types of contacts are analyzed: vertex-to-face and edge-to-edge.

A variant with the use of Unity® is presented here. A database of the particles was created for the previous variants and contains 50 particles, which are modified by random scaling independently in three directions after their rotation; it gives an unlimited number of unique particles. The database was adapted to Unity. Examples of powder deposition with atomized and arbitrary particles are presented in Figure 2.

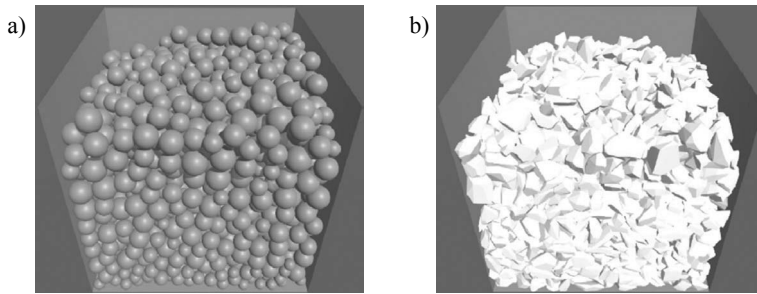


**Figure 2.** Examples of powder deposition for atomized (a) and arbitrary (b) particles.

After the deposition, particles are transferred to the LBM calculation module, where cycles of the SLM process were simulated. An example of such a simulation is presented in Figures 3a and 3b. Then, results are transferred to the Unity as terrain; and powder deposition is repeated.

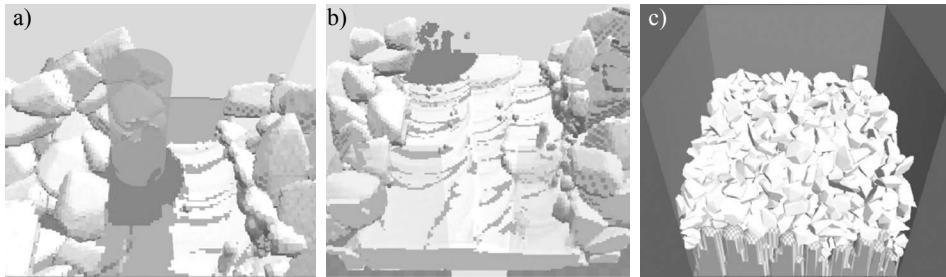


**Figure 3.** Simulation of SLM process (a and b), deposition of powder with particles of arbitrary shape on the terrain transferred from SLM simulation (c).

## References

1. Svyetlichnyy D.: *Development of the Platform for Three-Dimensional Simulation of Additive Layer Manufacturing Processes Characterized by Changes in State of Matter: Melting-Solidification*. *Materials*, 15, 2022, 1030.
2. Krzyzanowski M., Svyetlichnyy D., Stevenson G., Rainforth W.M.: *Powder bed generation in integrated modelling of additive layer manufacturing of orthopaedic implants*. *The International Journal of Advanced Manufacturing Technology*, 87, 2016, 519–530.
3. Svyetlichnyy D., Krzyzanowski M., Straka R., Lach L., Rainforth W.M.: *Application of cellular automata and Lattice Boltzmann methods for modelling of additive layer manufacturing*. *International Journal of Numerical Methods for Heat and Fluid Flow*, 28, 2018, 31–46.
4. Krzyzanowski M., Svyetlichnyy D., Bajda S.: *Additive Manufacturing of Multi Layered Bioactive Materials with Improved Mechanical Properties: Modelling Aspects*. *Materials Science Forum*, 1016, 2021, 888–893.
5. Krzyzanowski M., Svyetlichnyy D.: *A multiphysics simulation approach to selective laser melting modelling based on cellular automata and lattice Boltzmann methods*. *Computational Particle Mechanics*, 9, 2022, 117–133.

**Acknowledgements.** This work was supported by the National Science Centre (NCN) in Poland, partly by the projects no. DEC-2013/09/B/ST8/00141) and no. UMO-2018/31/B/ST8/00622.

# Application of ANN models to profile deformations analysis in RTH process

Hanna Sadłowska<sup>1</sup>, Andrzej Kochański<sup>1</sup>

<sup>1</sup> Warsaw University of Technology, Narbutta 85, 02-524 Warszawa, Poland  
hanna.sadlowska@pw.edu.pl, Andrzej.kochanski@pw.edu.pl

**Keywords:** ANN model, Rapid Tube Hydroforming, tube deformations

## 1. Introduction

This paper is a continuation publishing series on the developed new tube hydroforming technology known as Rapid Tube Hydroforming. The goal of the paper is the verification of the trend for ellipsoidality increase obtained in the ANN model for profiles hydroformed in the RTH process. The methodology is based on developing the process parameters obtained in ANN modelling calculations (based on FEM models) where ellipsoidality values exceed the current range regarding profile deformations in the RTH method. Then performing subsequent FEM simulations for parameters consistent with the trend of the direction indicated by the ANN models.

As reported in previous publications, this method uses dies made of granular materials to shape thin-walled metal tubes with an internal working liquid. The method was patented in 2020 [1] and so far, work is underway on its development. Its characteristic feature is the fact that in the process not only the profile deforms, but also the tool undergoes major deformations, while changing its mechanical properties and affecting the shaped profile in a variable way. This synergistic profile-die interaction introduces a complex process control system. It is not only about contact conditions or the very strengthening of the metal profile, but also about controlling its final shape being the result of the reaction of the die made of granular material. This phenomenon distinguishes it from classical hydroforming processes where the original geometry of the tool does not reflect the desired shape of the machined part [2].

## 2. Rapid Tube Hydroforming FEM modelling

In the initial phase of the study and development of the RTH method the authors examined the behaviour of the die itself under the influence of a fixed load like in the real process. For this purpose, a FEM model based on the Mohr-Coulomb criterion was developed to describe the behaviour of the RTH die. The simulation results calculated for a wide spectrum of die material properties allowed to recognize two characteristic types: one subject only to local compaction while the other also tends to move unsupported regions [3]. The formability of the moulding sand was also investigated for different modulus of elasticity  $E$  allowing to conclude that mass with high elasticity (small modulus  $E$ ) in most of the tested range cohesion  $c$  and internal friction coefficient  $\phi$  tends to local compaction (orange, in Figure 1a and b), while mass with low elasticity (large  $E$ ) is much more willing to move (green in Figure 1a and b).

---

The publication is co-financed from the state budget under the programme of the Minister of Education and Science called "Excellent Science" project no. DNK/SP/548041/2022



Doskonała  
Nauka



Ministry of Education and Science  
Republic of Poland



Republic  
of Poland

As part of further work a few real experiments were carried out on shaping 38×2 steel tubes in a die from moulding sands [2]. Based on these experiments, a FEM model describing the behaviour of the profile during the RTH process was developed and verified [3]. Nearly 150 simulations were performed in which the tube formability with different die properties was evaluated. To assess the degree of tube deformation in the RTH process an ellipsoidal measure was used obtained for the pre-round profile. The ellipsoidal analysis showed the significance of many variables studied, such as profile geometry and its material, moulding sand properties (including cohesion and internal friction angle) and contact conditions between the profile and the RTH die. As part of the study, some interesting observations were made, for example, the relationship of ellipsoidality with wall thinning, clearly distinguishable for different profile materials.

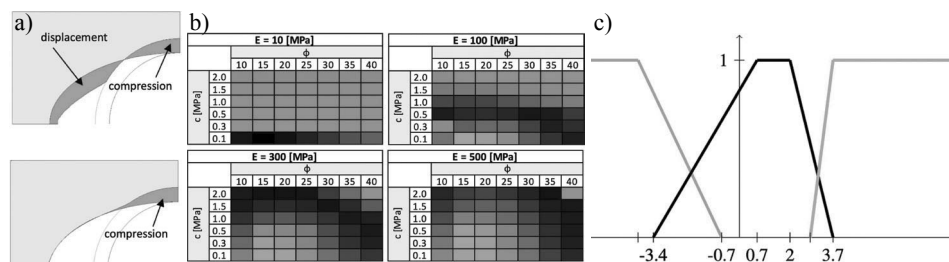


**Figure 1.** RTH die behaviour types: a) a scheme, b) for various material parameters, c) the membership curves obtained in fuzzy analysis.

Further research on the formability of the moulding sand in the RTH method based on fuzzy logic showed that there are in fact three characteristic types of die material in the RTH process [4]. It indicated that the deformations of the RTH die depend not only on the properties of the material itself but also on the shape of the die cavity. It explains the behaviour of the mass during the interaction with the expanded profile in a situation where the mass can move in the free space of the die cavity, Figure 1a. The three membership curves revealed in building the fuzzy model (see membership curves in Figure 1c) explain the behaviour of the mass during the interaction with the expanded profile in a situation where the mass can move in the free space of the die cavity (see green field in Figure 2a).

### 3. Rapid Tube Hydroforming process ANN modelling

As part of the development of the results obtained in FEM simulations several interesting observations were made, for example, the relationship of ellipsoidality with wall thinning, clearly distinguishable for different profile materials. An example for annealed and hardened steel is shown in Figure 2a. Observations made investigating the FEM model prompted the authors to reach for other methods of data analysis.

A soft model based on SSN was built due to the large set of results making it difficult to clearly assess the impact of individual parameters on the formability of the profile in the RTH die. The developed neural model supposed to predict the ellipsoidality of the profile revealed good agreement with the results obtained in numerical experiments based on FEM, Figure 2b. It allowed not only to develop the results in a more transparent way but also to put forward a hypothesis about the high influence of variables corresponding to the properties of mass [5]. Moreover, thanks to the information obtained from the neural model, it was possible to make many combinations that visually indicated the influence of certain parameters in selected states of the RTH process. An example may be the information on the influence of profile thickness on the obtained deformation measured by means of ellipsoidality where nature of deformations can be observed for annealed. Namely, the ellipsoidality for tubes with

relatively high thicknesses deformed in the die made of a material that tends to dominate compaction (low values of  $c$ ,  $f$  and  $E$ ) differs significantly from the formability of thin-walled tubes. This can be observed in Figure 2c, where the process variables are given in normalized values.

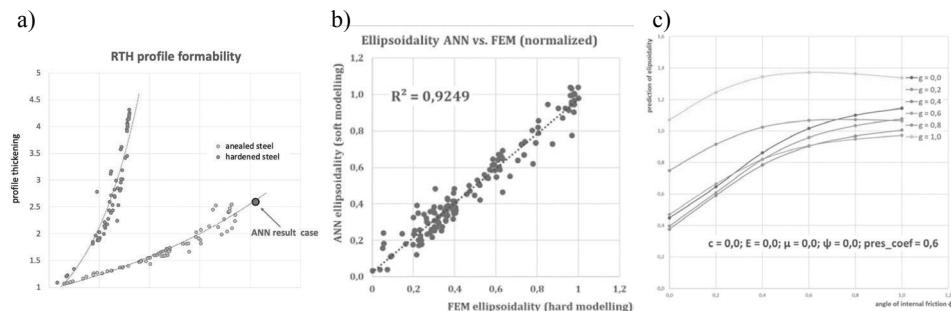


**Figure 2.** Ellipsoidality calculated by mathematical models for RTH process:  
a) FEM results for different tube materials, b) ANN and FEM model compatibility,  
c) ANN result for various tube thickness for “compactable” RTH die.

Basing on the results obtained in the neural model it was possible to determine the ellipsoidality for values higher than obtained in FEM modelling, where maximum values of ellipsoidality was 1.18. Furthermore, analysing the neural model it was possible to get the variables, and thus the process parameters, for which these values are obtainable. To check whether the information from the neural model works in the FEM model, variables with ellipsoidality greater than 1.2 were selected and then simulations were carried out for them. The results confirmed that for selected parameters obtained by ANN model higher ellipsoidality values can be established. One of the newly obtained ellipsoidality for annealed steel tube has been put on the chart in Figure 2a (as ANN result case).

Having already had a lot of information on how to regulate the properties of the RTH die to obtain maximum deformation, the issue of selecting the appropriate properties of the shaped profile seems to be a question worth further work on the development of RTH technology, especially difficult-to-deformable materials e.g., high strength steels.

## 4. Conclusions

Evaluation of the trend determined by ANN with the results of FEM simulations. Evaluation of ANN model.

## References

1. Kočański A., Sadłowska H.: *Sposób hydromechanicznego kształtowania profili cienkościennych i matryca do hydromechanicznego kształtowania profili cienkościennych*. Patent No. 235400, 2020.
2. Kočański A., Sadłowska H.: *A Casting Mould for Rapid Tube Hydroforming Prototyping*. Journal of Casting & Materials Engineering, 4, 2020, 29–33.
3. Sadłowska H., Kočański A., Czapla M.: *Application of the Numerical Model to Design the Geometry of a Unit Tool in the Innovative RTH Hydroforming Technology*. Materials, 13, 2020, 5427.
4. Sadłowska H., Kočański A., Grzegorzewski P.: *Multi-phase fuzzy modelling in the innovative RTH hydroforming technology*. 2021 IEEE International Conference on Fuzzy Systems (FUZZ-IEE), 2021.
5. Sadłowska H., Kočański A.: *Soft modelling of the shaping of metal profiles in rapid tube hydroforming technology*. Computer Methods in Materials Science, 22, 2022, 127–138.

# Numerical Model for Fast Predicting of Residual Stresses in Hot Rolled Profiles

Andrij Milenin<sup>1,2</sup>, Roman Kuziak<sup>3</sup>, Szczepan Witek<sup>1,2</sup>, Łukasz Rauch<sup>1,2</sup>,  
Ivan Milenin<sup>1</sup>, Krzysztof Bzowski<sup>1,2</sup>, Maciej Pietrzyk<sup>1,2</sup>

<sup>1</sup> AGH University of Science and Technology, Al. Mickiewicza 30, 30-059 Kraków, Poland

<sup>2</sup> ACC Cyfronet AGH, ul. Nawojki 11, 30-950 Kraków, Poland

<sup>3</sup> Łukasiewicz Research Network, Institute for Ferrous Metallurgy,  
ul. K. Miarki 12, 44-100 Gliwice, Poland

milenin@agh.edu.pl, roman.kuziak@imz.pl,  
switek@agh.edu.pl, lrauch@agh.edu.pl, imilenin@agh.edu.pl,  
kbzowski@agh.edu.pl, mpietrz@agh.edu.pl

**Keywords:** residual stress, dilatometric tests, hot rolling, profiles, FEM, cooling

## 1. Introduction

The influence of residual stresses in hot rolled products on their geometric dimensions, strength characteristics, material behavior during cutting and welding has been noted by researchers since the middle of the last century [1]. At present, due to the progress in civil and mechanical engineering, the importance of this problem has only increased [2]. For these reasons, beyond the demands regarding product microstructure, properties, and dimensions, the manufacturers of hot rolled profiles are interested also in the reduction of the level of residual stresses.

Cooling conditions after rolling are the main factor affecting the residual stresses. Beyond the thermal expansion, dilatation due to phase transformations is of particular importance. The influence of phase transformations has to be considered in two aspects – the thermal effect of the transformation and the non-linearity of thermal deformation. Moreover, the dependences of Young's modulus, flow stress, and stress relaxation on the temperature have a significant effect. The solution of the boundary value problem of the prediction of residual stresses is usually associated with the three-dimensional coupled thermomechanical problem solved by the FEM. In some cases (for example, if optimization is required), this is unacceptable due to the high costs of calculation. The paper proposes an alternative approach based on simplifying the description of the stress state in the profile.

## 2. Concept of the numerical model

The work consists of three parts. In the first, a numerical model of residual stresses is proposed. The mechanical part of the model is based on the representation of the profile as a system of bars connected at the ends. Thus, only longitudinal stresses in the profile are taken into account. This avoids solving the mechanical problem by the FEM and significantly speeds up the calculations. An elastic-plastic model of the material, which takes into account both the active load and the unloading when the temperature is equalized over the profile section is used. The thermal problem is solved for the cross-section of the profile using the FEM.

---

The publication is co-financed from the state budget under the programme  
of the Minister of Education and Science called "Excellent Science" project no. DNK/SP/548041/2022



**Doskonała  
Nauka**



Ministry of Education and Science  
Republic of Poland



**Republic  
of Poland**

The second part of the work is devoted to the development of the necessary material models: the dependence of Young's modulus, yield stress, phase transformations, and stress relaxation on temperature. Material model calibration was based on experimental tensile tests performed at different temperatures in the IMZ. Equipment used for testing is Zwick /Roell Z100, tests were performed according to PN-EN ISO 6892-2:2011 standard. To create a model of phase transformations, an approach based on modified Leblond model was used, which significantly accelerates the calculation of the kinetics of phase transformations. This approach improves the quality of the prediction of the phase composition of the material comparing to the JMAK approach. All models were calibrated based on appropriate mechanical and dilatometric tests on a range of steels.

The third part of the work is devoted to validation of the obtained model by comparing the calculation results with the measured residual stresses in the profiles. Practical application of the model to optimize the cooling process of the profiles under production conditions recapitulates the work.

### 3. Examples of calculations

The first variant of the calculation was made for air cooling of a round profile with a diameter of 50 mm made of steel 20MnCr5. The initial temperature was 970°C (it corresponds to the temperature of the metal in the last rolling pass). The calculated temperature-time curves for the surface and center of the profile are shown in Figure 1,a. The corresponding stress curves are shown in Figure 1,b.

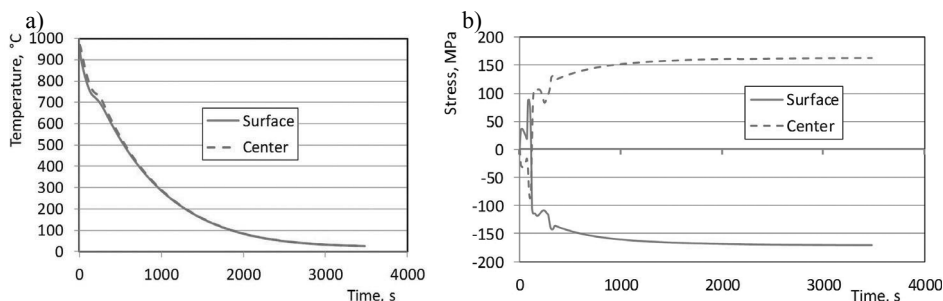


**Figure 1.** Modeling of the cooling of a round profile: (a) temperature; (b) longitudinal stress.

At the initial stage of cooling, tensile stresses arise on the surface of the profile due to a decrease in the volume of the cooled surface layers of the material. In this case, compressive stresses appear in the inner layers. If only elastic deformations occurred in the material, then when the temperature equalized, the stresses would disappear. However, elastic-plastic deformations occur in the material. The plastic component of thermal deformation changes the physical dimensions of metal volumes. Therefore, with the subsequent equalization of temperature, the signs of stresses change to the opposite. Thus, in a material with an initial zero stress level, after cooling compressive stresses are formed on the surface and tensile stresses in the center.

The influence of the phase transformation is exposed in the nonmonotonicity of the stress-time curves in Figs. 1b. In this calculation, the phase transformation coincides in time with the change in the stress sign. For this reason, the nonmonotonicity of the stress versus time curve occurs both before and after the change in the sign of the stress.

Measurement of residual stresses in this profile was performed in IMZ in laboratory conditions (see Figure 2). Experimental results confirms compressive residual stresses on profile surface and average value of experimental stresses (142 MPa) was very close to calculated value (155 MPa).

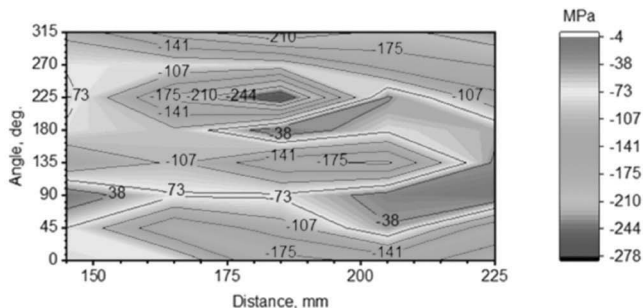


Figure 2. Measurement of longitudinal stress after cooling process.

In the next simulation, the model was verified on the example of an asymmetric profile. Cooling parameters and material model are taken as in the previous calculation. In this case, the classical patterns of the formation of residual stresses are also observed (Figure 3). At the first stages of cooling, the thin parts of the profile cool faster, and tensile stresses arise in them (see Figure 3, a). Next, the process of temperature equalization begins and the stress changes sign (see Figure 3,b).

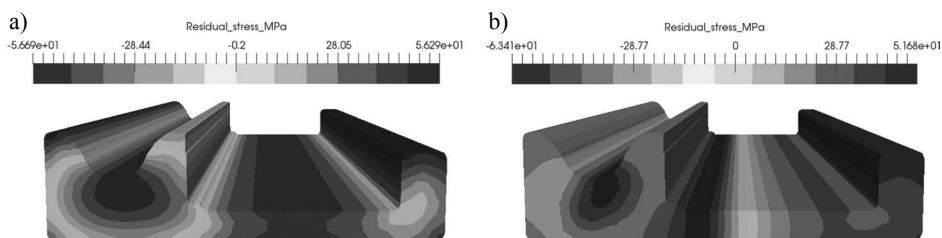


Figure 3. Modeling of the distribution of longitudinal stress on initial stage of cooling (a) and final distribution of residual stresses (b).

## References

1. Pozdejev A.A., Nashin Y.I., Trusov P.V.: *Ostatochnyje naprazhenija. Teorija i prilozhenije*. Moscow, Nauka, 1982 (in Russian).
2. Milenin A., Kuziak R., Lech-Grega M., Chochorowski A., Witek S., Pietrzyk M.: *Numerical modeling and experimental identification of residual stresses in hot-rolled strips*. Archives of Civil and Mechanical Engineering, 16, 2016, 125–134.

**Acknowledgements.** PROTEUS-RS project “Long product quality optimisation through enhancement and utilisation of residual stress minimising process strategies” is acknowledged.

# Concurrent algorithms for integrating three-dimensional B-spline functions into machines with shared memory such as GPU

Maciej Woźniak<sup>1</sup>, Anna Janina Szyszka<sup>1</sup>

<sup>1</sup> Institute of Computer Science,  
Faculty of Electronics, Telecommunication and Computer Science,  
AGH University of Science and Technology, Al. Mickiewicza 30, 30-059 Kraków, Poland  
macwozni@agh.edu.pl jerboamouse@gmail.com

**Keywords:** Isogeometric Finite Element Method, Numerical integration, Trace theory, Sum factorization

## 1. Introduction

The process of FEM calculations is split into two stages - the assembly of the discrete form and the resolution of algebraic equations. While there are various types of problems that require multiple integrations, modern solvers for IGA-FEM have greatly reduced the computation cost, such as by using the Alternating Direction Solver (ADS). In fact, with ADS, integration can make up as much as 80% of the overall cost. Historically, integration was done by processing each element concurrently, but now, with the advent of multi-level parallel computational clusters [4], there are additional two levels of parallelism available for the integration.

Incorporating concurrency in the integration process at the element level is key to improving performance. To achieve this, the use of Trace Theory [5] can be employed to derive the Foata Normal Form (FNF) and create a Diekert's dependency. By utilizing FNF, the creation and implementation of parallel algorithm on a GPU becomes much more manageable and efficient. Additionally, FNF offers near-optimal scheduling and GPU implementation, as well as theoretical validation of parallel algorithms. This methodology can be applied to a variety of integration algorithms to achieve improved results.

## 2. Model problem and IGA-discrete variational formulation

The goal of this study is to evaluate the cost of using different integration methods for assembling IGA matrices. To illustrate this, we will use the heat equation discretized in time using the forward Euler method and focus specifically on the cost of assembling the Mass matrix.

Find  $u \in C^1((0, T), H^1(\Omega))$  such that  $u = u_0$  at  $t = 0$  and, for each  $t \in (0, T)$ , it holds:

$$\int_{\Omega} \frac{\partial u}{\partial t} v dx = - \int_{\Omega} \nabla u \nabla v dx, \quad \forall v \in H^1(\Omega) \quad (1)$$

For simplicity, we consider a discrete-in-time version of problem by employing the forward Euler method.

$$\int_{\Omega} u_{n+1} v dx = \int_{\Omega} u_n v dx - \Delta_t \int_{\Omega} \nabla u_n \nabla v dx, \quad \forall v \in H^1(\Omega) \quad (2)$$

---

The publication is co-financed from the state budget under the programme of the Minister of Education and Science called "Excellent Science" project no. DNK/SP/548041/2022

This study focuses on utilizing 3D-tensor B-spline basis functions with a uniform polynomial degree order and regularity at the interior faces of the mesh for ease of demonstration. However, it should be noted that the techniques presented can be easily adapted to other types of B-spline basis functions. For construction of B-spline basis functions we used Cox-de-Boor recursive formulae [6].

$$B_{i,0}(\xi) := \begin{cases} 1 & \text{if } \gamma_i \leq \xi < \gamma_{i+1} \\ 0 & \text{otherwise} \end{cases} \quad (3)$$

$$B_{i,q}(\xi) := \frac{\xi - \gamma_i}{\gamma_{i+q} - \gamma_i} B_{i,q-1}(\xi) + \frac{\gamma_{i+q+1} - \xi}{\gamma_{i+q+1} - \gamma_{i+1}} B_{i+1,q-1}(\xi), \quad \text{for } 1 \leq q \leq p \quad (4)$$

### 3. Algorithms and computational cost

We compared two algorithms, the classical integration algorithm, and the sum factorization algorithm. In the classical integration algorithm, local contributions to the left-hand-side matrix  $A$  are represented as a sum over quadrature points. In this case, the associated computational cost scales, concerning the polynomial degree  $p$  as  $\mathcal{O}(p^9)$  [2].

$$A_{\beta,\delta}^\gamma = \sum_{n_1, n_2, n_3=1}^{P_1, P_2, P_3} \omega_3^n B_j(x_3^n) B_{m,p}(x_3^n) B_i(x_2^n) \omega_2^n B_{l,p}(x_2^n) D(i_3, j_3, k_1, k_2) \omega_1^n B_h(x_1^n) B_{k,p}(x_1^n) J(x^n) \quad (5)$$

On the other side, Sum factorization algorithm is based on reorganizing the integration terms to reduce the computational cost, in terms of the polynomial degree  $p$ , associated with the sum procedure  $\mathcal{O}(p^7)$  [2].

In practice is written as:

$$A_{\beta,\delta}^\gamma = \sum_{m=1}^{P_3} \omega_3^n B_j(x_3^n) B_{m,p}(x_3^n) C(i_2, i_3, j_2, j_3, k_1) \quad (6)$$

where

$$C(i_2, i_3, j_2, j_3, k_1) = \sum_{n_2=1}^{P_2} \omega_2^n B_i(x_2^n) B_{l,p}(x_2^n) D(i_3, j_3, k_1, k_2)$$

and

$$D(i_3, j_3, k_1, k_2) = \sum_{n_1=1}^{P_1} \omega_1^n B_h(x_1^n) B_{k,p}(x_1^n) J(x^n)$$

We applied methodology described in [1] to sum factorization algorithm, to obtain optimal scheduling and theoretical verification from trace theory method [3]. Next we made a series of numerical experiments to measure parallel performance. In Tables 1 and 2 we presented numerical results for both considered algorithms. We have obtained both maximum experimental speedup, as well as theoretical maximum combined one. In the Tables,  $\mathcal{P}$  denotes the percentage of the algorithm which benefits from the parallel speedup,  $\nu$  is the number of threads, and  $\mathcal{S}(\nu)$  is the measured speedup when using  $\nu$  threads.

We observed unexpected performance behaviour of the parallel sum factorization. Despite utilizing parallel loops across all elements, it was scaling only up to 4 cores. Beyond 4 cores, there was a plateau in speedup, indicating poor performance in multi-core environment.

The maximum speedup of the classical method, as shown in Table 1, mirrors findings from [1]. It is worth noting that sum factorization demands significantly more memory synchronization compared to the classical method.

**Table 1.** Classical integration method. Bottom index  $i$  stands for “inside element”,  $e$  over all elements, and  $c$  combined.

$p$	$t_{\text{base}}$	$v_i$	$\mathcal{O}_i(v)$	$\mathcal{P}_i$	$\mathcal{S}_i(\infty)$	$v_e$	$\mathcal{S}_e(v)$	$\mathcal{P}_e$	$\mathcal{S}_e(\infty)$	$\mathcal{S}_c(\infty)$
1	0.08	6	1.35	0.31	1.45	3	2.5	0.9	10.00	14.50
2	0.91	6	2.32	0.68	3.15	6	5.4	0.98	45.00	141.75
3	6.70	9	4.01	0.84	6.43	8	7.8	0.98	52.00	314.36
4	36.56	12	5.64	0.90	9.75	10	7.8	0.97	31.91	311.12
5	143.86	12	4.6	0.85	6.84	12	11.29	0.99	174.92	1 196.45
6	562.03	11	6.98	0.94	17.36	12	11.15	0.99	144.29	1 984.07
7	1 622.20	12	7.28	0.94	16.97	12	10.75	0.99	94.60	1 605.36
8	4 586.81	12	5.16	0.88	8.30	12	10.88	0.99	106.86	886.94
9	11 752.54	12	8.54	0.96	27.15	12	10.44	0.99	73.62	1 998.78

**Table 2.** Sum factorization. Bottom index  $i$  stands for “inside element”,  $e$  over all elements, and  $c$  combined.

$p$	$t_{\text{base}}$	$v_i$	$\mathcal{O}_i(v)$	$\mathcal{P}_i$	$\mathcal{S}_i(\infty)$	$v_e$	$\mathcal{S}_e(v)$	$\mathcal{P}_e$	$\mathcal{S}_e(\infty)$	$\mathcal{S}_c(\infty)$
1	0.05	1	1	0	1	2	1.5	0.67	3	3.00
2	0.29	1	1	0	1	4	2.9	0.87	7.91	7.91
3	1.38	1	1	0	1	4	2.9	0.87	7.91	7.91
4	5.12	10	1.16	0.15	1.18	4	3.3	0.93	14.14	16.69
5	15.15	11	1.34	0.28	1.39	4	3.5	0.95	21	29.19
6	40.63	10	1.44	0.34	1.51	4	3.5	0.95	21	31.71
7	109.47	11	1.68	0.45	1.80	4	3.2	0.92	12	21.60
8	202.17	9	1.52	0.38	1.63	4	3.4	0.94	17	27.71
9	394.28	10	1.63	0.43	1.75	4	3.5	0.96	21	36.75

Finally we evaluated the performance of classical integration and sum factorization in various scenarios by analysing the computational times from Tables 1 and 2. We focused on scenario of  $p = 9$  as it was expected to be the optimal scenario for sum factorization. We examined three scenarios for a mesh size of  $30^3$ : 1) single-core CPU execution, 2) shared-memory CPU computation, and 3) GPU execution. The **classical integration** on a single core took 11 752.54 seconds, the 12-core OpenMP implementation took 1125.72 seconds, and the estimated **GPU implementation** was expected to take **5.87 seconds**. For **sum factorization** integration, the single-core execution took 394.28 seconds, the 4-core OpenMP implementation took 112.65 seconds, and the estimated **GPU implementation** was expected to take **10.78 seconds**.

## 4. Conclusions

Our approach validates the scheduling for integration algorithm by utilizing trace theory. We compared the integration algorithm’s execution on both a CPU and GPU. We can extrapolate its scalability for various elliptic problems. Furthermore, the trace-theory based analysis of concurrency in the integration algorithm can be adapted to different integration methods. The methodology is versatile and can be expanded to include higher-dimensional spaces.

## References

1. Szyszka A., Woźniak M., Schaefer R.: *Concurrent algorithm for integrating three-dimensional B-spline functions into machines with shared memory such as GPU*. Computer Methods in Applied Mechanics and Engineering, 398, 2022, 115201.
2. Hiemstra R.R., Sangalli G., Tani M., Calabrò F., Hughes T.J.: *Fast formation and assembly of finite element matrices with application to isogeometric linear elasticity*. Computer Methods in Applied Mechanics and Engineering, 355, 2019, 234–260.
3. Woźniak M., Szyszka A., Rojas S.: *A study of efficient concurrent integration methods of B-Spline basis functions in IGA-FEM*. Journal of Computational Science, 64, 2022, 101857.
4. *Summit*, Oak Ridge National Laboratory, <https://www.olcf.ornl.gov/summit/>.
5. Diekert V., Rozenberg G.: *The Book of Traces*. World Scientific, 1995.
6. de Boor C.: *Subroutine package for calculating with B-splines*. SIAM Journal on Numerical Analysis, 14, 1971, 441–472.

**Acknowledgements.** The work has been supported by The European Union’s Horizon 2020 Research and Innovation Program of the Marie Skłodowska-Curie grant agreement No. 777778, MATHROCKs. Scientific paper published within the framework of an international project co-financed with funds from the program of the Ministry of Science and Higher Education entitled „PMW” in years 2022-2023; contract no. 5243/H2020/2022/2.

# Molecular dynamics simulations of the interdiffusion at $\alpha$ -Al<sub>2</sub>O<sub>3</sub>/AlSi12 interface

Masoud Tahani<sup>1,2</sup>, Eligiusz Postek<sup>1</sup>, Tomasz Sadowski<sup>3</sup>

<sup>1</sup> Institute of Fundamental Technological Research, Polish Academy of Sciences, Pawińskiego 5B, 02-106 Warsaw, Poland

<sup>2</sup> Department of Mechanical Engineering, Ferdowsi University of Mashhad, Mashhad, Iran

<sup>3</sup> Department of Solid Mechanics, Lublin University of Technology, 20-618 Lublin, Poland  
mtahani@ippt.pan.pl, epostek@ippt.pan.pl,  
t.sadowski@pollub.pl

**Keywords:** Self-diffusion, Interdiffusion, Metal-ceramic composite, Al<sub>2</sub>O<sub>3</sub>/AlSi12 interface, Molecular dynamics method

## 1. Introduction

Metal matrix composites (MMC) are used more and more in the aerospace, automotive, and bio-medical industries because of their high strength-to-weight ratio, high stiffness, and outstanding wear resistance. Aluminium, titanium, and magnesium are the most preferred matrix materials, whereas alumina and silicon carbide are the most used reinforcing elements for these composites. The overall mechanical and failure properties of MMCs depend on the mechanical properties of the constituents and the nature of the interface. The characteristics of the interface must be understood because they have the potential to significantly alter the properties of MMCs. The interface between phases is a fuzzy region because of diffusion. To this end, it is necessary to look into the diffusion between the two phases as the first step for determining the cohesive zone model of the interface.

In this study, AlSi12 metal alloy as matrix material reinforced with  $\alpha$ -Al<sub>2</sub>O<sub>3</sub> is considered. AlSi12 is an aluminium alloy that contains 12 wt.% silicon with excellent thermal conductivity, good corrosion resistance, and low density. The composite can be used in various high-temperature applications such as furnace linings, engine parts, and aerospace components. It is worth noting that the properties and performance of the composite will depend on the processing conditions, microstructure, the proportion of the components, and the interface's characteristics.

The investigation carried out by Milas et al. [1] regarding the diffusion of Al, O, Pt, Hf, and Y atoms on  $\alpha$ -Al<sub>2</sub>O<sub>3</sub>(0001) can be mentioned as an illustration of research that has been published in the literature. To the authors' knowledge, no studies have been done on  $\alpha$ -Al<sub>2</sub>O<sub>3</sub>/AlSi12 diffusion couple. To this end, the self-diffusion and interdiffusion at the interface are investigated in this research by heating the system to the desired temperature. The effect of annealing temperature and annealing time are studied on the diffusion zone and interdiffusion coefficients. The thickness of the diffusion zone and the interdiffusion coefficients are found to increase as expected with increasing annealing temperature and time.

## 2. Model and simulation details

Diffusion is the movement of atoms or molecules from an area of higher concentration to an area of lower concentration. Diffusion can occur between the two phases, resulting in the migration

---

The publication is co-financed from the state budget under the programme of the Minister of Education and Science called "Excellent Science" project no. DNK/SP/548041/2022



Doskonała  
Nauka



Ministry of Education and Science  
Republic of Poland



Republic  
of Poland

of atoms between the two materials. The rate of diffusion between the aluminium oxide and AlSi12 alloy depends on several factors, including the temperature, the chemical composition of the two materials, and the interface between the two phases. At high temperatures, the diffusion rate will be faster, and the atoms will have more energy to move through the material.

The molecular dynamics (MD) method is able to study very basic processes like diffusion by using Newton's second law to describe atomic interactions. The MD simulations in this study are conducted using the open-source MD program LAMMPS and the OVITO software is utilized for visualizing the evolution of the atomic structure. The third-generation many-body COMB potential [2] and the Tersoff potential [3] are used in this research for the Al-O and Si-O interactions, respectively. Furthermore, The Morse potential with parameters  $D_0 = 0.4824$  eV,  $\alpha = 1.322$  Å<sup>-1</sup>, and  $r_0 = 2.92$  Å [4] is employed for the Al-Si interactions.

The initial  $\alpha$ -Al<sub>2</sub>O<sub>3</sub>/AlSi12 interface is considered as a single crystal of AlSi12 and a single crystal of  $\alpha$ -Al<sub>2</sub>O<sub>3</sub> with an initial gap of 2 Å which is near the equilibration atomic distance in the interface. Both Al- and O-terminated interfaces are analysed. The typical dimension of the MD model is approximately 119×58×184 Å with a total of 109,986 atoms. The orientation relationship (0001)[2 $\bar{1}\bar{1}$ 0] <sub>$\alpha$ -Al<sub>2</sub>O<sub>3</sub></sub>||[(111)[ $\bar{1}\bar{1}$ 2]<sub>AlSi12</sub>] is considered. The lattice constant of fcc Al is 4.0495 and the lattice parameters of hexagonal  $\alpha$ -Al<sub>2</sub>O<sub>3</sub> are  $a = b = 4.759$  Å,  $c = 12.991$  Å,  $\alpha = \beta = 90^\circ$ , and  $\gamma = 120^\circ$ . 12 wt.% of Al atoms are replaced by Si atoms to produce AlSi12 single crystal.

The geometric configuration is optimized using the conjugate gradient energy minimization algorithm. The NVT canonical ensemble at a constant temperature of 300 K is imposed on the sample for 10 ps and then the NPT ensemble at a zero pressure and constant 300 K is used for 15 ps to adjust the volume and relax the assembled interface system. Then, the sample is heated to a preset temperature at a heating rate of 10 K/ps. Then, the temperature is maintained at the given temperature for 2 ns to study the interdiffusion and the movements of atoms are recorded during this period. The NPT ensemble with zero pressure with a 0.2 fs time-step is considered for all processes. The temperatures of 1500, 1800, and 2000 K are considered for the simulations.

### 3. Results and discussions

The elastic constants of  $\alpha$ -Al<sub>2</sub>O<sub>3</sub> and AlSi12 are obtained with the aforementioned potential functions and compared with the experimental and MD simulations in Table 1. It can be seen that the alumina results agree well with those obtained by other investigators. Next, each system is cut into thin slices of thickness 2 Å parallel to the interface plane and the number of each atom type is counted to obtain the concentration. Figures 1(a) and 1(b) illustrate the initial concentration profiles before diffusion and the concentration profiles after maintaining the system at 2000 K for 2 ns. The self-diffusion coefficients of each atom are determined from the slope of the mean square displacements. For example, the self-diffusion of atoms in an Al-terminated interface at 2000 K are  $D_{\text{Al(AlSi12)}} = 53.346$ ,  $D_{\text{Al(Al2O3)}} = 1.165$ ,  $D_{\text{O}} = 0.0282$ ,  $D_{\text{Si}} = 1.246$  (10<sup>-10</sup> m<sup>2</sup>/s).

**Table 1.** The elastic constants obtained by the present MD simulations and comparison with those obtained by other investigators.

Material	Method	C <sub>11</sub> (GPa)	C <sub>12</sub> (GPa)	C <sub>13</sub> (GPa)	C <sub>33</sub> (GPa)	C <sub>44</sub> (GPa)	C <sub>66</sub> (GPa)
$\alpha$ -Al <sub>2</sub> O <sub>3</sub>	Present	510	130	138	518	138	165
	Experiment [5]	497	164	111	498	147	167
	ES+ [6]	537	180	106	509	130	179
AlSi12	Present	268	134	154	214	108	105

The activation energy  $Q$  and pre-exponential factor  $D_0$  of atoms can be obtained by fitting the self-diffusion coefficients to the Arrhenius equation:

$$D = D_0 \exp\left(-\frac{Q}{RT}\right) \quad (1)$$

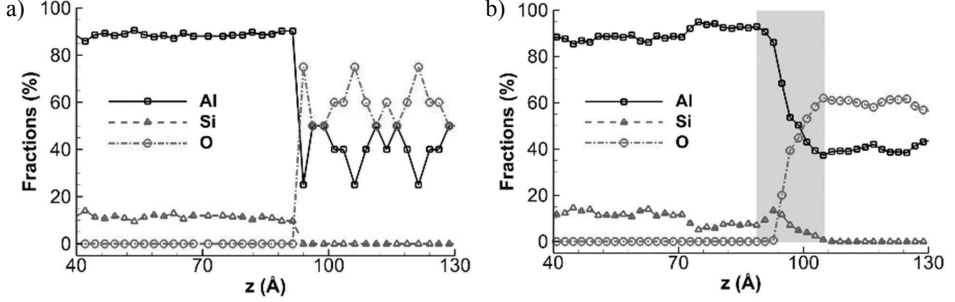


**Figure 1.** The concentration profiles of Al, Si, and O atoms along the  $z$ -direction during interdiffusion of the Al-terminated  $\alpha$ - $\text{Al}_2\text{O}_3/\text{AlSi12}$  interface.

(a) Initial system before relaxation and (b) after maintaining it at 2000 K for 2 ns. The grey region shows the diffusion zone.

A total of four independent interdiffusion coefficients are needed to describe the interdiffusion behavior in a ternary system. The interdiffusion coefficients are obtained by computing the interdiffusion flux of atoms using the present single diffusion couple. The Gaussian error function for each component is used to fit the concentration curve (e.g., see Ref. [7] for detail explanation about the method). The average values of the main and cross-interdiffusion coefficients of the Al- and O-terminated  $\alpha$ - $\text{Al}_2\text{O}_3/\text{AlSi12}$  diffusion couple are calculated and listed in Table 2. The diffusion systems are maintained at the annealing temperatures of 1500 and 2000 K for 2 ns.

**Table 2.** Average ternary interdiffusion coefficients for the Al- and O-terminated  $\alpha$ - $\text{Al}_2\text{O}_3/\text{AlSi12}$  diffusion couple ( $10^{-11} \text{ m}^2/\text{s}$ ).

Diffusion couple	Temperature (K)	$\bar{D}_{\text{Oo}}^{\text{Al}}$	$\bar{D}_{\text{Osi}}^{\text{Al}}$	$\bar{D}_{\text{SiO}}^{\text{Al}}$	$\bar{D}_{\text{Sisi}}^{\text{Al}}$
Al-terminated $\alpha$ - $\text{Al}_2\text{O}_3/\text{AlSi12}$	1500	0.584	$-2.6 \cdot 10^{-9}$	$-6.0 \cdot 10^{-6}$	3.728
	2000	0.911	$7.5 \cdot 10^{-8}$	$-3.5 \cdot 10^{-7}$	14.311
O-terminated $\alpha$ - $\text{Al}_2\text{O}_3/\text{AlSi12}$	1500	0.575	$-1.3 \cdot 10^{-6}$	$-2.2 \cdot 10^{-6}$	3.648
	2000	0.681	$-4.8 \cdot 10^{-6}$	$1.4 \cdot 10^{-8}$	13.781

It is seen from Table 2 that the main interdiffusion coefficients increase with increasing the annealing temperature, as expected, and all cross-interdiffusion coefficients are at least five orders of magnitude smaller than the main interdiffusion coefficients. Furthermore, the results in this table indicate that the diffusivity of Si and O atoms is slightly higher for the Al-terminated system compared with the O-terminated one.

## 4. Conclusions

A molecular dynamics method was employed to investigate the atomistic evolutions during the interdiffusion at  $\alpha$ - $\text{Al}_2\text{O}_3/\text{AlSi12}$  interface. The average main and cross interdiffusion coefficients were obtained using the concentration profiles of atoms during diffusion for the Al- and O-terminated systems. It was found that the interdiffusion coefficients increased with the increasing annealing

temperature and time. Moreover, there was no significant difference between Al- and O-terminated interfaces in terms of the interdiffusion.

## References

1. Milas I., Hinnemann B., Carter E.A.: *Diffusion of Al, O, Pt, Hf, and Y atoms on  $\alpha$ -Al<sub>2</sub>O<sub>3</sub>(0001): implications for the role of alloying elements in thermal barrier coatings*. Journal of Materials Chemistry, 21, 2011, 1447–1456.
2. Choudhary K., Liang T., Chernatynskiy A., Phillpot S.R., Sinnott S.B.: *Charge optimized many-body (COMB) potential for Al<sub>2</sub>O<sub>3</sub> materials, interfaces, and nanostructures*. Journal of Physics: Condensed Matter, 27, 2015, 305004.
3. Munetoh S., Motooka T., Moriguchi K., Shintani A.: *Interatomic potential for Si-O systems using Tersoff parameterization*. Computational Materials Science, 39, 2007, 334–339.
4. Zhao H., Chen N.: *An inverse adhesion problem for extracting interfacial pair potentials for the Al(001)/3C-SiC(001) interface*. Inverse Problems, 24, 2008, 035019.
5. Wachtman J.B., Jr.: *Mechanical and thermal properties of ceramics*. National Bureau of Standards: Washington, DC, 1969, 139–188.
6. Streitz F.H., Mintmire J.W.: *Molecular dynamics simulations of elastic response and tensile failure of alumina*. Langmuir, 12, 1996, 4605–4609.
7. Tahani M., Postek E., Motevalizadeh L., Sadowski T.: *Effect of vacancy defect content on the interdiffusion of cubic and hexagonal SiC/Al interfaces: A molecular dynamics study*. Molecules, 28, 2023, 744.

**Acknowledgements.** This research was funded by the Polish National Agency for Academic Exchange (NAWA) under grant number [BPN/ULM/2021/1/00115/U/DRAFT/00001]. We acknowledge the National Science Centre, Poland, grant No. UMO 2019/33/B/ST8/01263. The calculations were performed at PLGrid national facilities – Academic Computer Centre Cyfronet in Krakow, Academic Computer Centre in Gdańsk, and Interdisciplinary Centre for Mathematical and Computational Modelling, University of Warsaw, Poland.

# Selected aspects of modelling the process of forming nickel superalloys sheets and tubes

Monika Hycza-Michalska<sup>1</sup>

<sup>1</sup> Silesian University of Technology, 2A Akademicka Str., PL 44-100 Gliwice, Poland  
monika.hycza-michalska@polsl.pl

**Keywords:** stamping process, hydroforming, nickel superalloys, physical modeling, numerical modelling

## 1. Introduction and motivation

Designing the stamping processes of nickel superalloys – materials with high strength and durability at elevated temperatures – is a constant problem for production technologists. Depending on the form of the charge – sheet metal, tube blank, the shape of the target product and the selected manufacturing technology, the design task becomes more complicated. Thus, designing the production process of a given extrusion becomes difficult, and practically impossible without the use of methods of physical and numerical modeling of a given production process. In this paper, selected aspects important for the adequate modeling of the processing of nickel superalloys will be presented based on experience gained.

## 2. Selected aspects of modelling

On the example of the process of shaping selected drawpieces from nickel superalloy sheets, some aspects of modeling will be presented, and they are:

### 2.1. Selection of a material model for charges and building material databases based on deformability assessment experiments

The first aspect that plays a decisive role in the charge response to load is the plastic properties of the charge materials. For nickel superalloys, the values of these values required for effective processing by pressing become limited and very difficult to recognize based only on standard attestations of mechanical properties and melt analysis of chemical composition. The forming of modern heat-resistant and creep-resistant materials, such as nickel superalloys, requires obtaining information about their characteristic temperatures. Determination of phase transformations during heating and cooling of selected nickel superalloys, determination of characteristic temperatures: liquidus and solidus, calculation of enthalpies of determined transformations are the data necessary to select the parameters of plastic working at elevated temperature and to assess the possibility of designing heat treatment for these alloys. Thus, these data complement the material model used in the FEM simulation of plastic working processes of these alloys, specifically stamping. Possibilities of supplementing material databases or extending the material model with this data or the forming limit curve are necessary. As part of physical modeling and based on many years of experience [1–5], guidelines for the assessment

---

The publication is co-financed from the state budget under the programme of the Minister of Education and Science called "Excellent Science" project no. DNK/SP/548041/2022

of drawability with limited formability were formulated. The tests indicated in these guidelines should be extended to the pre-qualification of input materials for pressing when there are any technological problems with their processing. In numerical modelling, at the design stage, additional characteristics of this type of charges should be taken into account in the data set of the material model.

#### 2.2. The importance of selection of a model for tools and make changes to an existing model in the software possibility.

The importance selected model for tools and make changes to an existing model in the software possibility was demonstrated on the example of a conical cover. In the Dynaform 5.9 software, various ways of pressing a given drawpiece were numerically modeled: using rigid tools, liquid tools, liquid tools and elastomer tools. The results of numerical simulations, carried out with the use of the material model extended with limit pressing curves [6–10], enabled the selection of the most technologically and economically effective method of manufacturing a conical cover. Without the possibility of modifying the material model of the tools from rigid to elastomeric, the accuracy of the simulation results was lower from 20% to 45%.

#### 2.3. Selection of the most adequate software for numerical simulation due to the nature of the model task

The selection of the most adequate software for numerical simulation due to the nature of the model task is also important. This choice is often dictated by license availability and costs. For entrepreneurs, however, the universality of the software and the ability to design as many technological operations as possible are important. Such a selection example was presented for an aerospace company and project tasks related to the processing of nickel superalloy sheets.

#### 2.4. Interpretation of modeling results and the importance of practical verification of results from the modeling and simulation process.

The interpretation of the modeling results and the importance of practical verification of the results from the modeling and simulation process have been combined with a common goal – the most consistent representation of the real effects of shaping. Understanding the iterative nature of the modeling process, optimizing the solution, model sensitivity to subtle changes are some of the elements that require attention in the modeling process.

### 3. Summary and conclusions

It has been shown that in the process of modeling of nickel superalloys in the form of sheets and tubes stamping, there are many important aspects that must be taken into account, so that the obtained results are as compatible with the design assumptions as possible and do not require repetition of the calculation process. The most important aspects include:

- the requirement to build a material model of the charge based on extended characteristics of mechanical properties, deformability tests and determination of the forming limit curve and determination of phase transition temperatures,
- the ability to interfere in the tool model and the ability to set variable tool-charge contact conditions,
- the ability to select the most effective software for numerical simulations due to the nature of the model task, and not the price of available licenses,
- the need for practical verification of the results from the modeling and simulation process.

Taking into account the above-mentioned aspects will make it possible to perform design tasks based on numerical modeling in accordance with the best practice. The conclusions from this work are universal and concern the modeling of metallic materials, and not only nickel superalloys, which were used here as the object of research.

## References

1. Hycza-Michalska M.: *Drawability of advanced high strength steel and creep-resisting nickel superalloys*. Steel Research International, 81, 2010, 817–820.
2. Hycza-Michalska M.: *Wybrane problemy plastycznego kształtowania stali żarowytrzymałych i żaroodpornych stopów niklu*. Hutnik – Wiadomości Hutnicze, 77, 2010, 394–397.
3. Hycza-Michalska M., Płonka P., Mrugała T.: *Analiza podatności do tłoczenia stali żarowytrzymałych i żaroodpornych stopów niklu stosowanych na konstrukcje silników lotniczych*. Polska Metalurgia w latach 2006–2010, Komitet Metalurgii Polskiej Akademii Nauk, Kraków, 2010, 607–614.
4. Hycza-Michalska M.: *Badania symulacyjne swobodnego rozciągania ciecżą rur ze stali niskowęglowych oraz nadstopów niklu*. Oficyna Wydawnicza Politechniki Warszawskiej, Prace Naukowe, Mechanika, 238, 51–58.
5. Hycza-Michalska M.: *Physical and Numerical Research on Drawability of Nickel Superalloys*. Steel Research International, 83, 2012, 663–666.
6. Hycza-Michalska M.: *Research on mechanical properties of thin sheets blanks made of creep-resisting nickel superalloys*. [in:] *Technologies and properties of modern utility materials XXI*. Selected, peer reviewed papers from the XXI Conference on Technologies and Properties of Modern Utility Materials (TPMUM 2013), Katowice, Poland, May 17, 2013, eds. Mendala J., Gradoń P., Stafa-Zurich: Trans Tech Publications, 2014, 259–262, Solid State Phenomena, 212, 1012-0394.
7. Substantive report on the Development Project No. R15 0042 06 entitled *Development of methods for computer-aided design of product stamping processes for the aviation industry*. implemented in 2009–2014, head: PhD Eng. Monika Hycza-Michalska (unpublished materials).
8. Hycza-Michalska M.: *Badania granicznej krzywej tłoczenia cienkich blach żaroodpornych i żarowytrzymałych*. Hutnik – Wiadomości-Hutnicze, 82, 2015, 542–545.
9. Hycza-Michalska M.: *Research on liquid forming process of nickel superalloys thin sheet metals*. Archives of Metallurgy and Materials, 62, 2017, 2355–2358.
10. Hycza-Michalska M.: *Komputerowo wspomaganie metody przewidywania zjawisk ograniczających kształtowanie blach*. Hutnik – Wiadomości Hutnicze, 85, 2018, 264–266.

**Acknowledgements.** This work was supported by Polish Ministry for Science and Higher Education under internal grant BK221/RM0/2022 (11/030/BK\_21/1038) for Institute of Materials Engineering, Silesian University of Technology, Poland.

# Hot-rolling production planning and melt shop sequencing problems

Krzysztof Regulski<sup>1</sup>, Łukasz Rauch<sup>1</sup>, Krzysztof Bzowski<sup>1</sup>, Piotr Hajder<sup>1</sup>,  
Andrzej Opaliński<sup>1</sup>, Monika Pernach<sup>1</sup>, Michał Piwowarczyk<sup>2</sup>

<sup>1</sup> AGH University of Science and Technology, Faculty of Metals Engineering and Industrial  
Computer Science, Al. Mickiewicza 30, 30-059 Kraków, Poland  
<sup>2</sup> CMC Poland, ul. Piłsudskiego 82, 42-400 Zawiercie, Poland  
regulski@agh.edu.pl, lrauch@agh.edu.pl,  
kbzowski@agh.edu.pl, phajder@agh.edu.pl,  
opal@agh.edu.pl, pernach@agh.edu.pl,  
michal.piwowarczyk@cmc.com

**Keywords:** hot-rolling, production planning, scheduling, sequencing, knowledge engineering

## 1. Introduction

The aim of the research was to develop a mechanism for scheduling orders for steel mills, the task of which is to determine the optimal sequence of orders for heats to be carried out within the designated rolling campaigns. The planning model in this case includes the assumption of optimization on three levels: the basic level is to ensure the uptime operation of the rolling mill as the most important in this process model, which can only be achieved by providing the required material for rolling. The second level is the melt shop – it is necessary to plan the heating sequence in such a way as to prepare the material for rolling on time, and on the other hand to minimize the cost of production by maximizing the use of tundishes and main ladles. At the same time, the third level of optimization is production with a minimum stock level – storing billets in the warehouse is expensive, and their subsequent use may be associated with logistic difficulties due to their size, weight and storage method. Therefore, the algorithm must take into account many factors and boundary conditions. At the same time, it is necessary to create the sequence of heats on the continuous casting machine so that their order in the sequences is maintained by technological requirements. The permissible sequence of the individual materials in the tundish, where the melts from the main ladles are mixed, is described in great detail in the knowledge base. If it is not possible to plan material (described in the technological recipe TR) that could be sequentially planned, the sequence must be interrupted and the tundish replaced – this generates additional costs and time needed for rebuild. Therefore, sequences are planned in such a way as to maximize tundish utilization and minimize the number of material recipes transitions that cannot be sequenced.

## 2. Scheduling and sequencing algorithms

The concept of scheduling is defined as the location of activities in time, assuming a certain number of conditions or constraints [1]. It is closely related to the scheduling of tasks and operations that make up a given process (e.g. production process). In this case, scheduling concerns two processes. First, the Planner defines the rolling mill production plan (planning). The system uses this plan to organize the list of orders according to the rolling mill changeover order framework (queuing). In this way, the production scheduling of the rolling mill is made. In the

---

The publication is co-financed from the state budget under the programme  
of the Minister of Education and Science called "Excellent Science" project no. DNK/SP/548041/2022



**Doskonała  
Nauka**



Ministry of Education and Science  
Republic of Poland



**Republic  
of Poland**

second step, according to the rolling plan created in this way, the production plan of the steel mill (melt shop) is created to cover the demand for rolling material. As part of the scheduling of the work of the steel plant, the sequencing of melts of various materials is also carried out. Each material is casted according to a specific technological instruction (technological recipes – TR) and this activity constitutes a technological operation. The sequence of technological operations is therefore a sequence of several consecutive, different technological instructions. The algorithm uses TR symbols, hence the task of creating a schedule comes down to determining the order of TRs required in the order, taking into account the boundary conditions in the form of rules. The rules were obtained as a result of knowledge engineering from Technologists, which was the first stage of work on the system. The algorithm performs the task of creating a sequence for the given grades of steel and the size of the order (tonnage), so as to obtain an executable production sequence (Figure 1).

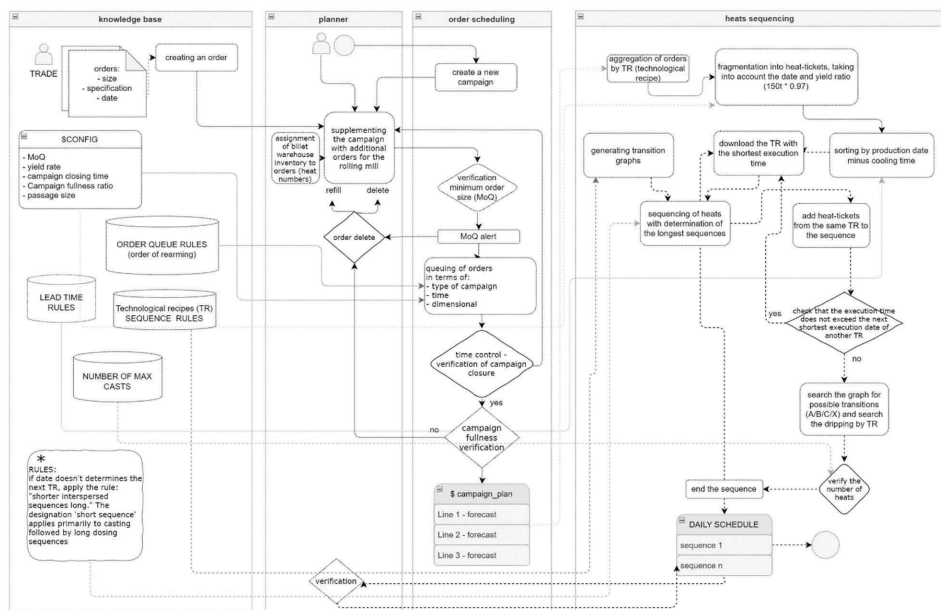


Figure 1. Flowchart of the solution framework.

### 3. Key knowledge sources

The algorithm uses knowledge bases developed on the basis of the knowledge of technologists. The most important is the base in the form of a matrix of connections in sequences between technological instructions (TRs). It allows to create rules for combining materials into sequences. The next base is the Maximum Number of Heats for each TR, which allows to indicate the maximum number of heats of a given material in the sequence. The next necessary knowledge base is the Lead Time Margin Matrix – storing for each TR the minimum times that are required for cooling down, and thus, the time that should be added to the time of TR melt execution. The basis of facts is the historical time of melting a given material, which is calculated on the basis of production data. The system also stores configuration data and a database of steelmaking rules, which also affect the form of the schedule – for example: do not cast singles (orders of one melt), or: short sequences alternating with long ones.

## 4. Results

The literature presents various methods used in planning and scheduling production. The use of various variations of linear and integer programming [2–3], as well as heuristic and artificial intelligence methods [4] is popular. In this case, none of the methods was directly able to provide a complete solution. The complexity of the process made it impossible to use only classic nor heuristic scheduling algorithms (i.e. Ant Colony Optimization (ACO), Evolutionary Algorithms (EC), Simulated Annealing, etc.), rule-based systems are also not suitable for such complex decision-making processes. Therefore, the solution had to take a hybrid form – the mechanism includes both elements of optimization (searching for connection graphs) and rule-based reasoning (steel rules). The main task of the algorithm in the proposed system was to determine the sequence for the given steel grades so that the boundary conditions in the form of allowed rules for transitions between grades were met. The developed system is based on knowledge engineering. This means that the system is incremental and has the adaptability. The learning mechanism is based on interaction with the system operator – technologist or planner. It is important to provide tools of this type with good quality and correct data, representing solutions that are tested and expected for given problems. The system operator should have expert knowledge in the field of the problem to be solved, so that such data can be provided to the system during its operation.

## References

1. Tan W., Khoshnevis B.: *Integration of process planning and scheduling – a review*. Journal of Intelligent Manufacturing, 11, 2000, 51–63.
2. Maravelias C.T., Sung C.: *Integration of production planning and scheduling: Overview, challenges and opportunities*. Computers and Chemical Engineering, 33, 2009, 1919–1930.
3. Zhong R.Y., Huang G.Q., Lan S., Dai Q.Y., Zhang T., Xu C.: *A two-level advanced production planning and scheduling model for RFID-enabled ubiquitous manufacturing*. Advanced Engineering Informatics, 29, 2015, 799–812.
4. Guzman E., Andres B., Poler R.: *Models and algorithms for production planning, scheduling and sequencing problems: A holistic framework and a systematic review*. Journal of Industrial Information Integration, 27, 2022, 100287.

**Acknowledgements.** The authors acknowledge financial support from the Intelligent Development Operational Program: POIR.01.01.01-00-0996/19.

# Feasibility of knowledge graphs as a tool for data storage in production planning systems

Maciej Krzywda<sup>1</sup>, Krzysztof Regulski<sup>2</sup>, Łukasz Rauch<sup>2</sup>

<sup>1</sup> AGH University of Science and Technology, Faculty of Physics and Applied Computer Science,  
Al. Mickiewicza 30, 30-059 Kraków, Poland

<sup>2</sup> AGH University of Science and Technology, Faculty of Metals Engineering and Industrial  
Computer Science, Al. Mickiewicza 30, 30-059 Kraków, Poland  
krzywda@agh.edu.pl, regulski@agh.edu.pl,  
lrauch@agh.edu.pl

**Keywords:** knowledge graph, production planning, manufacturing, knowledge representation

## 1. Introduction

In today's manufacturing industry, production planning systems are becoming increasingly complex and require efficient procedures to manage with the ever-increasing process of increasing and increasing in their complexity. Production planning systems have relied on relational databases as a standard for data storage and management. However, as the amount and complexity of data have increased, these systems have proven to be inadequate in handling and visualizing the data. The limitations of these systems can lead to inefficiencies in the planning process, such as delays in decision making, inaccuracies in conclusions, and difficulties in forecasting and planning for the future. This is because the processes become more and more complex, it becomes harder to understand and visualize them using traditional table-based systems. We propose utilizing knowledge graphs as a solution to this problem. By structuring and organizing data and knowledge in a clear and accessible way, knowledge graphs can help streamline the analysis process and improve overall planning efficiency.

## 2. Methodology

In our proposed solution, we turn to the power of knowledge graphs to tackle the knowledge storage and management challenges in production planning systems [1–2]. By utilizing a knowledge graph, we can effectively store and represent a wide range of information related to the production process, from orders and production schedules via equipment usage to potential links/transaction prediction which is not possible with a table-and-rule-based system.

## 3. Results

In this study, we propose a method for modeling and optimizing the production process in a steel works. By utilizing artificially generated data represented in a 3-column format, we are able to simulate various scenarios and identify potential bottlenecks in the production process. The data consists of Material A, Material B, and the method of transition between the two materials in the tundish during the casting process, with a total of 30 cases for each material and 3 possible methods of transition.

---

The publication is co-financed from the state budget under the programme  
of the Minister of Education and Science called "Excellent Science" project no. DNK/SP/548041/2022



**Doskonała  
Nauka**



Ministry of Education and Science  
Republic of Poland



**Republic  
of Poland**



Compared to traditional tabular data representation, our approach based on knowledge graphs offer several advantages, the major advantage is that they are able to capture the complex relationships between different entities in a much more intuitive and readable way. In the context of the production process, knowledge graphs can easily show the relationships between different materials and transition methods, and how they are interconnected.

## References

1. Schneider T., Šimkus M.: *Ontologies and Data Management: A Brief Survey*. *Künstl Intell*, 34, 2020, 329–353.
2. Ji S., Pan S., Cambria E., Marttinen P., Yu P.S.: *A Survey on knowledge Graphs: Representation, Acquisition, and Applications*. *IEEE Transactions on Neural Networks and Learning Systems*, 33, 2022, 494–514.

**Acknowledgements.** The authors acknowledge financial support from the Intelligent Development Operational Program: POIR.01.01.01-00-0996/19.

# Prediction of Bainite Formation during Hot Deformation Processes using a Macro-scale Finite Element Analysis

Missam Irani<sup>1</sup>, Towhid Faraji Shovay<sup>1</sup>, Grzegorz Korpala<sup>1</sup>, Ulrich Prahl<sup>1</sup>

<sup>1</sup> Institut für Metallformung, Bernhard-von-Cotta-Str. 4,  
Technische Universität Bergakademie Freiberg, 09599, Germany  
Missam.Irani@imf.tu-freiberg.de,  
Towhid.Faraji-Shovay@student.tu-freiberg.de,  
Grzegorz.Korpala@imf.tu-freiberg.de,  
Ulrich.Prahl@imf.tu-freiberg.de

**Keywords:** Bainite, Hot deformation, Kinetics, Finite element analysis

## 1. Introduction

Lightweight structures in automotive engineering require new steels with higher strength and adequate formability, which are simultaneously cost-effective. Unalloyed and low-alloy bainitic steels with retained austenite can meet this requirement [1]. Recent developments of pressing steel sheets use interrupted cooling with quasi-isothermal holding, yielding duplex or complex microstructures. When the quasi-isothermal holding falls in the bainite region, the resulting microstructure contains partial bainite and martensite. This technique is called bainitic press hardening. The optimum properties are achieved by tailoring a bainitic microstructure with a fraction of retained austenite [2]. With precise control of heat flow to the dies, a product with different local microstructures and properties can also be produced. Such robust control over the process requires accurate instruments and predicting tools to determine the processing parameters and obtain expected properties. A macro-scale finite elements analysis (FEA) is required to calculate the bainite fraction in entire of the product and reflect its influence on the mechanical properties of the deforming steel. In other words, the flow stress of the steel should be updated during the deformation using the calculated bainite fraction.

In return, the bainite formation is accelerated significantly in the presence of pre-strain or stresses. Bainite nucleates at the austenite grain boundaries in the case of stress-less and pre-strain-less transformations. At high stresses or pre-strain additional intragranular nucleation sites are activated [3]. Thus, the implemented bainite kinetics model should be coupled with the flow stress calculation of the steel to reflect the influence of bainite transformation on the flow stress and the variation in the flow stress on the bainite formation kinetics. Moreover, a volume change occurs when austenite transforms to bainite or bainitic ferrite, which also dimly influences the flow behavior but should be involved in the finite element model.

In this study, the available mathematical models for calculating the bainite fraction during the hot deformation of steel alloys are implemented in a finite element model. For this purpose, several side equations are employed to adopt the model for a macro-scale problem and reflect the influence of transformation on flow stress. The developed model is able to predict the flow behavior of the steel when austenite to bainite transformation occurs. Moreover, the deformation process parameters can be optimized using the FEA to produce the desired austenite and bainite combination in the final product microstructure.

---

The publication is co-financed from the state budget under the programme  
of the Minister of Education and Science called "Excellent Science" project no. DNK/SP/548041/2022



**Doskonała  
Nauka**



Ministry of Education and Science  
Republic of Poland



**Republic  
of Poland**

## 2. Mathematical Modelling of Bainite Formation Kinetics

Considering the mechanism of the displacive transformation of primary bainite formation, the kinetics of bainite formation that is stated in differential form as follows [4]:

$$\frac{d\xi}{dt} = \frac{uK_1}{\theta}(1 - \xi)(1 + \beta\theta\xi) \exp\left[-\frac{K_2}{RT}\left(1 + \frac{\Delta G_m^0}{r}\right) + \frac{K_2(\Delta G_m^0 - G_N)}{rRT}\right] \quad (1)$$

$$\beta = \lambda_1(1 - \lambda_2\bar{x}) \quad (2)$$

where  $\beta$  is the autocatalysis factor,  $\theta$  is the maximum volume fraction of bainite,  $\xi$  is the normalized volume fraction of bainite,  $u$  is the volume of bainite subunits,  $R$  is the gas constant, and  $\bar{x}$  is the mean carbon concentration. and  $r, K_1, K_2, \lambda_1, \lambda_2$  are empirical constants.  $\Delta G_m^0$  and  $G_N$  are the maximum possible energy change on nucleation and the universal nucleation function, respectively. To reflect the effect of stress on the kinetics of bainite formation  $\Delta G_m^0$  is calculated as follows:

$$\Delta G_m^0 = \Delta G_{chem} + \Delta G_{mech} \quad (3)$$

$$\Delta G_{mech} = V_m U \quad (4)$$

$$U = \sigma\delta + \tau s \quad (5)$$

where  $\Delta G_{chem}$  is the chemical and  $\Delta G_{mech}$  mechanical driving force for the bainite transformation.  $V_m$ ,  $\sigma$  and  $\tau$  are the molar volume, normal and shear components of the externally applied stress, respectively.  $\delta$  and  $s$  are the constants with values of 0.03 and 0.22, respectively [5]. As  $\sigma$  and  $\tau$  are stress components applied on the austenite and bainite interfaces on the microscopic scale. To scale up the problem and adopt it with a macro-scale model,  $U$ , the energy density, is recalculated as below:

$$U = A\sigma_{mises}\delta + (1 - A)\sigma_{mises}s \quad (6)$$

$$A = \max\left[\frac{s_2}{s_1}, \frac{s_2}{s_3}\right] \quad (7)$$

where  $\sigma_{mises}$  is the von-mises stress and  $s_1, s_2$  and  $s_3$  are the principal stresses.  $A$  value varies between zero and one (zero under the pure shear and one for a pure tensile condition).

## 3. Implementing the Model in Finite Element Analysis

Figure 1 depicts the procedure of calculating the bainite fraction, associated flow stress, and volume change in the developed FEA for a time increment. The value of the flow stress is updated in each time increment and for all elements using the following equation:

$$\sigma_f = [\sigma_\gamma(1 - \xi) + \sigma_\alpha\xi]\theta \quad (8)$$

where  $\sigma_\gamma$  and  $\sigma_\alpha$  are the flow stress of austenite and bainitic ferrite, respectively, that are given to the simulation using the Hensel-Spittel model (see box A in Figure 1):

$$\sigma_{\gamma} = A_{\gamma} \exp(m_{1\gamma} T) \epsilon_p^{m_{2\gamma}} \dot{\epsilon}^{-m_{3\gamma}} \quad (9)$$

$$\sigma_{\alpha} = A_{\alpha} \exp(m_{1\alpha} T) \epsilon_p^{m_{2\alpha}} \dot{\epsilon}^{-m_{3\alpha}} \quad (10)$$

The density is also recalculated when the transformation occurs using the following equation (see box B in Figure 1)

$$\rho = [\rho_{\gamma}(1 - \xi) + \rho_{\alpha}\xi]\theta \quad (11)$$

where  $\rho_{\gamma}$  and  $\rho_{\alpha}$  are the flow stress of austenite and bainitic ferrite, respectively.

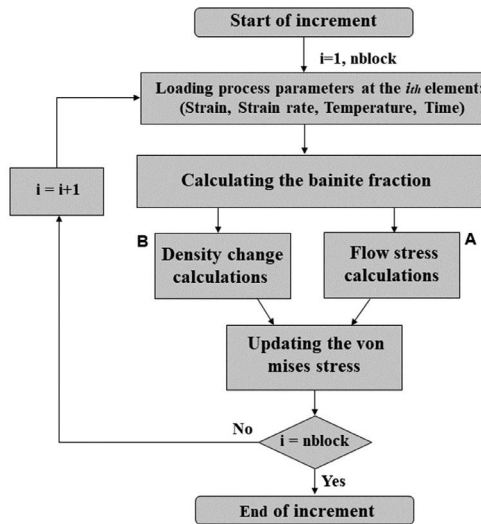


**Figure 1.** Conceptual procedure for predicting bainite fraction (nblock is the total number of elements in the model).

## 4. Summary

Macro-scale finite element analysis was conducted to predict the bainite formation during hot forming processes. The influence of bainite transformation on the flow behavior of the steel is modeled. The developed model can optimize the process parameters during deformation to control the steel's bainite fraction and flow stress.

## References

1. Sun L., Muszka K., Wynne B.P., Palmiere E.: *The interactions between strain path reversal and dynamic recrystallization in 316L stainless steel were n 316L stainless steel studied by hot torsion*. Materials Science and Engineering A, 568, 2013, 160–170.
2. Muszka K.: *Modelling of deformation inhomogeneity in the angular accumulative drawing process-multiscale approach*. Materials Science and Engineering A, 559, 2013, 635–642.
3. Freiwilling R., Kudrman J., Chraska P.: *Bainite Transformation in Deformed Austenite*. Metallurgical Transactions A, 7A ,1976, 1091–1097.

4. Chester N.A., Bhadeshia H.K.D.H.: *Mathematical modeling of bainite transformation Kinetics*. Journal de P hysique IV, 7, 1997.
5. Bhadeshia H.K.D.H.: *Bainite in steels*. The University Press Cambridge, London, 2001, 50–51.

**Acknowledgements.** This work was supported by German Research Foundation (Deutsche Forschungsgemeinschaft). The authors acknowledge the German Research Foundation for providing financial support.

# Electrical and thermal analysis for the copper removal process in an electric furnace

Radosław Zybala<sup>1</sup>, Sławomir Golak<sup>2</sup>, Tomasz Sak<sup>1</sup>, Piotr Madej<sup>1</sup>

<sup>1</sup> Lukaszewicz Research Network – Institute of Non-Ferrous Metals,  
ul. 5 Sowińskiego Street 44-100 Gliwice, Poland

<sup>2</sup> Department of Industrial Informatics, Faculty of Materials Engineering,  
Silesian University of Technology, ul. Krasynskiego 8, 40-019 Katowice  
radoslaw.zybala@imn.lukasiewicz.gov.pl,  
slawomir.golak@polsl.pl,  
tomasz.sak@imn.lukasiewicz.gov.pl,  
piotr.madej@imn.lukasiewicz.gov.pl

**Keywords:** numerical modelling, copper removal, resistance furnace

## Abstract

In the process of smelting a mixture of copper concentrates in single-stage flash smelting technology, the resulting waste slag contains a high copper concentration (11–15% Cu by weight). The cost-effectiveness of operating single-stage technology is determined by the ability to recover copper from the waste slag. The process is carried out using electric resistance furnaces and is based on the reduction of metal oxides contained in the slag. The product is waste slag depleted to ~0.5% by weight of copper and a metallic alloy containing copper as well as lead and iron.

Decopperisation of slag slurry is a high-temperature process, so thermal phenomena are particularly important. Because the main heat sources present in the process are due to the Joule phenomenon in the flow of electric current through electrodes, slag and reduced metallic alloy, the field of current flow is crucial in analysis.

This article discusses the methodology of the numerical model of the electric current flow process and the Joule heat generation process in decopperisation of slag slurry process using ANSYS Fluent. The starting point for the numerical simulation of the process was the formulation of an adequate geometrical model of the analysed object – a two-electrode furnace. A model of current and energy flow processes in the considered technological facility was formulated based on the definition in ANSYS Fluent of an additional scalar transport equation (UDS) based on Gauss's law for the electric field supplemented by the definitions of current density and Joule heat sources.

$$\nabla \cdot (\sigma \nabla V) = 0 \quad (1)$$

$$\mathbf{E} = -\nabla V \quad (2)$$

$$\mathbf{J} = \sigma \mathbf{E} \quad (3)$$

$$q_j = \frac{|\mathbf{J}|^2}{\sigma} \quad (4)$$

---

The publication is co-financed from the state budget under the programme of the Minister of Education and Science called "Excellent Science" project no. DNK/SP/548041/2022



**Doskonała  
Nauka**



Ministry of Education and Science  
Republic of Poland



**Republic  
of Poland**

where:  $\nabla$  – nabla operator,  $\mathbf{V}$  – electric potential [V],  $\mathbf{E}$  – electric field strength [ $\text{V}\cdot\text{m}^{-1}$ ];  $\sigma$  – electrical conductivity [ $\text{S}\cdot\text{m}^{-1}$ ],  $\mathbf{J}$  – current density [ $\text{A}\cdot\text{m}^{-2}$ ],  $q_j$  – volumetric density of Joule’s heat generated [ $\text{W}\cdot\text{m}^{-2}$ ].

In the prepared 3D model of current flow and heat generation, the phenomena of contact resistance between contact surfaces in the solid/fluid system were taken into consideration. Very few research works on the analysis of this issue are observed. The term contact resistance refers to the total resistivity of the system and occurs at the interface layer of two bodies. This effect causes a local strong reduction in the conductivity of the system, and its omission may limit the representativeness of the developed model.

Figure 1 shows an example of the current density distribution for the supply voltage of 45 V. The example shows the distribution for the base case – without the presence of contact resistance.

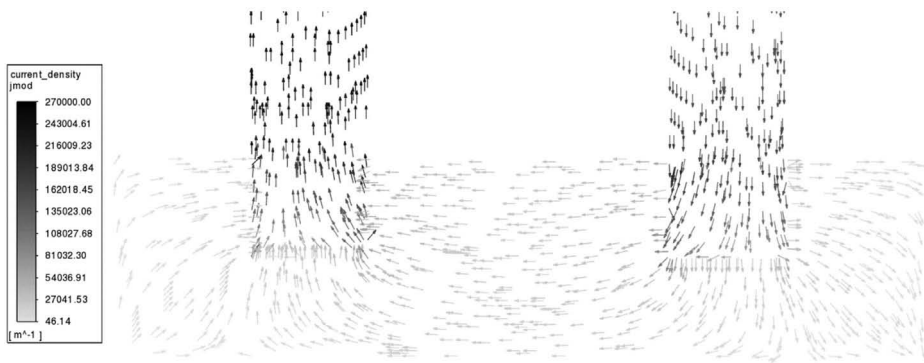


**Figure 1.** Distribution of current density on the furnace cross-section.

## References

1. Xia G., Tuo W., Li X., Liu X.: *Study on the Performance of Liquid-Solid Contact Resistance Based on Magnetohydrodynamic Micro-Angular Vibration Sensor*. *Sensors*, 22, 2022, 9204.
2. Yang H., Wolters J., Pischke P., Soltner H., Eckert S., Natour G., Fröhlich J.: *Modelling and simulation of a copper slag cleaning process improved by electromagnetic stirring*. *Materials Science and Engineering*, 228, 2017, 012007.

# The modelling of the diffusion process, review

Bartek Wierzba<sup>1</sup>

<sup>1</sup> Lukaszewicz Research Network, Warsaw Technological Institute,  
ul. Racjonalizacji 6/8, 02-673 Warszawa  
Bartlomiej.wierzba@wit.lukasiewicz.gov.pl

**Keywords:** diffusion, Onsager model

## Abstract

In this paper the modelling of the diffusion process will be reviewed. The models that allows for determination of the concentration profile in both binary and multi-component systems will be shown. In case of diffusion modeling in one phase binary system the Fick 2<sup>nd</sup> law [1] could be used. The concentration as a function of time and position can be calculated by Eq. 1.

$$\frac{\partial c}{\partial t} = \frac{\partial}{\partial x} \left( D \frac{\partial c}{\partial x} \right) \quad (1)$$

where  $c$  is concentration and  $D$  is the diffusion coefficient,  $x$  and  $t$  are the position and time.

The Fick second law can be solved analytically knowing the error function, erf. However, the analytical solution is rarely used, Eq. 2.

$$C(x) = \frac{C^-}{2} \left[ 1 - \operatorname{erf} \left( \frac{x}{2\sqrt{Dt}} \right) \right] \quad (2)$$

where:

$$\operatorname{erf}(z) = \frac{2}{\sqrt{\pi}} \int_0^z \exp(-y^2) dy$$

In case of modelling multi-component one-phase system, the two main methods can be distinguished, Onsager [2,3], which is the generalization of the Fick law and Darken [4] methods. In Onsager method the mass conservation can be calculated knowing the divergence of the fluxes of all components that takes place during diffusion process, Eq. 3.

$$\frac{\partial N_i}{\partial t} = \operatorname{div} \left( \sum_{j=1}^{n-1} \sum_{k=1}^{n-1} L_{jk} \frac{\partial(\mu_k - \mu_n)}{\partial N_j} \operatorname{grad} N_j \right) \quad (3)$$

where  $L_{ij}$  are the phenomenological coefficients,

---

The publication is co-financed from the state budget under the programme  
of the Minister of Education and Science called "Excellent Science" project no. DNK/SP/548041/2022



**Doskonała  
Nauka**



Ministry of Education and Science  
Republic of Poland



**Republic  
of Poland**

$$L_{ij} = c_i B_i \frac{\sum_{k=1, k \neq i}^n N_k B_k}{\sum_{k=1}^n N_k B_k}, \quad i = j, i = 1, \dots, n$$

$$L_{ij} = -c_i B_i \frac{N_j B_j}{\sum_{k=1}^n N_k B_k}, \quad i \neq j, i, j = 1, \dots, n$$

The Onsager method can also be solved analytically, but the solution is no trivial, Eq. 4.

$$[\Delta c] = [\alpha_1^{-1}] \frac{(\alpha_1][\Delta c^0]}{2} \operatorname{erfc}(z_1) + [\alpha_2^{-1}] \frac{(\alpha_2][\Delta c^0]}{2} \operatorname{erfc}(z_2) + \dots$$

$$+ [\alpha_{n-1}^{-1}] \frac{(\alpha_{n-1}][\Delta c^0]}{2} \operatorname{erfc}(z_{n-1}) \quad (4)$$

where

$$z_j = \frac{x}{2E_j t}$$

and  $\alpha$  denotes the eigenvalue of diagonal diffusion matrix  $[E] = [\alpha][D][\alpha^{-1}]$ .

The second model for multicomponent one-phase calculations is the generalized Draken method, where the mass conservation can be calculated when the diffusion and drift velocities are known, Eq. 5.

$$\frac{\partial c_i}{\partial t} = \operatorname{div} \left( c_i B_i \operatorname{grad} \mu_i - c_j \sum_{i=1}^n c_i B_i \operatorname{grad} \mu_i \right) \quad (5)$$

where  $B_i$  denote the mobility and  $\mu_i$  the chemical potential of the component.

The generalized Darken method can be used for determination unlimited number of components, e.g. in diffusion path between Rene88 and Inconel-718 at 1423 K [5], Figure 1.

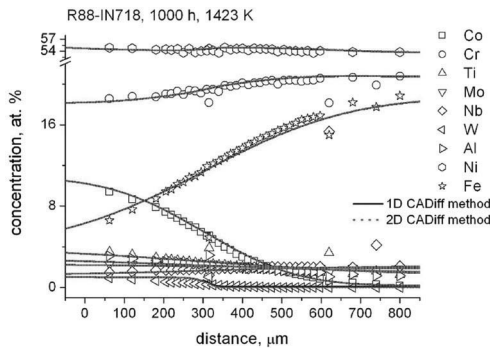


**Figure 1.** The results of modelling the diffusion process in multi-component diffusion-path between Rene88 and Inconel-718 system.

The generalized darken method can be supplemented by many other factors, e.g. by calculation the mechanical potential [6], Eq. 6, Figure 2.

$$\frac{3(1-2\nu)}{E} \frac{\partial p}{\partial t} = -\operatorname{div} \left( \sum_{j=1}^r \rho_j \Omega_j^m v_j \right) + \operatorname{div} v^{diff} \quad (6)$$

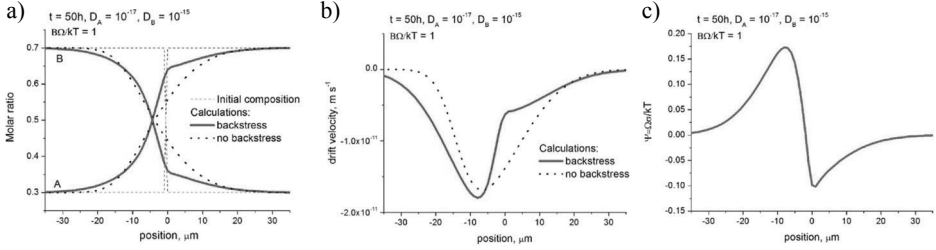


**Figure 2.** The results of modelling of the pressure generated during the diffusion process.

It can be also supplemented to calculate the diffusion under the gravity than the mechanical equilibrium should be assumed, Eq. 7.

$$0 = -\operatorname{grad} p + \rho \omega^2 r \quad (7)$$

where  $p$  is the pressure generated during the centrifugation,  $\rho$  denote the density of the component and  $\omega$  angular velocity. The results of the diffusion under the gravity force in Bi-Sb system show, that the heavier Bi atoms were moved accordingly with the gravity force [7], Figure 3.

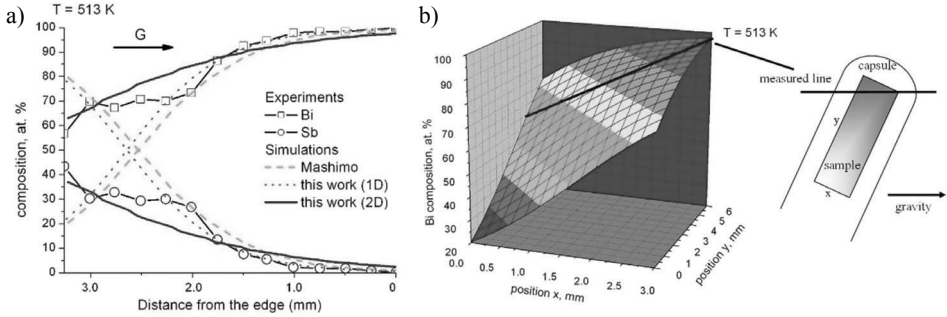


**Figure 3.** The calculations of the centrifugal force acting on the diffusion process.

The generalized darken method can also be used to calculate the diffusion in ternary multi-phase systems. In this case, the following mass balance equation should be calculated [8], Eq. 8.

$$\begin{aligned} f^\alpha \frac{\partial c_i^\alpha}{\partial k} \frac{\partial k}{\partial t} + f^\beta \frac{\partial c_i^\beta}{\partial k} \frac{\partial k}{\partial t} + (c_i^\alpha - c_i^\beta) \frac{\partial f^\alpha}{\partial t} = \\ = -\frac{\partial}{\partial x} \left( -D_i^{eff} \frac{\partial k}{\partial x} + f^\alpha c_i^\alpha v^\alpha + f^\beta c_i^\beta v^\beta \right), \quad i = 1, 2, 3 \end{aligned} \quad (8)$$

where  $\alpha$  and  $\beta$  denotes the phases between which the diffusion occurs.  $f_\alpha$  denote the fraction of  $\alpha$ -phase,  $k$  – denote the conode where the diffusion path will cross the two-phase zone and  $v_\alpha$  is the drift velocity in  $\alpha$  phase. The effective diffusion coefficient can be calculated by the sum of fraction in  $\alpha$  and  $\beta$  phases:

$$D_i^{eff} = f^\alpha D_i^\alpha \frac{\partial c_i^\alpha}{\partial k} + f^\beta D_i^\beta \frac{\partial c_i^\beta}{\partial k}, \quad i = 1, 2, 3$$

The generalized Darken method allows for determination of the diffusion path in multiphase ternary system. E.g. aluminization of Mar-M200 at 1273 K [8], Figure 4.

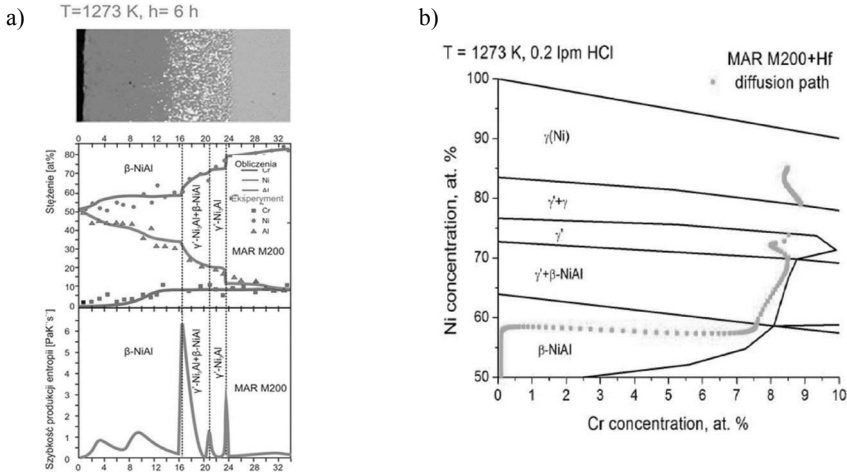


**Figure 4.** The comparison of the modelling of the diffusion process in ternary multiphase system. The aluminization of the MAR-M200+Hf alloy at 1273 K by 6 h.

Concluding, the generalized Darken method can be used in calculations of many diffusion phenomena's in one and multi-phase systems. Nowadays, the diffusion models are further generalized to calculate the competition of phase formation. It means, that the order of newly formed phases should be determined. To calculate this phenomena the maximization of entropy production can be used [9]. The generalization of Darken method gives many possibilities for determination of the diffusion path by simulation techniques.

## References

1. Fick A.E.: *Über diffusion*, Annalen der Physik, 170(1), 1855, 59–86.
2. Manning J.R.: *Correlation effects and activation energies for diffusion in alloys*. Zeitschrift für Naturforschung, 26a, 1971, 69.
3. Murch G.E., Belova I.V.: *Phenomenological coefficients in solid-state diffusion, An introduction*. Diffusion Fundamentals, 2, 2005, 8.1–8.13.
4. Darken L.S.: *Diffusion, Mobility and Their Interrelation through Free Energy in Binary Metallic Systems*. Transactions of AIME, 174, 1948, 184–201.
5. Danielewski M., Wierzbna B.: *Intrinsic Diffusivities and Modeling of the Diffusion Multiples*. Defect and Diffusion Forum, 273–276, 2008, 105–112.
6. Danielewski M., Wierzbna B.: *Thermodynamically consistent bi-velocity mass transport phenomenology*. Acta Materialia, 58, 2010, 6717–6727.
7. Wierzbna B., Danielewski M.: *Thermodynamically Consistent Formulation of the Sedimentation in Solids and Liquids*. Defect and Diffusion Forum, 309–310, 2011, 275–278.
8. Wierzbna B., Tkacz-Śmiech K.: *Diffusion zone formation in aluminized MAR-247 from Bi-velocity Phase Field Method*. Physica A, 392, 2013, 1100.
9. Wierzbna B., Nowak W.J., Serafin D.: *The Sequence of the Phase Growth during Diffusion in Ti-Based Systems*. High Temperature Materials and Processes, 38, 2019, 151–157.

# Virtual and Augmented Reality Applications in Manufacturing of Precision Assembly Systems

Tomasz Dębiński<sup>1</sup>, Danuta Szeliga<sup>1</sup>, Marcin Hojny<sup>1</sup>

<sup>1</sup> AGH University of Science and Technology, Al. Mickiewicza 30, 30-059 Kraków, Poland  
debinski@agh.edu.pl, szeliga@agh.edu.pl,  
mhojny@agh.edu.pl

**Keywords:** digital twin, virtual reality, artificial intelligence, augmented reality, precision assembly

## 1. Introduction

The possibilities offered by the digitalisation of technological processes make it is an increasingly used in industrial applications. The combination of artificial intelligence, digital twins, meta-modelling, VR and AR technologies allows work to be improved at many stages of production: in design, on assembly lines or quality control. As production should be as efficient as possible while ensuring safety and generating low costs, manufacturers are attempting to implement integrated technologies, in line with the Industry 4.0 concept, describing the process of technological and organisational transformation [1].

## 2. Solution for support manufacturing of precision assembly systems

As part of the paper, an overview of the ADAPTSYS IT system, supporting quality control and production optimisation of precision assembly systems based on artificial intelligence (AI), augmented reality (AR) and virtual reality (VR) will be presented (Figure 1).

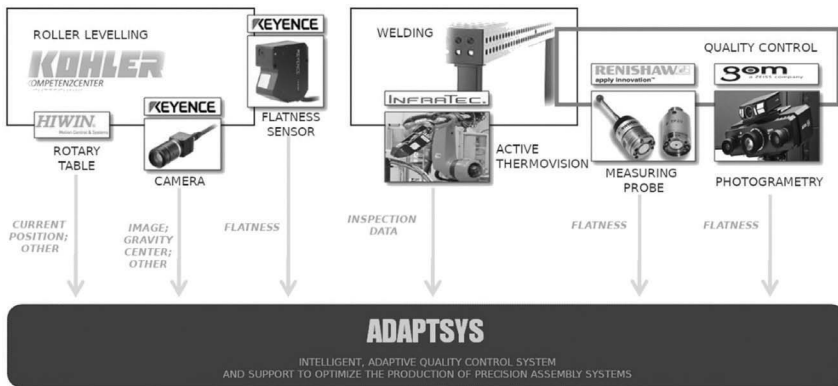


**Figure 1.** A set of modules included in the ADAPTSYS system.

The publication is co-financed from the state budget under the programme of the Minister of Education and Science called "Excellent Science" project no. DNK/SP/548041/2022

A key solution of the implemented system is the digital twin of roller levelling process. One of the innovations included in the digital twin, will be a module that allows fast calculations (time in seconds) to predict, among others, the strains and/or internal stresses in a band for a given levelling process parameters (Figure 2).

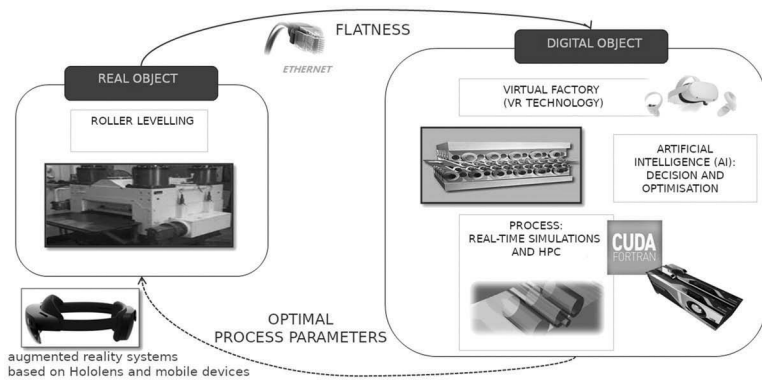


**Figure 2.** Data flow diagram for a digital twin model.

Coupling the computing module with an artificial intelligence (AI) module, will allow the process to be controlled according to the adopted parameters (Figure 3).



**Figure 3.** The digital twin of the roller levelling process in a virtual environment.

### 3. Augmented and Virtual Reality modules

The supporting solution will be an innovative mobile augmented reality (AR) module, enabling the monitoring and display of additional information about the real object, such as information from the laser sensors about flatness, information from the calculation module about deformation and stress values, or information about possible deviations of the semi-finished or final product from the reference model (CAD nominal) (Figure 4).

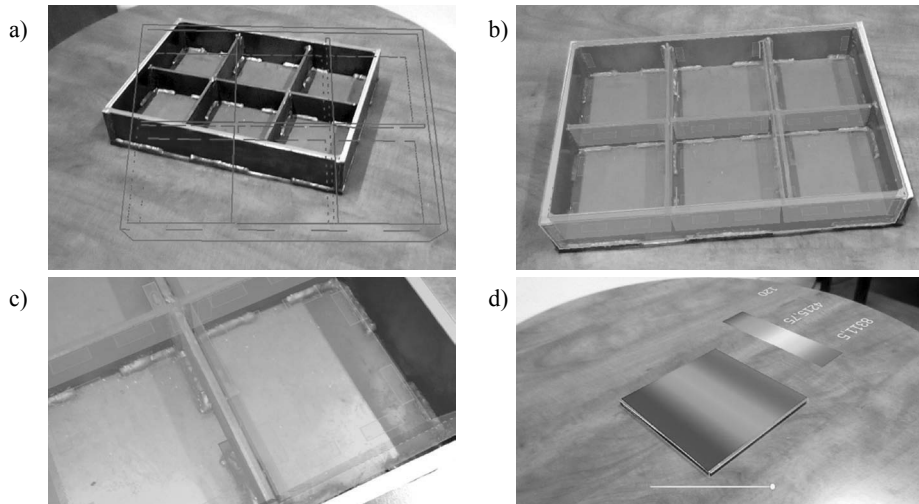


**Figure 4.** The use of augmented reality to monitoring a real object, a) model and real object, b) matching the model to the object, c) quality control, d) visualisation of sample information from the calculation module.

## References

1. Eswaran M., Raju Bahubalendruni M.V.A.: *Challenges and opportunities on AR/VR technologies for manufacturing systems in the context of industry 4.0: A state of the art review*. Journal of Manufacturing Systems, 65, 2022, 260–278.

**Acknowledgements.** The authors acknowledge financial support from the Intelligent Development Operational Program: POIR.01.01.01-00-0031/21.

# Linear welding power prediction measurement-based models

Krzysztof Regulski<sup>1</sup>, Łukasz Rauch<sup>1</sup>, Krzysztof Bzowski<sup>1</sup>,  
Piotr Hajder<sup>1</sup>, Monika Pernach<sup>1</sup>, Jan Kusiak<sup>1</sup>

<sup>1</sup> AGH University of Science and Technology, Al. Mickiewicza 30, 30-059 Kraków, Poland  
regulski@agh.edu.pl, lrauch@agh.edu.pl,  
kbzowski@agh.edu.pl, phajder@agh.edu.pl,  
pernach@agh.edu.pl, kusiak@agh.edu.pl

**Keywords:** linear welding, prediction, machine learning, fuzzy logic

## 1. Introduction

The linear welding process enables to manufacture parts for the construction, building and mining industries, where components such as brackets or anchors are used. These products are often responsible parts of constructions, making their quality a factor in human safety, and is therefore a key aspect of manufacturing. The speed of manufacturing in this process is high, and the fluctuation and variability of parameters is significant, making it imperative that maintaining quality at the manufacturing stage through parameter monitoring must also include predicting these parameters in advance to allow time for a possible response even before unacceptable deviations from acceptable process parameter values occur. Key process parameters include current parameters (power, amperage, voltage) and their derivative – welding temperature. Based on these, it can be predicted whether the resulting weld will have satisfactory strength [1–3]. Since the range of products produced at the plant is considerable, and the different dimensions and thickness of the pipe to be welded determine the setting of the right parameters for it, the models must receive the thickness and diameter of the given material at the input in order to correctly predict the power with which the process should be carried out to achieve the right welding temperature.

## 2. Temperature prediction models

The research aimed to develop models using data mining and machine learning from production data from the process to predict weld temperatures based on current parameters. A number of machine learning algorithms were used, which have already proven their effectiveness in materials engineering and metal processing applications [4–7]. Two different datasets were worked on. Among others, a model was developed based on results from a pyrometer placed on a measuring device. This was data from work-in-progress – cleared of downtime and changeovers, start-ups and process extinctions. Only data for work-in-progress production. Data: 12 575 records. Using the automatic network architecture search algorithm (Automatic Neural Networks), the space of possible architectures and different number of layers and neurons in hidden layers, as well as MLP and RBF architectures, different types of activation functions were searched, determining the optimal network architecture. Validation quality of correlation  $R = 0.945$  was obtained, determination coefficient was  $R^2 = 0.893$ . The second dataset included results from real production (with downtime, startup and quench), data was sampled every half second and temperature delay was added to represent the actual weld heating delay. Data: 50 400 records. The developed model had a correlation

---

The publication is co-financed from the state budget under the programme  
of the Minister of Education and Science called "Excellent Science" project no. DNK/SP/548041/2022



coefficient  $R = 0.992$ , determination coefficient  $R^2 = 0.984$ . Even better results were obtained using Random Forest (Table 1).

**Table 1.** Comparative analyses of temperature prediction results.

Model	MSE	RMSE	MAE	$R^2$
Random Forest	613.4	24.76	16.98	0.986
Ada Boost	690.4	26.27	16.81	0.984
Regression Tree	895.9	29.93	19.76	0.979
Linear Regression	926.7	30.44	22.21	0.978
Neural Network	2214.6	47.06	28.31	0.984

### 3. Power prediction models

The key process parameter affecting the welding temperature and thus the most important quality factor turned out to be the power of the current. Tasking the right power for a given size and material of the welded profile is the most important task of the operator. Based on material testing, it is possible to determine in what power range welds of the expected strength are produced, and where is the limit below which the process does not maintain the expected quality. However, material tests are expensive, and they are destructive tests, so they require the destruction of the sample and thus the product. Having production data and temperature prediction models to determine whether the process temperature was appropriate, it was possible to perform process data filtering obtaining learning sets with given characteristics, allowing the development of models that, as an output, made it possible to determine what power was appropriate for the process carried out for particular profiles: material, diameter and thickness. A knowledge base was acquired, which in the next step was used to develop inference models using fuzzy logic.

### 4. Results

The developed model allows prediction of safe power levels for given input parameters: material, diameter and wall thickness. The fuzzy logic model was implemented in the process control system. The Fuzzy Inference System (FIS) model derived from MATLAB is parsed into Fuzzy Lite Language (FLL) format, which enables the use of the fuzzylite library. Implementation of subsequent models involves using the base class FuzzyModel and implementing procedures, along the lines of PowerMaterialModel for subsequent aggregates. The model was tested on samples that had material test results and on real data from the welding process. A particularly important aspect was that the suggestions made by model should not indicate suggestions below the minimum acceptable power. An error in the opposite direction – excess power – is not so harmful. The results indicated a good fit of indications  $R^2 = 0.73$ , MAE = 9 kW, the predicted power never exceeded the allowable minimum. Average over-delivery relative to the minimum: 17.3 kW (Table 2).

**Table 2.** Comparative analyses of temperature prediction results.

Metric	Abbreviation	Value
Residual Sum of Squares	RSS	145.24
Mean absolute error	MAE	9.31
Relative mean square error	RMSE	0.014
Relative Average Deviation	d	0.09
Correlation coefficient	r	0.86

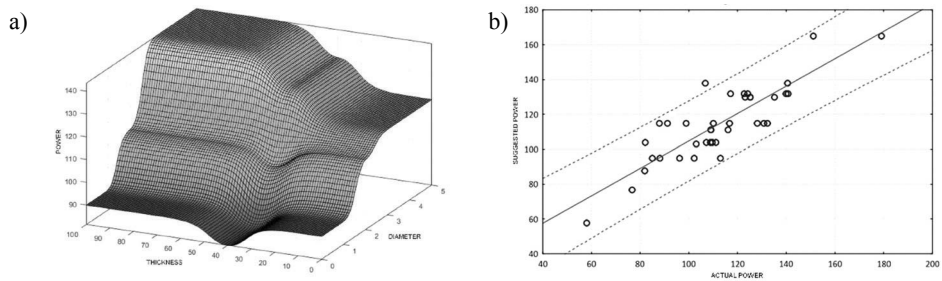


**Figure 1.** Inference surface in fuzzy logic (a). Prediction quality analysis –  $R^2 = 0.73$ , MAE = 9kW, the predicted power never exceeded the allowable minimum (b).

## References

1. Sun J., Dilger K.: *Reliability analysis of thermal cycle method on the prediction of residual stresses in arc-welded ultra-high strength steels*. International Journal of Thermal Sciences, 185, 2023, 108085.
2. Müller F.W., Schiebahn A., Reisgen U.: *Quality prediction of disturbed ultrasonic metal welds*. Journal of Advanced Joining Processes, 5, 2022, 100086.
3. Xiong X., Wang Ch., Wang F., Cui X., Li G.: *Optimization of process parameters for induction welding of composite materials based on NSGA-II and BP neural network*. Materials Today Communications, 33, 2022, 104749.
4. Fragassa C.: *Investigating the Material Properties of Nodular Cast Iron from a Data Mining Perspective*. Metals, 12, 2022, 1493.
5. Huang W., Lyu Y., Du M., Gao S-D., Xu R-J., Xia Q-K.: *Zhangzhou J., Estimating ferric iron content in clinopyroxene using machine learning models*. American Mineralogist, 107, 2022, 1886–1900.
6. Sika R., Szajewski D., Hajkowski J., Popielarski, P.: *Application of instance-based learning for cast iron casting defects prediction*. Management and Production Engineering Review, 10, 2019.
7. Chen S., Kaufmann T.: *Development of data-driven machine learning models for the prediction of casting surface defects*. Metals, 12, 2022.

**Acknowledgements.** The authors acknowledge financial support from the Intelligent Development Operational Program: POIR.01.02.00-00-0091/19.

# Spot-resistant welding process of profiled wire for precise filtration screens – experiments and modelling

Marcin Kwiecień<sup>1</sup>, Mateusz Kopyściański<sup>1</sup>,

Krzysztof Muszka<sup>1</sup>, Janusz Majta<sup>1</sup>

<sup>1</sup> AGH University of Science and Technology, Faculty of Metals Engineering and Industrial Computer Science, 30 Mickiewicza Ave, 30-059 Krakow, Poland  
mkwiecie@agh.edu.pl, kopyscianski@agh.edu.pl,  
muszka@agh.edu.pl, majta@agh.edu.pl

**Keywords:** Profiled wire, filtration screen, FE modelling, Spot-resistant welding

## 1. Introduction

Industrial filtration screens are widely used in various applications for separation purposes. Very often they have to be able to separate particles of a size about 20–40 micrometres what means that the gap between the profiled wire has to be smaller than that. This in turn, requires a very precise control of the manufacturing process. Screens are made of stainless steel (austenitic, ferritic or duplex). The manufacturing process involves wire rod rolling then cold drawing/rolling into a trapezoidal cross-section shape [1]. Then, screens are made by spot-resistant welding process of screen profiles – they can be either flat or cylindrical. Finally, the screens are made by formatting of the final shape by bending/rolling/ and welding of the final screen (conical baskets etc) [2]. In order to meet the final in-use properties (tight dimensional tolerances, strength and wear resistance) the interrelationships between process parameters and material parameters of the used steel grades have to be well understood. One of the most important steps of screen manufacturing is spot-resistant welding process. Its parameters (current, force, wire feed rate) play crucial role in the achievement of the final quality of the screen. If the current or force are not precisely selected, joint area may be too weak or then screen may not meet the dimensional tolerances. Spot-resistant welding process parameters may also influence on the level of residual stresses that build up in the screen. The results of the welding process can be also predicted based on the numerical modelling of the welding process [3]. In presented work, three different welding cases have been simulated using Abaqus Standard software. Effect of welding parameters on temperature distribution was studied and confronted with experimental data.

## 2. Experimental and modelling

For the calculations of the welding process flat screen made with thin profile wires shown in Figure 2a has been chosen. For the analysis of the effect of welding process a single weld point was used for calculations. In the paper the influence of the current parameters on the temperature distribution in the weld zone and the heat affected zone was taken into consideration. The process parameters were adopted according to the data gathered in Table 1.

The simulation was carried out using the thermal-electrical module. Boundary conditions for the welding process were assumed. For the calculations the heat transfer coefficient and electrical conductivity (both as a function of temperature) were assigned. Both were assumed between the copper

---

The publication is co-financed from the state budget under the programme of the Minister of Education and Science called "Excellent Science" project no. DNK/SP/548041/2022



**Doskonała  
Nauka**



Ministry of Education and Science  
Republic of Poland



**Republic  
of Poland**

electrodes and 304L steel as well as between 304L steel and 304L. The electrical potential at the bottom surface of the bottom electrode was assumed to be zero in order to direct the current flow accordingly. The initial temperature of all elements was also assumed to be equal to the ambient temperature (20°C).

**Table 1.** Welding parameters of the profile wires and the mechanical properties of the welded joints.

Name	Tested joints	Material	Welding parameters			Breaking strenght		Shear strength	
			Current [kA]	Time [ms]	Force [kg]	[N]		[N]	
1A	18sb/q55	AISI 304L	0,23	60	42	1 915	1 581	1 522	1 821
1B			0,4	80		1 367	1 553	1 581	1 483
1C			0,77	20		2 387	4 804	1 553	1 452

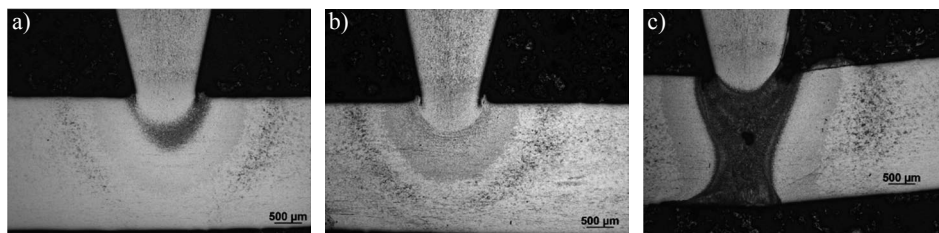


**Figure 1.** Macroscopy characterization of the joints of specimen for samples 1A (a), 1B (b), and 1C (c).

The mechanical properties of the tested welds show that the highest strength was obtained in the case of sample 1C. This is due to the very high temperature which was reached what caused phase transformation of the austenitic structure to martensitic ones. In the 1A and 1B the mechanical properties were lower and reached about 1500 MPa. The macroscopy characterization of the joints shows that in the 1A and 1B specimen the temperature did not affect the structure changes while in the 1C it can be observed that changes in the microstructure occurred due to the very high increase of the temperature.

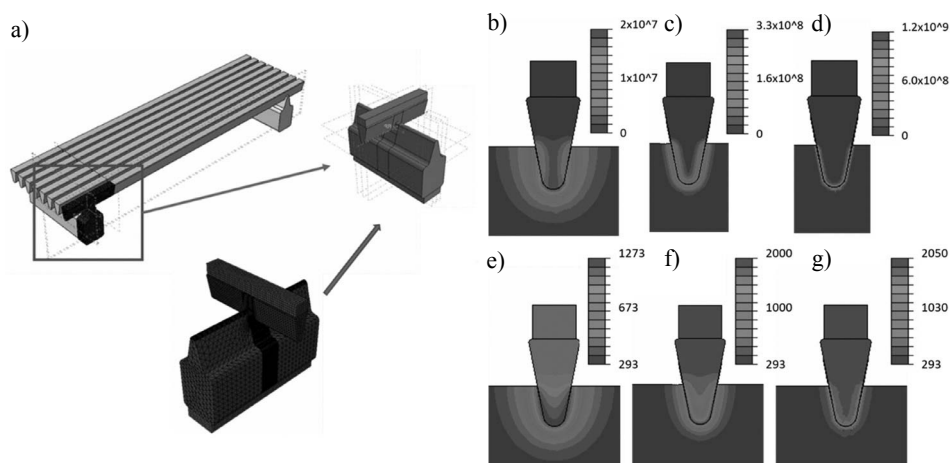


**Figure 2.** Spot welding model developed in Abaqus Standard (a). Heat flux distribution ( $J/K \cdot m^2$ ) within the weld for samples 1A (b), 1B (c), and 1C (d). Temperature distribution (K) within the weld for samples 1A (e), 1B (f), and 1C (g).

The modelling results in the form of heat flux distribution in the last welding time step are summarised in Figure 2(b–d). It can be seen that the welding parameters (current and welding time) have a crucial impact on the obtained results. When the smallest welding current (0.23 kA) is used, the maximum heat flux values are the smallest and did not exceed  $2 \cdot 10^7 \text{ J/K} \cdot \text{m}^2$ . In this case, however, the longest welding time was used, which is reflected in the heat flux distribution map. Here, the area of the heat affected zone is the largest.

The results of the temperature distribution in the weld area (in Kelvin) are shown in Figure 2(e–g). When the smallest welding current was used, the maximum temperature did not exceed 1273 K, while when a welding current of 0.4 kA was used, the maximum temperature reached 2000 K – that is, above the liquidus temperature (1773 K) – Figure 2(f). The use of a short welding time (20 ms) and the highest current (0.77 kA) increased the temperature to a maximum value of 2050 K – Figure 2 (g).

### 3. Summary

The simulations carried out were qualitatively compared with the results of the microstructure observations. The similar shape and size of the remelted zone and the heat affected zone indicate the correctness of the obtained results. The shape of the flash was not reflected in the results – due to the fact that, at this stage, the model is only developed in the thermal range – the thermo-mechanical model is not included – which does not allow, for example, the pressure force during welding to be taken into account. However, for temperature distribution calculations, such a limitation does not significantly affect the results. Based on the obtained results, the following relationships can be drawn between the process parameters and the obtained heat flux, temperature and HAZ distributions:

- as the welding current increases, the maximum temperature in the weld area increases,
- as the welding time increases, the area of the melted zone and the HAZ increases,

Therefore, the optimization of the flat screens welding process should be based on the principle of the correct choice of both current and welding time, so as to optimize the area of the remelted zone but not to overheat the joint, which can lead to defects and the generation of residual stresses.

The use of too short a welding time – even with a high welding current – may not produce a sufficiently large melted zone and lead to the formation of joints with insufficient mechanical properties.

### References

1. Kwiecień M., Majta J., Rumiński M., Kawalko J., Muszka K.: *Surface quality and mechanical properties in drawn stainless steel profile wires caused by process parameters*. Key Engineering Materials, 926, 2022, 980–991.
2. Muszka K., Kwiecień M., Perzyński K., Majta J., Madej Ł.: *Metal forming driven surface engineering of thin profile wires for high precision industrial filtration screens*. CIRP Annals Manufacturing Technology, 72, 2022, 265–268.
3. Nielsen C.V., Martins P.A.F., Zhang W., Bay N.: *Numerical methods in simulation of resistance welding*. [in:] COUPLED VI: proceedings of the VI International Conference on Computational Methods for Coupled Problems in Science and Engineering, 322–333, CIMNE.
4. Neid H.A.: *The Finite Element Modeling of the Resistance Spot Welding Process*, Welding Journal, 63, 1984, 123–132.

**Acknowledgements.** The support from the National Centre for Research and Development, Poland through the grant NCBiR POIR.01.01.01-00-0961/19.

# Computer modelling of the ablation casting process and prediction of strength properties of AC-42000 castings

Marcin Małysza<sup>1,2</sup>, Sabina Puzio<sup>2</sup>, Katarzyna Major-Gabryś<sup>2</sup>,  
Miroslaw Głowacki<sup>2</sup>, Dorota Wilk-Kołodziejczyk<sup>1,2</sup>, Jadwiga Kamińska<sup>1</sup>

<sup>1</sup> Center of Casting Technology, Łukasiewicz Research Network –  
Krakow Institute of Technology, Poland

<sup>2</sup> AGH University of Science and Technology, Al. Mickiewicza 30, 30-059 Kraków, Poland  
malysza@agh.edu.pl; sabina.puzio@gmail.com;  
katmg@agh.edu.pl; glowacki@metal.agh.edu.pl;  
dwilk@agh.edu.pl; jadviga.kaminska@kit.lukasiewicz.gov.pl

**Keywords:** casting, simulations, ablation, gravity sand casting, gravity die casting, mechanical properties

## 1. Introduction

Simulation process is a preliminary process before performing the real experiment and has already been included in the series of works related to the preparation of a new product manufactured in the casting technology. This approach allows for initial verification, in virtual conditions, of the correctness of the design assumptions. Computer simulations in the process of designing cast parts are already in common use. As a designer tool, they allow for the verification of design assumptions resulting from the nature of the work of the designed part. At the stage of designing the casting technology the possibility of a preliminary evaluation in the means of computer simulations allows to reduce the number of real time tests and prototypes, which allows to reduce costs [1–5]. One of the methods by which you can logically segregate subsequent design steps is the Integrated System for Modelling Materials and Engineering Processes – (ICME). This method is used in various solutions and is described in [6,7]. This consistent approach allows the integration of computer-aided engineering design systems at different levels for design evaluation and manufacturing methods. The presented topic is related to the method of gravity casting into the mould on a sand matrix, which is exposed to water after the filling process. This method is called ablative casting. The essence of the process consists in pouring the metal into sand moulds, which during the solidification of the casting are intensively cooled with water until complete disintegration. In this process, moulds with water-soluble binders are used [8,9]. Numerous authors have confirmed that the microstructure of castings made with this technology is much finer than in the case of the conventional technology of casting aluminium alloys [10-12] By increasing the cooling rate, both the secondary dendrite arm spacing (SDAS) and the size of the eutectic phases are reduced [13–15]. The ablation casting technology is therefore an economic process that enables the production of high-quality castings with a fine structure of dendrites and other secondary phases, characterized by an even distribution. This in turn improves the mechanical properties of the finished castings [16,17].

## 2. Research methodology

Computer simulations were carried out in Flow3D and Flow3D-Cast. Taking into account the process of physical degradation by washing with water flowing from nozzles under pressure

---

The publication is co-financed from the state budget under the programme  
of the Minister of Education and Science called "Excellent Science" project no. DNK/SP/548041/2022



**Doskonała  
Nauka**



Ministry of Education and Science  
Republic of Poland



**Republic  
of Poland**

requires taking into account a number of parameters. The following values of the program data should be introduced, such as: *saturation concentration in fluid, mass transfer coefficient at dissolving surface, solid solute density, mixture density coefficient, molecular diffusion coefficient*. These parameters describe the behaviour of the sand matrix in contact with the water flowing out of the nozzles at a given speed. The computer simulations were conducted in a coupled manner. The mathematical model describing the flow phenomena is not able to take into account two liquids in one analysis. In this case, there is a liquid casting alloy that cools down and solidifies, and there is water washing the sand mould. Therefore, it was assumed to combine the results of ablation simulations, and then, based on the obtained results, to conduct another simulation taking into account casting and solidification. Solidification is modelled on the basis of the chemical composition. The amount of microstructure components formed is predicted numerically as a function of the cooling rate. The analysis is conducted in the macro area and it is simplified. Table 1 shows the list of compound components predicted by numerical simulation [18–20].

**Table 1.** Relationships for calculating the liquidus slopes in AlSi-based alloys [20].

Element	Liquidus slope, ml, l, OC/wt%
Si	$-5.584 - 0.081 \cdot \text{Si} - 9.76\text{E-}04 \cdot \text{Si}^2 - 0.1169 \cdot \text{Cu} + 0.267 \cdot \text{Mg} - 0.1 \cdot \text{Zn} + 0.124 \cdot \text{Fe}$
Cu	$-2.695 + 6.574\text{E-}03 \cdot \text{Cu} - 8.191\text{E-}04 \cdot \text{Cu}^2$
Mg	$-4.033 - 0.088 \cdot \text{Mg} - 0.014 \cdot \text{Cu}$
Zn	$-1.449 + 0.092 \cdot \text{Zn} - 0.0395 \cdot \text{Cu}$
Fe	$-2.891 + 0.09 \cdot \text{Fe} - 0.1048 \cdot \text{Cu}$
Mn	-1.677

The solidification model of the liquid alloy and the change in the proportion of liquid and solid phases with a decrease in temperature is solved by the formula:

$$\rho C_p \frac{\partial T}{\partial t} = \nabla(k\nabla T) + \rho \Delta H_f \frac{\partial f_s}{\partial t} \quad (1)$$

where:  $T$  – temperature [°C],  $t$  – time [s],  $\rho$  – density [kg/m<sup>3</sup>],  $C_p$  – specific heat [J·kg<sup>-1</sup>·K<sup>-1</sup>],  $k$  – thermal conductivity [W·m<sup>-1</sup>·K<sup>-1</sup>],  $H_f$  – latent heat of fusion [J/kg],  $f_s$  – solid fraction.

The simulations are based on the CAD geometry (Figure 1A) and boundary conditions taking into account parameters such as initial temperature of the alloy, die temperature, pouring time, alloy chemical composition, the nozzle location, diameter and velocity of the water for the ablation process of sand mould. Examples of the results of the ablation process simulation are presented in the Figure 1B.

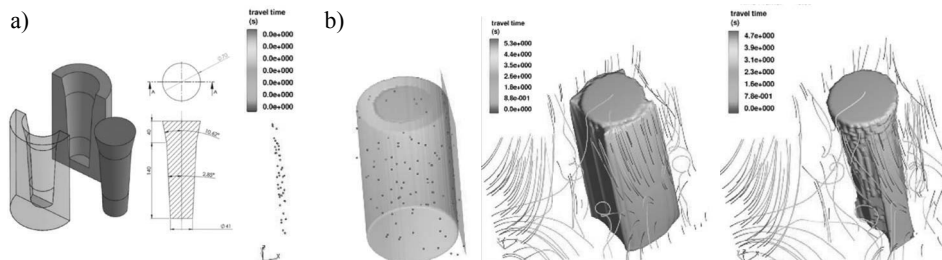


**Figure 1.** a) Model of the ingot and the mould used in the research;  
b) Mould ablation process simulation, red dots represent flow line tracing points.

Determining the value of the heat transfer coefficient is done dynamically by the solver. The calculated value is directly implemented in the next simulation in which the casting and solidification processes are analysed. The pouring temperature in the simulation is  $T_{zal} = 700^{\circ}\text{C}$ , the pouring time  $t_{zal} = 2$  s. Two measuring points were used in the cavity volume of the casting mould, the first in the lower part of the cavity, the second in the middle part. The simulation takes into account the prediction of final mechanical properties in the volume of the ingot. Figure 2 shows the example of a cross-section through a virtual ingot detailing the tensile strength and elongation. Additionally, the SDAS prediction is presented.

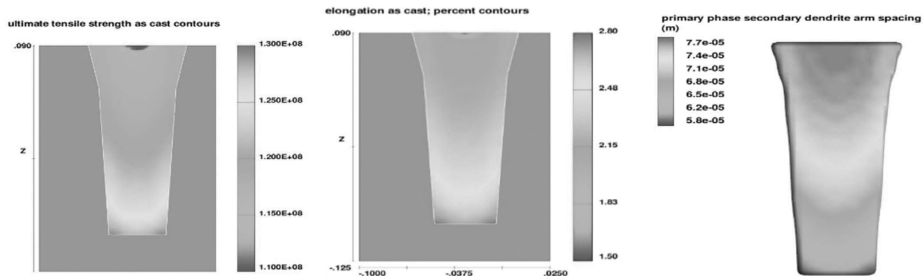


**Figure 2.** Predicted strength properties in the analysed ingot and SDAS for gravity sand casting.

In Figure 3 the comparison of the real ablation and virtual experiment are presented.

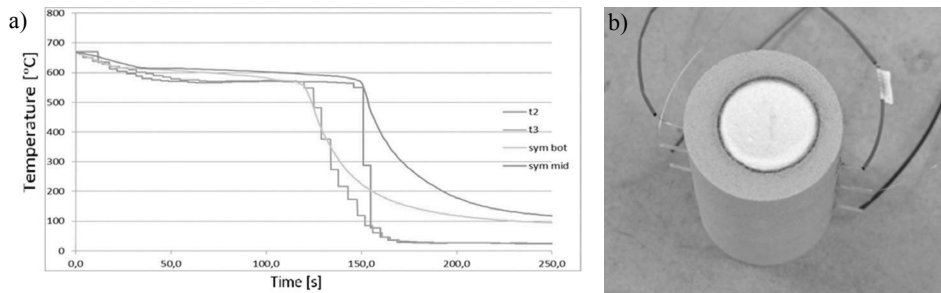


**Figure 3.** a) Comparison of solidification curves for ablation process real and virtual experiment; b) sand mould with thermocouples.

Simulation and real experiment has a good accuracy. The solidification process in the first phase is very similar. The point of quick cooling is very close to each other. The main crystallization and creation of microstructure occurs between  $680^{\circ}\text{C}$  and  $550^{\circ}\text{C}$ . In that temperature range the curves of simulation and real laboratory trial has convergence. Comparison of the simulation predictions of mechanical properties and DAS are presented in the table 2.

**Table 2.** Comparison of the simulation predictions of mechanical properties and DAS.

	Cast		Sim		DAS				Sim			
	Rm, MPa	A%	Rm, MPa	A%	bottom	middle	top	avg.	bottom	middle	top	avg.
Sand	109	0.4	130	2	36.1	45.8	36.3	39.4	45	50	55	50
Die	175	3.3	165	4	56.6	74.5	85.5	72.2	58	71	77	68.6
Ablation	172	2.7	170	5.5	33.5	41.2	42.1	38.9	25	29	33	29

The predicted mechanical properties under simulated conditions differ slightly in terms of tensile strength. The differences in sand casting, die casting and ablation casting successively are 19%, 6%, 2%. The biggest difference in strength prediction was observed for sand casting. Significant discrepancies were weighed in the prediction of elongation. For sand casting, the difference is 4 times, for die casting it is 20%, while for ablative casting the difference is 2 times. The prediction of dendrite growth was also compared. In this case, the mean value depending on the height is 25%, 5%, 26% respectively. The most similar results were obtained in the middle area of the ingot. The numerical model and the research carried out allow us to conclude that it is possible to use a computer program to simulate more complex parts in ablation casting technology. Additional simulations are required to correct the parameters related to the prediction of strength properties, especially elongation.

## References

1. Abro S.H., Shamsi H.A., Wahab S., Mohsin A.: *Design And Development Of Casting Part By Simulation, International Conference on Energy*. Water and Environment – ICEWE-2021 New Campus, University of Engineering and Technology Lahore 31st March 2021, Lahore, Pakistan, 2021, 452.
2. Dojka R., Jezierski J., Campbel J.: *Optimized Gating System for Steel Castings*. Journal of Materials Engineering and Performance, 27, 2018, 5152–5163.
3. Danylchenko L.: *Comparative analysis of computer systems for casting processes simulation*. [in:] International conference advanced applied energy and information technology 2021, Ternopil National Ivan Puluji Technical University, Ukraine, 2021.
4. Deepthi T., Balamurugan K., Uthayakumar M.: *Simulation and experimental analysis on cast metal runs behaviour rate at different gating models*. International Journal of Engineering Systems Modelling and Simulation, 12, 2021.
5. Jayal A.D., Badurdeen F., Dillon Jr O.W., Jawahir I.S.: *Sustainable manufacturing: Modeling and optimization challenges at the product, process and system levels*. CIRP Journal of Manufacturing Science and Technology, 2, 2010, 144–152.
6. Arrazola P.J., Özel T., Umbrello D., Davies M., Jawahir I.S.: *Recent advances in modelling of metal machining processes*. CIRP Annals, 62, 2013, 695–771.
7. Campbell J.: *Castings*. 2<sup>nd</sup> Edition, Butterworth-Heinemann, 2003.
8. United States Patent No. US 7,159,642 B2)
9. Puzio S., Kamińska J., Angrecki M., Major-Gabryś K.: *Effect of the type of inorganic binder on the properties of microwave-hardened moulding sands for ablation casting technology*. Archives of Metallurgy and Materials, 65, 2020, 1385–1390.
10. Dudek P., Fajkiel A., Regula T., Bochenek J.: *Badania nad technologią odlewania ablacyjnego stopów aluminium*. Prace Instytutu Odlewnictwa, tom LIV, 2014.
11. Ananthanarayanan L., Samuel F.H., Gruzelski J.: *Thermal analysis studies of the effect of cooling rate on the microstructure of 319 aluminium alloy*. AFS Trans, 100, 1992, 383–391.
12. Thompson S., Cockcroft L.M., Wells M.M.: *Advanced high metals casting development solidification of aluminium alloy A356*. Materials Science and Technology, 20, 2004, 194–200.
13. Jordon J.B., Wang L.: *Monotonic and Cyclic Characterization of Five Different Casting Process on a Common Magnesium Alloy*. International Manufacturing Science and Engineering Conference, Proceeding ASME, Corvallis, Oregon, USA, 2011, 7–16.
14. Jorstad J.L., Rasmussen W.M.: *Aluminum Science and Technology*. American Foundry Society, 368, 1997, 204–205.
15. Weiss D., Grassi J., Schultz B., Rohagti P.: *Ablation of hybrid metal matrix composites*. Transactions of American Foundry Society, 119, 2011, 35–42.
16. Taghipourian M., Mohammadalilhab M., Boutorabic S., Mirdamad S.: *The effect of waterjet beginning time on the microstructure and mechanical properties of A356 aluminium alloy during the ablation casting process*. Journal of Materials Processing Technology, 238, 2016, 89–95.

17. Grassi J., Campbell J.: *Ablation casting, Aluminum Alloys, Characterization and Applications*. eds, Weimin Y., Subodh K.D., 2010, 73–77.
18. Honda, Press materials: *New Technical Details for the Next Generation of the NSX Model*. SAE 2015 World Congress and Exhibition, 2015.
19. Catalina A.V., Xue L., Monroe C.A.: *A Solidification Model with Application to AlSi-Based Alloys*. Shape Casting, 2019, 201–213.
20. Flow3D-Cast manual, 2021.

# Parametrization of Sieverts' law for gaseous hydrogen solubility using electrochemical experiments – a feasibility study

Andreas Drexler<sup>1</sup>, Jonathan Nietzke<sup>2</sup>, Josef Domitner<sup>1</sup>,  
Klemens Mraczek<sup>3</sup>, Christof Sommitsch<sup>1</sup>, Thomas Böllinghaus<sup>2</sup>

<sup>1</sup> Graz University of Technology, Institute of Materials Science, Joining and Forming, Research Group of Lightweight and Forming Technologies, Inffeldgasse 11/I, 8010 Graz, Austria

<sup>2</sup> Bundesanstalt für Materialforschung und -prüfung (BAM), Department 9 – Component Safety, Unter den Eichen 87, 12205 Berlin, Germany

<sup>3</sup> voestalpine Stahl GmbH, voestalpine-Straße 3, 4020 Linz, Austria

andreas.drexler@tugraz.at, jonathan.nietzke@bam.de,  
josef.domitner@tugraz.at, klemens.mraczek@voestalpine.com,  
christof.sommitsch@tugraz.at, thomas.boellinghaus@bam.de

**Keywords:** Hydrogen embrittlement, Gaseous hydrogen solubility, Sievert's law, Electrochemical equivalent

## 1. Introduction

Hydrogen embrittlement (HE) of steels causing ductility and toughness losses has been a long standing issue in the steel industry [1,2]. However, as hydrogen emerges as a promising secondary energy carrier, resistant structural steels for transmission and storage of high-pressure hydrogen gas become increasingly important. Hydrogen from the gas phase is absorbed at the surface of steel components and diffuses through the lattice by jumping between interstitial sites. As hydrogen atoms are trapped at crystal defects, the hydrogen solubility is strongly affected by the microstructure of the steel. Drexler et al. [3] recently derived a law for hydrogen solubility from generalized thermodynamic potentials considering hydrostatic stresses, trapping and lattice diffusion. While the original Sieverts' law [4] predicts only hydrogen solubility at high temperatures and low pressures, the Drexler's law enables the extrapolation to low temperatures and/or high-pressures. Nevertheless, parametrizing the law of gaseous hydrogen solubility is difficult by using autoclave systems, not least because of the security issues related to handling high-pressure hydrogen gas. Therefore, this work presents a new parametrization approach based on measured thermal desorption spectra from electro-chemically charged samples.

## 2. Materials and methods

### 2.1. Material and experiments

A commercial dual phase (DP) steel with a composite-like microstructure of around 80 % ferrite and 20 % martensite [5] is used to study the hydrogen solubility. The chemical composition and mechanical properties of this steel are given elsewhere [5–7]. As martensite has a higher crystal defect density than ferrite, hydrogen is in homogeneously distributed in the microstructure. Samples of 100×10×1.2 mm were cleaned and subsequently electrochemically charged using three different electrolytes, namely (i) 3.5 vol% NaCl, (ii) 3.5 vol% NaCl + 1 g/L thiourea and

---

The publication is co-financed from the state budget under the programme of the Minister of Education and Science called "Excellent Science" project no. DNK/SP/548041/2022



Doskonała  
Nauka



Ministry of Education and Science  
Republic of Poland



Republic  
of Poland

(iii) 0.5 M  $\text{H}_2\text{SO}_4$  + 1 g/L thiourea. The current density was 0.01 mA/mm<sup>2</sup> and the minimum charging time for achieving hydrogen saturation in bulk was 2 hours. After charging the samples were cleaned with water. Thermal desorption spectra (TDS) were recorded for three heating rates of 0.3 K/s, 0.6 K/s and 1.0 K/s using a Bruker Galileo G8 device equipped with a thermal conductivity sensor. For validation, gaseous hydrogen charging at pressures of 200 bar, 500 bar and 1000 bar was performed for 3 weeks using an autoclave. The diffusible hydrogen content was isothermally measured at 400°C using a Bruker Galileo G8 equipped with a mass spectrometer.

## 2.2. Thermodynamic model

The solubility  $s$  of steel considers the lattice concentration  $c_L$  and the trap concentration  $c_T$  of hydrogen, i.e.,  $s = c_L + c_T$ . The lattice hydrogen atoms are occupying interstitial lattice sites in ferritic/martensitic steels [8], while trapped hydrogen atoms bind at crystal defects, e.g., at carbides, dislocations, vacancies or grain boundaries. In the presence of an outer hydrogen partial pressure, the lattice concentration in the sample can be calculated using Sievert's law:

$$c_L = K_0 \sqrt{f} \exp\left(-\frac{\Delta H_s - \sigma_H V_H}{RT}\right) \quad (1)$$

where  $K_0$  is a constant,  $\sigma_H$  is the hydrostatic stress,  $V_H$  is the partial molar volume,  $R$  is the universal gas constant and  $T$  is the absolute temperature. The fugacity  $f$  is calculated as:

$$f = p_{\text{H}_2} \exp\left(-\frac{p_{\text{H}_2} b}{RT}\right) \quad (2)$$

where  $p_{\text{H}_2}$  is the hydrogen partial pressure and  $b$  is the van der Waals constant. In thermodynamic equilibrium, the trapped hydrogen concentration can be calculated based on Oriani's theory [9]:

$$c_T = \frac{c_L N_T}{N_L \left( K + \frac{c_L}{N_L} (1 - K) \right)} \quad (3)$$

where  $N_T$  is the trap density and  $N_L$  is the density of interstitial lattice sites. The equilibrium constant  $K = \exp\left(-\frac{E_b}{RT}\right)$  depends on the characteristic binding energy  $E_b$  between the hydrogen atom and the crystal defect site.

## 2.3. Parametrization

The thermodynamic model for calculating the gaseous hydrogen solubility is parametrized by fitting measured thermal desorption spectra (TDS) as shown in Figure 1. The inverse fitting procedure is outlined in [10]. The fit parameters and the parameters taken from literature are summarized in Table 1. As shown in Figure 1 the parametrized model is able to describe the heat rate dependency and the influence of the electrolyte using a constant set of trapping parameters.

## 2.4. Validation

The model validation was performed by comparing measured and calculated diffusible hydrogen contents. As shown in Figure 2a, the inversely parametrized thermodynamic model agrees with the measured contents in a broad range of hydrogen partial pressures. The inversely fitted lattice concentrations were different for the three electrolytes. They are compared with the lattice

hydrogen uptake according to Sieverts' law, as shown in Figure 2b. The lattice hydrogen uptake in the NaCl electrolytes and in gaseous atmospheres at pressures of about 10 bar and 390 bar, respectively, are virtually identical, whereas the lattice hydrogen uptake in the  $\text{H}_2\text{SO}_4$  electrolyte and at the pressure of 1330 bar are almost identical.

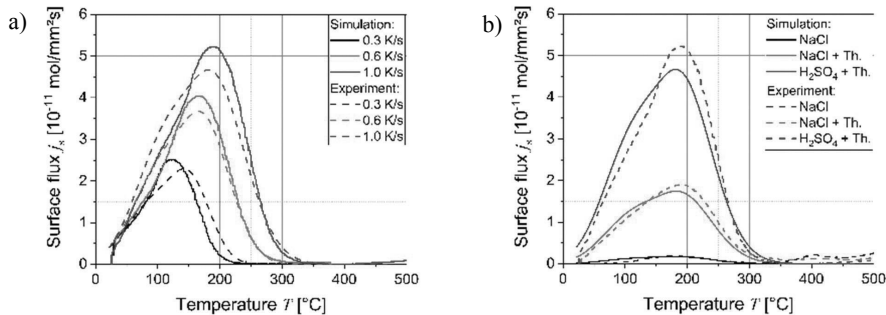


**Figure 1.** Simulated and measured TDS as function of (a) heating rate using  $\text{H}_2\text{SO}_4$  electrolyte and (b) different electrolytes at 1 K/s.

**Table 1.** Summary of the model parameters.

Parameter	Symbol	Unit	Value	Reference
Binding energy	$E_b$	kJ/mol	28.6	inverse parametrization
Trap density	$N_T$	mol/mm $^3$	$2.27 \cdot 10^{-7}$	inverse parametrization
Migration energy	$E_m$	kJ/mol	10	[5]
Jump frequency	$D_{j,0}$	mm $^2$ /s	0.01	[5]
Solution enthalpy	$\Delta H_s$	kJ/mol	27	[11]
Partial molar volume	$V_H$	mm $^3$ /mol	2000	[12]
Density of interstitial lattice sites	$N_I$	mol/mm $^3$	$2 \cdot 10^{-4}$	[9]
Lattice concentration	$c_l$	mol/mm $^3$	see Figure 2b	inverse parametrization
Constant	$K_0$	mol/mm $^3$ MPa $^{0.5}$	$8.17 \cdot 10^{-7}$	based on pure iron [13]
Van der Waals constant	$b$	mm $^3$ /mol	$15.84 \cdot 10^3$	[14]

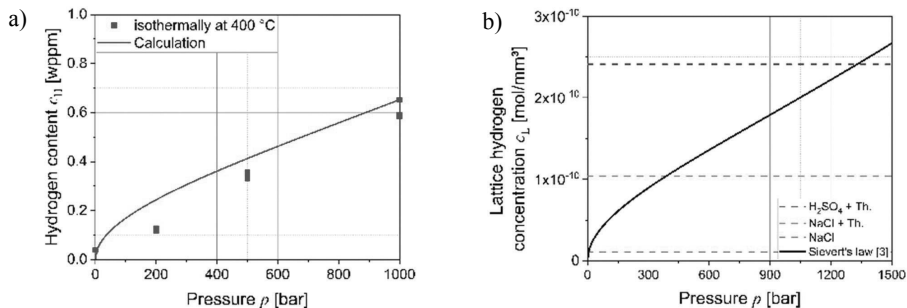


**Figure 2.** a) Comparison of measured and calculated diffusible hydrogen contents. b) Lattice hydrogen concentration as function of hydrogen partial pressure and electrolyte composition.

## References

1. Polyanskiy V.A., Belyaev A.K.: *Advances in Hydrogen Embrittlement Study*. 2021.
2. Nagumo M.: *Fundamentals of Hydrogen Embrittlement*. Springer Singapore, Singapore, 2016.
3. Drexler A., Konert F., Sobol O., Rhode M., Domitner J., Sommitsch C., Böllinghaus T.: *Enhanced Gaseous Hydrogen Solubility in Ferritic and Martensitic Steels at Low Temperatures*. International Journal of Hydrogen Energy, 47, 2022, 39639–39653.
4. Sieverts A.: *Palladium und Wasserstoff. I*. Zeitschrift für Physikalische Chemie, 88U, 1914, 103–127.
5. Drexler A., Helic B., Silvayeh Z., Mraczek K., Sommitsch C., Domitner J.: *The Role of Hydrogen Diffusion, Trapping and Desorption in Dual Phase Steels*. Journal of Materials Science, 57, 2022, 4789–4805.
6. Drexler A., Helic B., Silvayeh Z., Sommitsch C., Mraczek K., Domitner J.: *Influence of Plastic Deformation on the Hydrogen Embrittlement Susceptibility of Dual Phase Steels*. Key Engineering Materials, 926, 2022, 2077–2091.
7. Drexler A., Estilaei H., Helic B., Mraczek K.: *Dependency of Internal Hydrogen Embrittlement on the Hydrogen Distribution in Industrial DP600 Dual Phase Steel*. Proceedings of the SteelyHydrogen, Ghent, 2022, 1–14.
8. Kholobina A.S., Pippin R., Romaner L., Scheiber D., Ecker W., Razumovskiy V.I.: *Hydrogen Trapping in Bcc Iron/* Materials, 13, 2020, 2288.
9. Svoboda J., Fischer F.D.: *Modelling for Hydrogen Diffusion in Metals with Traps Revisited*. Acta Materialia, 60, 2012, 1211–1220.
10. Drexler A., Depover T., Leitner S., Verbeken K., Ecker W.: *Microstructural Based Hydrogen Diffusion and Trapping Models Applied to Fe–C[Sbnd]X Alloys*. Journal of Alloys and Compounds, 826, 2020, 154057.
11. Wipf H.: *Solubility and Diffusion of Hydrogen in Pure Metals and Alloys*. Physica Scripta, T94, 2001, 43.
12. Wagenblast H., Wriedt H.A.: *Dilation of Alpha Iron by Dissolved Hydrogen at 450° to 800°C*. Metallurgical Transactions, 2, 1971, 1393–1397.
13. Quick N.R., Johnson H.H.: *Hydrogen and Deuterium in Iron, 49–506°C*. Acta Metallurgica, 26, 1978, 903–907.
14. Marchi C.S., Somerday B.P., Robinson S.L.: *Permeability, Solubility and Diffusivity of Hydrogen Isotopes in Stainless Steels at High Gas Pressures*. International Journal of Hydrogen Energy, 32, 2007, 100–116.

# Evaluation of the hardware counters for neighbours' selection algorithms in the random cellular automata grain growth model

Mateusz Sitko<sup>1</sup>, Kacper Pawlikowski<sup>1</sup>, Lukasz Madej<sup>1</sup>

<sup>1</sup> AGH University of Science and Technology, Al. Mickiewicza 30, 30-059 Kraków, Poland  
msitko@agh.edu.pl, kpawliko@agh.edu.pl,  
lmadej@agh.edu.pl

**Keywords:** random cellular automata, dynamic recrystallization

## 1. Introduction

The predictive capabilities of classical finite element models are commonly increased using a digital material representation (DMR) concept [1]. Depending on the approach, the whole procedure can be time-consuming and thus drastically increase the computation time of subsequent model runs. The most straightforward approach for preparing DMRs is processing metallographic images acquired by light or electron microscopy. It is particularly effective for 2D studies because it allows even complex microstructures to be directly mapped to a numerical model based, for example, on finite elements, cellular automata, or Monte Carlo methods. Often, however, such models are insufficient, and the inhomogeneities appearing in 3D space require more sophisticated experimental solutions to provide input data. Therefore, to speed up the process of generating DMR data, various algorithmic solutions have been proposed over the years [2–4]. A frequently used method, especially for 3D investigations, is simulating unconstrained grain growth using various cellular automata (CA) algorithms. However, the results' quality can be drastically limited by the regularized nature of the cellular automaton space. A simple grain growth algorithm based on the random cellular automata (RCA) method can be used as a potential solution to provide high-quality DMR for further analysis [5]. However, the most time-consuming part of that approach, the neighbour-search algorithm, should be optimized from an algorithmic point of view before practical application in full-field analysis. Minimizing computation time is crucial because simulations with large amounts of CA cells need to be done in reasonable simulation time. It involves much more effort during model implementation to optimise the algorithm in terms of execution time, which has to be at an acceptable time. The main goal of the current work is to evaluate the hardware counters to establish the capabilities of each implemented method. The presented research has shown that significantly reducing RCA simulation time with the adequately developed neighbour-search algorithm is possible.

## 2. Methodology

The generation of a digital material representation model of single-phase Fe-30Ni alloy characterized by stable austenitic microstructure up to room temperature was selected as a case study (Figure 1). Mentioned RCA approach operates in a mesh-free environment within a dynamic cloud of CA cells. Similarly to the classical CA method, the evolution of CA cell states is directly related

---

The publication is co-financed from the state budget under the programme  
of the Minister of Education and Science called "Excellent Science" project no. DNK/SP/548041/2022



Doskonała  
Nauka



Ministry of Education and Science  
Republic of Poland



Republic  
of Poland

to the definition of transition rules that have to be applied for each cell, knowing all its neighbors (Figure 1a). Therefore, four neighbor-search algorithms dedicated to the RCA method were benchmarked within the work for the algorithm’s complexity and the impact of individual parameters on computational efficiency. The work presents a comparison of the Basic brute-force neighbours search algorithm performance with the developed, more advanced approaches. The first investigated solution is *SortDimension* algorithm [6] which reduces the number of cell comparisons by sorting CA cells according to the selected coordinate axis. The second is a quadtree-based approach (*Quad-Tree*) [7] adapted to the needs of RCA, and finally, the third is *FixedGrid* algorithm in which cells are grouped into specific subregions.

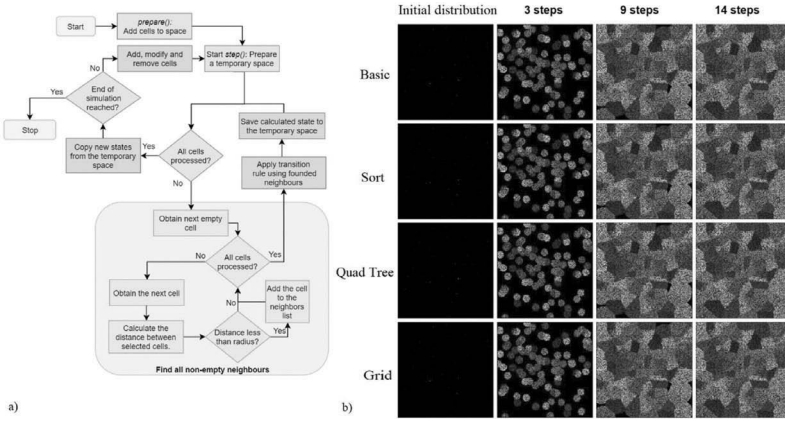


**Figure 1.** a) general flow of the RCA algorithm, b) RCA simulation results in the form of material microstructure from different neighbor searching algorithms.

### 3. Results

In order to calculate the average data transfer from RAM, the PAPI\_L3\_TCM hardware counter and sectional timing were used. The counter mentioned above indicates misses to the L3 cache, which is equivalent to DRAM access. To convert the raw number into bytes, it was multiplied by 64, since, on modern processors, access to memory is done to the entire line, which is most often 64 bytes. The number thus obtained was divided by the time of a given step.

The inspection of branch counters revealed that the smallest number of branch instructions characterized *FixedGridGroup*. This is expected as optimizations incorporated in the algorithms reduced the number of checks. The slowest algorithm has the highest number of conditional branches. Interestingly, the number of accesses to DRAM (misses to L3 cache) was not different among the tested algorithms in the *step()* stage. In the case of *prepare()* stage, the situation is different. The memory on the benchmark machine was DDR4 RAM configured at 2133 MT/s with a bus width of 64bits (single channel). That is around 16GiB/s of theoretical throughput. *FixedGridGroup* algorithm reached a throughput of 7 GiB/s which is only 44% of the theoretical maximal throughput. This stage is not composed only of memory accesses; some minor computations and conditional branches are performed along. This could mean that memory bandwidth is the bottleneck or the algorithm is nearing it.

### 4. Summary

Various approaches and optimization techniques give the possibility to identify the strong and weak sides of neighbor-searching algorithms. For the simple generation of digital microstructure

representation using grain growth algorithm, where cell positions do not change, the method *Fixed-GridGroup* is fastest, as *step()* stage was optimized at the cost of slowing down *prepare()* stage. In the family of *FixedGrid* algorithms, *FixedSubgrid* showed that mitigating performance penalties for large neighborhoods are possible, but no clear methodology to pick the parameter was found. Further analysis using hardware counters allowed us to gather more detailed information about implemented algorithms and revealed potential bottlenecks. In the *step()* stage, speed was seemingly correlated with the number of conditional branches. In the case of *prepare()* stage, the memory bandwidth is the bottleneck.

## References

1. Schmauder S., Schafer I.: *Multiscale Materials Modeling: Approaches to Full Multiscale*. Walter De Gruyter, 2016.
2. Yang H., Wu C., Li H., Fan X.: *Review on cellular automata simulations of microstructure evolution during metal forming process: Grain coarsening, recrystallization and phase transformation*. Science China Technological Sciences, 54, 2011, 2107–2118.
3. Pal P., Abhishek G.S., Karagadde S.: *A Monte Carlo approach to simulate dendritic microstructures during binary alloy solidification*. Modelling and Simulation in Materials Science and Engineering, 28, 2020, 0–17.
4. Van Nuland T.F.W., Palmeira Belotti L., Van Dommelen J.A.W., Geers M.G.D.: *A novel 3D anisotropic Voronoi microstructure generator with an advanced spatial discretization scheme*. Modelling and Simulation in Materials Science and Engineering, 29, 2021.
5. Czarnecki M., Sitko M., Madej Ł.: *The role of neighborhood density in the random cellular automata model of grain growth*. Computer Methods in Materials Science, 21, 2021, 1–10.
6. Baskett F., Shustek L.J.: *An Algorithm for finding nearest neighbors*. IEEE Transactions on Computers, C-24, 1975, 1000–1006.
7. Samet H.: *The Quadtree and related hierarchical data structures*. ACM Computing Surveys, 16, 1984, 187–260.

**Acknowledgements.** The financial assistance of the National Science Centre project No. 2019/35/B/ST8/00046 is acknowledged. This research was supported in part by PLGrid Infrastructure.

# Application of Finite Element Method based simulations and metamodeling techniques for prediction of liquid steel cooling rate in main ladles

Łukasz Rauch<sup>1</sup>, Monika Pernach<sup>1</sup>,  
Michał Piwowarczyk<sup>2</sup>, Łukasz Sztangret<sup>1</sup>

<sup>1</sup> AGH University of Science and Technology, Al. Mickiewicza 30, 30-059 Kraków, Poland  
2 CMC Poland Sp. z o.o., Piłsudskiego 82, 42-400 Zawiercie, Poland  
lrauch@agh.edu.pl, pernach@agh.edu.pl,  
Michal.Piwowarczyk@cmc.com, szt@agh.edu.pl

**Keywords:** steelmaking process, molten steel temperature, heat transfer, numerical modelling, data filtering

## 1. Introduction

Measurements of temperature distribution of liquid steel inside a ladle is very difficult or sometimes even impossible task in industrial conditions, due to the safety reason and high cost of equipment. On the other hand precise knowledge about the overheating level is crucial to maintain optimal range of temperatures during Continuous Steel Casting process to obtain the highest quality of casted billets.

This paper is focused on the description of the system for the real time prediction of the liquid steel temperature in the ladle based on the FEM model. Results of simulations were verified with measurements performed in the production line, which were filtered using the Weibull distribution. It was shown that the model correctly predicts the temperature of liquid steel. The mean relative error of the calculations was in the range: 0.12–0.18.

### 1.1. Numerical model

Model describes the heat transfer in molten steel during transport of the ladle between the stations: refining - tundish. Scheme of the ladle was shown in Figure 1, while both its shape and dimensions correspond to the real ones. The side wall of the ladle consists of three layers of different materials in order to meet specific mechanical and thermal requirements: steel shell (1), safety insulation layer (2) and working lining (3), the thicknesses of which are 0.028, 0.101, and 0.203 m, respectively. The weight of the molten steel was 150 tons. Input data, including: temperature of molten steel measured after the refining process, temperature of ladle armor and transport time, were received from the monitoring system.

The values of the thermophysical parameters introduced into the model are summarized in Table 1. The data for the lining came from the material cards. The thermal conductivity coefficient  $\lambda$  of the slag was determined on the basis of experimental studies. The specific heat and emissivity data for each of the materials were literature data [1,2].

---

The publication is co-financed from the state budget under the programme of the Minister of Education and Science called "Excellent Science" project no. DNK/SP/548041/2022

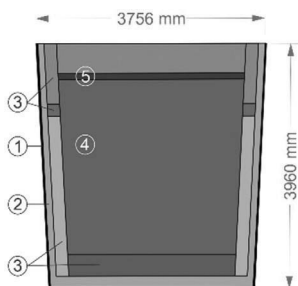


**Figure 1.** Scheme of the ladle furnace: 1 – armor, 2 – insulation layer, 3 – lining, 4 – molten steel, 5 – slag.

**Table 1.** Thermophysical parameters.

Material	Temperature	Density	Thermal conductivity	Heat capacity	Emissivity	
	°C	ton/mm <sup>3</sup>	W/mm·K	J/ ton·K	—	
Ladle armor	measurement	$7.80 \cdot 10^{-9}$	$5,20 \cdot 10^{-2}$	787 000	0.8	
Insulation	1 000	$2.75 \cdot 10^{-9}$	$9,50 \cdot 10^{-4}$	1 056 000	0.75	
Lining	ANCARBON C SIT12-EU	1 100	$2.96 \cdot 10^{-9}$	$8,00 \cdot 10^{-3}$	800 000	0.75
	SYNCARBON C F7T05P	1 100	$3.04 \cdot 10^{-9}$	$6,00 \cdot 10^{-3}$ (1 000°C) $5,00 \cdot 10^{-3}$ (1 200°C)	800 000	0.75
	SINDOFORM C-EU	1 100	$2.90 \cdot 10^{-9}$	$3,00 \cdot 10^{-3}$	800 000	0.75
	SINDOFORM C5-EU	1 100	$2.88 \cdot 10^{-9}$	$3,50 \cdot 10^{-3}$	800 000	0.75
Molten steel	measurement	$7.10 \cdot 10^{-9}$	$4,10 \cdot 10^{-2}$	750 000	—	
Slag	measurement	$3.81 \cdot 10^{-9}$	$1,21 \cdot 10^{-2}$	838 000	0.8	

The FEM solution of the Fourier equation (1) was carried out in the 2D system using Abaqus.

$$\rho c_p \frac{\partial T}{\partial t} = \frac{\partial}{\partial x} \left( k_x \frac{\partial T}{\partial x} \right) + \frac{\partial}{\partial y} \left( k_y \frac{\partial T}{\partial y} \right) \quad (1)$$

where:  $\rho$  – the material density,  $c_p$  – the specific heat of the material,  $k_x$ ,  $k_y$  – coefficient of heat conduction of material.

The following boundary conditions were assumed in the model: the temperature of the inner surface of the ladle is equal temperature of the molten steel, heat transfer inside liquid steel, insulation layer and lining carried out by conduction, heat transfer from the outer surface of the ladle and the slag layer occurs by convection  $q_c$  and radiation  $q_r$  (2).

$$\begin{aligned} q(y, t) &= q_c(y, t) + q_r(y, t) \\ q_c(y, t) &= \lambda (T_e(y, t) - T) \\ q_r(y, t) &= \varepsilon \delta (T^4(y, t) - T_e^4) \end{aligned} \quad (2)$$

where:  $\lambda$  – convective heat transfer coefficient,  $\varepsilon$  – emissivity,  $\delta$  – Stefan-Boltzman constant,  $T_e$  – ambient temperature.

## 2. Results

Numerical simulations were carried out for the following steel grades: B500SP, S355J2, S235JR, STRETCH500, B500B, C45E, 30MnB4, 16MnCr5. The temperature distribution in the molten steel is presented in Figure 2. In all the analyzed cases, the temperature drop was observed only under the slag layer and in the contact zone with the ladle lining.

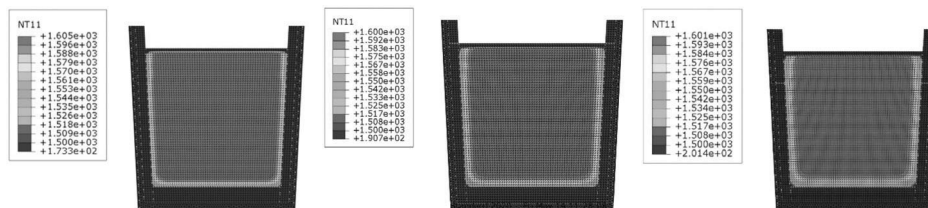


**Figure 2.** Temperature distribution in the molten steel – 16MnCr5 steel: a) melt I – 1587°C, 19 min, b) melt II – 1570°C, 18 min, c) melt III – 1607°C, 10 min.

The obtained results were compared with measurement data from the process monitoring system (Figure 3). The data was filtered using the Weibull distribution [3], because reliability tests have shown that 6.5% of the data is burdened with a gross error. The cooling rate varied within the range of 1.18°C/min for STRETCH500 steel and 1.39°C/min for 16MnCr5 steel. The mean relative error of the calculations was in the range: 0.12–0.18.

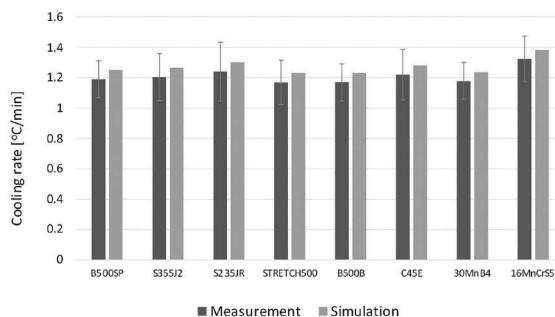


**Figure 3.** Cooling rate of liquid steel – comparison of calculated (orange column) and filtered measurement data (blue column).

## 3. Conclusions

The model allows the determination of liquid steel cooling rate in main ladle. Measurements of temperature in the tundish confirm the correctness of the model. Due to the long computation time ~35 min, it is necessary to create a metamodel that will enable the use of the prediction model in industrial conditions.

## References

1. Santos M.F., Moreira M.H., Campos M.G.G., Pelissari P.I.B.G.B., Angélico R.A., Sakoa E.Y., Sinnema S., Pandolfelli V.C.: *Enhanced numerical tool to evaluate steel ladle thermal losses*. *Ceramics International*, 44, 2018, 12831–12840.

2. Xia J.L., Ahokainen T.: *Transient Flow and Heat Transfer in a Steelmaking Ladle during the Holding Period*. Metallurgical and Materials Transactions B, 32, 2001, 733–741.
3. Luko S.N.: *A Review of the Weibull Distribution and Selected Engineering Applications*. SAE Technical Paper, 1999.

**Acknowledgements.** Financial support of the NCBiR, Project No. POIR.01.01.01-00-0996/19, is acknowledged.

# Model of heat transfer in High Frequency Welding – numerical approach and laboratory investigation

Ivan Milenin<sup>1</sup>, Monika Pernach<sup>1</sup>, Łukasz Rauch<sup>1</sup>,  
Bogdan Pawłowski<sup>1</sup>, Dorota Tyrała<sup>1</sup>

<sup>1</sup> AGH University of Science and Technology, Al. Mickiewicza 30, 30-059 Kraków, Poland  
imilenin@agh.edu.pl, pernach@agh.edu.pl,  
lrauch@agh.edu.pl, bpawlow@agh.edu.pl, dtyrala@agh.edu.pl

**Keywords:** high frequency welding, heat transfer, numerical modelling, finite element method

## 1. Introduction

Numerical model of the process of high-frequency (HF) pipes welding was presented in this paper. The thermomechanical analysis in the 3D was carried out using FEM. The influence of the welding speed, frequency, and voltage on the quality of welded joint was investigated. The simulations performed for pipe profiles of various diameters made of S355 and S420 steel allowed to determine the heat-affected zone. Measurement of the temperature in the production line was used to verify the correctness of the model. The obtained results allowed to formulate the optimal process parameters.

### 1.1. Numerical model

Process of high frequency welding of closed profiles consists of the mechanical forming of a steel strip, and then joining the edges of the sheet by fast, local induction heating to the range of high plasticization, followed by pressing them with rollers (Fig. 1a). The joint formed by welding has a key impact on the strength of the product. It is particularly important when round profiles are intended for friction anchors used in the construction and mining industries, which, after installation in the rock mass, are expanded with water under a pressure of approx. 300 bar.

The quality of the weld is strictly dependent on the mechanical factors, such as the geometry of the welding area, the size of the Vee angle, as well as electrical factors, including frequency, voltage and current, which determine the welding temperature. It is precisely the maintenance of the welding temperature at the level of approx. 1350°C is the main task of the manufacturing process. Too high temperature increases the range of the heat-affected zone, leads to grain growth and deterioration of the strength properties of the material. When the temperature is too low, due to insufficient plasticization of the edges, there is a risk of a significant deterioration of the durability of the resulting seam, including the appearance of the “open seam” defect. A properly made weld should have the shape of hourglass with a possible thin decarburized layer in the weld axis. Optimum fracture toughness is ensured by the microstructure of the fine acicular ferrite [1,2].

HF welding of pipes is a complex, dynamic process in which the occurring thermomechanical phenomena combine mechanical, electrical, thermal and metallurgical factors. Performed numerical analysis taking into account the coupling of the electromagnetic field with the thermal field by

---

The publication is co-financed from the state budget under the programme  
of the Minister of Education and Science called “Excellent Science” project no. DNK/SP/548041/2022



solving the Maxwell (1) and Fourier (2) equations. The general scheme of the algorithm is shown in Figure 1b. The electrical solution generates a heat source (Joule Heat) that sets the boundary condition in the thermal solution. Thermal analysis includes simulation of heat losses by radiation and convection from open surfaces of the pipe. The solution in the 3D was realized using FEM on the basis of program package ANSYS.

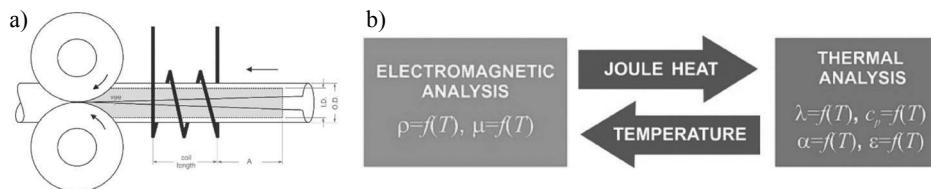


**Figure 1.** a) Schematic diagram of HF welding of pipes, b) algorithm of transient coupled electromagnetic-thermal analysis.

The electromagnetic field is described by Maxwell equation in the form:

$$\nabla \times \vec{B} = \vec{\mu}j + \mu\varepsilon \frac{\partial \vec{E}}{\partial t} \quad (1)$$

where:  $\vec{B}$  – magnetic field intensity,  $\mu$  – magnetic permeability,  $j$  – current density,  $\varepsilon$  – electric permittivity,  $E$  – electric field intensity.

The transient thermal field is determined from the Fourier equation (2):

$$\rho C \frac{\partial T}{\partial t} + \nabla(-k\nabla T) = Q \quad (2)$$

where:  $k$  – thermal conductivity,  $\rho$  – density,  $C$  – specific heat,  $Q$  – heat source, obtained from electromagnetic field analysis.

Boundary conditions of convection and radiation applied on the outer surface of the pipe:

$$q_{conv} = h(T - T_{int}) \quad (3)$$

$$q_{rad} = \varepsilon\sigma(T - T_{int}) \quad (4)$$

where:  $h$  – heat transfer coefficient,  $T_{int}$  – external bulk temperature.

## 2. Results

The simulations performed for pipe profiles of various diameters made of S355 and S420. The model takes into account the process parameters: power, current frequency and material data: thermal and electrical (table I). Results of numerical simulations of HF welding are presented in Figure 2–3. the welding temperature determined from the model covered the range 1196–1353°C.

**Table 1.** Thermal and electrical parameters.

	Specific heat, J/kg·K	Thermal conductivity, W/m·K	Thermal expansion, K <sup>-1</sup>	Electrical conductivity, S/m	Resistance, Ω·m
S355	680	44	16.2·10 <sup>-6</sup>	2·10 <sup>6</sup>	10·10 <sup>-8</sup>
S420	470	41	13.2·10 <sup>-6</sup>	2·10 <sup>6</sup>	10·10 <sup>-8</sup>

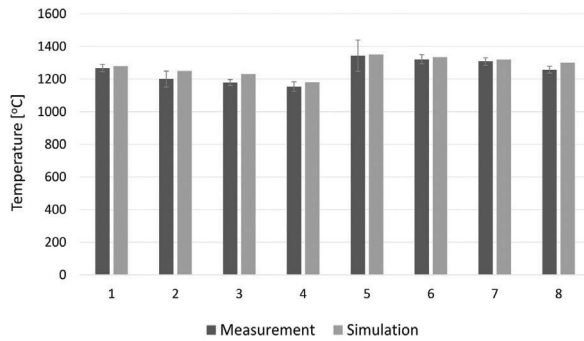


**Figure 2.** Comparison of calculated (orange column) and measured (blue column) temperature of weld.

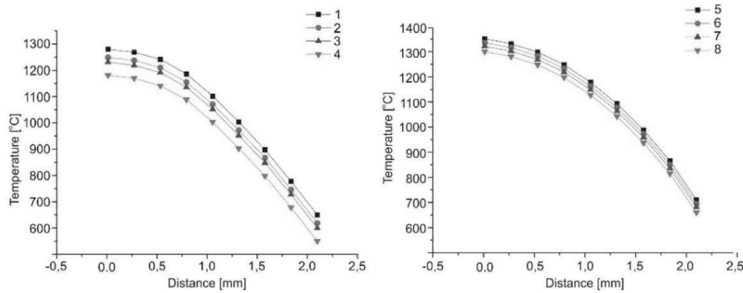


**Figure 3.** Calculated temperature gradient in the heat affected zone.

### 3. Conclusions

The model allows the determination of the temperature of the weld and temperature gradient in the heat-affected zone for variable process parameters process parameters: power, frequency, profile diameter. Measurements of temperature made in the technological line confirm the correctness of the model. As a result, the model can be used to optimize the HF welding process.

### References

1. Christian E., Lüchinger M., Schreiner M., Tillmann W.: *Numerical Simulation of Tube Manufacturing Consisting of Roll Forming and High-Frequency Induction Welding*. Materials, 15, 2022, 1270–1284.
2. Nikanorov A., Baake E., Brauer H., Weil C.: *Approaches for Numerical Simulation of High Frequency Tube Welding Process*. International Conference on Heating by Electromagnetic Sources 2013 (HES-13), Padua, 2013.

**Acknowledgements.** The work is financed by National Centre for Research and Development within a project no. POIR.01.02.00-00-0091/19.

# Distributed system for monitoring of welding processes and prediction of final products quality

Krzysztof Regulski<sup>1</sup>, Łukasz Rauch<sup>1</sup>, Krzysztof Bzowski<sup>1</sup>,

Piotr Hajder<sup>1</sup>, Monika Pernach<sup>1</sup>, Jan Kusiak<sup>1</sup>

<sup>1</sup> AGH University of Science and Technology, Al. Mickiewicza 30, 30-059 Krakow, Poland

regulski@agh.edu.pl, lrauch@agh.edu.pl,  
kbzowski@agh.edu.pl, phajder@agh.edu.pl,  
pernach@agh.edu.pl, kusiak@agh.edu.pl

**Keywords:** high frequency induction welding, industry 4.0, process monitoring, non-destructive investigation

## 1. Introduction

Products welded linearly in high frequency induction process, like pipes or sheet-metal sections, are nowadays a major part of the market of customers from construction, furniture and mining industry, where the most important products are bolts and bended elements. These products are usually crucial from safety point of view, therefore online monitoring and investigation of their quality is of the highest importance. Currently testing of products mechanical properties is performed only selectively. This approach is mutual for all the companies producing welded section, but it does not guarantee that all products are tested and free of defects. The main problem of online investigation is significant velocity of the manufacturing process and its conditions precluding stable measurements. Up till now, there is no company in the world which implemented fully automated non-destructive investigation of products quality and control of the process. Thus, the main objective of the project was development of the hybrid system allowing non-destructive online investigation based on sensors monitoring manufacturing devices supported by numerical procedures, analyzing stability of the process and predicting properties of the welded products. The set of monitoring sensors were equipped with thermovision and optical cameras, Hall-effect measuring devices and others. Numerical procedures will be realized by using data mining and machine learning methods mapping state of the process and product properties. Realization of such process maps required series of laboratory experiments, which were performed in one of the project stages. Additionally, sensitivity analysis was applied after experiments and maps creation to confirm, which parameter of the process has the highest influence on the properties of the product. The proposed approach is convergent with augmented intelligence [1–3], supporting human work as a domain expert with experience of highly qualified engineers.

## 2. System architecture

### 2.1. Main idea of the system

The proposed system is based on Industry 4.0 idea integrating monitoring of sensors reading process parameters and modelling of the products quality on the basis of numerical models or metamodels. The software design includes a physical data acquisition module – one at each aggregate

---

The publication is co-financed from the state budget under the programme of the Minister of Education and Science called "Excellent Science" project no. DNK/SP/548041/2022



**Doskonała  
Nauka**



Ministry of Education and Science  
Republic of Poland



**Republic  
of Poland**

(main production device). The data are exchanged between the aggregate and a server with storage module. The main task of the data acquisition module is to operate the software that communicates directly with the PLCs and other sensors (monitoring devices) operating at an aggregate. Each type of sensor has a separate communication interface, for which software had to be implemented. The system design includes the ability to communicate with:

- PLCs using UNIX sockets (binary telegrams),
- an industrial printer using UNIX sockets (XML messages),
- MSSQL database - start-stop (ODBC communication),
- defectomat (limited, local ODBC communication),
- Basler high-speed camera (communication via dedicated device SDK),
- scanCONTROL line scanner (communication via dedicated device SDK).

Each communication module receives a data packet from the device, performs data analysis and/or executes local transformation if required, and then publishes it to the Apache Kafka communication bus. Apache Kafka is a message broker capable of handling real-time data from multiple nodes, offers stream processing mechanisms and allows multiple technologies to be combined into a cohesive and reliable information system. According to the nomenclature of the Kafka environment, each communication module is a data producer. Data is read from the broker by consumers (programmes listening to messages published on the broker). In the system, the main data consumer is the TimescaleDB database, a PostgreSQL-based solution designed to handle time series.

TimescaleDB provides number of functionalities focused on continuous aggregation and filtering of data using materialised views (MATERIALIZED VIEW). A materialised view is a type of special table that stores the results of a query aggregating data. The primary use for materialised views is in the results of spatial analyses, which require a lot of time and computational power to compute. Materialised view data is retrieved from persistent storage (disk), and is not generated on demand like classic SQL views.

## 2.2. Visualization and main Graphical User Interface

The user interfaces is divided into main part dedicated for managers and module for operators. The main view is refreshed at 1-minute intervals and includes data changed in the last hour. If the view is used to aggregate actual data, aggregation will be performed on demand. Similar views have been implemented for each device from which the system acquires data. In order to speed up readings, the data in the database has been split into historical and current data. Current data is stored on a fast SSD and historical data is moved to a slower HDD. Data older than one month is considered historical. The data archiving task has been implemented as a Postgres database stored procedure and is run daily.

Data presentation is handled by a dedicated web service implemented using the NodeJS environment and the NestJS library in TypeScript. The communication architecture with the application's browser client is based on GraphQL technology. GraphQL is a flexible way of communicating between the client and server application, in which the client decides what data it needs to perform a given task in the user interface. Communication is based on a central access point and is distinguished by a strongly typed schema (communication is based on data in a well-defined type). GraphQL supports a subscription mechanism based on WebSockets, enabling real-time communication. This functionality has been used to develop a view of both the current operating status of the selected aggregate and the items currently produced. The client application subscribing to the events is informed in real time of any change on the server side. This treatment was dictated by the lack of stable support for implementing message consumption mechanisms directly from the Apache Kafka broker in web browsers. The client application was implemented using the React library and adapted to work in web browsers. The design of the client application was divided into 4 panels. An example of the application's screen content is shown in Figure 1.

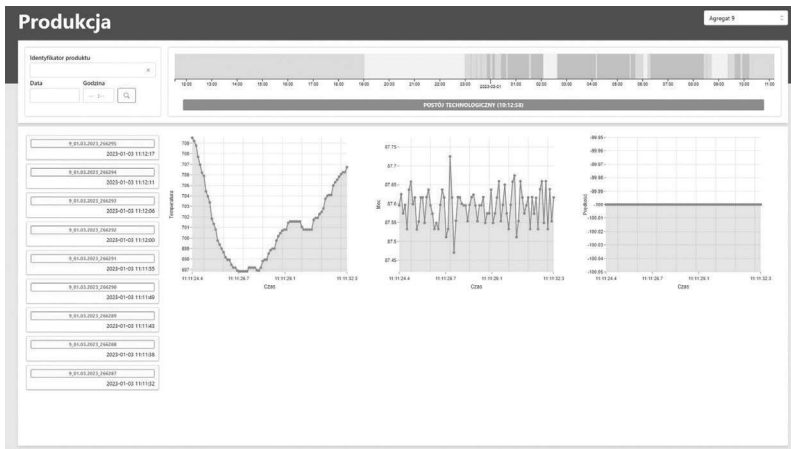


**Figure 1.** The main interface for users managing and monitoring production.

### 2.3. Support of operators

Part of the system supporting operators of the process is built on WebWorker and WebAPI architecture – in the background, data is downloaded using the hardware manufacturer’s library functions, at a set sampling rate, processed, filtered and sent to a message broker (Apache Kafka) from where it is transferred to the database. The application client has been implemented using the React library with unattended use in mind. This means that it will attempt to retransmit data intermittently every 60 seconds if sensor reading errors are detected or a failure occurs or there is a power failure. This decision was dictated by the requirement for implementation on the production floor, where the prevailing conditions are not conducive to operating the application using peripherals such as a mouse or keyboard. The user interface was implemented with modularity and flexibility in mind. Data from each sensor is displayed in a separate independent component, making system development and maintenance easy. Also, failures of individual devices do not bring the client application to a halt. The connection of each visualization component to the corresponding data source is asynchronous and independent of the others. If data cannot be displayed, the component will display an appropriate error message and attempt to establish a connection until successful. An example of working operator’s GUI is shown in Figure 2.

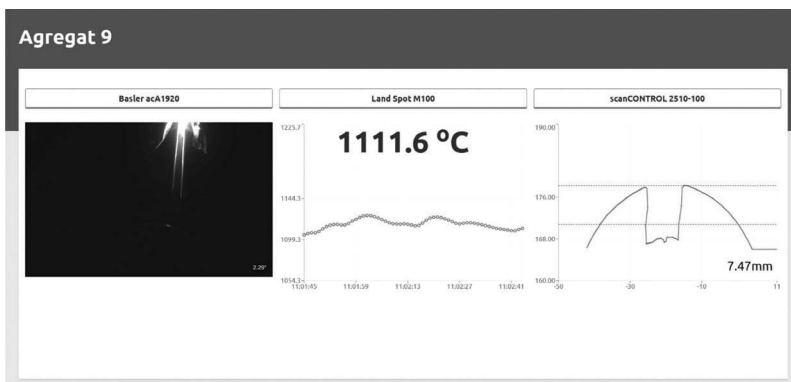


**Figure 2.** Additional graphical interface for users operating the process.

## References

1. Jan Z., Ahamed F., Mayer W., Patel N., Grossmann G., Stumptner M., Kuusk A.: *Artificial intelligence for industry 4.0: Systematic review of applications, challenges, and opportunities*. Expert Systems with Applications, 216, 2023, 119456.
2. Alicioglu G., Sun B.: *A survey of visual analytics for Explainable Artificial Intelligence methods*. Computer&Graphics, 102, 2022, 502–520.
3. Arrieta A.B., Díaz-Rodríguez N., Del Ser J., Bennetot A., Tabik S., Barbado A., Garcia S., Gil-Lopez S., Molina D., Benjamins R., Chatila R., Herrera F.: *Explainable Artificial Intelligence (XAI): Concepts, taxonomies, opportunities and challenges toward responsible AI*. Information Fusion, 58, 2020, 82–115.

**Acknowledgements.** The work is financed by National Centre for Research and Development within a project no. POIR.01.02.00-00-0091/19.

# Fast model of phase transformations for cooling of Pyroware 53 steel

Łukasz Rauch<sup>1</sup>, Władysław Zalecki<sup>2</sup>, Bogdan Garbarz<sup>2</sup>,  
Krzysztof Raga<sup>3</sup>, Krzysztof Bzowski<sup>1</sup>, Maciej Pietrzyk<sup>1</sup>

<sup>1</sup> IAGH University of Science and Technology, al. Mickiewicza 30, 30-059 Kraków, Poland

<sup>2</sup> Łukasiewicz Research Network, Institute for Ferrous Metallurgy,  
ul. K. Miarki 12, 44-100 Gliwice, Poland

<sup>3</sup> Pratt & Whitney Rzeszów S.A., ul. Hetmańska 120, 35-078 Rzeszów, Poland  
lrauch@agh.edu.pl, wladyslaw.zalecki@imz.pl,  
Bogdan.Garbarz@imz.pl, Krzysztof.Raga@pwrze.utc.com,  
kbzowski@agh.edu.pl, maciej.pietrzyk@agh.edu.pl

**Keywords:** Pyrowear 53, phase transformations, fast model, identification, validation

## 1. Introduction

Gear wheels are important parts of the airplane engines, in particular as helicopter transmission gears, and their properties are critical for the safety of passengers. Among materials, which meet the severe requirements, Pyrowear 53 steel seems to be the most popular. This is a carburizing steel possessing good temper resistance and high hot hardness while maintaining high core impact strength and fracture toughness. It is characterized by good wear resistance and fracture resistance in cycling loading [1]. The exceptional properties of this steel are obtained in thermo-chemical treatment composed of carbonizing followed by austenitizing annealing, quenching, freeze-branding and low temperature tempering. While low pressure vacuum carburizing is generally used [1,2], high pressure process is under investigation by many researchers [3]. There is the fundamental difference between the liquid and gas quenching. It has been proven that gas quenching with constant heat transfer coefficient cannot generate the similar cooling rates compared to liquid quenching [4]. Thus, design of this new process requires numerical models, which describe heat exchange between furnace atmosphere and the part as well as phase transformations during cooling. Advanced CFD (Computer Fluid Dynamics) software has to be used in the microscale. These programs are characterised by very high computing costs. On the other hand, both models (macro CFD and micro phase transformations) have to be coupled as shown in [5]. It means that reduction of the computing costs of the phase transformation model is crucial for the effectiveness of the simulations. Thus, development of the fast and reliable phase transformation model for the Pyrowear 53 steel was the main objective of our work.

## 2. Model and results

Two models were considered and compared regarding their reliability and effectiveness. The first was an upgrade of the well-known JMAK (Johnson-Mehl-Avrami-Kolmogorov) equation:

$$X = 1 - \exp(-kt^n) \quad (1)$$

where:  $t$  – time,  $X$  – volume fraction of a new phase,  $k$ ,  $n$  – coefficients.

---

The publication is co-financed from the state budget under the programme  
of the Minister of Education and Science called "Excellent Science" project no. DNK/SP/548041/2022



**Doskonała  
Nauka**



Ministry of Education and Science  
Republic of Poland



**Republic  
of Poland**

The upgrade of this equation composed [6]: i) Coefficient  $k$  depends on the temperature and the grain size. Modified Gauss function proposed in [7] was used for the temperature and power function was used for the grain size; ii) Equilibrium carbon and molybdenum concentration in the austenite was calculated accounting for precipitation of carbides, mainly  $M_6C$ . Equation describing kinetics of precipitation during cooling was introduced; iii) Effect of the current composition of the austenite on the bainite start ( $B_s$ ) and martensite start ( $M_s$ ) temperatures was accounted for.

The second model is based on the Leblond equation [8]. The main assumption of Leblond was that the rate of the transformation is proportional to the distance from the equilibrium:

$$\frac{dX}{dt} = k(X_{eq} - X) \quad (2)$$

In equation (2)  $X_{eq}$  is an equilibrium volume fraction of the considered phase, which for ferrite is a function of the temperature:

$$X_{eq}(T) = \frac{c_{\gamma\alpha}(T) - c_0}{c_{\gamma\alpha}(T) - c_\alpha(T)} \quad (3)$$

where:  $c_0$  – carbon concentration in the steel,  $c_{\gamma\alpha}$ ,  $c_{\gamma\beta}$  – carbon concentration in the austenite at the  $\gamma/\alpha$  and at the  $\gamma/cementite$  interface, respectively. These equilibrium carbon concentrations were calculated using ThermoCalc software.

Equilibrium volume fractions for pearlite and bainite are equal 1. Similarly to the JMAK model, coefficient  $k$  in equation (2) depends on the temperature and the grain size. Since equation (2) is the 1st order differential equation, the incubation time has to be introduced to account for the delay of the material response due to nucleation. Identical equations are used for ferrite, pearlite and bainite transformations but the coefficients are different. The incubation time is calculated from the equation:

$$\tau(T) = a_i D_\gamma^{n_2} \exp\left(\frac{a_3}{RT_K}\right) \frac{1}{(T_s - T)^{n_4}} \quad (4)$$

In both models  $X$  represents volume fraction of each phase with respect to the maximum volume fraction of this phase in given temperature ( $X \in [0,1]$  for each phase) and  $F$  represents volume fraction of each phase with respect to the whole volume of the material, what means that  $\sum_{i=1}^n F_i = 1$  ( $i$  represents ferrite, pearlite, bainite and martensite).

Thus, for each phase we have  $F = X_{eq} X$ . Both models contain several material coefficients, which had to be determined for the steel Pyrowear 53. Inverse algorithm developed by the Authors in [6] was used for an identification of the coefficients on the basis of results of dilatometric tests performed at various cooling rates. The tests were carried out for the samples with the nominal chemical composition of the Pyrowear 53 (0.065% C, 0.38% Mn, 1% Cr, 2% Ni and 0.86% Si) and for the samples with the 1% of carbon. The former supplied the data for identification of the phase transformation models for the core of the gear and the latter for the carburised material of the teeth. Various preheating cycles before the tests were applied and, as a consequence, various grain size prior to transformations was obtained. In consequence grain size could be introduced as a variable in the model.

Numerical tests have shown that the predictions of the models are close to each other, therefore, the results for the JMAK only are presented below. Selected results of the validation of the models are shown in Figure 1. Validation confirmed very good accuracy of both models.

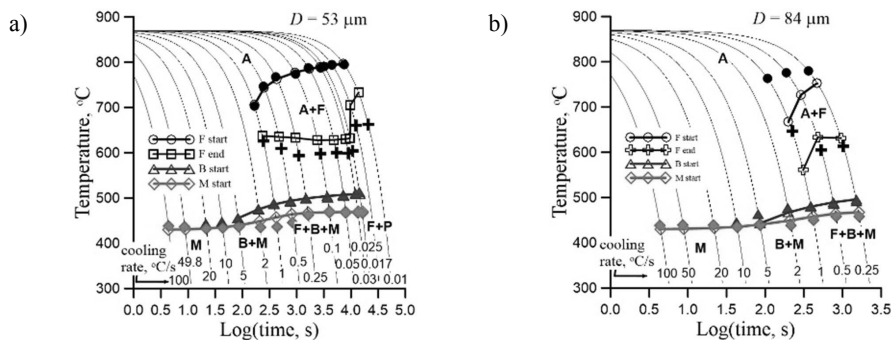


**Figure 1.** Measured (full symbols) and calculated (open symbols) start and end temperatures of phase transformations in the CCT tests for the grain size  $53 \mu\text{m}$  (a) and  $84 \mu\text{m}$  (b).

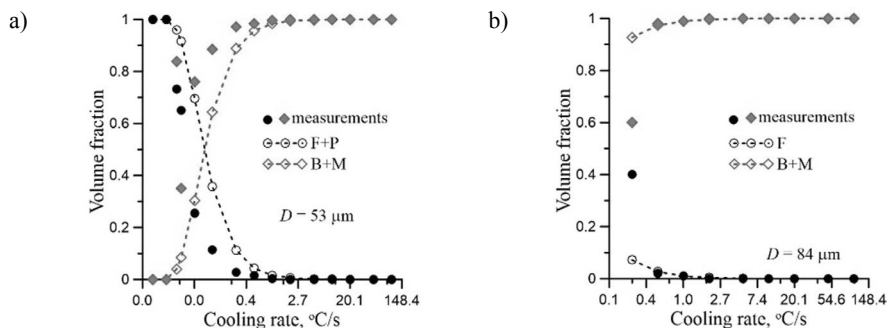


**Figure 2.** Measured (full symbols) and calculated (open symbols) volume fractions of phases for the grain size  $53 \mu\text{m}$  (a) and  $84 \mu\text{m}$  (b).

The following conclusions were drawn on the basis of experimental results and numerical modelling: i) Precipitation of carbides, in particular M<sub>6</sub>C, has influence on the phase transformation in the Pyrowear 53. Therefore, changes of the carbon and molybdenum concentration were accounted for in the model; ii) Kinetics of the phase transformations was simulated using upgrades of the JMAK and Leblond models. Both models gave good results comparable with the experiments. The Leblond model, which does not need application of the additivity rule, was selected as better for coupling with the FE software; iii) The critical cooling rate for the core samples with nominal chemical composition was about 1°C/s, which is attainable in the gas quenching. For lower cooling rates ferrite with ultra-fine precipitates appeared. Purely ferritic microstructure was obtained for very low cooling rates below 0.02°C/s. The critical cooling rate for the carburized samples was about 0.1°C/s. For very low cooling rates pearlite appeared in the microstructure but martensite was observed in the whole investigated range of the cooling rates.

## References

1. Wojtyczka A., Iżowski B.: *Microstructure and hardness of Pyrowear 53 steel after low-pressure vacuum carburizing at 921°C*. Advances in Manufacturing Science and Technology, 44, 2020, 109–112.
2. Korecki M., Wołowicz-Korecka E., Bazel M., Slut M., Kreuzaler T.D.: *Outstanding hardening of Pyrowear® alloy 53 with low pressure carburizing*. 70° Congresso Anual da ABM, Rio de Janeiro, 2017, 1311–1320.

3. Wang J., Gua J., Shan X., Hao X., Chen N., Zhang W.: *Numerical simulation of high pressure gas quenching of H13 steel*. Journal of Materials Processing Technology, 202, 2008, 188–194.
4. Lu Y.: *Heat transfer, hardenability and steel phase transformations during gas quenching*. PhD Thesis, Worcester Polytechnic Inst., 2015.
5. Li Z., Lynn Ferguson B., Greif D., Kovacic Z., Urbas S., Kopun R.: *Coupling CFD and oil quench hardening analysis of a gear component*. Proc. 28<sup>th</sup> ASM Heat Treating Society Conference, Detroit, 2015, 40–43.
6. Rauch L., Bachniak D., Kuziak R., Kusiak J., Pietrzyk M.: *Problem of identification of phase transformation models used in simulations of steels processing*. Journal of Materials Engineering and Performance, 27, 2018, 5725–5735.
7. Donnay B., Herman J.C., Leroy V., Lotter U., Grossterlinden R.: *Microstructure evolution of C-Mn Steels in the hot deformation process: The STRIPCAM model*. Proc. 2<sup>nd</sup> Conf. Modelling of Metal Rolling Processes, London, 1996, 23–35.
8. Leblond J.B., Devaux J.: *A new kinetic model for anisothermal metallurgical transformations in steel including effect of austenite grain size*. Acta Metallurgica, 32, 1984, 137–146.

**Acknowledgements.** Financial support of the NCBiR, project no. TECHMATSTRATEG2/406725/1/NCBR/2020 is acknowledged.

# Modelling of roller levelling of plates using machine learning algorithms

Łukasz Sztangret<sup>1</sup>, Danuta Szeliga<sup>1</sup>

<sup>1</sup> AGH University of Science and Technology, Al. Mickiewicza 30, 30-059 Kraków, Poland  
szt@agh.edu.pl, szeliga@agh.edu.pl

**Keywords:** roller levelling, machine learning, linear regression, logistic regression, correlation analysis

## 1. Introduction

Precision metal plates characterized by good mechanical properties and surface qualities are important materials in aerospace, automotive and many other industries. Rolling, cold or hot, is the main processing method for metal plates. This process causes flatness imperfections due to internal stresses. One of the methods to increase the flatness of a plate is the multiroll leveller consisting of a set of rolls for bending the plates with different loads to achieve better levelling. The aim of this work is to build a model which will be able to predict a plate flatness after roller levelling process using machine learning algorithms [1–3]. Two models were developed. The linear regression model predicts the plate curvature factor after the levelling. The logistic regression model classifies whether the plate after levelling will be sufficiently flat. The developed models will be next used to determine the optimal control of the roller levelling machine.

## 2. Modelling

### 2.1. Data preparation

The collected data contains measurements of 34 plates before and after the levelling and the roller machine settings. The experimental data consists of 1225 flatness measurements. Due to the errors which often occur close to the edge of the plate, the values along all the edges were removed from the dataset. To normalize the measurement values, the mean value was subtracted from each of them. The roller machine settings included four parameters: inlet size (*in*), outlet size (*out*), roller conveyor velocity (*v*) and the angle ( $\alpha$ ) between the plate (*y*-axis) and the roller. Only three values of angle were examined:  $\alpha = 0^\circ$ ,  $\alpha \approx 26.5^\circ$ ,  $\alpha = 90^\circ$ . Specification of the plate surface in the form of many flatness measurements are useless for model design purposes. Therefore, the plate curvature must be first described using just a few coefficients. Curvature factor (*cf*) was used to designate the quantity of flatness and it was defined as the difference between the highest and the lowest flatness value of the plate. The second used coefficient determines the curvature direction (*cd*). In order to calculate the curvature direction the plate was approximated by the two-dimension square function:

$$f(\mathbf{x}) = \mathbf{x}^T \mathbf{A} \mathbf{x} + \mathbf{b}^T \mathbf{x} + c \quad (1)$$

---

The publication is co-financed from the state budget under the programme of the Minister of Education and Science called "Excellent Science" project no. DNK/SP/548041/2022



Doskonała  
Nauka



Ministry of Education and Science  
Republic of Poland



Republic  
of Poland

Next, the eigenvalues and eigenvectors of the matrix  $\mathbf{A}$  were computed. The curvature direction was defined as the angle between the eigenvector of matrix  $\mathbf{A}$  which corresponds to eigenvalue with the higher absolute value and the  $y$ -axis. The exemplary plate metal, its square approximation and the eigenvector of matrix  $\mathbf{A}$  are presented in Figure 1.

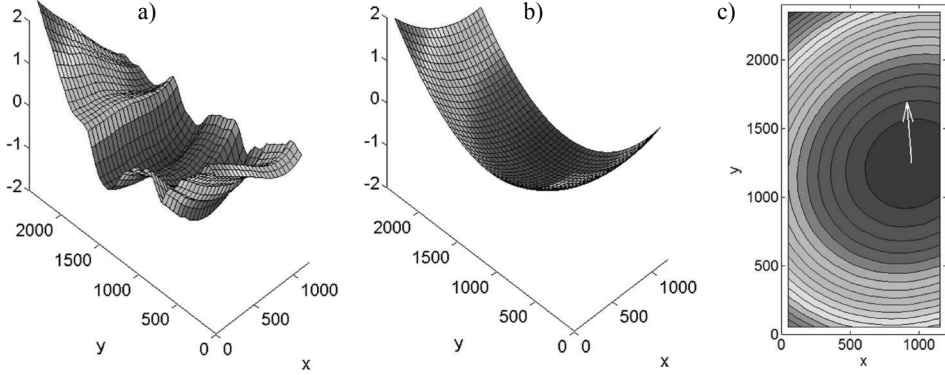


**Figure 1.** The exemplary plate metal (a), its square approximation (b) and the eigenvector which defines the curvature direction (c).

## 2.2. Features selection

Before the model can be developed, the vector of input values (features) must be defined. Based on the knowledge about the modelled process, the input vector for both models was set to five values:  $\mathbf{x} = [cf, in, out, v, |cd - \alpha|]^T$ . To validate the importance of selected features the linear correlation coefficient was calculated. The results are presented in Table 1.

**Table 1.** Values of linear correlation coefficient computed for initially selected features.

$cf$	$in$	$out$	$v$	$ cd - \alpha $
0.68	0.53	-0.11	0.10	0.25

Based on the obtained results, inputs  $out$  and  $v$  were removed from the feature vector. Reducing the number of features decreases the risk of variance problem, especially when the number of available training records is low. However, using too few features many cause the bias problem. Therefore, in many cases new features, which are based on already used ones, are introduced. Due to the low number of available training records, new features were defined only as the second power of initial features and product of each two ones. The linear correlation coefficient computed for the new features are presented in Table 2.

**Table 1.** Values of linear correlation coefficient computed for initially selected features.

$cf^2$	$cf \cdot in$	$cf \cdot  cd - \alpha $	$in^2$	$in \cdot  cd - \alpha $	$ cd - \alpha ^2$
0.70	0.72	0.60	0.52	0.28	0.20

The final feature had the following form:

$$\mathbf{x} = [cf, in, |cd - \alpha|, cf^2, cf \cdot in, cf \cdot |cd - \alpha|, in^2, in \cdot |cd - \alpha|, |cd - \alpha|^2] \quad (2)$$

### 2.3. Modelling results

The dataset was divided into training and testing set in the ratio of 70/30 what results in 24 training and 10 testing records. Hypothesis used for linear and logistic regression are given by equations (3) and (4), respectively:

$$h_{\theta}(\mathbf{x}) = \boldsymbol{\theta}^T \mathbf{x} \quad (3)$$

$$h_{\theta}(\mathbf{x}) = (1 + e^{-\boldsymbol{\theta}^T \mathbf{x}})^{-1} \quad (4)$$

where:  $\boldsymbol{\theta}$  – vector of model parameters,  $\mathbf{x}$  – vector of features (2) with added element  $x_0 = 1$ .

The aim of the linear regression model was to predict the curvature factor of the plate after levelling process, while the aim of the logistic regression model was to classify whether the plate after the levelling process will be sufficiently flat, i.e. the curvature factor will be less than 2. The training was performed using gradient optimization procedure from the Matlab software. The evaluation of models was made using mean absolute error (5) and accuracy (6) in case of linear and logistic regression, respectively:

$$MAE = \frac{1}{m} \sum_{i=1}^m |\hat{y}_i - y_i| \quad (5)$$

where:  $m$  – number of testing records,  $\hat{y}_i$  – model prediction,  $y_i$  – testing value.

$$ACC = \frac{TP + TN}{TP + TN + FP + FN} \quad (6)$$

where:  $TP$  – true positive prediction,  $TN$  – true negative prediction,  $FP$  – false positive prediction,  $FN$  – false negative prediction.

Each run of the training procedure returns slightly different results due to random splitting of the data. Therefore, training of each model was performed 100 times and the results presented in Table 3 are mean values.

**Table 3.** The error of linear and logistic regression.

<i>MAE</i>	2.1612
<i>ACC</i>	0.827

### 3. Conclusion and future work

The analysis of the obtained preliminary results reveals that accuracy of the models is not entirely satisfactory but still promising. The mean absolute error is greater than the assumed threshold determining the sufficient flatness of the plate. The results for logistic regression model are better. However, the possibility of using it to determine the optimal control of the rolling leveller is more problematic.

The main way to improve the models accuracy is enlargement of the dataset. Moreover, different forms of feature vector can be tested and the regularization term should be included in the cost function.

## References

1. Joshi A.V.: *Machine learning and artificial intelligence*. Cham : Springer Nature Switzerland AG, 2020.
2. Kung S.Y.: *Kernel methods and machine learning*. Cambridge : Cambridge University Press, 2014.
3. Seber G.A.F., Lee A.J.: *Linear regression analysis*. Hoboken: Wiley-Interscience : John Wiley & Sons, 2003.

**Acknowledgements.** Financial assistance of the Intelligent Development Operational Program, project no. POIR.01.01.01-00-0031/21.

# Optimisation of production and quality improvement with computational fluid dynamics in the steelmaking industry

Monika Zielińska<sup>1,2</sup>, Hongliang Yang<sup>3</sup>, Łukasz Madej<sup>2</sup>, Łukasz Malinowski<sup>1</sup>

<sup>1</sup> Corporate Technology Center CTC, ABB Sp. z o. o., Zeganska 1 st., 04-713 Warsaw, Poland

<sup>2</sup> AGH University of Science and Technology, Department of Applied Computer Science and Modelling, Mickiewicza 30 av., 30-059 Krakow, Poland

<sup>3</sup> ABB AB/Metallurgy, Terminalvagen 24, Bldg 340, Vasteras 72159, Sweden  
monika.zielinska@pl.abb.com, hongliang.yang@se.abb.com,  
lmadej@agh.edu.pl, lukasz.malinowski@pl.abb.com

**Keywords:** Computational Fluid Dynamics, steelmaking industry, electromagnetic stirring, gas stirring, non-metallic inclusions

## 1. Introduction

The steelmaking industry is one of the crucial industries in the world, where increasing requirements regarding the quality of the final products and environmental regulations force the continuous development and optimisation of production to obtain high efficiency with reduced power consumption. Moreover, each device in the production line must be properly designed to avoid the risk of the faults like improper solidification and sedimentation.

Optimisation of the process during production focused on quality improvement based on the high cleanliness of the steel [1,2] is difficult to carry out in real conditions. Often, the water models in a laboratory scale are used, but the main disadvantage of the method is that the preparation of the test equipment and hence, the design changes are time-consuming. Moreover, all of the phenomena occurring in the real melt are impossible to be covered by water models. Therefore, the numerical approaches to support the experimental investigation and simulate the phenomena in the molten steel are being intensively developed. The simulations from Computational Fluid Dynamics (CFD) domain enable understanding of the processes inside the melt, like the flow distribution, the efficiency of the mixing and the behaviour of the non-metallic inclusions. At the same time, such analysis tools allow optimisation of the manufacturing technology to increase its efficiency. Furthermore, based on the analysis of the flow, the prevention of faults can be realised via the reduction of dead zones and clogging [3]. Nowadays, different methods like the injection of argon gas [4–6], baffle walls (dams, weirs), and dedicated devices like electromagnetic stirrers [7,8] are under development to increase the mixing process and hence, the quality of the steel. All of the mentioned concepts can be easily tested via numerical methods without the long-lasting and expensive laboratory tests or industrial trials.

Within the presented work, the process of secondary steelmaking for continuous casting is taken into consideration, as it significantly influences the final product's quality. The analysis is focused mainly on the ladle furnace and tundish, the two last manufacturing steps before casting, where the high cleanliness of the steel is required. The current analysis includes the implementation of the CFD methods to track the flow behaviour, mixing process and an introduction to the inclusions modelling to understand the mechanisms of its removal phenomenon. The developed

---

The publication is co-financed from the state budget under the programme  
of the Minister of Education and Science called "Excellent Science" project no. DNK/SP/548041/2022



Doskonała  
Nauka



Ministry of Education and Science  
Republic of Poland



Republic  
of Poland

numerical model can be used as a base for its future improvement and correlations of the results with the real test measurements.

## 2. Methodology

The research is focused on the CFD approach to simulate phenomena occurring in molten steel during steelmaking. The analysis covers the flow behaviour of the melt, including the mixing process and non-metallic inclusions modelling mainly in the ladle furnace and tundish. Different types of additional stirring are used during the investigation to improve the flow distribution, avoid the dead zones, and increase the amount of the inclusions removed from molten steel. For both, ladle furnace and tundish, the electromagnetic stirring with different electromagnetic power can be considered. The processes in the ladle furnace include gas stirring and a combination of gas and electromagnetic stirring, but mixing in the tundish can be accomplished by baffle walls which are commonly used.

### 2.1. Electromagnetic stirring

The electromagnetic stirring in the CFD approach is realised as an additional momentum source, where the dependence between the electromagnetic forces and velocity is considered:

$$\vec{F} = \vec{F}_0 \left( 1 - \frac{\vec{F}_0 \cdot \vec{V}}{2\tau f \cdot |\vec{F}_0|} \right) \quad (1)$$

where:  $\vec{F}_0$  – stirring force calculated for stationary melt [ $\text{N}/\text{m}^3$ ],  $\vec{F}$  – stirring force after compensation with moving melt [ $\text{N}/\text{m}^3$ ],  $\tau$  – pole pitch [m],  $f$  – frequency [Hz],  $\vec{V}$  – velocity of melt [m/s].

Obtained forces are then interpolated on the fluid domain in each direction, and the whole process is realised by the user-defined scripts implemented in the commercial software.

### 2.2. Gas stirring

The gas stirring is realised by the multiphase approach, where both, Euler and Lagrange approaches are included. The main assumption is based on the Eulerian VOF (Volume of Fluid) model, where the phase of the molten steel, slag and air can be tracked. The approach enables understanding the behavior of the free surface in the ladle under the stirring process, but does not cover the inert gas behavior. To implement the gas bubbles and its influence on the flow, hence the slag and free surface layer, the Lagrangian DPM (Discrete Phase Model) is applied. Due to the complexity of the phenomena and inert gas bubbles behavior, some simplifications are included like the assumption of the ideal gas, where the diameter of the bubbles is changing with the height. Moreover, the bubbles have a constant mass during the whole process and are removed from the simulation when touching the free surface of the melt. Therefore, the coalescence and breakup of bubbles are not included at this stage and will be developed in the future.

### 2.3. Non-metallic inclusions modelling

The measurements of the non-metallic inclusions are difficult to realise due to the very expensive apparatus and the necessity to analyse the results in real conditions. Advanced CFD methods enable understanding the behavior of the inclusions and improve the possibilities to reduce its amount in the molten steel. The tracking of the aggregation of non-metallic inclusions is realised by the additional multiphase module PBM (Population Balance Model). The PBM is based on the

definition of different sizes of the particles corresponding to different bins, which are tracked during the simulation. The concentration of the bins changes in time according to the aggregation process controlled by the following phenomena:

- Brownian collisions,
- Stokes collisions,
- Turbulent collisions.

Moreover, the inclusions can be removed when they reach the slag layer under special conditions like the proper value of relative velocity between the slag and inclusion, collision time and rupture time.

### 3. Results and discussion

The research results include the analysis of the flow behaviour on the velocity vectors distribution under different types of stirring, mainly electromagnetic stirring, which is being intensively developed due to the noticeable increase in the mixing process and prevention of the dead zones. The results are obtained for the two important parts of the continuous casting process namely the ladle furnace and tundish, where the high mixing and cleaning occurs. Based on the CFD simulations, the clogging of the outlets is tracked by RTD (Residence Time Distribution) curves to understand the problem and optimise the device construction. Moreover, complex phenomena like inclusions modelling are implemented, which enable understanding the issues with the appearance of the non-metallic inclusions above critical diameters. Obtained data is analysed separately to improve the effectiveness of the whole process and prepare more advanced and efficient solutions.

### 4. Conclusions

The research confirms the importance of the CFD methods in the steelmaking industry, where the real tests are difficult to carry out due to the high temperature and costs of the measurement equipment. Thanks to the numerical simulations, the optimisation of the production line can be realised.

The strong mixing process without high power input is realised by electromagnetic stirring, which enables to increase the efficiency of the mixing, the homogeneity of the steel structure and the cleanliness of the steel.

The presented numerical approach will be still further developed to obtain better results, validated with real industrial tests.

### References

1. Zhang L., Thomas B.G.: *Inclusions in continuous casting of steel*. [in:] XXIV National Steelmaking Symposium, Morelia, Mich, Mexico, 2003.
2. Reis B.H., Bielefeldt W.V., Vilela A.C.F.: *Efficiency of inclusion absorption by slags during secondary refining of steel*. ISIJ International, 54, 2014, 1584–1591.
3. Sahai Y., Emi T.: *Melt Flow Characterization in Continuous Casting Tundishes*. ISIJ International, 36, 1996, 667–672.
4. Chang S., Cao X., Zou Z., Isac M., Guthrie R.I.L.: *Micro-bubble formation under non-wetting conditions in a full-scale water model of a ladle shroud/tundish system*. ISIJ International, 58, 2018, 60–67.
5. Yang H., Vanka S.P., Thomas B.G.: *Mathematical modeling of multiphase flow in steel continuous casting*. ISIJ International, 59, 2019, 956–972.
6. Souza G.M., Mendonça A.F.G., Tavares R.P.: *Physical and mathematical modeling of inclusion behavior in a tundish with gas curtain*. International Journal of Engineering, 73, 2020, 531–538.

7. Zhang L., Taniguchi S., Cai K.: *Fluid flow and inclusion removal in continuous casting tundish*. Metallurgical and Materials Transactions B, 31, 2000, 253–266.
8. Li B., Lu H., Zhong Y., Rens Z., Lei Z.: *Numerical simulation for the influence of EMS position on fluid flow and inclusion removal in a slab continuous casting mold*. ISIJ International, 60, 2020, 1204–1212.

**Acknowledgements.** The research within the industrial doctorate project co-financed by the Ministry of Science and Education.

# Evolutionary Optimization Managed by Agents with Socio-Cognitive Traits

Krzysztof Czech<sup>1</sup>, Aleksandra Urbańczyk<sup>1</sup>,  
Marek Kisiel-Dorohinicki<sup>1</sup>, Aleksander Byrski<sup>1</sup>

<sup>1</sup> AGH University of Science and Technology, Al. Mickiewicza 30, 30-059 Kraków, Poland  
kczech@student.agh.edu.pl, aurbanczyk@agh.edu.pl,  
doroh@agh.edu.pl, olekb@agh.edu.pl

**Keywords:** agent-based computing, metaheuristics, global optimization, socio-cognitive computing

## 1. Introduction

Tackling difficult optimization problems requires the use of metaheuristics [1]. According to Talbi [2], new ones must often be created, for example, by hybridizing or modifying existing algorithms [3]. Because metaheuristics are frequently inspired by nature, their hybridization frequently brings together different phenomena observed in the real world. Many metaheuristics that process a large number of individuals, particularly when individuals are perceived to be somewhat autonomous, use socio-cognitive inspirations, e.g. EMAS [4]. Among them there is a group of algorithms with dedicated mechanisms rooted in Social-Cognitive Theory by Albert Bandura [5], e.g. s-c evolution strategies [6], s-c PSO and s-c ACO [7]. In our current work we decided to explore possibilities of such modification based on the theory of different, prominent social psychologist – Elliot Aronson [8]. His reward theory of attraction states that attraction is a form of social learning. According to Aronson, we can usually understand why people are attracted to each other by looking at the social costs and benefits. In summary, reward theory states that we prefer those who provide maximum rewards at the lowest possible cost. Social psychologists have discovered four particularly powerful predictors of interpersonal attraction: proximity, similarity, self-disclosure, and physical attractiveness [9]. We use this inspiration to design a novel socio-cognitive algorithm described below.

## 2. Socio-cognitive Parallel Evolutionary Algorithm Managed by Agents

The algorithm is based on the concept of the Evolutionary Multi-Agent System with addition of socio-cognitive elements. A flock-based architecture extends the traditional sequential model into the parallel EA, providing an additional level of system organization [10]. The population of individuals is divided into flocks, that are managed by agents. Every cycle of the algorithm includes the evolutionary part and socio-cognitive part. During the evolutionary part, every agent performs an evolutionary algorithm on his flock. The socio-cognitive part consists of a series of communication between two agents. During every communication, one of the agents is gaining information about part of the flock belonging to the other agent, and after a quality check of the acquired data, the agent assimilates part of its own flock to the individuals included in acquired information. The amount of information transferred between agents is determined by the trust between them.

---

The publication is co-financed from the state budget under the programme of the Minister of Education and Science called "Excellent Science" project no. DNK/SP/548041/2022



**Doskonała  
Nauka**



Ministry of Education and Science  
Republic of Poland



**Republic  
of Poland**

The concept of trust is implemented as a global token market where each of the agents starts with a certain amount of trust tokens which can be passed by the agents during every event of single communication based on the outcome of this event. The more trust agents have, the more information they will acquire from other agents and the better it is going to be. The assimilation of flocks is based on the use of simple and fast operators to reduce the distance between two individuals. The algorithm continues until it performs a given number of cycles, the best solution found by the agents is assumed as the solution found by the algorithm.

### 3. Preliminary results

The preliminary results of the algorithm run on three standard 100-dimensional benchmark functions: Rastrigin, Ackley and Griewank are shown in Figures 1, 2 and 3, respectively. Each experiment was repeated 10 times and the results were averaged. Each benchmark was tested on 5-agent and 10-agent versions, with single-agent run as a reference. In both experimental settings, in each cycle of the algorithm, every agent does 50 iterations of the evolutionary algorithm and then every agent attempts to communicate with others 2 times. In the referential system, one agent is making the same amount of evolutionary algorithm iterations as in other experiments.

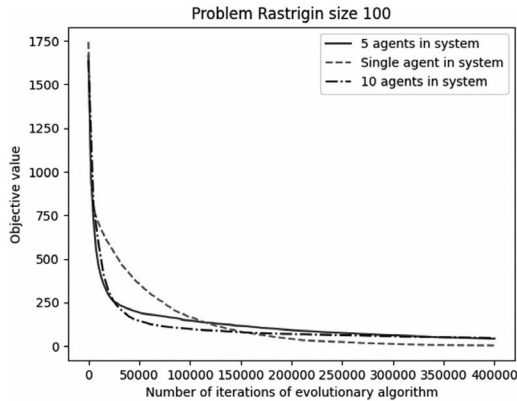


Figure 1. Preliminary results for Rastrigin benchmark.

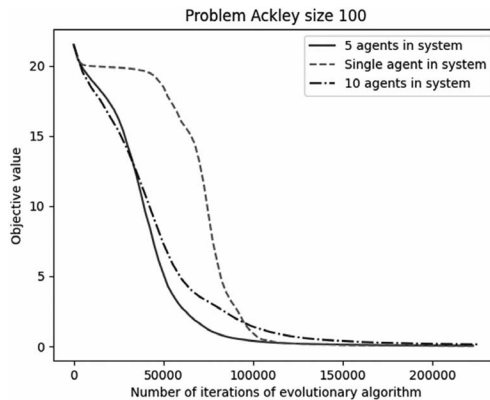


Figure 2. Preliminary results for Ackley benchmark.

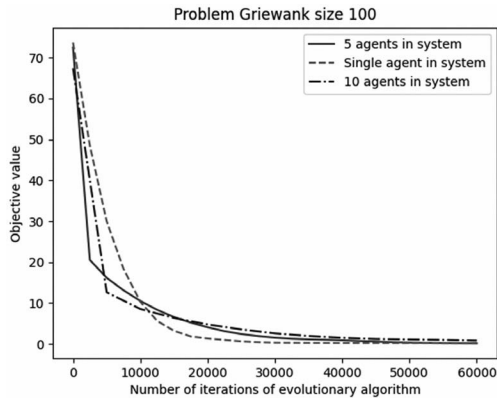


Figure 3. Preliminary results for Griewank benchmark.

## 4. Conclusion

In the run of the experiment, promising results were obtained. Both, 5-agent and 10-agent versions have found better solutions much faster than a single-agent version. To conclude, communication between agents, based on socio-cognitive mechanisms, facilitates faster convergence in tested benchmark algorithm. In addition to testing the algorithm against various other benchmarks, we intend to use the flock architecture more extensively in our future work, by differentiating variation operators' settings among the agents.

## References

1. Michalewicz Z., Fogel D.: *How to Solve It: Modern Heuristics*. Springer Berlin Heidelberg, 2004.
2. Talbi E.-G.: *Metaheuristics: from design to implementation*, John Wiley & Sons, 2009.
3. Wolpert D., Macready W.: *No free lunch theorems for optimization*, IEEE Transactions on Evolutionary Computation, 1, 1997, 67–82.
4. Byrski A., Dreżewski R., Siwik L., Kisiel-Dorohinicki M.: *Evolutionary multi-agent systems*. The Knowledge Engineering Review, 30, 2015, 171–186.
5. Bandura A.: *Social Foundations of Thought and Action: A Social Cognitive Theory*. Prentice-Hall series in social learning theory. Prentice-Hall, 1986. <https://books.google.pl/books?id=HJhQAAAAMAAJ>.
6. Urbańczyk, A., Nowak B., Orzechowski P., Moore J.H., Kisiel-Dorohinicki M., Byrski A.: *Socio-cognitive evolution strategies*, Computational Science–ICCS 2021: 21<sup>st</sup> International Conference, Krakow, Poland, June 16–18, 2021, 329–342.
7. Bugajski I., Listkiewicz P., Byrski A., Kisiel-Dorohinicki M., Korczyński W., Lenaerts T., Samson D., Indurkha B., Nowé A.: *Enhancing particle swarm optimization with socio-cognitive inspirations*, Procedia Computer Science, 80, 2016, 804–813.
8. Aronson E., Aronson J.: *The Social Animal*, Macmillan Learning, 2018.
9. Zimbardo P., Johnson R., McCann V.: *Psychology: Core Concepts*. Always learning, Pearson, 2012.
10. Kisiel-Dorohinicki M.: *Flock-based architecture for distributed evolutionary algorithms*. Artificial Intelligence and Soft Computing – ICAISC 2004, eds, Rutkowski L., Siekmann J.H., Tadeusiewicz R., Zadeh L.A., Berlin, Heidelberg, 2004, 841–846.

**Acknowledgements.** The research presented has been financially supported by: Polish National Science Center Grant no. 2019/35/O/ST6/00570 “Socio-cognitive inspirations in classic metaheuristics.” (AU); Polish Ministry of Science and Higher Education funds assigned to AGH University of Science and Technology (AB, MKD).

# Long-product quality optimization through enhancement and utilisation of residual stress minimizing process strategies

Volker Diegelmann<sup>1</sup>, Hagen Krambeer<sup>1</sup>,  
Andreas Wolff<sup>1</sup>

<sup>1</sup> VDEh-Betriebsforschungsinstitut GmbH (BFI), Sohnstr. 69, 40237 Düsseldorf, Germany  
volker.diegelmann@bfi.de, hagen.krambeer@bfi.de,  
andreas.wolff@bfi.de

**Keywords:** residual stress, hybrid model, digital twin

## 1. Problem, Research Questions and Objectives

Rolling, straightening and thermal processes generate residual stresses that affect the material properties of the products and lead to material distortion due to stress relief mechanisms. The characteristics of these effects are still subject to a high degree of uncertainty, also because a direct online measurement of the residual stresses is not possible. On the other hand, online-capable residual stress determination methods are imperative for a more accurate prediction of the effects of the various processing steps on product quality. In summary, it can be stated that the description of the residual stresses developing during the entire production process is not yet sufficiently given due to the unavailability of suitable measuring devices. This would also make it possible to control the process with a view to the developing residual stresses as a decisive influencing factor on shape and straightness deviations. Therefore, an improved and state-of-the-art process technology is required that combines hybrid process models (physical and statistical) with a virtual plant model (digital twin) and enables online simulation of material conditions and properties, e.g. residual stresses, using soft sensors.

## 2. Proposed technical solution

A digital twin (Figure 1) is a digital representation of a product, whereby all product properties are gathered from all relevant sources throughout the production process and linked to a specific production unit. All relevant data are gathered in product related digital twin. They also serve as a repository for relevant models to calculate non-measurable data. The data of the digital twin are stored in a noSQL database hosted on the server [1].

The Digital Twin has also a logistic model to track the block through the whole process together with the information about trigger points when new data are to be gathered and models can be run with this new data. By using the hybrid models developed in this project the Digital Twin can always reproduce the current state of the block within the scope of the possible model outputs (residual stresses, temperature, ...) [2]. So, this software concept is ideal to support the idea of an online residual stress prediction for a long product carried through the whole process (Figure 2).

---

The publication is co-financed from the state budget under the programme of the Minister of Education and Science called "Excellent Science" project no. DNK/SP/548041/2022

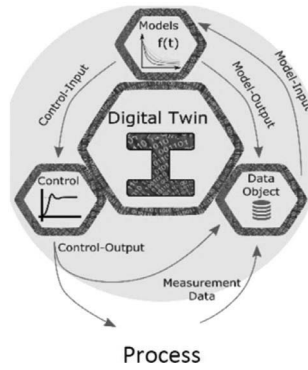


**Figure 1.** Schematic diagram of a digital twin and its functionalities and internal communication.

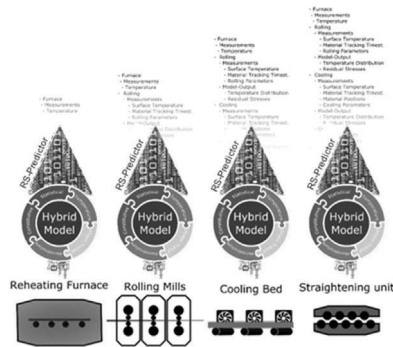


**Figure 2.** Realization of basic project idea along the long product production chain – digital twin technology with hybrid process model and soft sensor.

A hybrid approach is chosen combining material, physical and data-based process models for prediction of residual stresses (Figure 3) [3]. It comprises experimentally gained material data and process data, which are analytically and statistically evaluated to generate knowledge for the realisation of a “residual stress-based” process strategy. As a direct online measurement of residual stresses is not possible, the development of a digital twin for prediction of residual stresses will solve this technological gap and can be used for further process control.



**Figure 3.** Realization of the digital twin through hybrid models for predicting the internal stresses.

### 3. Preliminary results

The material was characterised regarding microstructural and mechanical properties. The elaborated constitutive models were implemented and used in FE-simulations of rolling, cooling, and straightening, enabling consistent tracking of the existing material states at different positions along the production process. The material state finally will be evaluated based on its residual stresses. Residual stress measurements are ongoing. They are used for validation of model gained residual stress results. A correlation will be established between stress distribution and process and product specific conditions. An optical straightness measuring device specially developed regarding customer-specific conditions will be used for the optimisation of the straightening process. The first model of residual stresses is based on a full 3D FE approach. The results are used to verify the reliability of calculation results from simplified models. The experimental measurements of residual stresses show that longitudinal residual stresses dominate in long products, allowing for using an alternative simplified approach with reasonable and very fast results.

The digital twin infrastructure was designed and filled up with material, process and model acquired data. The data acquisition software is hosted on the server as well. Now specific calculations regarding the residual stress state can be performed on the data resulting into a residual stress related soft sensor allowing for use in process control. To ensure a platform independent result output a web-based HMI is planned.

### 4. Preliminary conclusions

The given process boundary conditions only allow for marginal intervention possibilities. However, the approach will allow a monitoring and documentation of the processes and prediction of the resultant material state (e.g. residual stress). The available digital twin enables a process control with view on resultant best possible optimal residual stress state. Additionally, a risk assessment will be possible regarding possible distortions due to thermal and/or mechanical interventions at e.g. customer sites.

### References

1. Neuer M., Lathe R., Wolff A., Loos M., Polzer J., Kremeyer J.: *Quo Vadis, automation? – From intelligent products and machines to machine learning control*. Proceedings of the European Steel Technology and Application Days, Düsseldorf, 2019.
2. *Virtual Design of Cyber-Physical Production Optimization Systems for Long Production Factories (CYBER-POS)*. 01.07.2016- 31.12.2019, Grant Agreement No. 709669 (2016).
3. Milenin, Kuziak R., Lech-Grega M., Chochorowski A., Witek S., Pietrzyk M.: *Numerical modeling and experimental identification of residual stresses in hot-rolled strips*. Archives of Civil and Mechanical Engineering, 16, 2016, 125–134.

**Acknowledgements.** This project receives funding from the Research Fund for Coal and Steel under grant agreement No 899455.

# Cyber-physical system for integrated management of steel and rolling mills – architecture and implementation details

Krzysztof Bzowski<sup>1</sup>, Monika Pernach<sup>1</sup>, Piotr Hajder<sup>1</sup>, Krzysztof Regulski<sup>1</sup>

<sup>1</sup> AGH University of Science and Technology, Al. Mickiewicza 30, 30-059 Krakow, Poland

kbzowski@agh.edu.pl, pernach@agh.edu.pl,

phajder@agh.edu.pl, regulski@agh.edu.pl

**Keywords:** cyber-physical system, electrosteel plant, rolling mill, system architecture, implementation details

## 1. Introduction

Cyber-Physical Systems (CPS) are systems of collaborating computational modules which are in intensive connection with the surrounding physical world and its on-going processes, providing and using, at the same time, data-accessing and data-processing services available on the internet [1]. In other words, these systems enables objects and processes residing in the physical world (e.g. manufacturing facility), to be tightly coupled with computing, communication and control systems in the cyber world [2]. In industrial applications the CPS systems are usually called Cyber-Physical Production Systems (CPPS) and are one of the key technical enablers of 4th industrial revolution (often referred to as Industry 4.0 [3]). In the past years tremendous amount of work was done on implementing CPPS in many branches of industry. Many concepts like holonic or agent-based systems [4,5], cloud, fog, dew, edge computing [6–8], Wireless Sensor Network [9] and many others were successfully implemented to address Industry 4.0 requirements. This Presentation is a part of the work undertaken in the project aiming to create computer system integrating management of the steel and rolling mills producing billets and long products. The main goal of the Project is to conduct R&D works aimed at development of globally innovative, integrated with the infrastructure of steelmaking facility (Electric Arc Furnace “EAF” – Ladle Furnace “LF” – Continuous Casting Machine “CCM”), hybrid IT system for optimizing and modeling steel billets production process i.e. solution significantly contributing to the quality of CMC Poland Sp. z o.o. (CMC, Company, Applicant) products by providing full control over liquid steel temperature, including superheating temperature.

## 2. System architecture

### 2.1. Dependency on other systems in company infrastructure

The proposed System (called also SWP from Polish shortcut System Wspomagania Produkcji) plays important role in IT infrastructure of the company, communicating at least three of the most important systems (Figure 1). The first one is SAP responsible for management of sales gathering data of customers, orders, dates of contracts and material indexes with tonnage of sales. The data are exported to SWP system automatically every two hours in form of external database. The records of contracts are used further for purposes of rolling campaigns planning and scheduling of the

---

The publication is co-financed from the state budget under the programme of the Minister of Education and Science called “Excellent Science” project no. DNK/SP/548041/2022



**Doskonała  
Nauka**



Ministry of Education and Science  
Republic of Poland



**Republic  
of Poland**

wok in steel mill. The plans of rolling campaigns are proposed automatically according to specific rules delivered by the rolling mill and department of sales. On the basis of each campaign as well as contract dates the System schedules casting sequences for steel mill according to metallurgical knowledge about joining of particular heats in each sequence, working calendar and rules delivered by steel plant managers.

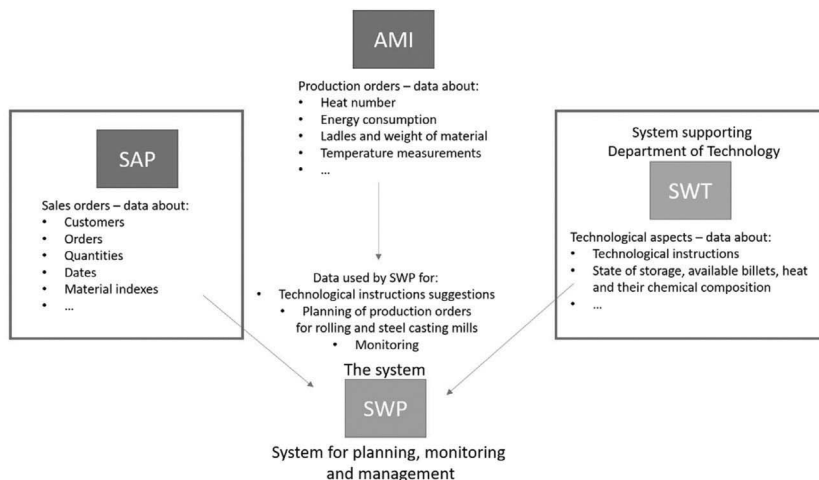


**Figure 1.** The proposed System in infrastructure of CMC Poland Sp. z o.o.

SWT system delivers information on technological instructions, which are crucial for chemical composition of the casted steel and all the technological issues related to the way of heat preparation and casting. These data are also important for steel plant work scheduling, but also for prediction of liquid steel cooling rate inside the main ladles, what is the most interesting between LF and CCM to maintain casting temperature regimes for each grade of steel. The information needed for such prediction is supported also by AMI system, which is responsible for gathering all the data related to production processes including static as well as time-dependent parameters of production devices. The data are copied redundantly and gathered in external database to be used also for monitoring process and support of process operator by prediction and suggestion of energy usage.

## 2.2. Architecture of the system based on microservices

The System was designed to be implemented on the basis of microservices architecture. Such approach allows to design and implement each module separately according to specific technical or functional requirements e.g. monitoring module is based on implementation techniques, which allow to use Artificial Intelligence procedures to analyze images captured from CCTV cameras, while on the other hand SAP communication module is implemented as a typical back-end service in C#. Additional advantage of such solution is also maintenance of the software during lifetime, which can generate problems and high costs – in this approach maintenance is divided between each module and can be done separately assuming that communication protocol and the way of information exchange through the message broker do not change. The design with selected modules is presented in Figure 2 and it will be presented in details during conference presentation.

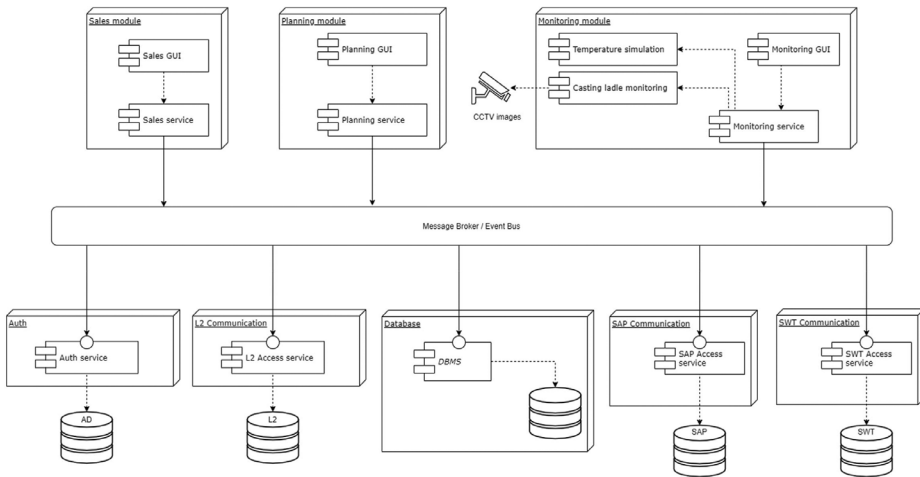


**Figure 2.** Architecture of the system in form of the microservices components.

## References

1. Monostori L.: *Cyber-physical production systems: Roots, expectations and R&D challenges*. *Procedia CIRP* 17, 2014, 9–13.
2. Bagheri B., Yang S., Kao H.A., Lee J.: *Cyber-physical systems architecture for self-aware machines in industry 4.0 environment*. *IFAC-PapersOnLine*, 28, 2015, 1622–1627.
3. Lins T, Oliveira R.A.R.: *Cyber-physical production systems retrofitting in context of industry 4.0*. *Computers and Industrial Engineering*, 139, 2019.
4. Wang L., Haghighi A.: *Combined strength of holons, agents and function blocks in cyber-physical systems*. *Journal of Manufacturing Systems*, 40, 2016, 25–34.
5. Demesure G., Defoort M., Bekrar A., Trentesaux D., Djemaï M.: *Navigation Scheme with Priority-Based Scheduling of Mobile Agents: Application to AGV-Based Flexible Manufacturing System*. *Journal of Intelligent and Robotic Systems: Theory and Applications*, 82, 2016, 495–512.
6. O'Donovan P., Gallagher C., Bruton K., O'Sullivan D.T.: *A fog computing industrial cyber-physical system for embedded low-latency machine learning Industry 4.0 applications*. *Manufacturing Letters*, 15, 2018, 139–142.
7. Zhou Y., Zhang D., Xiong N.: *Post-Cloud Computing Paradigms: A Survey and Comparison*. *Tsinghua Science and Technology*, 22, 2017, 714–732.
8. Skala K., Davidovic D., Afgan E., Sovic I., Sojat Z.: *Scalable Distributed Computing Hierarchy: Cloud, Fog and Dew Computing*. *Open Journal of Cloud Computing*, 2, 2015, 16–24.
9. Piyare R., Park S., Maeng S.Y., Park S.H., Oh S.C., Choi S.G., Choi H.S., Lee S.R.: *Integrating Wireless Sensor Network into Cloud services for real-time data collection*. *International Conference on ICT Convergence*, 2013, 752–756.

**Acknowledgements.** The work is financed by National Centre for Research and Development within a project no. POIR.01.01.01-00-0996/19.

# Pressure influence during gas quenching on mechanical properties of gears

Artur Wojtyczka<sup>1,2</sup>, Bartosz Izowski<sup>1,2</sup>, Kamil Dychtoń<sup>2,3</sup>, Ryszard Filip<sup>2,3</sup>

<sup>1</sup> Research and Development Center, Pratt & Whitney Rzeszów S.A., 35-078 Rzeszów, Poland

<sup>2</sup> Faculty of Mechanical Engineering and Aeronautics, Rzeszow University of Technology, 12 Powstańców Warszawy Ave., 35-959 Rzeszów, Poland

<sup>3</sup> Research and Development Laboratory for Aerospace Materials, Rzeszow University of Technology, 4 Żwirki i Wigury Str., 35-959 Rzeszów, Poland

artur.wojtyczka@pwrze.utc.com, bartosz.izowski@pwrze.utc.com, kdychton@prz.edu.pl, ryfil@prz.edu.pl

**Keywords:** high pressure gas quenching, vacuum carburizing, Pyrowear 53, mechanical properties

## 1. Introduction

Gears are one of the main power transmission elements in aerospace vehicles. Due to high power density requirements of aerospace vehicles gears suffer both tooth surface failures and tooth fracture due to cyclic loadings. Different materials have been developed for improving performance of gears. Pyrowear 53 low-alloy steel was developed to enhance safety margin in comparison to AISI 9310. Carburization and quench hardening of this steel produce high strength case and toughness core. Pyrowear 53 is also characterized by ability to resistance to tempering at high temperatures [1–3]. High pressure gas quenching (HPGQ) was developed as an important advancement in heat treatment technology of carburized steel grades. During quenching a high thermal gradients and rapid phase transformation rates are produced. This phenomena enhance a fatigue life and wear resistance of carburized layer of gears [3,4]. HPGQ in comparison to oil quenching guarantee a better surface quality and an improvement of the distortion. However depending on parameters applied during the quenching, different microstructural constituents may develop in the case and core of carburized steel substantially influencing mechanical properties [5]. A comprehensive understanding influence of a quench parameter such a gas pressure on mechanical properties is highly important. It enable an effective comparison of numerical simulation analysis with effective results obtained during thermo-chemical treatment of gears made from Pyrowear 53. Based on the obtained results, it can be shown that the mechanical properties of carburized layer are similar both after quenching in oil and quenching in nitrogen. Moreover despite the differences in pressure of quenching gas the overall mechanical properties of case and core of carburized parts of gears are similar.

## 2. Materials and Methods

The Star Gear used in GTF Gearbox Transmission System was partitioned into four pieces and used as a specimens. The chemical composition of the Pyrowear 53 low-alloyed steel met the requirements presents in [6]. The heat treatment processes of all specimens were presented in Table 1. All specimens were carburized in vacuum furnace (ALD MonoTherm HK.446.VC.10.gr)

---

The publication is co-financed from the state budget under the programme of the Minister of Education and Science called "Excellent Science" project no. DNK/SP/548041/2022



Doskonała  
Nauka



Ministry of Education and Science  
Republic of Poland



Republic  
of Poland

and cooled down slowly to room temperature. The LPC process at 921°C consisted of 16 boost-diffusion cycles. The carbon carrier boosts' total time was 17 min, while the entire process time was approximately 7.5 h. Two different technique of quenching were used. HPGQ with nitrogen was performed on specimens Nos. 1,2 and 3 with three different pressures. Oil quenching was performed on specimen No. 4. Before quenching all specimens were carried out in 913°C temperature for a sufficient period of time to ensure a homogeneous austenitic microstructure in the whole volume.

**Table 1.** Heat treatment processes carried out on Star Gear parts.

Specimens No.	LPC	HPGQ 0.15 MPa	HPGQ 0.40 MPa	HPGQ 0.90 MPa	Oil quenching	Sub-zero treatment	Tempering
1	+	+				+	+
2	+		+			+	+
3	+			+		+	+
4	+				+	+	+

The cryogenic treatment at -75°C was performed to finish the martensitic transformation. Tempering was performed at 230°C for 4 h.

To determine the influence of pressure in HPGQ on mechanical properties of carburized layers and core, the hardness measurements were made. The change of microhardness in the carburized layer with distance from the surface was presented in Figure 1. Case and core hardness with effective case depth were presented in Table 2. Additionally, measurements of yield strength and tensile

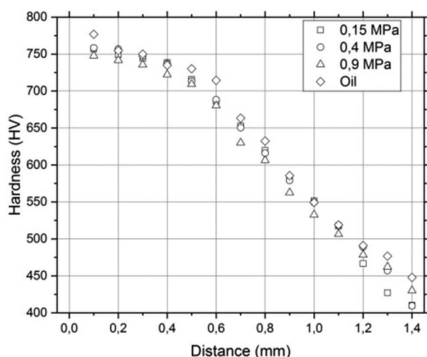


**Figure 1.** Microhardness changes in carburized layer obtained for different quenching medium.

**Table 2.** Impact of quenching medium and its parameters on mechanical properties of case and core carburized gears.

Mechanical properties	HPGQ 0.15 MPa	HPGQ 0.40 MPa	HPGQ 0.90 MPa	Oil quenching
ECD, mm	1.12	1.12	1.05	1.11
Case hardness, HRA	82.1	82.0	82.2	82.4
Core hardness, HRC	36–37	37.5–38.0	38.0–38.5	36.5
Yield strength, MPa	935	928	928	932
Tensile strength, MPa	1 161	1 157	1 157	1 163

strength were made from cut samples out of the specimens core subjected to thermo-chemical treatment and presented in Table 2.

## References

1. Vardar M., Erdogan F., Yildirim N.: Recent developments in aerospace gears and gearbox design, *International Journal of Scientific and Technological Research*, 4, 2018, 145-155.
2. Ferguson B.L., Li Z., Freborg A.M.: Modeling heat treatment of steel parts, *Computational Materials Science*, 34, 2005, 274-281.
3. Ferguson B.L., Freborg A.M., Li Z.: Residual stress and bending fatigue strength in carburized and quench hardened Pyrowear 53 steel gears, *Proc. IFHTSE'23 Congress, USA, 2016*, 374-381.
4. Antraszkiewicz R., Januszewicz B., Kaczmarek L., Stachurski W., Dybowski K., Rzepkowski A.: High pressure gas quenching: Distortion analysis in gears after heat treatment, *Materials Science & Engineering A*, 558, 2012, 550-557.
5. Farivar H., Deepu M.J., Hans M., Phanikumar G., Bleck W., Prah U.: Influence of post carburizing heat treatment on the core microstructural evolution and the resulting mechanical properties in case-hardened steel components, *Materials Science & Engineering A*, 744, 2019, 778-789.
6. AMS6308 rev. F-Steel: *Bars and Forgings 0.90Si-1.0Cr-2.0Ni-3.2Mo-2.0Cu-0.10V (0.07-0.13C) Vacuum Arc or Electroslag Remelted*. SAE International: Warrendale, PA, USA, 2018.

**Acknowledgements.** Results gathered within the framework of the development project in the TECHMATSTRATEG2/406725/1/NCBR/2020 program of the National Center for Research and Development were used.

# Computer aided design of rotary forming technology with laser beam material heating

Barbara Mrzygłód<sup>1</sup>, Izabela Olejarczyk-Wożeńska<sup>1</sup>, Marcin Hojny<sup>1</sup>,  
Tomasz Dębiński<sup>1</sup>, Przemysław Marynowski<sup>1</sup>

<sup>1</sup> AGH University of Science and Technology, Faculty of Metals Engineering and Industrial  
Computer Science, Al. Adama Mickiewicza 30, 30 - 059 Krakow, Poland  
mrzyglod@agh.edu.pl, iolejarc@agh.edu.pl,  
mhojny@metal.agh.edu.pl tdebinsk@metal.agh.edu.pl,  
pmarynow@agh.edu.pl

**Keywords:** rotary forming processes with laser beam heating, artificial neural networks, metamodel, numerical modelling, virtual reality system

## 1. Introduction

The rotary forming process is a plastic forming operation used mainly when shaping thin-walled, axisymmetric products (high plasticity and low strength materials). The design concept for rotary forming with material reheating during forming was developed at the Fraunhofer Institute [1]. A laser beam heats a small part of the surface (in front of the forming roller), and thanks to the coordinated movement of the crushing roller, it is possible to form the material on the rotating pattern.

The selection of process parameters for the forming of new products or the modification of an existing process involves a lot of expensive and time-consuming experimental research to develop new technological guidelines. In the design of these processes, numerical simulations are exceptionally helpful, allowing the virtual design of new processes and the selection of process parameters [2]. Numerical simulations of rotary forming processes have not yet been widely used in operational process control due to the time limitations of these simulations, which can take up to tens of hours.

## 2. Research methodology

The purpose of this study was to develop a new design approach using advanced numerical modeling of rotary forming processes with laser beam heating (GPU-assisted calculations) and the capabilities of virtual reality (VR) systems. To speed up computation times, implemented in the developed VR system, work was undertaken using artificial intelligence methods to develop a metamodel.

To acquire learning data for the metamodel, the developed numerical model was used [2]. The metamodel was developed using artificial neural networks. Figure 1 shows the process of acquiring the learning set. Computer simulations were carried out for a pipe made of 316 L stainless steel with a wall thickness of 2 mm. The rotational speed, laser power and temperatures were taken as input parameters for the simulation. The heating time was taken as the output parameter. 102 simulations were carried out, one of which took about 4–5 days.

---

The publication is co-financed from the state budget under the programme  
of the Minister of Education and Science called "Excellent Science" project no. DNK/SP/548041/2022



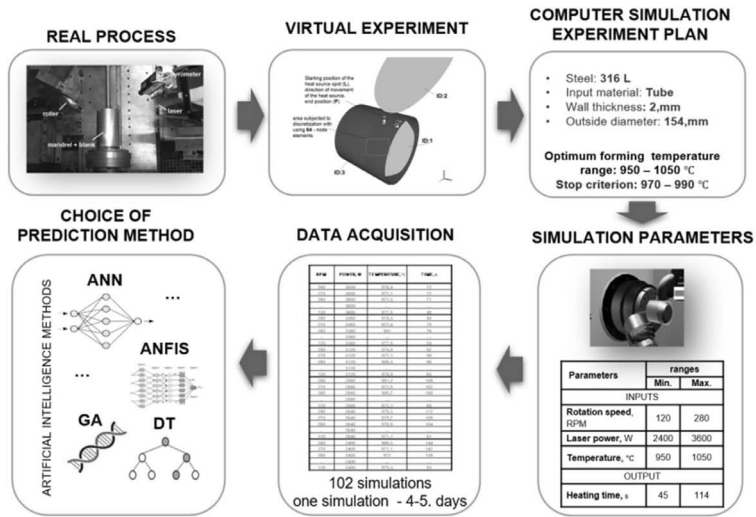


Figure 1. Research methodology.

### 3. Summary

The developed metamodel allows to acquire information about the required heating time for the set input parameters in real time. The developed methodology was verified for 316L stainless steel and can be adopted to design new metamodels for other materials. The metamodel will be a component of the designed and developed interactive interface, based on VR technology. The designed system can be a useful tool to support the design and realization of industrial processes.

### References

1. Klocke F., Wehremeister T.: *Laser-Assisted Metal Spinning of Advanced Materials*. WLT-Conference on Lasers Manufacturing, 2003.
2. Hojny M., Marynowski P., Lipski G., Gądek T., Nowacki Ł.: *Application of virtual reality and high performance computing in designing rotary forming processes*. Archives of Metallurgy and Materials, 67, 2022, 1099–1105.

# The true stress–strain curve evaluation in post-necking phase of tensile test using DIC and numerical simulation

Sławomir Świłło<sup>1</sup>, Robert Cacko<sup>1</sup>

<sup>1</sup> Warsaw University of Technology, Faculty of Mechanical and Industrial Engineering,  
02-524 Warszawa, ul. Narbutta 85  
slawomir.swillo@pw.edu.pl, robert.cacko.itw@pw.edu.pl

**Keywords:** stress-strain curve, post-necking hardening, tensile test, DIC method, numerical simulation

## 1. Introduction

The industry's dynamic development of manufacturing technology leads to the constantly growing demand for new, more accurate and practical material testing techniques. Further measuring solutions dedicated to a uniaxial tensile test are continually being developed, mainly due to progress in physics and optoelectronics. These methods include especially machine vision based solutions, such as digital image correlation (DIC) and surface strain measurement [1,2]. However, a quick and thorough analysis is expected to determine mechanical properties and an extended description of material hardening. Knowledge of the stress-strain curve is often necessary to simulate large material deformations. These comprehensive characteristics of the material are increasingly expected due to the requirements for industrial techniques, such as: displacement and deformation measurement systems. These solutions are expected to perform complicated fatigue and fracture or stress distribution predictions, since selected material parameters can be crucial for component strength analysis in sheet metal forming.

However, the characteristics of strengthening of the material in post-necking phase are challenging to determine due to the triaxial state of stress. The most practical stress-strain curve correction procedure includes analytical methods to predict hardening effects for large deformations. Therefore, the mathematical evaluation of the stress-strain curve in the post-necking phase for cylindrical and flat specimens has been conducted by many authors such as Bridgman and Siebel. Bridgman's analytical correction model has been found successfully as was incorporated in the field of round bar tensile test. However, for the flat sample, additional modifications are continuously added, and new formulas are still investigated [3]. The main reason of these investigations is to identify accurately necking geometry that takes place at the final stage of the tensile test (neck localization). Therefore, the final necking contour is less deformed, not smooth, and not symmetrical and therefore difficult to identify. Many investigators, while conducting the calculations for the extended stress curve for the Bridgman solution, faced the problem of the accurate recognition of the necking geometry, especially using machine vision technology. The main reason of this situation is that the developed methods are too complicated to be applied in practice [4].

Increasingly, however, numerical simulation are proposed, which allow determining with high accuracy the materials behaviour in the zone of triaxial stress. One such solution is Zhang's proposal [5], using reverse FEM analysis to assess the cross-section of the sample in the neck area. In this method, the total area-reducing ratio of the stretching sample with a minimum cross-section can

---

The publication is co-financed from the state budget under the programme  
of the Minister of Education and Science called "Excellent Science" project no. DNK/SP/548041/2022



Doskonała  
Nauka



Ministry of Education and Science  
Republic of Poland



Republic  
of Poland

be divided into a proportional part (calculated based on thickness reduction) and a nonproportional part (resulting from the shape change) by:

$$\frac{\Delta A}{A_0} = \frac{\Delta A_p}{A_0} - \frac{\Delta A_s}{A_0} \quad (1)$$

The proportional part can be saved as a sample thickness reduction function for the minimum cross-section:

$$\frac{\Delta A_p}{A_0} = 2\left(\frac{\Delta t}{t_0}\right) - \left(\frac{\Delta t}{t_0}\right)^2 \quad (2)$$

where  $\Delta t/t_0$  – thickness reduction,

However, the nonproportional part of equation (1) can be saved as:

$$\frac{\Delta A_s}{A_0} = f_s(S) f_i\left(\frac{\Delta t}{t_0} - \left(\frac{\Delta t}{t_0}\right)_{P_{\max}}\right) f_m\left(\frac{\Delta t}{t_0}\right)_{P_{\max}} \quad (3)$$

where  $P_{\max}$  – maximum tensile load and,  $f_s, f_i, f_m$  – functions describe sample geometry in the appropriate deformation states.

Therefore, the evaluation of the extended stress-strain curve (according to Zhang's proposal) should be reduced to the experimental measurement of only the load curve depending on the changes in the thickness (in the distributed necking zone – minimum cross-section).

## 2. Experimental and numerical simulation

The authors present the results of the extended stress-strain curve for DC04 steel using the Zhang method for flat samples. Three-stage tests were conducted for this purpose. First, an assessment of strengthening the material in the stable phase was carried out. The obtained results were introduced to the numerical model, simulating the stretching test in the stable phase. Then, the obtained numerical results were verified, comparing the effects of deformation calculations and geometry with the experimental course. Second, numerical simulation for the unstable phase were launched, and the experimental results of deformations and geometry based on digital image analysis were performed (based on stochastic grid). Third, the minimum cross-sectional reducing ratio of the rectangular sample surface was determined (using FEM calculations), seeking the appropriate (for a given case) description of the function (according to equation 3) changes in geometry.

The conducted experimental research concerns flat samples, which are the most widespread form of geometry in tests of sheet metal, Figure 1a. Therefore, the surface of the specimen with a thickness of 1mm was marked with a stochastic pattern by spraying (irregular dot pattern – Figure 1b). When stretching on the tensile testing machine (Figure 1c), the image of the surface was captured, correlating them with the values of the load. As a result of digital numerical analysis of the captured images of the sample, the displacements with the corresponding load was obtained. This experimental measurement procedure allowed to determine the stress as a deformation function.

In addition, using commercial MSC.Marc software, based on the finite element method, the numerical simulation were conducted. The numeric model optimisation procedure was carried out first, and on this basis, the size and type of elements were proposed (hexahedral 8-node, 0,8 mm edge). The numerical model and sample results are shown in Figure 1d.

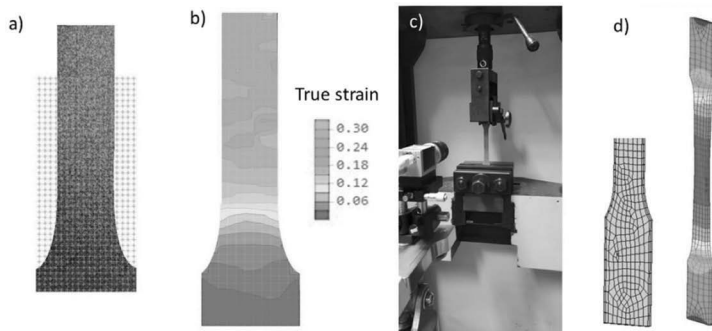


**Figure 1.** Experimental procedure and simulation: a) flat specimen with stochastic grid pattern, b) experimental strain measurement using DIC, c) tensile testing, d) FEM simulation.

## References

1. Paul S.K., Roy S., Sivaprasad S. Tarafder S.: *A Simplified Procedure to Determine Post-necking True Stress–Strain Curve from Uniaxial Tensile Test of Round Metallic Specimen Using DIC*. Journal of Materials Engineering and Performance, 27, 2018, 4893–4899.
2. Shahrjerdi A., Ranjbar B.: *Correction of post-necking stress–strain curve of copper using surface strain method*. Archive Applied Mechanics, 92, 2022, 199–219.
3. Tu S., Ren X., He J., Zhang Z.: *Stress–strain curves of metallic materials and post-necking strain hardening characterization: A review*. Fatigue & Fracture of Engineering Materials & Structures, 43, 2019, 3–19.
4. Mirone G.: *A new model for the elasto-plastic characterization and the stress–strain determination on the necking section of a tensile specimen*. International Journal of Solids and Structures, 41, 2004, 3545–3564.
5. Zhang Z.L., Odegard J., Sovik O.P.: *Determining true stress- strain curve for isotropic and anisotropic materials with rectangular tensile bars: method and verifications*. Computational Materials Science, 20, 2001, 77–85.

# Core structure analysis of dislocations in TWIP steel under the Meta-atom framework: An assessment

Sri Sadgun Reddy Pulagam<sup>1</sup>, Amlan Dutta<sup>1</sup>

<sup>1</sup> Department of Metallurgical and Materials Engineering,  
Indian Institute of Technology Kharagpur, West Bengal - 721302, India  
sadgun.pulagam@iitkgp.ac.in,  
amlan.dutta@metal.iitkgp.ac.in

**Keywords:** Meta-atom framework, Peierls-Nabarro model, dislocations, TWIP steel, Atomistic simulations

## 1. Introduction

Atomistic simulations of complex alloys are of major interest owing to their exceptional mechanical properties. However, the molecular dynamics simulations of such multi-component systems are hindered due to a lack of interatomic potentials. The advent of the meta-atom method to compute the atomistic simulations of such complex alloys has shown a promising alternative. In the meta-atom framework, all the elements in the alloy are represented as a single meta-atom whose force-field interactions are fitted to the primary properties of the real alloy obtained from the first principle calculations [1,2]. The technique has been used for extensive simulations of plastic deformation which is a tertiary property. Kumari and Dutta [3], in a recent work, noted that although the meta-atom potential is tuned to the primary properties of the alloy, the molecular dynamics simulations performed using the potential investigate the tertiary properties like the overall deformation behavior of simulation samples. This leaves a grey region consisting of secondary properties through which the primary properties are transferred to the tertiary properties. In the context of the deformation of metallic alloys, the secondary properties concern dislocation mobility, cross-slip, etc. Even though the development of the meta-atom potential entails the computation of primary properties, the succeeding research has specifically focused on the tertiary properties. Hence, a critical examination of the secondary properties employing the potential is necessary to assess the transferability of the properties. In the current work, we compute the core structure and Peierls stress of full and twinning dislocations in TWIP steel employing the semi-discrete variational approach to Peierls Nabarro (SVPN) model in conjunction with the meta-atom framework. Also, the same method is used to examine the effect of Escaig stress on the stacking fault width. The results thus obtained are then compared to the critical length scale of the meta-atom potential.

## 2. Results and discussions

The two-dimensional generalized stacking fault energy (GPFE) of TWIP steel constructed over the  $\langle 111 \rangle$  plane is shown in Figure 1(a). The one-dimensional projection along  $\langle 112 \rangle$  can also be depicted in Figure 1(b). A stable stacking fault is observed for a shift of Burgers vector i.e.,  $a\langle 112 \rangle/b$ . Figure 1(c) exhibits the generalized planar fault energy (GPFE) of TWIP steel constructed over the  $\langle 111 \rangle$  plane and its one-dimensional projection along the  $\langle 112 \rangle$  is shown in Figure 1(d). Unlike the GSFE plot, the GPFE does not exhibit a stable stacking fault energy for

---

The publication is co-financed from the state budget under the programme  
of the Minister of Education and Science called "Excellent Science" project no. DNK/SP/548041/2022



a displacement of the Burgers vector. This can be attributed to the fact that the energy remains unchanged for the displacement and only the twin boundary is migrated by one atomic plane.

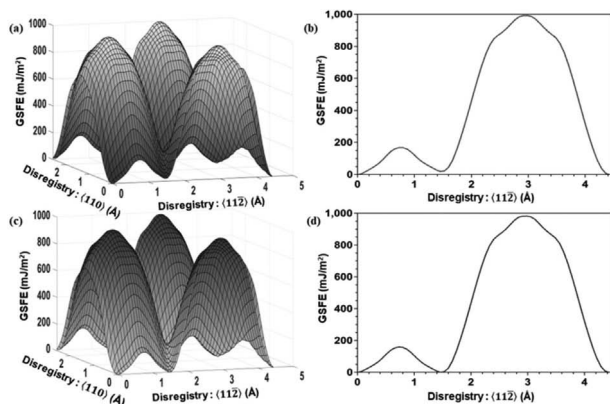


**Figure 1.** a) Two and b) one-dimensional GSFE vs the misfit for the TWIP steel over the  $\langle 111 \rangle$  slip plane in. c) Two and d) one-dimensional GPF constructed for the misfit over the twin boundary.

Figure 2 reveals the disregistry and disregistry density profiles of perfect edge and screw dislocations obtained from the SVPN model. The first important observation is that the full dislocations have dissociated into Shockley partials owing to the low stable stacking fault energy (Figure 1(a)). Also, the stacking fault ribbon of the screw dislocation  $\sim 53 \text{ \AA}$  is smaller compared to the edge counterpart  $\sim 102 \text{ \AA}$ . The values are also validated through the atomistic simulations performed for the same defects considered. The disregistry density profiles disclose that the edge Shockley partials are wider than the screw partials. Positive Escaig stress computed from the SVPN model for edge and screw Shockley partials were found to be 200 MPa and 250 MPa respectively. Employing the same SVPN model, the core structure of edge and screw twinning dislocations are also computed.

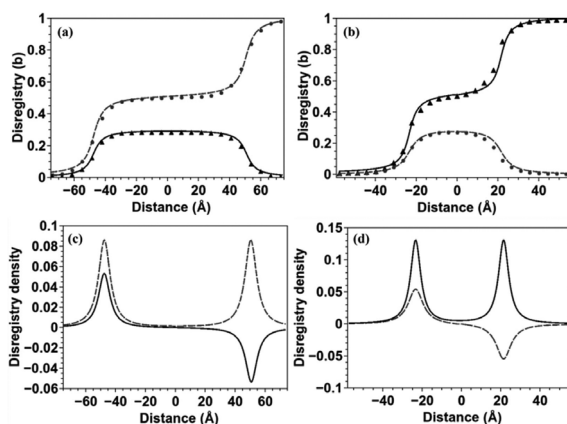


**Figure 1.** Disregistry vector of (a) edge and (b) screw dislocations with Burgers vector,  $a\langle 110 \rangle/2$ , obtained from the SVPN model (lines) and molecular statics simulations (scattered). The dashed lines correspond to the edge components of the Shockley partials, whereas the solid lines represent their screw counterparts. (c) and (d) show the disregistry densities for the same edge and screw dislocations, respectively.

### 3. Conclusions

- The core width and the Peierls stress of perfect dislocations computed through the SVPN model are in good agreement with the atomistic simulation data.
- The stacking fault widths obtained from the model are in accordance with the atomistic simulations.
- The positive Escaig stress calculated from the simple analytical model overestimates the value obtained from the SVPN model emphasizing the finer elements missing in the linear continuum model.
- The core widths obtained through the meta-atom framework can be considered as average values, as their length scales are one order less in magnitude when compared to the statistical lengths scales of the framework.

### References

1. Wang P., Xu S., Liu J., Li X., Wei Y., Wang H., Gao H., Yang W.: *Atomistic simulation for deforming complex alloys with application toward TWIP steel and associated physical insights*. Journal of Mechanics and Physics of Solids, 98, 2017, 290.
2. Wang P., Wang H.: *Meta-Atom Molecular Dynamics for Studying Material Property Dependent Deformation Mechanisms of Alloys*. Journal of Applied Mechanics, 84, 2017, 111002.
3. Kumari S., Dutta A.: *Assessment of meta-atom scheme for nucleation of dislocation loops in TWIP steel*. Computational Materials. Science, 209, 2022, 111430.

**Acknowledgements.** SRP is thankful to the Tata Consultancy Services foundation for the financial assistance provided through the TCS scholarship program.

# Modelling of phase transformations in steels accounting for a stochastic character of the austenite grain size after hot forming

Danuta Szeliga<sup>1</sup>, Natalia Czyżewska<sup>2</sup>, Jan Kusiak<sup>1</sup>,  
Piotr Oprocha<sup>2</sup>, Maciej Pietrzyk<sup>1</sup>, Paweł Przybyłowicz<sup>2</sup>

AGH University of Science and Technology, al. Mickiewicza 30, 30-059 Kraków, Poland

<sup>1</sup> Faculty of Metals Engineering and Industrial Computer Science

<sup>2</sup> Faculty of Applied Mathematics

szeliga@agh.edu.pl, nczyzew@agh.edu.pl,

kusiak@agh.edu.pl, oprocha@agh.edu.pl,

maciej.pietrzyk@agh.edu.pl, przybyl@agh.edu.pl

**Keywords:** Stochastic model, hot rolling, grain size, phase transformations, uncertainty

## 1. Introduction

Exploring a possibility of a stochastic modelling of thermomechanical processing is the objective of our research. Motivations for these research were twofold. Firstly, the continuous development of the industry is associated with the search for construction materials with exceptional properties. Heterogeneous materials meet these requirements and they are now widely used in forms of metallic alloys, among which multiphase steels are a leading example [1]. Secondly, a problem of the uncertainty of predictions of product microstructure and properties is important today [2]. Knowledge of the possible spread of the predicted target values, such as microstructural parameters, is needed for a reliable process design. Investigation of both these aspects requires advanced models, which can predict distribution of microstructural features instead of their average values. Although a number of material models with various complexity and predictive capabilities has been recently developed [3], mean-field models are still commonly used in the design of processes. It is due to low computing costs of these models. On the other hand, predictive capabilities of the mean-field models are limited and it leads to limitations of the design methodologies. Therefore, we focused on a search for a possibility to extend predictive capabilities of the mean-field model while the computing costs are kept on a reasonably low level. It has been shown in [4], that the model with internal stochastic variables allows description of the heterogeneous microstructure of metals accounting for distributions of various features. Following this, we developed the stochastic model, which describes evolution of the dislocation density and the grain size during hot deformation. Analysis and optimization of the numerical parameters of this model are described in [5] while its identification, validation and application to the hot rolling is presented in [6]. It should be pointed out, however, that properties of product are obtained by a control of phase transformations during cooling after hot forming. In our first approach to this process the deterministic phase transformation model was used with the stochastic initial conditions in the form of dislocation density and grain size histograms calculated by the hot deformation model.

---

The publication is co-financed from the state budget under the programme of the Minister of Education and Science called "Excellent Science" project no. DNK/SP/548041/2022



**Doskonała  
Nauka**



Ministry of Education and Science  
Republic of Poland



**Republic  
of Poland**

## 2. Model and results

Details of the stochastic hot deformation model are described in [5,6]. In this model, the critical time for dynamic recrystallization in the deterministic model [7], which is not a physical quantity, was replaced by the stochastic variable  $\xi(t_i)$ . After discretization in time, the evolution of the dislocation density in function of time is governed by the following equation [5]:

$$\rho(t_i) = \rho(t_0)[1 - \xi(t_i)] + \{\rho(t_{i-1}) + [A_1 \dot{\epsilon} - A_2 \rho(t_{i-1}) \dot{\epsilon}^{1-a_7}] \Delta t\} \xi(t_i) \quad (1)$$

where:  $t$  – time,  $\rho$  – dislocation density,  $A_1, A_2$  – coefficients responsible for hardening and recovery and defined in [5],  $a_7$  – a coefficient responsible for the strain rate sensitivity of the recovery.

The parameter  $\xi(t_i)$ , accounts for a random character of the recrystallization and its distribution is described by the conditions:

$$\begin{cases} \mathbf{P}[\xi(t_i) = 0] = \begin{cases} p(t_i) & \text{if } p(t_i) < 1 \\ 1 & \text{otherwise} \end{cases} \\ \mathbf{P}[\xi(t_i) = 1] = 1 - \mathbf{P}[\xi(t_i) = 0] \end{cases} \quad (2)$$

where:  $p(t_i) = a_4 \rho(t_{i-1})^{a_5} \frac{3\gamma(t_i)\tau}{D(t_{i-1})} \exp\left(\frac{-a_6}{RT}\right) \Delta t$

where:  $D$  – grain size,  $R$  – gas constant,  $T$  – temperature in K,  $\tau$  – energy per unit dislocation length,  $\gamma$  – a mobile fraction of the recrystallized grain boundary,  $a_4, a_5, a_6$  – coefficients.

Presented model calculates distributions of the dislocation density and the grain size during hot deformation. This model was used to supply the input data for the simulations of phase transformations. The kinetics of transformations was calculated from the upgrade of the JMAK equation described in [3]. This upgrade accounts for the influence of the state of the austenite (grain size, dislocation density) on the transformations. All calculations were performed for the multiphase CP steel. The hot strip rolling process in the 6-stand finishing mill was considered as an example. The slab thickness was 66 mm and the pass schedule 66 → 40.6 → 19.1 → 9.4 → 5.43 → 3.58 → 2.9 mm was investigated, see [6] for details. The entry temperature to the finishing mill was 1010°C and the rolling velocity in the last stand was 5 m/s. The innovative route for the multiphase steel strips, which assumes ultra-fast cooling (UFC) after stands 4 and 5, was simulated. In consequence, rolling in the stands 5 and 6 was below the recrystallization temperature. Typical results for these two passes are shown in Figure 1. The distributions of the dislocation density and the grain size at the temperature  $A_{e3}$  were used as an input data for simulations of phase transformations.

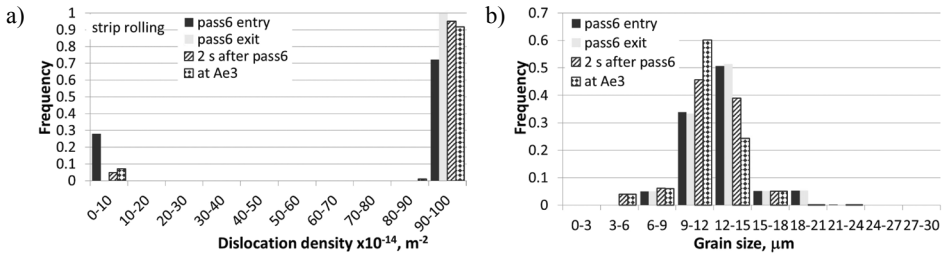
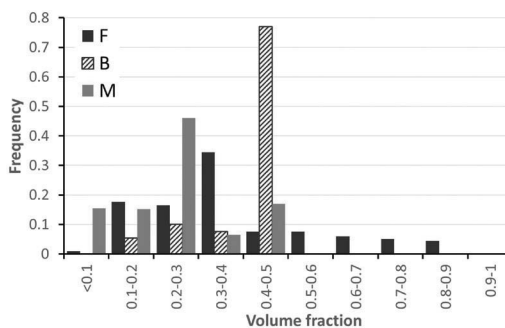


Figure 1. Calculated distributions of the dislocation density (a) and the grain size (b) at various stages of the process.

A typical system of laminar cooling after hot rolling [8] was considered as an example of a practical application of the model. The system is composed of two sections each divided into 4 zones. Cooling conditions, which compose water fluxes and corresponding heat transfer coefficients, are given in [8]. Rolling velocity, strip thickness and entry temperature, as well as histograms of the grain size and the dislocation density (Figure 1) at the beginning of phase transformations, were an input data for the simulations. The optimal cooling sequence, which should give 42% of ferrite, 44% of bainite and 14% of martensite for the strip thickness 2.9 mm, strip velocity 5 m/s and average grain size 15  $\mu\text{m}$ , was considered. The effect of the dislocation density on the phase transformations was accounted for following the data published in [9]. Beyond the grain size, a stochastic character of the temperatures was accounted for. This was done in a qualitative manner only. Due to a lack of the large data set necessary for the statistical analysis, a Gauss distribution of the entry temperature with the standard deviation of 12°C was assumed on the basis of measurements in one of the hot strip mills. Time-temperature profile during cooling for the optimal cooling conditions was calculated by the FE program. The stochastic model predicted distributions (histograms) of such parameters as volume fractions of phases and size of ferrite grains. Selected result of calculations for the volume fractions is shown in Figure 2.



**Figure 2.** Calculated histograms of the phase composition after cooling.

It is seen that the heterogeneity of the microstructure prior to transformations and uncertainty of the temperatures result in heterogeneity of the phase composition. Although the volume fraction of the bainite is reasonably stable, the fractions of the ferrite and the martensite are more sensitive to variations of the parameters. On the basis of all simulations it was concluded that: i) Heterogeneity of the dislocation density and the grain size results in the heterogeneity of the phase composition in the final product. When the cooling rate increases, the heterogeneity of the microstructure increases; ii) Increase of the dislocation density prior to phase transformations accelerates ferritic transformation. In consequence, the volume fractions of bainite and martensite are lower. This effect is stronger for larger cooling rates; iii) In simulations we assumed stochastic character of the temperatures during cooling. It allowed to show the capability of the model to account for the uncertainty of the boundary conditions. Large number of the temperature measurements, which will allow statistical analysis of the data, is necessary for the reliable prediction of the uncertainty of the simulations.

In the presented solution deterministic model of phase transformations was used. Randomness was introduced in the solution by a stochastic character of the input data and the boundary conditions. Accounting for the stochastic character of the nucleation of the new phase during phase transformations should improve the reliability of the solution, what will be an objective of our future works.

## References

1. Chang Y., Lin M., Hangen U., Richter S., Haase C., Bleck W.: *Revealing the relation between microstructural heterogeneities and local mechanical properties of complex-phase steel by correlative electron microscopy and nanoindentation characterization*, Materials and Design, 203, 2021, 109620.
2. Henke T., Bambach M., Hirt G.: *Quantification of uncertainties in grain size predictions of a microstructure-based flow stress model and application to gear wheel forging*. CIRP Annals – Manufacturing Technology, 62, 2013, 287–290.
3. Pietrzyk M., Madej Ł., Rauch Ł., Szeliga D.: *Computational Materials Engineering: Achieving high accuracy and efficiency in metals processing simulations*. Butterworth-Heinemann, Elsevier, Amsterdam, 2015.
4. Szeliga D., Czyżewska N., Klimczak K., Kusiak J., Kuziak R., Morkisz P., Oprocha P., Pidvysotsk'yy V., Pietrzyk M., Przybyłowicz P.: *Formulation, identification and validation of a stochastic internal variables model describing the evolution of metallic materials microstructure during hot forming*. International Journal of Material Forming, 15, 2022, 53.
5. Klimczak K., Oprocha P., Kusiak J., Szeliga D., Morkisz P., Przybyłowicz P., Czyżewska N., Pietrzyk M.: *Inverse problem in stochastic approach to modelling of microstructural parameters in metallic materials during processing*. Mathematical Problems in Engineering, 2022, article ID 9690742.
6. Szeliga D., Czyżewska N., Klimczak K., Kusiak J., Kuziak R., Morkisz P., Oprocha P., Pietrzyk M., Poloczek Ł., Przybyłowicz P.: *Stochastic model describing evolution of microstructural parameters during hot rolling of steel plates and strips*. Archives of Civil and Mechanical Engineering, 22, 2022, 239.
7. Davies C.H.J.: *Dynamics of the evolution of dislocation populations*. Scripta Metallurgica et Materialia, 30, 1994, 349–353.
8. Pietrzyk M., Kusiak J., Kuziak R., Madej Ł., Szeliga D., Gołąb R.: *Conventional and multiscale modelling of microstructure evolution during laminar cooling of DP steel strips*. Metallurgical and Materials Transactions B, 46B, 2014, 497–506.
9. Pietrzyk M., Kuziak R., Kondek T.: *Physical and numerical modelling of plastic deformation of steels in two-phase region*. Proc. 45<sup>th</sup> MWSP Conf., Chicago, 2003, 209–220.

**Acknowledgements.** Financial assistance of the NCN, project no. 2021/43/B/ST8/01710, is acknowledged.

# Experimental and numerical investigation of extrudate swell of polylactic acid (pla) via material extrusion (mex) additive manufacturing process

Hong Wang<sup>1</sup>, Abel Cherouat<sup>1</sup>, Alexandre Gilbin<sup>2</sup>, Thierry Barriere<sup>2</sup>

<sup>1</sup> University of Technology of Troyes-GAMMA3, 12 Rue Marie Curie, Troyes, 10004, France

<sup>2</sup> FEMTO-ST Institute/Applied Mechanics Department,  
24 rue de l'épitahe, 25000 Besancon, France  
hong.wang@utt.fr abel.cherouat@utt.fr  
alexandre.gilbin@ens2m.fr,  
thierry.barriere@univ-fcomte.fr

**Keywords:** MEX, Additive manufacturing, Extrudate swell, Polylactic acid, Level Set

## Abstract

Extrudate swell is a rheological phenomenon of polymers taking place after emerging the extrusion die due to the residual molecular stress relaxation, which is of great essential for ensuring the precision and stability of products manufactured by Material Extrusion (MEX) Additive Manufacturing (AM) process. Extrudate swell can be affected by multiple factors including the material properties and processing parameters that can be coupled and make it challenging to fully understand their effects, especially in absence of precise online measurement techniques. In this study, we investigated experimentally the extrudate swell as a function of the extrusion rate, melt temperature and nozzle diameter for polylactic acid (PLA). The Computational Fluid Dynamic (CFD) and Level Set (LS) method in COMSOL Multiphysics were used to simulate the polymer flow exiting the extrusion nozzle exit. The simulation results match well with experimental results and show that the swell ratio decreases with increasing temperature and nozzle diameter and decreasing extrusion rate. These results can be used to optimize the parameters of EAM processes.

## 1. Introduction

Material Extrusion (MEX) Additive Manufacturing (AM) process [1], among the most widely used AM processes, involves extruding materials in their molten state through a die/nozzle and depositing them layer by layer to build complex shapes. The materials can be thermoplastics polymers or feedstocks composed of a binder and metal or ceramic powders, in filament or pellet shape. However, the viscoelasticity of the polymer melt would result in swelling of the extrudate, which can reduce the dimensional accuracy of the part or even lower the mechanical strength due to poor adhesion among the extrudates [2]. The extrudate swell can be affected by multiple factors, such as imposed shear stress, temperature, molecular weight and channel geometry [3]. Thus, understanding and tailoring the effect of the processing parameters on the extrudate swell is an important aspect in improving the quality of MEXAM manufactured parts.

This study presents the experimental measurements of the extrudate swell of polylactic acid (PLA) regarding melt temperature, extrusion rate and nozzle diameter. The numerical simulation

---

The publication is co-financed from the state budget under the programme of the Minister of Education and Science called "Excellent Science" project no. DNK/SP/548041/2022



Doskonała  
Nauka



Ministry of Education and Science  
Republic of Poland



Republic  
of Poland

was realized using COMSOL Multiphysics software. These results and analyses allow to predict and optimize the extrudate swell in MEXAM process.

## 2. Material and methodology

A dynamic camera was used to capture the images of the extrudate swell and an infrared was used to measure the temperature of the extrudate. Both cameras were installed perpendicular to the extrudate flow direction. Two nozzles with same extrusion length  $L$  and different nozzle diameter  $D$  were tested. The temperatures of 190°C, 200°C and 210°C were tested, and each temperature was related to four extrusion speed (Rotation speed of the screw at 10, 20, 30 and 40 rpm).

The shear viscosity is determined at low shear rate with a rotational rheometer and at high shear rate with a capillary rheometer. The shear viscosity (1) depends on shear rate and temperature, and the dependencies are modelled by Carreau- Yasuda model (2) and Arrhenius model (3) respectively:

$$\eta(\dot{\gamma}, T) = a_T \eta(\dot{\gamma}, T_0) \quad (1)$$

$$\eta = \eta_\infty + (\eta_0 - \eta_\infty) \left(1 + (\lambda \dot{\gamma})^n\right)^{\frac{n-1}{n}} \quad (2)$$

$$a_T = \exp\left[\frac{E_a}{R} \left(\frac{1}{T} - \frac{1}{T_0}\right)\right] \quad (3)$$

where  $\eta_0$  is the viscosity for zero shear rate,  $\eta_\infty$  the viscosity at infinite shear rate,  $\lambda$  the characteristic time of the material,  $a$  the parameter adjusting the transition regime between the Newtonian plateau and the shear-thinning regime,  $n$  the pseudo- plasticity index,  $\dot{\gamma}$  the shear rate,  $T$  the temperature,  $T_0$  the reference temperature,  $E_a$  the activation energy and  $R$  the gas constant.

The numerical simulation was carried out by using Computational Fluid Dynamics (CFD) in COMSOL Multiphysics software. In addition to the built-in Navier-Stokes equations which describes the motion of the fluid, the Level Set (LS) method (4) was used to track the interface of two immiscible fluids (polymer and air in this case).

$$\frac{\partial \phi}{\partial t} + \nabla \cdot (\mathbf{u} \phi) = \gamma \nabla \cdot \left( \epsilon_{ls} \nabla \phi - \phi(1 - \phi) \frac{\nabla \phi}{|\nabla \phi|} \right) \quad (3)$$

where  $\phi$  is the volume fraction of the polymer in the computational volume,  $t$  the time,  $\mathbf{u}$  the velocity vector,  $\gamma$  the reset parameter and  $\epsilon_{ls}$  the interface thickness control. The volume fraction varies between 0 and 1, with 1 indicating a complete filling of the designed volume by the polymer. The value 0.5 is assigned to the interface between the polymer and the air.

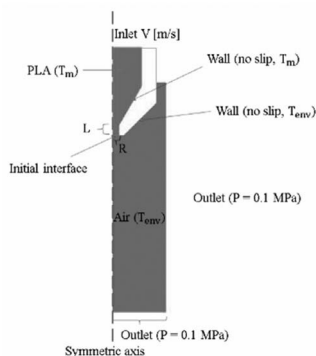
Figure 1 represents the geometry of the model and the boundary conditions for the simulation of flow existing the nozzle.

$T_m$  and  $T_{env}$  represent the melt temperature and the environment temperature respectively.

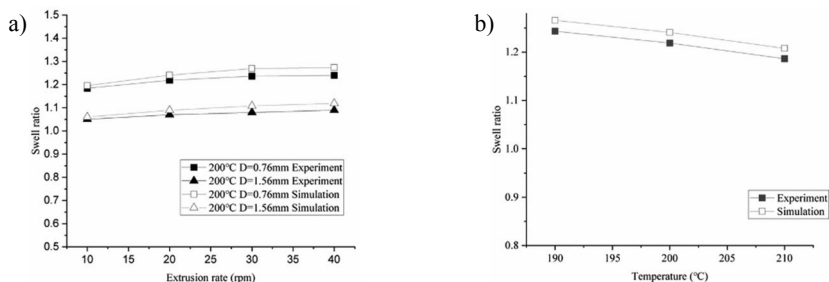
## 3. Results and discussion

Figure 2 compares the swell ratio (ratio of extrudate diameter to nozzle diameter) between experimental and numerical results. Figure 2 (a) shows that for the extrusion of PLA at 200°C, the swell ratio increases with increasing the extrusion rate for both nozzles while the nozzle of larger diameter has lower swell ratio, which is in accordance with literature [4]. Figure 2(b) shows that the

swell ratio decreases with increasing the temperature. The deviation between the simulation results and experimental results was within 4%, which proves that the simulation correlates well with the experimental results and can be used to investigate and optimize the processing parameters. According to the above results, it can be concluded that reducing the extrusion swell can be achieved by decreasing the extrusion rate, increasing the melt temperature and nozzle diameter, but the printing speed and dimensional resolution should be considered.



**Figure 1.** Geometry of the model and related boundary conditions for the swelling simulation.



**Figure 2.** Comparison of experimental and numerical results of swell ratio for (a) extrusion rate and (b) temperature (20 rpm).

## References

1. Rane K., Strano M.: *A comprehensive review of extrusion-based additive manufacturing processes for rapid production of metallic and ceramic parts*. Advances in Manufacturing, 7, 2019, 155–173.
2. Turner B.N., Strong R., Gold S.A.: *A review of melt extrusion additive manufacturing processes: I. Process design and modeling*. Rapid Prototyping Journal, 20, 2014, 192–204.
3. Sinthavathavorn W., Nithitanakul M., Grady B.P., Magaraphan R.: *Melt rheology and die swell of PA6/LDPE blends by using lithium ionomer as a compatibilizer*. Polymer Bulletin, 63, 2009, 23–35.
4. Serdeczny M.P., Comminal R., Pedersen D.B., Spangenberg J.: *Experimental and analytical study of the polymer melt flow through the hot-end in material extrusion additive manufacturing*. Additive Manufacturing, 32, 2019, 100997.

# Environment monitoring and sensor layers data integration in the production process of the electrosteel plant

Andrzej Opaliński<sup>1</sup>, Piotr Hajder<sup>1</sup>, Monika Pernach<sup>1</sup>, Łukasz Sztangret<sup>1</sup>,  
Krzysztof Regulski<sup>1</sup>, Krzysztof Bzowski<sup>1</sup>, Łukasz Rauch<sup>1</sup>, Michał Piwowarczyk<sup>2</sup>  
<sup>1</sup> AGH University of Science and Technology, Al. Mickiewicza 30, 30-059, Kraków, Poland  
<sup>2</sup> CMC Poland sp. z o.o. ul. Piłsudskiego 82, 42-400 Zawiercie, Poland  
opal@agh.edu.pl, phajder@agh.edu.pl,  
pernach@agh.edu.pl, szt@agh.edu.pl,  
regulski@agh.edu.pl, kbzowski@agh.edu.pl,  
lrauch@agh.edu.pl, michal.piwowarczyk@cmc.com

**Keywords:** sensors integration, pattern recognition, Industry 4.0

## 1. Introduction

Modern production systems consist of an increasing number of devices, most of which provide digital interfaces enabling access to information about the production process at individual stages of production. This feature is used in the concept of Industry4.0 systems, in which the real production process is mapped to a virtual model on which advanced methods of optimization and support of the production process can be applied [1]. A similar type of solution was presented in this work. Its main component enables monitoring the state of the technological process in the hall of the CMC Zawiercie electrosteel plant. This module is based on the integration of data from heterogeneous sensor systems of the electrosteel plant and the component of visual detection of main ladles (MLs) from CCTV system. The work presents the general concept and main components of the system and the mechanism of its operation.

## 2. System architecture

A known problem in the production of steel products [2,3] and the main functionality of the solution implemented under this project is the optimization of the production process by maintaining the appropriate time and temperature parameters of this process, required to produce products in specific steel grades. Failure to meet such parameters by overheating or cooling down the charge or too much extension of the charge transport time in the main ladle (ML) on the way from the electric arc furnace (EAF) through the ladle furnace (LF) to the continuous steel casting station (CSC) makes it impossible to produce final products with specific parameters (steel grades).

The scheme of the system enabling the implementation of such functionality is presented in Figure 1 (a). One of the main components of this system is the metamodeling module which enables optimization of production volume and minimization of risk associated with a temperature. The optimization is performed by metamodel based on linear regression and neural network for the temperature drop which is occurring during the transport of liquid steel to the casting machine. The data on which the process optimization metamodel works comes from several heterogeneous data sources.

---

The publication is co-financed from the state budget under the programme of the Minister of Education and Science called "Excellent Science" project no. DNK/SP/548041/2022



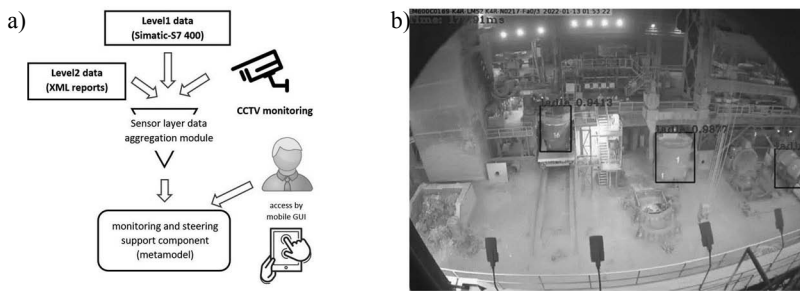


**Figure 1.** Overall system architecture (a) and main ladle (ML) detection module GUI (b).

These are: the sensor layer (Level1 and Level2 systems) and the ML recognition module operating on the basis of the CCTV system (Figure 1 b). The whole is aggregated by the sensory data integration component, enabling the implementation of two main functionalities provided by the system:

- Optimization of the production process (metamodeling component),
- Monitoring the status of the steelmaking process – based on mobile applications used by the staff.

## 2.1. Sensor layers

The two main sensory sources containing numerical data, on the basis of which the subsequent components of the system operate, are the Level1 and Level2 systems.

Level1 is a low-level hardware layer, integrated directly with the device controllers involved in the production process (EAF station, LF station, CSC station) which provides parameters (in real time) about the current state of these devices. Integration with this layer was based on the connection with Siemens Simatic S7 400 controller implemented by Sharp7 library, which is C# port of SnaIp7 library. The data obtained from this layer include: the current temperature of the ML armor, the latest values of liquid steel temperature measurements, the current duration of the process at the EAF or LF station and the current amount of energy consumed at individual stations.

The Level2 system is another sensory layer of the steelworks hall, which provides data on the parameters of the process after the end of charge processing in the main ladle (ML) at individual stages of the production process (EAF, LF, CSC stations). This layer provides additional data on the production process regarding the entire production plan and a specific melt carried out in a given ML (grade, sequence in the production process, charge weight, chemical composition, oxygen and carbon content, total processing time on a given station, melting process efficiency) . This information is supplementary to the data from the Level1 system, however, it is not provided in real time, and appear in the system only at the end of ML processing at a particular station. Numerical data from the Level2 system is delivered in the form of XML file reports, which are detected and parsed using FileWatcher, xsd tools and standard C# libraries used to parse XML documents.

## 2.2. Vision processing

The image processing component performs two main functionalities - vat detection and identification of vat numbers. As part of the work on the vat detection issue, 4 different machine learning models were tested to check their effectiveness – Mask-RCNN, MobileNet, YOLOv3 and its tiny version. All were trained on a group of more than 8000 images where about 2000 were additionally modified with ImgAug tool. In addition, about 700 images of the electrosteel hall without MLs

have been added. The test data was divided into the classic 80%-training; 20%-validation sets. Two models were used in the problem of identifying the ladle number: pretrained CRAFT[4] and custom convolutional recurrent neural network. The results of the runtimes and vat detection efficiency are presented in Table 1. Python 3.10 and tensorflow 2.10 were used to implement the solution, and the models were built using the Keras library.

**Table 1.** Training and accuracy results of model used.

Parameter	Mask RCNN	MobileNet	YOLOv3	YOLOv3 tiny
Training time, h	6.32	3.57	2.51	0.89
Detection time CPU, ms	1 840	1 380	430	101
Detection time GPU, ms	680	450	173	37
Accuracy (typical position), %	96	95	94	92
Accuracy (overall), %	88	85	82	68

Vat detection performance at standard locations does not vary much between models. The difference starts to be visible only when atypical locations are taken into account (lower efficiency of the YOLOv3 tiny model). It has also been observed that the effectiveness of vat detection and identification of the vat number decreases slightly in situations where there is smoke or violent light flashes on the stage, which is a difficult case, because in such cases even the vision system operator has trouble recognizing the vat number.

### 2.3. Data aggregation component

Integration of data from various sensory layers (Level1, Level2, CCTV) is carried out in the system in the component that aggregates this data and makes it available to the optimization (metamodeling) and the process monitoring (by a mobile application) components. The exchange of information between these components is based on the open source message broker RabbitMQ. The component of monitoring the condition of the steelworks hall itself takes into account the accuracy and reliability of data from individual components in its operation. Data from the Level2 system have the highest priority (they are partially verified by the operator). They are then supplemented with data on the current state of the process provided from the Level1 layer (up-to-date data, but without information on the general state of the process). Data from the CCT system enable precise positioning of individual MLs within the entire hall (but they are the least accurate – there are situations of detecting a ML without recognizing its number or detecting a ML with an incorrect number). Adjustments to the ladle numbering are made based on data from the Level2 system, taking into account the sequencing of the ML processing scheme in the electrosteel hall.

## 3. Results and further works

As part of the presented works, an IT system was developed, which during the 18 months of operation (from the implementation phase of the prototype version) collected data on the production process in the steelworks hall. The currently collected data relate to: over 16 000 reports on melts at CSC, LF and EAF stations; number of temperature measurements: over 33 000 at the EAF, over 94 000 at LF stations, over 81 000 at CSCs; 58 000 tests of the chemical composition of steel, 75 different grades of steel. Currently, the system is in the phase of integrating its individual components, testing its effectiveness and implementing it to the production environment. Initial tests of individual components within the infrastructure tested in CMC Sp. z o. o. in Zawiercie (Poland) show that they work properly and can successfully support the process of continuous casting of steel carried out in the hall of the electrosteel plant of a given company.

## References

1. Gajdzik B., Wolniak R.: *Framework for R&D&I activities in the steel industry in popularizing the idea of industry 4.0*. Journal of Open Innovation: Technology, Market, and Complexity, 8, 2022, 133.
2. Xu Z., Zheng Z., Gao X.: *Energy-efficient steelmaking-continuous casting scheduling problem with temperature constraints and its solution using a multiobjective hybrid genetic algorithm with local search*. Applied Soft Computing, 95, 2022, 106554.
3. Myers R.H., Montgomery D.C., Anderson-Cook C.M.: *Response surface methodology: process and product optimization using designed experiments*. John Wiley & Sons, 2016.
4. Baek Y., Lee B., Han D., Yun S., Lee H.: *Character region awareness for text detection*. Proc. IEEE Conference on Computer Vision and Pattern Recognition, 2019, 9365–9374.

**Acknowledgements.** Financial support of the NCBiR, Project No. POIR.01.01.01-00-0996/19, is acknowledged.

## Index of Authors

### A

Amirthalingam Murugaiyan ..... 31

### B

Bairagi Darothi ..... 35  
Barriere Thierry ..... 192  
Bastl Pavel ..... 39  
Beitelschmidt Michael ..... 65  
Böllinghaus Thomas ..... 138  
Byrski Aleksander ..... 168  
Bzowski Krzysztof 94, 108, 127, 152, 156,  
174, 195

### C

Cacko Robert ..... 182  
Chakraborti Nirupam ..... 17, 20, 39  
Cherouat Abel ..... 192  
Chiu ChenChun ..... 71  
Czech Krzysztof ..... 168  
Czyżewska Natalia ..... 188

### D

Datta Shubhabrata ..... 26  
David Petr ..... 17  
Devadula Sivasrinivasu ..... 31  
Dębiński Tomasz ..... 124, 180  
Dhason Raja ..... 26  
Diegelmann Volker ..... 171  
Dobija Mateusz ..... 51  
Domitner Josef ..... 138  
Drexler Andreas ..... 138  
Dutka Łukasz ..... 81  
Dutta Amlan ..... 23, 185  
Dychtoń Kamil ..... 177

### F

Filip Ryszard ..... 177

Foryś Jakub ..... 75

### G

Garbarz Bogdan ..... 156  
Gilbin Alexandre ..... 192  
Głowacki Mirosław ..... 133  
Golak Sławomir ..... 118  
Gronostajski Zbigniew ..... 68

### H

Hajder Piotr ..... 108, 127, 152, 174, 195  
Hanoglu Umut ..... 84  
Hojny Marcin ..... 124, 180  
Hrcek Slavomir ..... 13  
Hrytsyna Maryan ..... 13  
Hyrcza-Michalska Monika ..... 105

### I

Irani Missam ..... 114  
Iżowski Bartosz ..... 177

### J

Jabłońska Magdalena Barbara ..... 68  
Jasiak Katarzyna ..... 68  
Jiregna Iyasu Tafese ..... 62

### K

Kamińska Jadwiga ..... 133  
Kisiel-Dorohinicki Marek ..... 168  
Kitowski Jacek ..... 81  
Kochański Andrzej ..... 91  
Kopyściański Mateusz ..... 130  
Korpala Grzegorz ..... 71, 114  
Kovačič Miha ..... 84  
Kowalczyk Karolina ..... 68

Krambeer Hagen.....	171
Krentzien Maximilian.....	65
Krishnaswamy Hariharan.....	31
Kryza Bartosz.....	81
Krzywda Maciej.....	111
Kumari Sweta.....	23
Kusiak Jan.....	127, 152, 188
Kuś Waław.....	62
Kuziak Roman.....	75, 94
Kwiecień Marcin.....	130

## L

Lypchanskyi Oleksandr.....	71
Łoś Marcin.....	51

## M

Maczuga Paweł.....	55
Madej Łukasz.....	142, 164
Madej Piotr.....	118
Mahanta Bashista Kumar.....	31
Major-Gabryś Katarzyna.....	133
Majta Janusz.....	130
Malinowski Łukasz.....	164
Małysz Marcin.....	133
Mandal Sumantra.....	35, 44
Mareš Tomáš.....	17, 20
Marynowski Przemysław.....	180
Matuszyk Dominika.....	88
Milenin Andrij.....	94
Milenin Ivan.....	94, 149
Mraczek Klemens.....	138
Mrzyglód Barbara.....	180
Mucha Waldemar.....	62
Muszka Krzysztof.....	130

## N

Nietzke Janathan.....	138
-----------------------	-----

## O

Olejarczyk-Wożeńska Izabela.....	180
Opaliński Andrzej.....	108, 195
Oprocha Piotr.....	188

Orzechowski Michał.....	81
-------------------------	----

## P

Padovec Zdeněk.....	20
Paliwal Manas.....	35
Panda Sushanta Kumar.....	44
Paszkowicz Wojciech.....	79
Paszyńska Anna.....	51
Paszyński Maciej.....	47, 51, 55
Pawlikowski Kacper.....	142
Pawłowski Bogdan.....	149
Pernach Monika.....	108, 127, 145, 149, 152, 174, 195
Pietrzyk Maciej.....	75, 94, 156, 188
Piwowarczyk Michał.....	108, 145, 195
Poloczek Łukasz.....	75
Postek Eligiusz.....	101
Prahl Ulrich.....	71, 114
Przybyłowicz Paweł.....	188
Pulagam Sri Sadgun Reddy.....	185
Puzio Sabina.....	133

## Q

Qayyum Faisal.....	71
--------------------	----

## R

Raga Krzysztof.....	156
Rakshit Rahul.....	35, 44
Ramteke Manojkumar.....	42
Rauch Łukasz.....	94, 108, 111, 127, 145, 149, 152, 156, 195
Regulski Krzysztof.....	108, 111, 127, 152, 174, 195
Roy Sandipan.....	26

## S

Sadłowska Hanna.....	91
Sadowski Tomasz.....	101
Sak Tomasz.....	118
Šarler Božidar.....	84
Shovay Towhid Faraji.....	114
Sitko Mateusz.....	142

Sladek Jan .....	13
Sladek Vladimir .....	13
Słota Renata G. ....	81
Służalec Tomasz .....	47
Sommitsch Christof .....	138
Svyetlichnyy Dmytro .....	88
Szeliga Danuta .....	75, 124, 160, 188
Sztangret Łukasz .....	145, 160, 195
Szyszka Anna Janina .....	97
Świłło Sławomir .....	182

### T

Tahani Masoud .....	101
Tiwari Jai .....	31
Tkocz Marek .....	68
Tyrała Dorota .....	149

### U

Urbańczyk Aleksandra .....	168
----------------------------	-----

### V

Valášek Michael .....	39
Vertnik Robert .....	84

Vondráček Dominik .....	20
-------------------------	----

### W

Wang Hong .....	192
Wędrychowicz Przemysław .....	59
Wierzbę Bartek .....	120
Wilk-Kołodziejczyk Dorota .....	133
Witek Szczepan .....	94
Wojtyczka Artur .....	177
Wolda Ataklit Kahsay .....	42
Wolff Andreas .....	171
Woźniak Maciej .....	97
Wrzeszcz Michał .....	81

### Y

Yang Hongliang .....	164
----------------------	-----

### Z

Zalecki Władysław .....	156
Zielińska Monika .....	164
Zupanc Aljaž .....	84
Zybała Radosław .....	118





The publication is co-financed from the state budget under the programme of the Minister of Education and Science called "Excellent Science" project no. DNK/SP/548041/2022 subsidy amount 63 470 PLN, total project value: 263 470 PLN



Ministry of Education and Science  
Republic of Poland



Republic  
of Poland

